ПУБЛИКАЦИЈЕ АСТРОНОМСКЕ ОПСЕРВАТОРИЈЕ У БЕОГРАДУ
PUBLICATIONS OF THE ASTRONOMICAL OBSERVATORY OF BELGRADE
Св. 99 No. 99

30th Summer School and International Symposium on the Physics of Ionized Gases

Šabac, Serbia,
August 24 -28, 2020

CONTRIBUTED PAPERS

&

ABSTRACTS of INVITED LECTURES, TOPICAL INVITED LECTURES and PROGRESS REPORTS

Editors:
Luka Č. Popović, Duško Borka,
Dragana Ilić and Vladimir Srećković

БЕОГРАД
2020

PUBL. ASTRON. OBS. BELGRADE No. 99, 1 - 344 BELGRADE, AUGUST 2020

30th Summer School and International Symposium on the Physics of Ionized Gases

August 24 – 28, 2020, Šabac, Serbia

S P I G 2020

CONTRIBUTED PAPERS

&

ABSTRACTS OF INVITED LECTURES,
TOPICAL INVITED LECTURES AND
PROGRESS REPORTS

Editors

Luka Č. Popović, Duško Borka,
Dragana Ilić and Vladimir Srećković

Faculty of Mathematics
(Department of Astronomy)
Astronomical Observatory
of Belgrade

Institute of Physics,
University of Belgrade

Belgrade, 2020

PUBLICATIONS OF THE ASTRONOMICAL OBSERVATORY OF BELGRADE

FOUNDED IN 1947

All papers in this Publication are peer reviewed.

Director of the Astronomical Observatory: Dr. Gojko Djurašević

Typesetting: Tatjana Milovanov

Internet address http://www.aob.rs

ISSN 0373-3742
ISBN 978-86-80019-94-9

Number of copies / tiraž : 250
Production: Skripta Internacional, Mike Alasa 54, Beograd

CIP - Каталогизација у публикацији - Народна библиотека Србије, Београд

537.56(082)
539.186.2(082)
539.121.7(082)
533.9(082)

SUMMER School and International Symposium on the Physics of Ionized Gases (30 ; 2020 ; Šabac)

Contributed papers & abstracts of invited lectures, topical invited lectures and progress reports / 30th Summer School and International Symposium on the Physics of Ionized Gases - SPIG 2020, August 24 - 28, 2020, Šabac, Serbia ; [organized by] Faculty of Mathematics (Department of Astronomy) [and] Institute of Physics, University of Belgrade [and] Astronomical Observatory of Belgrade ; editors Luka Č. Popović ... [et al.]. - Belgrade : Astronomical Observatory, 2020 (Beograd : Skripta Internacional). - 344 str. : ilustr. ; 24 cm. - (Публикације Астрономске опсерваторије у Београду, ISSN 0373-3742 ; св. 99 = Publications of the Astronomical Observatory of Belgrade ; no. 99)

Tiraž 250. - Str. 17-18: Preface / editors. - Bibliografija uz svaki rad. - Registar.

ISBN 978-86-80019-94-9

а) Јонизовани гасови -- Зборници б) Атоми -- Интеракција -- Зборници
в) Плазма -- Зборници

COBISS.SR-ID 18580233

SPIG 2020

SCIENTIFIC COMMITTEE

D. Borka (Co-chair), Serbia
L. Č. Popović (Co-chair), Serbia

R. White, Australia
J. Burgdörfer, Austria
J. Cvetić, Serbia
E. Danezis, Greece
Z. Donko, Hungary
V. Guerra, Portugal
D. Ilić, Serbia
M. Ivković, Serbia
I. Mančev, Serbia
D. Marić, Serbia
N. J. Mason, UK
A. Milosavljević, France
K. Mima, Japan
Z. Mišković, Canada
L. Nahon, France
B. Obradović, Serbia
G. Poparić, Serbia
P. Roncin, France
I. Savić, Serbia
Y. Serruys, France
N. Simonović, Serbia
M. Škorić, Japan
M. Trtica, Serbia
S. Tošić, Serbia

ADVISORY COMMITTEE

D. Belić
N. Bibić
M. S. Dimitrijević
S. Đurović
N. Konjević
M. M. Kuraica
J. Labat
G. Malović
B. P. Marinković
Z. Mijatović
M. Milosavljević
Z. Lj. Petrović
L. Č. Popović
J. Purić
B. Stanić

ORGANIZING COMMITTEE

D. Ilić (Co-chair)
V. Srećković (Co-chair)

J. Kovačević-Dojčinović (Co-secretary)
N. Cvetanović (Co-secretary)

J. Aleksić
A. Kovačević
S. Marčeta-Mandić
A. Nina
D. Onić
S. Simić
V. Zeković

CONTENTS

Contributed Papers

Section 2. PARTICLE AND LASER BEAM INTERACTIONS WITH SOLIDS

Invited Lecture

Topical Invited Lectures

Contributed Papers

Section 3. LOW TEMPERATURE PLASMAS

Invited Lectures

Topical Invited Lectures

Progress Reports

Contributed Papers

Section 4. GENERAL PLASMAS

Invited Lecture

Topical Invited Lectures

Progress Reports

Contributed Papers

Special Session "Atomic Collisions in Plasmas"
Devoted to Ratko Janev

PREFACE

This special issue of the Publication of Astronomical Observatory in Belgrade (PubAOB) contains the contributed papers and abstracts of Plenary Lectures, Topical Invited Lectures and Progress Reports that will be presented at the 30th International Symposium on the Physics of Ionized Gases (SPIG2020) which will be held from 24 to 28 August, 2020, in Šabac, Serbia. This period will be known as a very hard time, since COVID-19 pandemic affects all our activity, especially meetings. Therefore, the Organizing Committees of the SPIG2020 conference have carefully considered the current situation with the COVID-19 pandemic, and have decided that the conference should be organized as initially planned, but taking into account all the necessary measures and recommendations in order to make the safe environment for the SPIG2020 participants. We have faced additional challenges due to travel restrictions, therefore we introduced the virtual attendance for both Invited lecturers and participants for those who could not participate regularly. We expect to have virtual and regular participants, who will present 13 plenary invited talks, 17 topical invited 25 progress reports, 6 talks in honor of Ratko Janev and 60 posters.

The SPIG reflects the progress in the plasma physics and related fields. The conference has a long tradition, first meeting was organized in Belgrade in 1962. under the title: ”1st Yugoslav Symposium on the Physics of Ionized Gases”(SPIG), and this SPIG2020 will start with the session dedicated to 30th jubilee of SPIG conferences. This issue of PubAOB presents new results in the fundamental and frontier theories and technology in the area of plasma physics. There are 58 abstracts of invited lectures and 63 contributed papers from mainly four disciplines connected with physics of ionized gasses which have strong interactions in numerous applications: Atomic Collision Processes, Particle and Laser Beam Interactions with Solids, Low Temperature Plasmas and General Plasmas. Also, SPIG2020 Special Session: "Atomic Collisions in Plasmas" is organized in honor of Ratko Janev (1939-2019), who gave a significant contribution to the series of SPIG

conferences in the past. The SPIG2020 is organized by the University of Belgrade – Faculty of Mathematics and Institute of Physics, with the support of the Astronomical Observatory in Belgrade.

Editors would like to thank the members of the Scientific and Advisory Committees of SPIG 2020 for their efforts in proposing the invited lectures and review of the contributed papers, as well as to thank the authors for their contribution and support to this Publication. We are grateful to the Serbian Ministry of Education, Science and Technological Development for their continuing help.

Editors: Luka Č. Popović, Duško Borka,
Dragana Ilić and Vladimir Srećković

Belgrade, August 2020.

Section 1.

ATOMIC COLLISION PROCESSES

THE MEASUREMENT OF ELECTRON AND ION SWARMS TRANSPORT AND REACTIVITY: CURRENT STATE AND FUTURE CHALLENGES

J. de URQUIJO

Instituto de Ciencias Físicas, Universidad Nacional Autónoma de México
E-mail jdu@icf.unam.mx

Abstract. There is an increasing need of electron and ion swarm data due to the multiple industrial and fundamental applications of low-temperature plasma physics, such as materials processing, plasma medicine, biomolecules, atmospheric and high voltage insulation. Plasma simulation plays nowadays a fundamental role in the design of reactors for semiconductor fabrication and many other applications in which knowledge of either electron and ion swarm transport parameters such as drift velocity, Casey et al. 2019, and diffusion, on the one hand, and reactive processes such as ionization (electron impact, Penning, positive ion impact on surfaces and photon ionization in the realm of the gas), electron attachment and detachment and, on the other hand, a large number of ion-molecule reactions which play a fundamental role in the development of the plasma. The measurement and calculation of electron/ion-molecule cross sections are also essential for the above purposes. The link between electron/ion swarm coefficients and cross sections will be discussed. New gases for industrial applications and biomolecules have recently appeared, de Urquijo et al. 2019, J, Casey M.J.E. et al: 2019, González-Magaña et al. 2018, demanding the measurement and calculation of the cross sections involved the evolution of the plasma.

This talk reviews the present status of the experimental methods and analytical techniques to measure the above coefficients, their advantages and limitations, and also the collision cross sections derived from the measured swarm parameters. A particular emphasis will be placed in the discussion of the experimental limitations and suggest means to overcome some of them and expand the realms of measurement and accuracy of the above transport properties.

References

Casey, M. J. E., Cocks, D. G. et al.: 2019, *Plasma Sources Sci. Technol*., **28**, 115005.
de Urquijo, J., Casey, M. J. E. et al.: 2019, *J. Chem. Phys.*, **151**, 054309.
González-Magaña, O., de Urquijo, J.: 2018, *Plasma Sources Sci. Technol.*, **27**, 06LT02.

SYMPOSIUM ON PHYSICS OF IONIZED GASES: 60 YEARS OLD AND STILL GOING STRONG

ZORAN LJ. PETROVIĆ[1,2]

[1]*Serbian Academy of Sciences and Arts, Kneza Mihaila 35, 11001 Belgrade, Serbia*
[2]*School of Engineering, University of Ulster, CO Antrim BT37 0QB UK*
E-mail zoran@ipb.ac.rs

Abstract. A chance meeting of prof. B. Perović from the Vinča Institute and prof A von Engel has completely transformed national conference on Physics of Ionized Gases (Symposium on Physics of Ionized Gases-SPIG). Von Engel has suggested and brought top level invited speakers from the leading laboratories. For its third installment SPIG has become a truly international conference. Throughout its initial thirty years SPIG has quickly established certain principles and modus operandi. First it was a marriage of four distinct fields that may have been together in the past but were becoming separate. Those were atomic and molecular collisions; Collisions with surfaces; Low temperature plasmas and (high temperature) Plasma physics. Top experts in some fields commented that they liked SPIG for providing them an opportunity to hear news from the fields that are not their specialization but are still highly relevant to them. Originally there were mainly invited lectures (by foreign speakers) and progress reports by young scientists that recently defended their Ph.D. That provided an opportunity for young scientists from former Yugoslavia to measure their performance against the top experts in their respective fields and also to gain experience in presenting their own results. In addition, many young students were able to negotiate visits to the leading international laboratories thus gaining experience and bringing back topical science and techniques to their original laboratories. But both professional and personal connections were made at all levels and from all locations. Soon, upon the initiative from the leading foreign scientists leading scientists from Yugoslavia were offered invited lectures, while the institution of progress reports was extended to young scientists from many countries. Number of participants from around the world increased rapidly even overtaking number of scientists from the former Yugoslavia. This may have been helped by the beautiful locations at the Adriatic coast that are no longer available to SPIG. Another important SPIG characteristic was that all invited speakers were asked to split their presentation into introductory and historical part (thus 'Summer school and…' was often part of its moniker) and a more technical up to date section. That was time when invited lectures were written up in extension and were amazing pedagogical texts. The big blue books with invited lectures were sought after in many centers by young and experienced scientists alike. SPIG has perhaps maintained the institution of the written up invited lectures much longer than the other conferences in the field but eventually it had to turn to special issues of technical papers in respected international journals such as European Physical Journal D. That development was not for the better but it was due to the necessity. SPIG has survived breakup of the former Yugoslavia and is now centered in Serbia, it has followed numerous changes in the fields that it represents and is now one of three or four conferences with the longest lasting tradition in the field of the physics of ionized gases. SPIG has shared the destiny of science in former Yugoslavia, Serbia and also followed the topical research in the world. It is the main reason why fields related to SPIG are more developed and with a higher relative percentage of the overall science than elsewhere in the world.

ION PROCESSING OF ASTROPHYSICAL ICES

ALICJA DOMARACKA, HERMANN ROTHARD and PHILIPPE BODUCH

Centre de Recherche sur les Ions, les Matériaux et la Photonique (CIMAP) Normandie Univ, ENSICAEN, UNICAEN, CEA, CNRS, CIMAP 14000 Caen, France

E-mail domaracka@ganil.fr

Abstract. Astrophysical ices, mainly composed of simple molecules such as H_2O, CO, CO_2, NH_3 and others are ubiquitous in space: they are present in comets, satellites of planets (e.g Jovian moons) and on the grains of the dense molecular clouds in the interstellar medium. They are constantly exposed to complex and diverse radiation fields and interact with solar/stellar winds, magnetospheres or/and cosmic rays (UV, X-rays, electrons, H, He and heavier ions). This induces several physico-chemical processes such as radiolysis and subsequent formation of new molecules, release of molecules to the gas phase (sputtering, desorption) and structural ice modifications.

Since several decades, laboratory studies are performed extensively to investigate energetic processing of astrophysical ice analogues. However, for a long time, those investigations were mainly focused to evaluate effects induced by weakly ionizing radiation such as UV photons and keV-MeV light ions (H, He). In the talk, I will present an overview of results obtained for swift heavy ion irradiation of ices containing small molecules as well as films of complex organic molecules (e.g. nucleobases) performed at large scale ion beam facilities such as GANIL (Caen, France) or GSI (Darmstadt, Germany) (e.g. recent reviews: Ada Bibang et al. 2019, Rothard et al. 2018). Those experiments simulate interaction with swift heavy ions from Galactic Cosmic Rays in a new energetic window. Astrophysical application of obtained results will be also discussed.

References

Ada Bibang, P.C.J., Agnihotri, A.N, Augé, B., Boduch, P., Desfrançois, C., Domaracka, A., Lecomte, F., Manil, B., Martinez, R., Muniz, G.S.V, Nieuwjaer, N., Rothard, H.: 2019, *Low Temp. Phys.* **46**, 590.

Rothard, H., Domaracka, A., Boduch, P., Palumbo, M.E., Strazzulla, G., Da Silveira, E. F., Dartois, E.: 2018, *J. Phys. B*, **50**, 062001.

ELECTRON COLLISIONS WITH DIELECTRIC GASES CONSIDERED AS SF_6 REPLACEMENT

M. RANKOVIĆ[1*], R. KUMAR T P[1], P. NAG[1], J. KOČIŠEK[1] and J. FEDOR[1]

[1]*J. Heyrovský Institute of Physical Chemistry, Czech Academy of Sciences, Dolejškova 3, 18223 Prague, Czech Republic*
E-mail [*]milos.rankovic@jh-inst.cas.cz

Abstract. During the past decades, sulfur hexafluride (SF_6) has been globally used as an insulating medium in high-voltage power distributing circuits such as switchgears. It has a very high dielectric strength and ability to recombine itself in reactions driven by electric discharge, but on the other hand, it also has an alarmingly high global warming potential (GWP of 23.5k). Given the rising ecological awareness, there are big efforts to find a suitable replacement gas which at the same time is environmentally friendly and has good dielectric properties, among other criteria. Several candidates have been suggested already, but so far, a little is known about their fundamental physical and chemical properties, namely electron collision processes which govern their behavior under electric discharge.

We probe these insulating gas candidates with electrons in vacuum under single collision conditions, on three elementary channels: (i) electron attachment, (ii) electron impact ionization and (iii) elastic and inelastic electron scattering. By combining results from three electron-molecule collision setups, we are able to quantify all three channels and provide corresponding absolute cross sections for each process. In this talk, some of the experimental results will be presented with focus on the dynamics of atomic nuclei during the scattering, especially in the bond-breaking channels like dissociative ionization (Ranković et al. 2019), dissociative electron attachment and dissociation into neutral fragments (Ranković et al. 2020).

References

Ranković, M., Chalabala, J., Zawadzki, M., Kočišek, J., Slavíček, P., and Fedor, J. : 2019*, Phys. Chem. Chem. Phys.,* **21***,* 16451.

Ranković, M., Kumar T P, R., Nag, P., Kočišek, J., and Fedor, J. : accepted in 2020*, J. Chem. Phys.*

SEMICLASSICAL TWO-STEP MODEL FOR STRONG-FIELD IONIZATION: FURTHER DEVELOPMENTS AND APPLICATIONS

N. I. SHVETSOV-SHILOVSKI

Institut für Theoretische Physik, Leibniz Universität Hannover, D-30167, Hannover, Germany
E-mail nikolay.shvetsov@itp.uni-hannover.de

Abstract. Trajectory-based semiclassical models are widely used in strong-field, ultrafast, and attosecond physics. The semiclassical models apply classical mechanics to describe the electron motion in the continuum. The semiclassical two-step model (SCTS) allows to describe interference effects in above-threshold ionization and accounts for the ionic potential beyond the semiclassical perturbation theory (Shvetsov-Shilovski et al. 2016).

We discuss the application of the SCTS model to the new and promising method of time-resolved molecular imaging – strong-field holography with photoelectrons (Huismans et al. 2011, Walt et al. 2017, Shvetsov-Shilovski and Lein 2018). We modify the SCTS model to account for a multielectron polarization-induced dipole potential (Shvetsov-Shilovski et al. 2018). Thus, we analyze the imprints of multielectron effects in the electron momentum distributions from ionization by a linearly polarized laser pulse. We predict narrowing of the distributions along the laser polarization direction due to electron focusing by the induced dipole potential. It is also found that the polarization of the core modifies the interference patterns in the photoelectron momentum distributions: The number of fanlike interference structures in the low-energy part of momentum distributions may change. Furthermore, we extend the SCTS model to strong-field ionization of the hydrogen molecule (Shvetsov-Shilovski et al. 2019).

Finally, we present the further development of the SCTS model: semiclassical two-step model with quantum input (SCTSQI) (Shvetsov-Shilovski and Lein 2019). In the SCTSQI model the initial conditions for classical trajectories are governed by the exact quantum dynamics. As the result, the SCTSQI corrects the inaccuracies of the SCTS model and other trajectory-based models in description of the ionization step. For ionization of a one-dimensional model atom the SCTSQI model yields quantitative agreement with the direct numerical solution of the time-dependent Schrödinger equation.

References

Huismans, Y., Rouzée, A., Gijsbertsen, A. et al. : 2011, *Science*, **331**, 61.
Shvetsov-Shilovski, N. I., Lein, M. : 2018, *Phys. Rev. A*, **97**, 013411.
Shvetsov-Shilovski, N. I., Lein., M : 2019, *Phys. Rev. A*, **100**, 053411.
Shvetsov-Shilovski, N. I., Lein, M., Madsen L. B. et al. : 2016, *Phys Rev. A*, **94**, 013415.
Shvetsov-Shilovski, N. I., Lein, M., Madsen L. B. : 2018, *Phys. Rev. A*, **98**, 023406.
Shvetsov-Shilovski, N. I., Lein, M., Tőkési, K. : 2019, *Eur. Phys. J. D*, **73**, 37.
Walt., S. G., Ram, N. Bhargava Ram, Atala, M. et al. : 2017, *Nat. Commun.,* **8**, 15651.

THE FULLY RELATIVISTIC MULTI-CONFIGURATION DIRAC-HARTREE-FOCK METHOD FOR ATOMIC STRUCTURE CALCULATIONS FOR MULTIPLY CHARGED IONS: THE EXAMPLE OF Ca XV

N. ALWADIE[1,2], A. ALMODLEJ [1], N. BEN NESSIB [1,3] and M. S. DIMITRIJEVIĆ [4,5]

[1] *Department of Physics and Astronomy, College of Sciences, King Saud University, Saudi Arabia*
E–mail almodlej@ksu.edu.sa

[2] *Department of Physics, College of Sciences, King Khalid University, Saudi Arabia*
E–mail nalwadie@ksu.edu.sa

[3] *GRePAA, INSAT, Centre Urbain Nord, University of Carthage, Tunis, Tunisia*
E–mail nbennessib@ksu.edu.sa

[4] *Astronomical Observatory, Volgina 7, 11060 Belgrade 38, Serbia*
E–mail mdimitrijevic@aob.rs

[5] *Sorbonne Université, Observatoire de Paris, Université PSL, CNRS, LERMA, F-92190 Meudon, France*

Abstract. In this work, fully relativistic multi-configuration Dirac-Hartree-Fock (MCDHF) approach (see Froese Fischer et al. 2019) for calculating atomic structure parameters has been presented and compared to other approaches as Hartree-Fock pseudo-Relativistic (HFR) method (see Kramida 2019). As an example of application, results of fully relativistic calculations for the ion Ca XV have been obtained and compared to Hartree-Fock pseudo-relativistic calculations (Alwadie et al. 2020) and to NIST database values (Kramida et al. 2019). This example is important for plasma diagnostic and astrophysical studies because Ca XV atomic data of high accuracy are still very scarce.

References

Alwadie, N., Almodlej A., Ben Nessib, N., Dimitrijević M. S.: 2020, *Contrib. Astron. Obs. Skalnate Pleso*, **50**, 86.

Froese Fischer, C., Gaigalas, G., Jönsson, P., et al.: 2019, *Computer Physics Communications*, **237**, 184.

Kramida, A., NIST Public DATA Repository https://dx.doi.org/10.18434/T4/1502500 (2018).

Kramida, A., Ralchenko, Yu., Reader, J., and NIST ASD Team (2019): NIST Atomic Spectra Database (ver. 5.7.1), [Online]. Available: https://physics.nist.gov/asd [2020, February 14]. National Institute of Standards and Technology, Gaithersburg, MD.

STUDY OF STRUCTURAL MODIFICATIONS IN POLY(L-LACTIDE) (PLLA) INDUCED BY HIGH-ENERGY RADIATION

DEJAN MILICEVIC and EDIN SULJOVRUJIC

Department of Radiation Chemistry and Physics, „VINČA" Institute of Nuclear Sciences - National Institute of the Republic of Serbia, University of Belgrade, Belgrade, Serbia

E-mail dejanmilicevic@vinca.rs
E-mail edin@vinca.rs

Abstract. The high-energy radiation is frequently applied to tailor specific properties of polymeric materials, achieve sterility of medical devices, preserve food or modify waste materials. In this process, the transfer of the radiation energy, from typical sources like particle accelerators (electrons and X-rays) or Co-60 (the gamma radiation) to absorbing materials is achieved through secondary electrons, while the revealed physical and biological effects are very similar for both types of radiation sources.

Poly-L-lactide (PLLA) is a well-known biodegradable and biocompatible semi-crystalline polymer, used in a wide variety of applications, from implantable medical devices and drug release matrices to environmentally friendly packaging materials; diversity in the initial preparation, morphology and crystallinity plays a significant role in most of these applications. In this report, we will show the PLLA response to high-energy radiation and for that reason, two varieties of samples with substantial and in practice almost maximal reachable differences in microstructure and crystallinity are prepared and exposed to the gamma radiation to various absorbed doses (up to 300 kGy). Since the PLLA morphology is sensitive to preparation conditions and radiation, surface microstructures are analysed by scanning electronic microscopy (SEM). The chain scission degradation is followed using a gel permeation chromatography (GPC), while the additional characterization is conducted by differential scanning calorimetry (DSC), wide-angle X-ray diffraction (WAXD) method and IR spectroscopy (FTIR). The presence and evolution of free radicals are monitored using electron spin resonance (ESR) spectroscopy. The annealing treatment is also applied to part of the samples. Presented results show that depending on the initial preparation conditions, the radiation-induced changes in the structure and properties of PLLA, as well as the evolution of free radicals, can differ significantly. The low crystalline samples are found to be initially more susceptible to the gamma radiation than the high crystalline ones. On the other hand, due to the presence of long-lived free radicals the high crystalline samples are more prone to the post-irradiation degradation. Finally, the applied annealing treatment substantially reduces the concentration of long-lived radicals, but can also induce additional crystallisation.

Acknowledgements: The research was funded by the Ministry of Education, Science and Technological Development of the Republic of Serbia

AUTOMATIC COMPUTATION OF GLOBAL INTERMOLECULAR POTENTIAL ENERGY SURFACES FOR QUANTUM DYNAMICAL SIMULATIONS

R.L. PANADÉS-BARRUETA[1], E. MARTÍNEZ-NÚÑEZ[2] and D. PELÁEZ[3]
[1] *Laboratoire de Physique des Lasers, Atomes et Molécules, France*

[2] *Universidad de Santiago de Compostela, Spain*

[3] *Institut des Sciences Moléculaires d'Orsay, France*
E–mail daniel.pelaez-ruiz@u-psud.fr

We aim at simulating full quantum mechanically the processes of adsorption and photoreactivity of NO_2 adsorbed on soot particles modeled as large Polycyclic Aromatic Hydrocarbons in atmospheric conditions. A detailed description of these processes is necessary to understand the differential day-nighttime behavior of the production of HONO (Guan *et al*). In particular, the specific mechanism of the soot-mediated interconversion between NO_2 and HONO is to date not fully understood. The first stage in this study consisted in the determination of all transition states and minima of the NO_2-Pyrene system. To this end, we have used the van der Waals Transition State Search Using Chemical Dynamics (vdW-TSSCDS) method (Kopec *et al*). Starting from a single input geometry, vdW-TSSCDS permits the characterization of the topography of a intermolecular Potential Energy Surface (PES) in a fully automated fashion. This topographical information is used to obtain a global description of the interaction potential, necessary for the dynamical elucidation of spectroscopic properties. For this, we have developed the Specific Reaction Parameter Multigrid POTFIT (SRP-MGPF) algorithm and associated software (Panadés *et al*). This method computes chemically accurate PESs through reparametrization of semiempirical methods which are subsequently tensor decomposed using MGPF. This software has been interfaced with the Heidelberg version of the Multiconfiguration Time-Dependent Hartree (MCTDH) package [8].

References

C. Guan, X. Li, W. Zhang and Z. Huang: 2017, *J. Phys. Chem. A*, **121**, 482-492.
S. Kopec, E. Martínez-Núñez, J. Soto, D. Peláez: 2019, *Int. J. Quant. Chem.*, e26008
R.L.Panadés-Barrueta, E. Martínez-Núñez, D. Peláez: 2019, *Front. Chem.*, 7:576
M. H. Beck, A. Jäckle, G. A. Worth, and H.-D. Meyer: 2010, *Phys. Rep.*, **324**

DISSOCIATION DYNAMICS OF THE DIAMONDOID ADAMANTANE UPON PHOTOIONIZATION BY XUV FEMTOSECOND PULSES

JASPER PESCHEL[1,*], SYLVAIN MACLOT[1,2], JAN LAHL[1], HAMPUS WIKMARK[1], FABAIN BRUNNER [3], SUVASTHIKA INDRAJITH[4], PATRICK ROUSSEAU[4], BERND A. HUBER[4], SERGIO DIAZ-TENDERO[5], N´ESTOR F. AGUIRRE[6], ANNE LHUILLIER[1] and PER JOHNSSON[1]

[1] *Department of Physics, Lund University, P. O. Box 118, 221 00 Lund, Sweden*

[2] *Department of Physics, University of Gothenburg, Gothenburg, Sweden*

[3] *Physics Department, Institute of Quantum Electronics, ETH Zürich, Switzerland*

[4] *Normandie Université, ENSICAEN, UNICAEN, CEA, CNRS, CIMAP, France*

[5] *Departamento de Quımica, C-9, Universidad Autónoma de Madrid Spain*

[6] *Theoretical Division, Los Alamos National Laboratory, Los Alamos, USA*

Abstract. This work presents photodissociation studies of the diamondoid adamantane using extreme ultraviolet (XUV) femtosecond pulses. Lately, diamondoids are attracting increasing interest for use as an applied nanomaterial (Stauss *et al.*). Further, diamondoids have been found to be the most abundant component of presolar grains in space, and due to their high stability they are thus also expected to be abundant in the interstellar medium (Anders *et al.*, Henning *et al.*).

I will present a recent study (Maclot *et al.*), in which we demonstrate that the dissociation dynamics of adamantane dications takes place in a two-step process: barrierless cage opening followed by Coulomb repulsion-driven fragmentation. The experiment was carried out at the Intense XUV beamline at the Lund Laser Centre, where high-flux high-order harmonics are generated with photon energies up to 60 eV, pulse energies in the J regime and pulse durations on the femto- and attosecond time scale (Manschwetus *et al.*). To get insight into the dynamics, we use a theoretical approach combining potential energy surface determination, statistical fragmentation methods and molecular dynamics simulations. We found that the most stable structures of the dication exhibit an open-cage geometry at ∼4 eV below the double ionization threshold, that can be reached in a few tens of femtoseconds after the ionization. However, these structures are metastable and dissociate into several fragments in a Coulomb repulsion process.

References

Stauss, S. , Terashima, K.: 2017 , *CRC Press*, Synthesis, Properties, and Applications.
Anders, E. *et al.*: 1993, *Meteorit.* **28**, 490–514.
Henning, T. *et al.*: 1998, *Sci.* **282**, 2204–2210.
Maclot, S., Lahl, J., Peschel, J. *et al.*: 1998, *Sci. Rep.* **10**, 2884.
Manschwetus, B. *et al.*: 2016, *Phys. Rev. A* **93**, 061402.

KINETIC AND FLUID MODELLING OF NON-EQUILIBRIUM TRANSPORT OF CHARGED-PARTICLE SWARMS IN NEUTRAL GASES AND NON-POLAR LIQUIDS

I. SIMONOVIĆ[1], D. BOŠNJAKOVIĆ[1], R. D. WHITE[2], Z. LJ. PETROVIĆ[3]and S. DUJKO[1]

[1]*Institute of Physics, University of Belgrade, Pregrevica 118, 11080 Belgrade, Serbia*

[2]*College of Science and Engineering, James Cook University, Townsville 4811, Australia*

[3]*Serbian Academy of Sciences and Arts, KnezMihailova 35, 11000 Belgrade, Serbia*

Abstract. This work contains two parts. The first part deals with the study of the third-order transport coefficients. The components of the third-order transport tensor are required for the conversion of the hydrodynamic transport coefficients into transport data that is measured in the arrival time spectra and the steady-state Townsend experiments. In this work, we have determined the structure of the third-order transport tensor in all configurations of the electric and magnetic fields, by using the group projector method, see Simonović et al. 2020. Moreover, we have carefully analyzed the physical interpretation of the individual components of this tensor, by examining their contribution to the flux gradient relation and to the approximate solution of the generalized diffusion equation. We have also examined the dependence of the third-order transport coefficients on the elementary scattering processes in a wide range of model and real gases, by using Monte Carlo simulations and multi term theory for solving the Boltzmann equation.The second part of this work deals with the electron transport in liquid argon, liquid krypton, and liquid xenon (the high mobility liquids), as well as with the transition of an electron avalanche into a negative streamer in these liquids. These three liquids represent the simplest systems in which quasi-free electrons exist in the liquid-phase medium, and they are an excellent starting point for the modeling of charged particle transport and electrical discharges in liquids. In this work, the transport of electrons in the high mobility liquids is investigated by employing Monte Carlo simulations, see Simonović et al. 2019. Our existing Monte Carlo code has been modified in order to enable a good representation of the coherent scattering effects. A special emphasis has been placed on studying the structure induced negative differential conductivity in liquid xenon, by employing the spatially resolved swarm data. Another point of interest was the influence of various representations, of the inelastic scattering in the liquid phase, on the ionization rate coefficient. The transport properties of electrons in the high mobility liquids, that were obtained by employing Monte Carlo simulations, were used as an input data in the 1.5D implementation of the first order fluid model. This fluid model was used to investigate the formation and propagation of negative streamers in these liquids. Among several important points, we have investigated the influence of various representations of the inelastic collisions on the dynamics of the formation and propagation of negative streamers in these liquids.

References

Simonović, I., et al.: 2020, *Phys. Rev. E*, **101**, 023203.
Simonović, I., et al.: 2019*, Plasma Sources Sci. Technol.*, **28**, 015006.

Publ. Astron. Obs. Belgrade No. 99 (2020), 31- 34 *Contributed Paper*

ANALYTICAL FORMULISM FOR THE OUTPUT FACTOR CALCULATION OF SMALL RADIATION BEAMS

SAED J. Al ATAWNEH[1], LINA M. ABU-ARIDA[2] and K TOKESI[1]

[1]*Institute for Nuclear Research, ATOMKI, Debrecen, Hungary*

E-mail: saed.al-atawneh@atomki.mta.hu

[2]*Al-Balqa Applied University, Faculty of Science, AL SALT, Jordan*

E-mail: Lina_23@yahoo.com

[1]*Institute for Nuclear Research, ATOMKI, Debrecen, Hungary*

E-mail: tokesi@atomki.mta.hu

Abstract. We present new analytical formula to calculate the output factor (OF). With the established formula we present OF for collimated radiation beams. Pinpoint ion chambers (radiation detectors) was utilized to measure the radiation output factor (OF) for different collimated beams extending from (10x10 cm^2) down to (1x1 cm^2) utilizing a medical linear accelerator (Elekta) motorized with 3D-water phantom. As a result, the OFs of multileaf collimator (MLC/Jaw) beams were accomplished and the deviation between the two values were expected due to MLC leakage which becomes more significant for the small fields. The OF for MLC/Jaw-shaped beam was deviated by 2% for field size larger than 4 cm^2 and within 39% for ultra-small field size (<1.5 cm^2).

1. EXPERIMENT

1.1. INTRODUCTION

The output factor measurements were complicated by two concerns: 1) first one was the size of the ion chamber compare to the field size, 2) the lack of charge particle equilibrium (dis-CPE) (Laub and Wong 2003, Das, Ding et al. 2008, Zhu, Ahnesjö et al. 2009, Huq, Hwang et al. 2018). The distinctive ion chamber was used with various field sizes starting from 10x10 cm^2 down to 1x1 cm^2 at 10 cm depth in the water phantom for MLC/Jaw-shaped beams.

The International Atomic Energy Agency (IAEA) Technical Reports Series (TRS) no.483 provides extensive data for the small field dosimetry using a different kind of ion chambers and detectors (Palmans, Andreo et al. 2018). Several

studies had been discussed the small field dosimetry (Das, Ding et al. 2008, Zhu, Ahnesjö et al. 2009, Huq, Hwang et al. 2018), using different size detectors under charge particle dis-equilibrium conditions to provide the same conclusion; the smaller the detector the better (more accurate) the output factor readings are. But none of the previous studies were concerned to find an analytical formula to calculate the output factor for the small radiation beams.

Our recent study aims to find the analytical formula to calculate the output factor (OF) for multileaf collimator (MLC)-shaped small radiation beams under charge particle dis-equilibrium condition for Elekta (Synergy platform) medical linear accelerators.

1.2. METHODOLOGY

The Water phantom was placed in such way that the surface to source distance (SSD) was 100 cm from the radiation source (medical linear accelerator). The ion chamber is set up within the phantom such that its axis should always be parallel to the beam central axis (CAX), and the center of the ionization chamber assumed to be located at the depth of 10 cm (d=10 cm). This depth was kept constant while changing the field size of the photon beam for each measurement. Readings for the OF were taken for field sizes 10x10 cm^2 down to 1x1 cm^2 for both collimators shapes, the MLC-shaped fields with constant jaw-opening of 10x10 cm^2 and Jaw-shaped fields only. Readings were normalized to the reference field size of 10x10 cm^2.

1.3. RESULTS

The MLC device suffers from leakage radiation between the "leaves". So, it is expected that this extra leakage dose will affect the output factor readings as compared with the Jaw-shaped fields. Table 1 and Figure 1 show the OF readings as taken for 6 MV photon energy using Pinpoint ion chamber,

Table 1: Output factors with for 6MV beam, measured with Pinpoint ion chamber at depth of 10 cm of SSD 100 cm.

Pinpoint			
Field Size(cm^2)	**6MV (Jaws)**	**6MV (MLC)**	**%Diff**
1x1	0.599	0.832	38.955
2x2	0.835	0.868	3.88
4x4	0.917	0.917	0
6x6	0.947	0.947	0
8x8	0.98	0.98	0
10x10	1	1	0

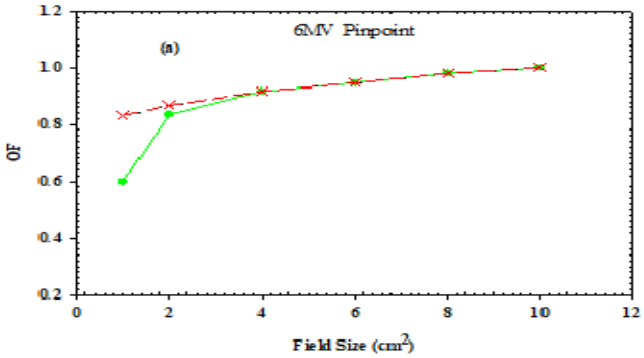

Figure 1: The Output Factor (OF) versus field size (cm^2) for MLC/Jaw beams, 6MV beam energy using Pinpoint ion chamber. MLC (Red Cross-Red dash line), Jaw (Green Circle-Green Sold line).

According to Tables 1 and Figure 1, the OFs at the large fields (>4 cm^2) for both MLC and Jaw-shaped collimator data are similar with less than 2% due to the presence of charge particle equilibrium (CPE) at the point of measurement (Hrbacek, Lang et al. 2011). The field sizes being too large that the leakage through the MLC is far away from the point of measurement and the output factor readings were not affected.

1.4. ANALYTICAL FORMULA OF OUTPUT FACTOR

For analytical formula, all OFs were calculated based on OFs that measured utilizing the distinctive ion chamber through 3D-water phantom according to equation 1.

$$\Omega_{f_{clin}Q_{msr}}^{f_{clin},f_{msr}} = \frac{D_{W,Q_{clin}}^{f_{clin}}}{D_{W,Q_{msr}}^{f_{msr}}} \qquad (1)$$

where $D_{W,Q_{clin}}^{f_{clin}}$ and $D_{W,Q_{msr}}^{f_{msr}}$ are the absorbed dose to water in the clinical field f_{clin} with beam quality Q_{clin} and absorbed dose to water in the machine specific reference field f_{msr} with beam quality Q_{msr}, respectively (Zhu, Ahnesjö et al. 2009, Huq, Hwang et al. 2018). Curves in figure 1 was fitted employing least-square fit "ideal" straight line for the large field sizes that could be represented by equation 2.

$$(OF|_{Energy} = a_0 + a_1 * Field\ size\ )_{ion\ chamber} \qquad (2)$$

where a_0 and a_1 are fitting parameters, energy-dependent and ion chamber size independent.

1.5. EXPERIMENT VALIDIAION

Analytical Formula for the output factor was validated and compared with measured data for both MLC and Jaw-shaped beams (see table 2).

Table 2: The Analytical Formula Readings vs Measured Readings for 6MV beam, measured with Pinpoint ion chamber at depth of 10 cm of SSD 100 cm.

Pinpoint					
Field size (cm^2)	**Measured OF MLC**	**Measured OF Jaws**	**Analytical**	**diff (MLC)**	**diff (Jaws)**
10	1	1	1	0	0
8	0.98	0.98	0.98	0	0
6	0.947	0.947	0.947	0	0
4	0.917	0.917	0.917	0	0
2	0.868	0.835	0.891	0.023	0.056
1	0.832	0.599	0.862	0.03	0.263

Table 2 show the "Analytical Formula Values" for the ideal straight lines based on the equation (2), the last two columns show the difference between linear value and the MLC/Jaw values. The deviation of the straight line indicates the amount of charge particle equilibrium losses. The OFs of the small filed size less than 1x1 cm^2 for the pinpoint ion chamber is deviated by 3.6% and 43.9% from analytical formula for MLC and Jaw-shaped beams respectively.

References

Das, I. J., Ding, G. X. and Ahnesjo, A.: 2008, *Med. Phys.*, **35**(1), 206-215.

Hrbacek, J., Lang, S. and Klock, S.: 2011, *Int. J. Radiat. Oncol. Biol. Phys.*, **80**(4), 1228-1237.

Huq, M. S., Hwang, M.-S., Teo, T. P., Jang, S. Y., Heron, D. E. and Lalonde, R. J.: 2018, *Medical Physics*, **45**(9), 4257-4273.

Laub, W. U. and Wong, T.: 2003, *Med. Phys.*, **30**(3), 341-347.

Palmans, H., Andreo, P., Huq, M. S., Seuntjens, J., Christaki, K. E. and Meghzifene, A.: 2018, *Medical Physics*, **45**(11), e1123-e1145.

Zhu, T. C., Ahnesjö, A., Lam, K. L., Li, X. A., Ma, C.-M. C., Palta, J. R., Sharpe, M. B., Thomadsen, B. and Tailor, R. C.: 2009, *Medical Physics*, **36**(11), 5261-5291.

Publ. Astron. Obs. Belgrade No. 99 (2020), 35 - 38 *Contributed Paper*

SELECTIVE MULTIPHOTON IONIZATION OF SODIUM BY FEMTOSECOND LASER PULSES

A. BUNJAC, D. B. POPOVIĆ and N. S. SIMONOVIĆ
Institute of Physics, University of Belgrade, Pregrevica 118, 11080 Belgrade, Serbia

Abstract. Multiphoton ionization of sodium by femtosecond laser pulses of 800 nm wavelength is studied in the range of laser peak intensities from 3.5 to 8.8 TW/cm^2. Photoelectron probability distributions and the energy spectra are determined numerically by solving the time dependent Schrödinger equation. The calculated spectra agree well with recent experimental results. A partial wave analysis of the spectral peaks related to Freeman resonances has shown that under specific conditions the resonantly enhanced multiphoton ionization may be realized through a single energy level.

1. INTRODUCTION

A remarkable feature of the photoelectron energy spectra (PES) obtained at the multiphoton ionization (MPI) of atoms using short (sub-picosecond) laser pulses is the existence of the so-called Freeman resonances. The mechanism which is responsible for occurrence of these spectral structures is the dynamic (or AC) Stark shift which brings the atomic energy levels into resonance with an integer multiple of the photon energy. Freeman et al. (1987) have shown that when atomic states during the laser pulse transiently shift into resonance, the resonantly enhanced multiphoton ionization (REMPI) takes place, increasing the photoelectron yield, and one observes peaks at the corresponding values of photoelectron energy. Thus, the peaks in the PES are related to the REMPI occurring via different intermediate states. A particular challenge would be the selective ionization of the atom through a single energy level which could produce a high ion yield. By increasing the laser intensity one increases the yield, but also spreads the electron population over multiple energy levels and, in turn, reduces the selectivity. Hart et al (2016) have shown that improved selectivity and yield could be achieved by controlling the resonant dynamic Stark shift of sodium states via intensity of the laser pulse of an appropriate wavelength.

Here we study the MPI of the sodium atom by the laser pulse of 800 nm wavelength and 57 fs full width at half maximum (FWHM) with the peak intensities ranging from 3.5 to 8.8 TW/cm^2, which are the same values as used in the experiment by Hart et al. Using the single-active-electron approximation we calculate the photoelectron probability distribution and the PES by solving numerically the time dependent Schrödinger equation (TDSE). In order to make a deeper insight into the ionization process, we perform, in addition, a partial-wave analysis of the photoelectron outgoing wave.

2. THE MODEL, ENERGY SCHEME AND PHOTOIONIZATION CHANNELS

Within the single-electron model the dynamics of the valence (active) electron of sodium atom in an alternating electric field $F(t)$ is described by Hamiltonian (in atomic units)

$$H = \frac{\mathbf{p}^2}{2} + V_{\text{core}}(r) - F(t)z. \tag{1}$$

The effective core potential $V_{\text{core}}(r)$ describes the interaction of the valence electron with the atomic core (inner electrons + atomic nucleus). For this purpose we use the Hellmann's pseudopotential $V_{\text{core}}(r) = -1/r + A\,e^{-ar}/r$. The parameters $A = 21$ and $a = 2.54920$ provide the correct value for the ionization potential of lithium $I_{\text{p}} = 5.1391\,\text{eV} = 0.18886\,\text{a.u.}$ and reproduce approximately the energies of singly-excited states (see Fig. 1).

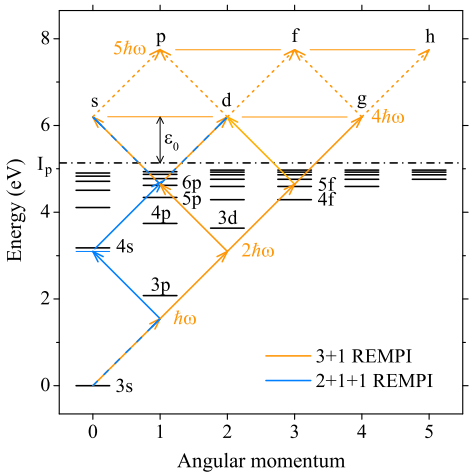

Figure 1: The unperturbed energy levels (short black lines) corresponding to singly excited states of sodium (Sansonetti, 2008) relative to its ground state (3s) and possible four-photon and five-photon absorption pathways (arrows) from the ground state to continuum for the radiation of 800 nm wavelength ($\hbar\omega \approx 1.55\,\text{eV}$). The continuum boundary is drown by the dash-dot line and ϵ_0 is the excess energy of photoelectrons produced in the nonresonat four-photon ionization.

We consider a linearly polarized laser pulse of the form

$$F(t) = F_{\text{peak}} \sin^2(\pi t/T_{\text{p}}) \cos(\omega t), \quad 0 < t < T_{\text{p}} \tag{2}$$

(otherwise $F(t) = 0$). Here ω, F_{peak} and T_{p} are the frequency of laser field, the peak value of its electric component and the pulse duration ($2\times$ FWHM), respectively. Due to the axial symmetry of the system, the magnetic quantum number m of the valence electron is a good quantum number and we set $m = 0$ (the ground state value).

The photoionization process is simulated by calculating the evolution of the wave function of valence electron $\psi(\mathbf{r}, t)$, which is initially ($t = 0$) chosen to be the lowest eigenstate of Hamiltonian (1) (then $F = 0$) that describes the sodium ground state. The evolution is calculated by integrating the TDSE (see Bunjac et al., 2017).

Fig. 1(a) shows the lowest energy levels corresponding to singly-excited states of sodium and possible multiphoton absorption pathways during the interaction of the atom with a laser radiation of 800 nm wavelength ($\hbar\omega = 0.05695$ a.u. ≈ 1.55 eV). At this wavelenghth there are three dominant REMPI channels: (i) (3+1)-photon ionization via excitation of 5p, 6p and 7p states, giving rise to photoelectrons with s and d-symmetry; (ii) (3+1)-photon ionization via excitation of 4f, 5f and 6f states, producing photoelectrons with d and g-symmetry; (iii) (3+1+1)-photon ionization via nearly resonant two-photon transition 3s $\rightarrow$ 4s and subsequent excitation of P-states, giving rise to photoelectrons with s and d-symmetry.

3. PARTIAL WAVE ANALYSIS

In order to determine the PES, the outgoing part of the active electron wave function $\psi(\mathbf{r}, t)$ at a time $t > T_p$ is transformed from the coordinate to momentum representation $\bar{\psi}(\mathbf{k}, t)$ by the Fourier transform and expanded in terms of partial waves

$$\bar{\psi}(\mathbf{k}) = \sum_l \Phi_l(k) Y_{l0}(\vartheta), \tag{3}$$

where $Y_{l0}(\vartheta)$ are the spherical harmonics with $m = 0$ and $\Phi_l(k) = \int Y^*_{l0}(\vartheta)\, \bar{\psi}(\mathbf{k})\, \mathrm{d}\Omega$ are the corresponding radial functions. Using the representation of $\bar{\psi}$ in cylindrical coordinates, the radial functions can be calculated as

$$\Phi_l(k) = 2\pi \int_0^\pi \bar{\psi}(k \sin\vartheta, k\cos\vartheta)\, Y_{l0}(\vartheta)\, \sin\vartheta\, \mathrm{d}\vartheta. \tag{4}$$

According to partial wave expansion (3), the radial probability density of photoelectrons in momentum space is the sum $w(k) = \sum_l w_l(k)$, where

$$w_l(k) = |\Phi_l(k)|^2\, k^2 \tag{5}$$

are the partial probability densities. These quantities for $l = 0, \ldots, 5$, as functions of the photoelectron excess energy $\epsilon = \hbar^2 k^2 / 2m_e$, are shown in the left column of Fig. 2 for three values of the laser peak intensity: 3.5, 4.9 and 8.8 TW/cm^2. The corresponding total probability densities w represent the PES for these three values of laser intensity. They are shown in the right column of Fig. 2 together with the corresponding spectra obtained experimentally (Hart et al., 2016).

The spectra, both the calculated and experimental, exhibit a typical above threshold ionization (ATI) structure with prominent peaks separated by the photon energy $\hbar\omega \approx 1.55$ eV. Fig. 2 shows the peaks corresponding to lowest three orders of ATI (MPI by $4 + s$ photons, $s = 0, 1, 2$) which are located approximately at $\epsilon = 0.8\,\mathrm{eV} + s\hbar\omega$. The partial wave analysis recovers the character of these peaks. We see in Fig. 2 (left) that for the photoelectron energies around the main peak ($s = 0$, $\epsilon \approx 0.8$ eV) and around the second-order ATI peak ($s = 2$, $\epsilon \approx 3.9$ eV) dominant contributions in the total probability density come from the partial waves with even l (s, d, g-waves). Thus, the photoelectrons with these energies are generated by absorbing an even number of photons ($N = 4$ and 6). Contrarily, in the vicinity of the first-order ATI peak ($s = 1$, $\epsilon \approx 2.35$ eV) the partial waves with even l are suppressed and those with odd l (p, f, h-waves) dominate. Therefore, in this case odd number of photons is absorbed (here $N = 5$).

Fig. 2 (left column) shows that at the laser peak intensity of 3.5 TW/cm^2 dominant contribution in the main peak (around 0.8 eV) comes from d-electrons, while at the intensity of 8.8TW/cm^2 the electrons of g-symmetry dominate. In conclusion, by changing the laser intensity, one selects the main ionization channel – in the first case this is the 3+1 (or 2+1+1) REMPI via 5p state, while in the second case it is the 3+1 REMPI via 4f state.

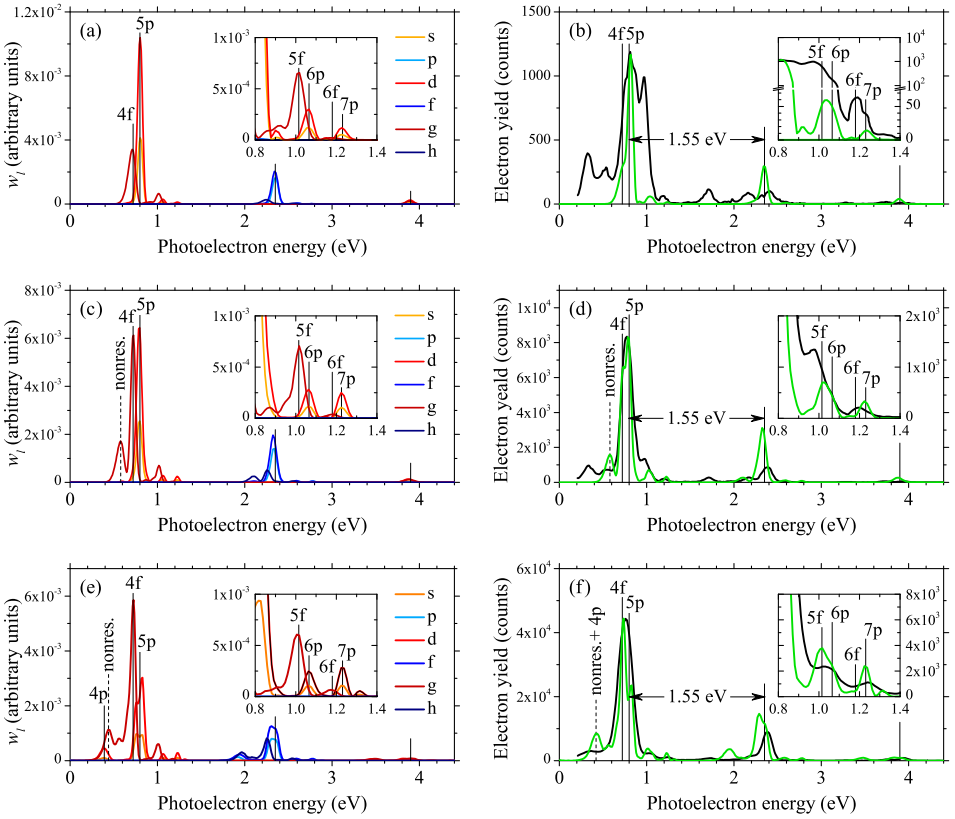

Figure 2: Partial probability densities w_l for $l = 0, \ldots, 5$ (left column) and the total probability density w (right column, green line) as functions of the photoelectron energy $\epsilon = \hbar^2 k^2/(2m_e)$ obtained at three values of the laser peak intensity: (a,b) 3.5 TW/cm^2, (c,d) 4.9 TW/cm^2, (e,f) 8.8 TW/cm^2. Experimental results (Hart et al., 2016) are represented by full black lines (right column). The full vertical lines mark the energies of two REMPI channels (via f and p states) of the threshold peak as well as the position of 5p subpeak in the higher order ATI peaks.

References

Bunjac A., Popović D. B. and Simonović N. S. : 2017, *Phys. Chem. Chem. Phys.*, **19**, 19829.

Freeman, R. R., Bucksbaum, P. H., Milchberg, H., Darack, S., Schumacher, D. and Geusic, M. E., : 1987, *Phys. Rev. Lett.*, **59**, 1092.

Hart, N. A., Strohaber, J., Kolomenskii, A. A., Paulus, G. G., Bauer, D., and Schuessler, H. A. : 2016, *Phys. Rev. A* **93**, *063426*.

Sansonetti, J. E. : 2008, *J. Phys. Chem. Ref. Data* **37**, 1659.

Publ. Astron. Obs. Belgrade No. 99 (2020), 39 - 42 *Contributed Paper*

RESONANT ELECTRON SCATTERING BY METASTABE NITROGEN - REVISITED

IZTOK ČADEŽ

Jožef Stefan Institute, Jamova 39, 1000 Ljubljana, Slovenia
E-mail iztok.cadez@ijs.si

Abstract. Here we discuss the resonant electron scattering by a metastable nitrogen molecule in the $A^3\Sigma_u^+$ state, in particular the resonant electron impact quenching. This process was studied to some extent in the past but it has mainly been ignored in the recent nitrogen plasma modelling. The intention of this contribution is to draw attention to its potential importance. A classical local complex potential was used to evaluate cross sections for the vibrational excitation/de-excitation within the A-state vibrational manifold and for the resonant quenching of the $A^3\Sigma_u^+$ state to the $X^1\Sigma_g^+$ ground state.

1. INTRODUCTION

The modelling of nitrogen plasma has advanced significantly in its complexity in recent times due to various modern needs and improvements of modelling tools as well as updated data bases (e.g. see Loureiro et al., 2011). Pure nitrogen plasma has its fundamental importance for in-depth understanding of complex multitude of individual radiative and collisional processes among ions and neutral atoms and molecules and therefore it is a key test object for modelling techniques. However, a plasma of various gas mixtures, containing nitrogen has a much broader practical importance for understanding many phenomena in different environments ranging from planetary atmospheres (e.g. Campbell et al., 2010) to plasma processing. Enhanced interest in studies of the hydrogen – nitrogen plasma is recently present due to the needs of modelling the edge plasma in tokamak fusion reactors (Touchard et al., 2019). Nitrogen is introduced to the hydrogen (mainly its isotope, deuterium) plasma into the tokamak divertor region in order to enhance radiative dissipation of energy in this region. Production of ammonia occurs under such a condition and a corresponding detailed plasma modelling was performed (Carrasco et al., 2011; Sode et al., 2015; Body et al., 2018).

Among many of ionic, atomic and molecular electronic states of particles in a nitrogen containing plasma, the metastable $A^3\Sigma_u^+$ state of N_2 is often abundantly present. It plays a specific role due to the fact that it is the lowest triplet state and

thus it is also populated by radiative decay of higher triplet states. It has long life-time, about 2s, and high excitation energy, 6.169 eV, between v=0 vibrational levels of $A^3\Sigma_u^+$ and ground $X^1\Sigma_g^+$ electronic states of N_2. Various processes involving $N_2(A)$ are included in present time modelling and their relative relevance to the studied plasma depends on composition, pressure and temperature. Population of $N_2(A)$ in p~1 Torr nitrogen discharge is strongly dependent on the excitation transfer between neutral molecules $N_2(A)$, vibrationally excited ground state, $N_2(X,v)$ and $N_2(B^3\Pi_g)$ (Loureiro et al., 2011). Nine different reactions in nitrogen involving $N_2(A)$ are included in the modelling of Body et al., 2018. Also, the role of $N_2(A)$ in the so-called breakdown memory effect in nitrogen was vividly discussed (e.g. Bošan et al., 1997, Petrović et al., 2001). Colonna and Capitelli, 2001 have shown strong influence of metastable nitrogen on characteristics of the electron energy distribution in a study of nitrogen expansion flow. They considered both, the atomic and molecular electronic metastable states and showed, that under studied conditions, the atomic species have more important role than the molecular ones. The superelastic collision of an electron with $N_2(A)$ was shown to strongly influence the electron energy distribution during the post-discharge regime, Laporta, 2017.

Here, we are interested in electron collisions with a neutral nitrogen molecule which involves molecules in the lowest triplet state, $A^3\Sigma_u^+$.

2. ELECTRON IMPACT EXCITATION OF $A^3\Sigma_u^+$ STATE OF N_2

Electron collisions with a nitrogen molecule have been studied in detail since the very beginning of experimental and theoretical studies of atomic collision processes. A detailed overview of available data on e-N_2 collisions was presented by Itikawa (Itikawa, 2006) who also provided sets of recommended cross sections. The most detailed experimental differential cross sections (DCS) for excitation of this state, together with seven other states of N_2, were presented by the JPL group (Khakoo et al., 2005) for electron impact energies of 10, 12.5, 15, 17.5, 20, 30, 50, and 100 eV. The electron impact excitation of electronic states of nitrogen, including the $A^3\Sigma_u^+$ state, was also studied by *ab initio* calculations using the R-matrix technique by Gillan et al., 1996.

2.1 RESONANT EXCITATION

Resonances in electron molecule scattering are common phenomena when the incident electron is temporaly trapped to the target molecule and, on this way, allowing for increased energy exchange with molecule. The famous 2.3 eV resonance in nitrogen is the most studied prototype of shape resonances and it is produced by electron trapping to the ground electronic state of N_2 (e.g. Laporta et al. 2014). Similar resonances, core excited shape resonances, also occur when incoming electron is temporarily trapped in the potential of an excited molecular state. Such resonances are usually less pronounced than resonances associated to the ground electronic state of molecule because in this case two-electron transition

is involved, trapping of the incoming electron and promoting a target electron to the excited orbital. Such core excited resonances associated to the $A^3\Sigma_u^+$ and $B^3\Pi_g$ state in nitrogen were first studied by Mazeau et al. 1973 and oscillatory structures in DCS were observed. Such structures are characteristic for resonance life-time being comparable to the vibrational period of the parent molecular state. The resonance in the excitation of $A^3\Sigma_u^+$ state which was attributed to the first excited $^2\Pi_u$ state of N_2^- was later studied in more detail by Paris group (Huetz et al.,1980a, b, c, and Čadež et al., 1986). It was also observed and commented by M. Allan in a review on electron impact excitation of triplet states (Allan, 1989). Our old relative experimental DCS for excitation of v=6 vibrational level of $N_2(A)$ from Čadež et al., 1986, renormalized to the recent absolute DCS of Khakoo et al., 2005 at electron energy, Ee=10 eV are shown in Fig. 1. Absolute recommended total cross section (TCS) for excitation of $N_2(A)$ from Itikawa, 2006 is also shown.

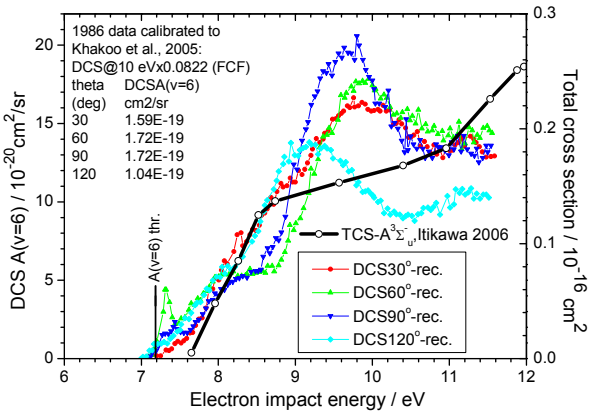

Figure 1: Renormalized DCS for excitation of the v=6 vibrational level of $A^3\Sigma_u^+$ at the 30°, 60°, 90° and 120° scattering angles from Čadež et al., 1986. Recommended absolute TCS for excitation of $N_2(A)$ from Itikawa, 2006 is also shown.

It is important to note that resonant enhancement of the CS, unambiguously detected experimentally in v=6 DCS, does not show up in the TCS which is possibly due to a relatively small probability for the needed two electron transition in the incident reaction channel as commented in Allan, 1989 and also possibly due to the weaker Franck-Condon overlap with other then the v=6 vibrational level of $N_2(A)$.

3. RESONANT ELECTRON SCATTERING BY $A^3\Sigma_u^+$ STATE

Even though the ~9.5 eV resonance, attributed to the $^2\Pi_u$ state of N_2^-, appears not to have an appreciable contribution to the excitation of $N_2(A)$ by electron impact, its existence has potentially strong importance to processes involving $A^3\Sigma_u^+$ state in

the discharges. An electron colliding with $N_2(A)$ can be more easily trapped to the $^2\Pi_u$ state of N_2^- as the $A^3\Sigma_u^+$ state is its parent state and, therefore, only one electron transition is involved, similarly to formation of the 2.3 eV $^2\Pi_g$ resonance in electron scattering by the ground state nitrogen. Besides this, the formation of a temporary $^2\Pi_u$ state of N_2^-, can importantly increase the electron impact quenching of $N_2(A)$ thus increasing the population of higher energy electrons in the electron energy distribution by this resonant superelastic channel which was also recently stressed out in Laporta, 2017. Both these aspects of the $^2\Pi_u$ were earlier treated in connection with processes in ionosphere (Čadež, 1983) using a local complex potential model for the resonance similar to the one used in Huetz et al., 1980. We are now re-examining the model by taking into account more accurate available potentials and some later theoretical development (e.g. Gianturco and Schneider, 1996).

References

Allan M., 1989, *J. Electron. Spectrosc. Relat. Phenom.*, **48**, 219-351.

Body T., Cousens S., Kirby J. and Corr C.: 2018, *Plasma Phys. Control. Fusion* **60** 075011.

Bošan Dj. A., Jovanović T. V. and Krmpotić Dj. M.: 1997, *J. Phys. D: Appl. Phys.* **30** 3096.

Čadež I., 1983, *Planet. Space. Sci.*, **31**, 843.

Čadež I., Hall R.I., Landau M., Pichou F. and Schermann C., 1986, *Contributed papers, SPIG'86*, Šibenik Sept. 1-5, 1986, Ed. M.V. Kurepa, Univ. of Belgrade, 19-22.

Campbell L., Kato H., Brunger M. J. and Bradshaw M. D. J. 2010, *Geophys. Res.*, **115**, A09320.

Carrasco E., Jiménez-Redondo M., Tanarro I. and Herrero V. J.: 2011, *Phys. Chem. Chem. Phys.* **13** 19561.

Colonna G. and Capitelli M., 2001, *J. Phys. D: Appl. Phys.,* **34**, 1812.

Gianturco F.A. and Schneider F., 1996, *J. Phys. B: At. Mol. Opt. Phys.*, **29**, 1175.

Gillan C.J., Tennyson J., McLaughlin B.M. and Burke P.G., 1996, *J. Phys. B: At. Mol. Opt. Phys.*, **29**, 1531–1547.

Huetz A., Čadež I., Gresteau F., Hall R.I., Vichon D. and Mazeau J., 1980a, *Phys. Rev. A*, **21**, 622.

Itikawa Y., 2006, *J. Phys. Chem. Ref. Data*, **35**, 31-53.

Khakoo M.A., Johnson P.V., Ozkay I., Yan P., Trajmar S. and Kanik I., 2005, *Phys. Rev. A*, **71**, 062703.

Laporta V., Little D.A., Celiberto R. and Tennyson J., 2014, *Plasma Sources Sci. Technol.*, **23**, 065002.

Laporta V., 2017, Habilitation Thesis, Normandie Universite - Universite du Havre (France); https://www.researchgate.net/publication/327160186.

Loureiro J., Guerra V., Sa P. A., Pintassilgo C. D., and Lino da Silva M.: 2011, *Plasma Sources Sci. Technol.*, **20**, 024007.

Mazeau J., Gresteau F., Hall R.I., Joyez G. and Reirlhardt J., 1973, *J. Phys. B: At. Mol. Phys.*, **6**, 862.

Petrović Z. Lj., Marković V. Lj., Pejović M. M. and Gocić S. R.: 2001, *J. Phys.D: Appl. Phys.* **34** 1756.

Sode M., Jacob W., Schwarz-Selinger T. and Kersten H.: 2015, *J. Appl. Phys.* **117** 083303.

Publ. Astron. Obs. Belgrade No. 99 (2020), 43 - 46 *Contributed Paper*

DETERMINING EXTRAPOLATED DIFFERENTIAL CROSS SECTIONS FROM DATA SETS IN BEAMDB USING MACHINE LEARNING ALGORITHMS

STEFAN IVANOVIĆ[1,2], NEBOJŠA USKOKOVIĆ[1], BRATISLAV P. MARINKOVIĆ[1] and NIGEL J. MASON[3]

[1]*Institute of Physics Belgrade, University of Belgrade, Laboratory for Atomic Collision Processes, Pregrevica 118, 11080 Belgrade, Serbia*
E-mail nesauskokovic@gmail.com, bratislav.marinkovic@ipb.ac.rs

[2]*The School of Electrical and Computer Engineering of Applied Studies, Belgrade, 11010 Vozdovac, Vojvode Stepe Street 283, Serbia*
E-mail stefan.ivanovic992@gmail.com

[3]*School of Physical Sciences, University of Kent, Canterbury, Kent, CT2 7NZ, U.K.*
E-mail n.j.mason@kent.ac.uk

Abstract. Here we exploit a large data set maintained in the Belgrade electron-atom/ molecule database (BEAMDB) to explore the possibilities how to determine extrapolated differential cross sections (DCS) obtained in experimental investigations by using machine learning algorithms. DCSs for different atomic and molecular species are represented by squared weighted sum of Legendre polynomials

1. INTRODUCTION

The importance of electron collisions with atomic particles (atoms, molecules, ions, radicals) is evident in the fields of plasma processes (Petrović et al. 2014), astrophysical plasmas (Jevremović et al. 2020), radiation damage (Mason 2008), etc. In low-temperature non-equilibrium molecular plasmas electron interactions are responsible for vibrational non-equilibrium and electron-driven ionization and dissociation that produces reactive species. The strength of electron interaction with atomic species is usually characterized by cross sections which can be state specific and angle and energy resolved. In classical experiments with electron spectrometers that are not equipped with the magnetic-angle-changing device (Cho et al. 2006) determination of electron differential cross sections, DCS(θ), is performed in the limited range of scattering angles. In order to obtain integral cross

sections, σ_i (1), or momentum transfer, σ_{mt} (2), one needs to extrapolate experimental data to zero and 180^o angles and then to carry out the integrations:

$$\sigma_i(\theta) = 2\pi \int_0^{\pi} DCS(\theta) \sin\theta \, d\theta \tag{1}$$

$$\sigma_{mt}(\theta) = 2\pi \int_0^{\pi} DCS(\theta) \left[1 - \left(1 - \frac{\Delta E}{E_o}\right)^{1/2} \cos\theta\right] \sin\theta \, d\theta \tag{2}$$

The question that arises is how to conduct the extrapolation procedure, either to use calculated values obtained by some theoretical approximation (see e.g. Bartschat et al. 2017) or to perform complex phaseshift analysis (Brunger et al. 1992). In this contribution we explore the possibility to use a large set of DCS(θ) data curated within BEAMDB database (http://servo.aob.rs/emol) to determine extrapolated values using machine learning techniques.

2. BELGRADE ELECTRON-ATOM/MOLECULE (BEAM) DATABASE

Belgrade Electron –Atom/Molecule (BEAM) database (Marinković et al. 2017) is a node of a common portal "Virtual Atomic and Molecular Data Centre", VAMDC, (https://portal.vamdc.eu/vamdc_portal/home.seam) and it collects and maintains a series of data on electron interaction with atomic particles. It holds electron differential and integral cross sections for elastic scattering, electronic excitations and ionization as well as electron energy loss-spectra and threshold photoelectron spectra. Numerous atomic species (Ag, Ar, Bi, Ca, Cd, He, Hg, Kr, Mg, Na, Ne, Pb, Rb, Sb, Xe, Yb) are accompanied by 18 other molecular species. Differential cross sections are organized as four raw data (E_o, θ, DCS, error) where E_o is impact energy, θ is scattering angle, DCS is the value of differential cross section for E_o and at scattering angle θ, error is the value of the absolute uncertainty of DCS values. These data sets represent a pool for implementing machine learning technique.

3. MACHINE LEARNING ALGORTIMS

Machine learning (ML) techniques nowadays are becoming a "New tool in the box" for physics researchers (Zdeborová, 2017). ML is a new paradigm of performing research, like taking experiment, providing theoretical approximation or execute numerical simulation (ibid.). Mapping the relation and structure of scientific knowledge in physical disciplines could be efficiently obtained and then visualized by a ML approach (Chinazzi et al. 2019). Since early and classical textbook of Michel (1997), the learning to classify new astronomical structures has been recognized as one of the examples of usefulness of ML concepts. Recently, Stokes et al. (2019) utilized a deep neural networks for the solution of the inverse swarm problem of deriving cross sections from swarm transport data.

3.1. TASK, PERFORMANCE MEASURE, EXPERIENCE

We define a task for our ML algorithm as determining the extrapolated differential cross sections from a given data of experimentally measured values at a limited range of scattering angles. The performance measure would be the value of $\chi 2$ defined as a goodness of fit by Pearson's chi-squared test. Training experience is provided as a database of calculated DCS(θ) values existing in the BEAMDB under all available theoretical approximations (distorted wave, optical potential, convergent close-coupling, B-spline R-matrix semi-relativistic or fully relativistic calculations). Additionally, the performance is measured in comparison of integrated cross sections (integral and momentum transfer) obtained with combination of experimental data and extrapolated data that resulted in such ML process with those already contained within the BEAM database or if existing, recommended set of data.

3.2. LEARNING ALGORITHMS

We performed inductive learning algorithm which at best guarantee that the output hypothesis fits the target concept over the training data (Mitchell, 1997). Our inductive bias assumption is that extrapolated DCS(θ) values can be represented by the scattering amplitudes $f(\theta,k)$, k being wave vector. Scattering amplitude consists of the sum of the phaseshifts δ_l and Legendre polynomials P_l (cos θ) as defined in (3).

$$\mathrm{DCS}(\boldsymbol{\theta}) = |\boldsymbol{f(\theta, k)}|^2 = \frac{1}{k^2}\left|\sum_{l=0}^{\infty}(2l+1)e^{i\delta_l}\sin\delta_l P_l(\cos\theta)\right|^2 \qquad (3)$$

All data are divided in three subsets, validation, training and test sets (Maček, 2019). Validation set accounts for less than one third of all data and is used to resolve overfitting problem while test set is used to provide an estimate of accuracy over new data sets.

4. DISSCUSSION

The first results of squared weighted sum of Legendre polynomials up to 60^o are given in Fig.1. Although data sets in BEAMDB seemed to be large, it turns out that it is a limited number examples that could be used in ML process. This fact urges data curators to enlarge the coverage of data entries. Also, provided software within Service of VAMDC portal, like XSAMS Convertor or graphical tool used for data visualization (http://www.vamdc.org/activities/research/software/) need to be implemented within BEAMDB in its further developments.

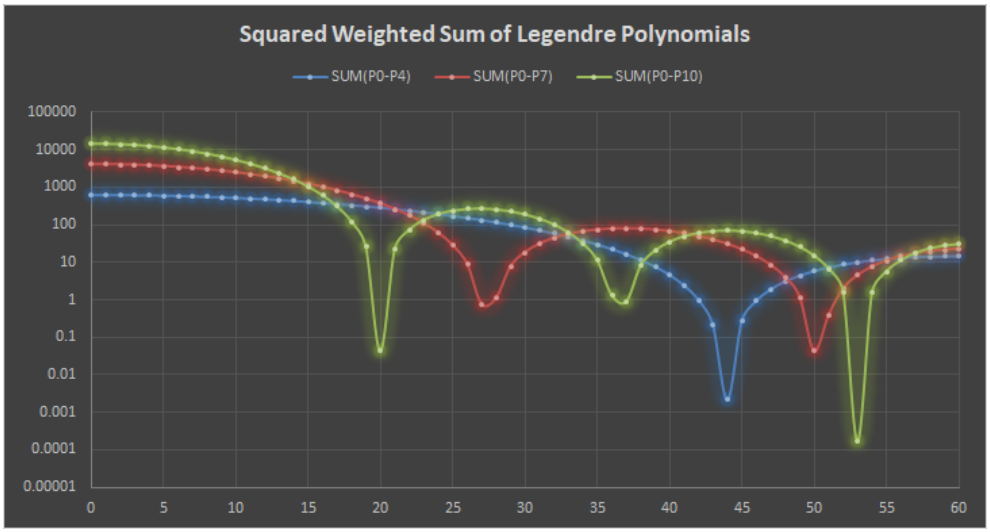

Figure 1: Squared weighted sum of 4, 7 and 10 first Legendre polynomials.

Acknowledgements

This work has been supported by the Institute of Physics Belgrade, through the grant by the Ministry of Education, Science, and Technological Development of the Republic of Serbia.

References

Bartschat, K., Tennyson, J., Zatsarinny, O. : 2017, *Plasma Process. Polym*., **14**, 1600093.

Brunger, M.J., Buckman, S. J., Allen, L.J., McCarthy, I.E., Ratnavelu, K. : 1992, *J. Phys. B: At. Mol. Opt. Phys.* **25**, 1823.

Chinazzi, M., Gonçalves, B., Zhang, Q., Vespignani, A. 2019, *EPJ Data Science*, **8**, 33.

Cho, H., McEachran, R.P., Buckman, S.J., Filipović, D.M., Pejčev, V., Marinković, B.P., Tanaka, H., Stauffer, A.D., Jung, E.C. : 2006 *J. Phys. B: At. Mol. Opt. Phys.* **39**, 3781.

Jevremović, D., Srećković, V.A., Marinković, B.P. Vujčić, V. : 2020, *Contrib. Astron. Obs. Skalnaté Pleso* **50**, 44.

Maček, N. : 2019, *Introduction in machine Learning*, Lecture material at The School of Electrical and Computer Engineering of Applied Studies, Belgrade, unpublished.

Marinković, B.P., Jevremović, D., Srećković, V.A., Vujčić, V., Ignjatović, Lj.M., Dimitrijević, M.S., Mason, N.J. : 2017, *Eur. Phys. J. D: At. Mol. Clusters & Opt. Phys.* **71**, 158.

Mason, N.J. : 2008, *AIP Conf. Proc.* : *Radiation Dmage in Biomolecular Systems*, **1080**, 3.

Mitchell, T.M. : 1997, *Machine Learning*, WCB/McGraw-Hill, ISBN: 0-07-042807-7.

Petrović, Z.Lj., Marjanović, S., Dujko, S., Banković, A., Šašić, O., Bošnjaković, D., Stojanović, V., Malović, G., Buckman, S., Garcia, G., White, R., Sullivan. J., Brunger, M. : 2014, *J. Phys.: Conf. Ser.* **488**, 012047.

Stokes, P.W, Cocks, D.G., Brunger, M.J., White, R.D. : 2019, arXiv:1912.05842v1.

Zdeborová, L. : 2017, *Nature Phys.* **13**, 420.

Publ. Astron. Obs. Belgrade No. 99 (2020), 47 - 50 *Contributed Paper*

THE $M_{4,5}NN$ AUGER SPECTRUM OF KRYPTON IN KINETIC ENERGY REGION 24 – 64 eV

BRATISLAV P. MARINKOVIĆ[1], JOZO J. JURETA[1] and LORENZO AVALDI[2]

[1] *Institute of Physics Belgrade, University of Belgrade, Laboratory for Atomic Collision Processes, Pregrevica 118, 11080 Belgrade, Serbia*
E-mail bratislav.marinkovic@ipb.ac.rs, jureta@ipb.ac.rs

[2] *CNR-Istituto di Struttura della Materia, Area della Ricerca Roma 1, Roma, Italy*
E-mail lorenzo.avaldi@ism.cnr.it

Abstract. A high resolution electrostatic analyzer in combination with a non-monochromatic electron beam has been used to investigate the Krypton $M_{4,5}NN$ Auger spectrum in the kinetic energy region from 24 to 64 eV at 505 eV incident electron energy and at 90° ejection angle. A large number of features produced by Auger and satellite transitions are observed due to the high experimental resolution. The energies and assignments of the observed features are compared with previous experiments and a good agreement is found.

1. INTRODUCTION

The krypton electronic configuration is $[Ar]3d^{10}4s^24p^6$. The energies of the $M_{4,5}$ edges of krypton 3*d* shell are M_5 ($^2D_{5/2}$) = 93.788 eV and M_4 ($^2D_{3/2}$) = 95.038 eV (King et al. 1977) leading to the energy separation between $3d_{5/2,\ 3/2}$ of 1.25 eV. The natural width of the 3*d* shell is (88 ± 4) meV. The ionization potentials of the Kr^{2+} ($4p^{-2}\ ^3P_2$) is 38.358 eV and Kr^{3+} is 74.197 eV (Palaudoux et al. 2010). The binding energies of the 3*s* (M_1), $3p_{1/2}$(M_2) and $3p_{3/2}$(M_3) are 292 eV, 222 eV and 214.6 eV, respectively (Mehlhorn, 1965). The spin-orbit splitting $3p_{3/2}$-$3p_{1/2}$ is 7.6 eV. The widths of the $3p_{1/2}$ and $3p_{3/2}$ are 1.80 eV and 1.48 eV, respectively.

Systematic studies by electron impact with high resolution of krypton $M_{4,5}NN$ Auger spectrum have been done by Mehlhorn (1965), Werme et al. (1972), Askela et al. (1984) (and ref's there in). Kr^{2+} ($4p^4nl$) satellite lines have been investigated by Hall et al. (1990), Jauhiainen et al. (1995), Kikas et al. (1996), Yoshii et al. (2007) (and ref's there in) by photoelectron spectroscopy. In this work, we present high resolution Auger spectrum of krypton in the kinetic energy region 24 to 64 eV obtained at 505 eV of incident energy.

2. EXPERIMENT

The apparatus used in the present measurements has been described previously Jureta et al. (2016). Shortly, it consists of a non-monochromatic electron gun (10-2500 eV) and a high-resolution hemispherical analyzer (R_0 = 125 mm) equipped by seven channeltrons to detect ejected electrons. A 20 mm long platinum-iridium non-biased needle with internal diameter of 0.5 mm has been used to produce an atomic beam in the perpendicular direction to the scattering plane. The cylindrical interaction region (50 mm in diameter) is made from the two cylinders of thin μ-metal foils 10 mm apart the collisional plane in order to avoid collection of scattered electrons from metal surfaces. The pass energy of 1 eV was set and then the analyser was operated in the Constant Retarding Ratio (CRR) mode i.e. the ratio (K) of the kinetic energy (E_k) and the analyser pass energy (E_p) during the scan is held constant. ($K \approx E_k/E_p$).

The background and working pressures with krypton gas in the vacuum chamber were 6×10^{-8} and 2×10^{-6} mbar respectively. With an electron current of about 10^{-6} A, the typical accumulation time for short interval of kinetic energies per spectrum was 30 min with energy step of 20 meV per channel. Each presented spectrum is the result from three measurements accumulated in the same experimental conditions. The transmission was not uniform in lower energy part and all spectra are presented with subtracted background without any further normalization of the data. The calibration of the kinetic energy scale was achieved using the line at 11.72 eV from the Ar [$3s3p^6 3d(^1D)$] excited state (27.48 eV excitation energy) in Ar-Kr mixture at 300 eV. The scale of the incident energies was calibrated using the elastic channel. For higher energies until 2000 eV, the fit made below 200 eV was applied. The FWHM of the elastic peak was roughly 0.80 eV.

3. RESULTS AND DISCUSSION

The krypton $M_{4,5}NN$ Auger spectrum measured at 505 eV incident energy and ejection angle of 90^o is shown in Fig.1. The present spectrum well compares with the one by Werme et al. (1972), although the different approach in calibration procedure leads to a systematic difference in energies of about 0.150-0.170 eV. Both Auger transitions and their satellites contribute to the observed spectrum making a difficulty in their identification. The Auger spectra produced by electrons are complex because they are composed from ejection of one or two electrons from 3*d* shell, but also other transitions can contribute to the spectrum in form of satellites produced either by ionization of the outer valence or inner shells and shake-up and shake-off transitions. The first assignments of the features have been done in comparison of their energies with optical data and shake-up transitions. New data from optical spectroscopy and theoretical calculations helped to complete assignments of large number of measured features. Those are correlation satellites and shake-off transitions. The shake-up and shake-off processes occur when the inner shell is ionized and another electron in simultaneous excitation can either populate other unoccupied orbital (shake-up) or be promoted to the continuum

(shake-off). On the other side, the correlation satellites are typical for closely-spaced states with the same total angular momentum and parity (Jauhiainen et al. 1995). They occur in a process of creation of a hole in *s* subshells of the same shell. This hole is filled by a *p* electron from the same shell followed by the simultaneous excitation of another electron to an unoccupied *d* or *s* orbitals.

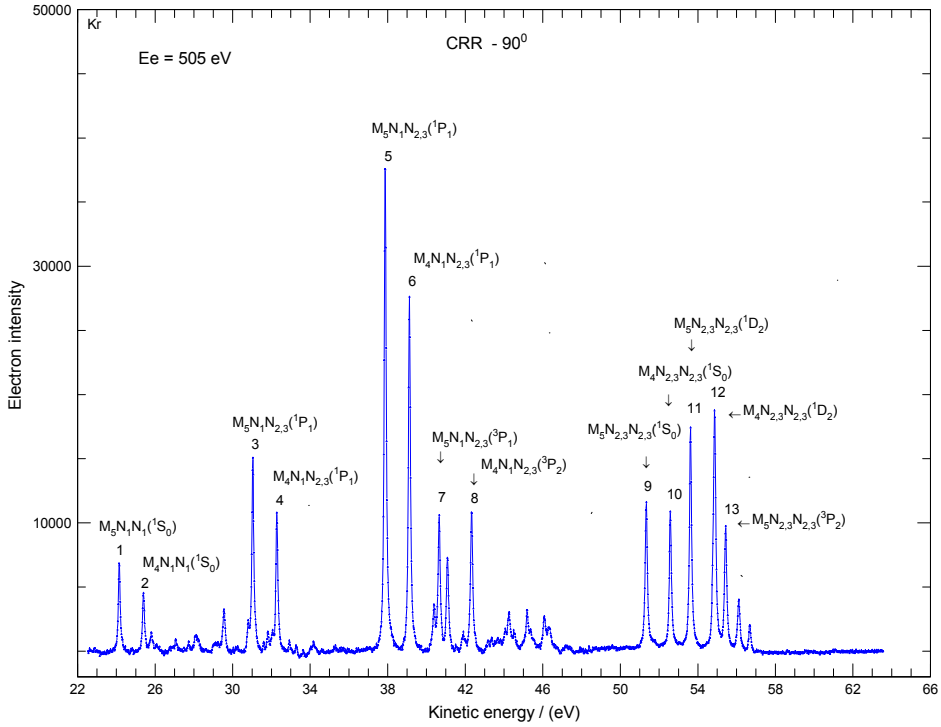

Figure 1: The $M_{4,5}NN$ Auger spectrum of krypton obtained at 505 eV of electron incident energy and 90^0 of ejection angle. Only main lines are assigned. The spectrum is presented with subtracted background with energy step of 0.020 eV. Energies of the peaks (eV) are: (1) 24.14; (2) 25.39; (3) 31.04; (4) 32.28; (5) 37.86; (6) 39.10; (7) 40.64; (8) 42.31; (9) 51.32; (10) 52.57; (11) 53.60; (12) 54.86; (13) 55.43 eV. The FWHM is approximately 110 meV.

Detailed analysis of all spectrum shows that the first kinetic energy region 24 – 34 eV is composed from several pairs of features with energy separation close or equal to the spin orbit splitting of 3*d* shell (1.25 eV). Many features are recognized as satellites produced by either shake-up or shake–off transitions. The first two features (1, 2) are assigned as Auger lines $M_{5,4}N_1N_1(^1S_0)$. The region 34 – 48 eV is composed from 4 pairs of features with energy separation close or equal to the spin orbit splitting of 3*d* shell. The last group of features in kinetic energy region 50 – 58 eV is composed from well-known $M_{5,4}N_{2,3}N_{2,3}$ Auger lines.

Acknowledgements

This work was supported by the Institute of Physics Belgrade, through the grant by the Ministry of Education, Science, and Technological Development of the Republic of Serbia and performed within the bilateral project between Italy and Serbia of particular relevance (Grande Rilevanza) "Nanoscale insights in radiation damage". B.P.M. and L.A. acknowledge the COST Action CA18212 " Molecular Dynamics in the GAS phase (MD-GAS)".

References

Aksela, H., Aksela, S., Pulkinnen, H.: 1984, *Phys. Rev*. **A 30**, 2456.

Hall, R.I., Avaldi, L., Dawber, G., Zubek, M., King, G.C.: 1990, *J. Phys. B: At. Mol. Opt. Phys.* **23**, 4469.

Jauhiainen, J., Aksela, H., Aksela, S., Kivimaki, A., Sairanen, O.P., Nommiste, E., Vegh, J.: 1995, *J. Phys. B: At. Mol. Opt. Phys.* **28**, 3831.

Jureta, J.J., Marinković, B.P., Avaldi, L.: 2016, *Eur. Phys. J. D* **70**, 199.

Kikas, A., Osborne, S. J., Ausmees, A., Svensson, S., Sairanen, O.P., Aksela, S.: 1966, *J. El. Spec. Rel. Phenom*. **77**, 241.

King, G.C., Tronc, M., Read, F.H., Bradford, R.C.: 1977, *J. Phys. B: At. Mol. Phys*. **10,** 2479.

Mehlhorn, W.: 1965, *Z. Physik* **187**, 21.

Palaudoux, J., Lablanquie, P., Andrić, L., Ito, K., Shigemasa, E., Eland, J.H.D., Jonauskas, V., Kučas, S., Karazija, R., Penent, F.: 2010, *Phys. Rev. A* **82**, 043419.

Werme, L.O., Bergmark, T., Siegbahn, K.: 1972, *Phys. Scripta* **6**, 141.

Yoshii, H., Aoto, T., Morioka, Y., Hayaishi, T.: 2007, *J. Phys. B: At. Mol. Opt. Phys.* **40**, 2765.

Publ. Astron. Obs. Belgrade No. 99 (2020), 51 - 54 *Contributed Paper*

HYPERFINE SPLITTING OF THE LOWEST STATE ENERGY OF POSITRONIUM IN STRONG ELECTRIC FIELD

M. Z. MILOŠEVIĆ, A. BUNJAC, D. B. POPOVIĆ and N. S. SIMONOVIĆ
Institute of Physics, University of Belgrade, Pregrevica 118, 11080 Belgrade, Serbia

Abstract. The lowest state energy of positronium in an external electric field is calculated in the range of field strengths belonging to the tunnelling and over-the-barrier ionization regimes, using the wave-packet propagation method and the complex-rotation method. It is found that the hyperfine splitting of this level in the tunnelling domain decreases by increasing the field strength, but in the over-the-barrier domain the additional splitting occurs for triplet states.

1. INTRODUCTION

The electron-positron (e^-e^+) bound system, known as positronium (Ps), is an unstable exotic atom due to a non-negligible probability for annihilation of its constituents (see e.g. Rich et al. 1981). The lifetimes of the singlet (1^1S_0) and triplet (1^3S_1) components of the ground-state of Ps, the so-called para-positronium (p-Ps) and orto-positronium (o-Ps), are 125 ps and 142 ns, respectively. The ground state energy of Ps is about half of that of hydrogen ($E \approx -6.8\,\mathrm{eV}$), but its hyperfine splitting (HFS) $E_{\text{o-Ps}} - E_{\text{p-Ps}} = 0.845\,\mathrm{meV}$, when compared to that for hydrogen, is more than three orders of magnitude larger. This splitting is a consequence of two spin-dependent interactions: (i) the spin-spin coupling (the interaction of individual magnetic momenta of e^- and e^+) and (ii) "the annihilation force" (the possibility of virtual annihilation and re-creation of the e^-e^+ pair, see Deutsch, 1952).

However, when positronium is placed in an electric field, another kind of instability arises – the ionization of Ps by the field. In this case the Coulomb potential of e^-e^+ pair and the external electric field form a potential (Stark) barrier through which the system can decay by tunnelling. The limiting case of this process when the barrier is suppressed below the energy of the atomic state, which takes place at very strong fields, is usually referred to as over-the-barrier ionization (OBI). The HFS of energy levels of Ps, on the other hand, is not directly affected by the external electric field. A weak dependence of HFS on electric field, however, occurs due to the change of form of the lowest state wave function of positronium when the field increases. In order to calculate this effect and the influence of electric filed generally, we apply two different numerical methods: the wave-packet propagation (WP) method and the complex-rotation (CR) method, used previously in the studies of ordinary atoms in strong fields (see Bunjac et al., 2017; Milošević and Simonović, 2015).

2. THE MODEL

2. 1. INTERACTION WITH ELECTRIC FIELD

The first step in the analysis of electric field effects on the positronium lowest levels will be the calculation of energies and ionization rates without the HFS terms. The corresponding unperturbed Hamiltonian describing the relative motion of the e^-e^+ pair, placed in the external electric field of strength F, reads (in atomic units)

$$H_0 = -\frac{1}{2\mu}\nabla^2 - \frac{1}{r} - Fz, \tag{1}$$

where r is the inter-particle distance, z is its component in the field direction and μ is the reduced mass which for positronium takes the value $1/2$. When $F \neq 0$ the Coulomb potential $-1/r$ and the external field form the potential barrier with the saddle point of hight $V_{\rm sp} = -2\sqrt{F}$ located at $\mathbf{r}_{\rm sp} = (0, 0, 1/\sqrt{F})$. Since the potential energy outside the barrier asymptotically tends to $-\infty$, the system can decay by tunnelling at any energy E. Therefore, all bound states of the field-free atom become resonant (autoionizing) states when $F \neq 0$.

As it was already mentioned in Introduction, two ionization regimes can be distinguished: (i) the tunnel ionization (tunnelling) regime, when $E < V_{\rm sp}$, and (ii) over-the-barrier ionization (OBI) regime, when $E > V_{\rm sp}$. Here we consider the lowest resonant state which in the limit $F \to 0$ approaches the ground state of the field-free atom. The value of the field strength which separates the ionization regimes F^* is the root of equation $E(F^*) = V_{\rm sp}(F^*) \equiv -2\sqrt{F^*}$. Using numerically determined values for the lowest state energy, this equation gives $F^* = 0.016$ a.u. for Ps. Thus, the tunnelling and OBI take place for: (i) $F < F^*$ and (ii) $F > F^*$, respectively.

2. 2. THE SPIN-SPIN COUPLING AND ANNIHILATION INTERACTION

The interactions which lead to the energy splitting between the o-Ps and p-Ps ground states, the spin-spin coupling and the annihilation interaction, are described by two additional terms in the Hamiltonian for relative motion (Berestetskii et al., 1982)

$$V_{\rm ss} = \frac{\alpha^2}{4}\left[\frac{3(\vec{\sigma}_1\cdot\mathbf{r})(\vec{\sigma}_2\cdot\mathbf{r})}{r^5} - \frac{\vec{\sigma}_1\cdot\vec{\sigma}_2}{r^3} + \frac{8\pi}{3}\,\vec{\sigma}_1\cdot\vec{\sigma}_2\,\delta(\mathbf{r})\right], \tag{2}$$

$$V_{\rm ann} = \frac{\pi\alpha^2}{2}(3 + \vec{\sigma}_1\cdot\vec{\sigma}_2)\,\delta(\mathbf{r}). \tag{3}$$

Here $\mathbf{r} = \mathbf{r}_1 - \mathbf{r}_2$ is the relative radius vector of e^-e^+ pair, $\vec{\sigma}_{1,2}$ are the Pauli matrices describing the spin of these two particles and $\alpha = 1/137.036$ is the fine-structure constant. In analogy with ordinary atoms, this energy splitting is called the hyperfine splitting (HFS), although for Ps it is of the same order as the fine structure corrections.

Assuming that the interaction with electric field is fully described by the dipole term $-Fz$, the Hamiltonian for positronium in electric field, which takes into account the HFS, reads

$$H = H_0 + V_{\rm ss} + V_{\rm ann} = H_0 + V_{\rm hfs}. \tag{4}$$

Using relations $\vec{\sigma}_1\cdot\vec{\sigma}_2 = 2\,\mathbf{S}^2-3$ and $(\vec{\sigma}_1\cdot\mathbf{r})(\vec{\sigma}_2\cdot\mathbf{r}) = 2\,(\mathbf{S}\cdot\mathbf{r})^2-r^2$, where $\mathbf{S} = (\vec{\sigma}_1+\vec{\sigma}_2)/2$ is the total spin, and writing $\mathbf{r} = r\,\mathbf{e}_r$, the HFS term becomes

$$V_{\rm hfs} = \frac{\alpha^2}{2\,r^3}\left[3(\mathbf{S}\cdot\mathbf{e}_r)^2 - \mathbf{S}^2\right] + \pi\alpha^2\left(\frac{7}{3}\,\mathbf{S}^2 - 2\right)\delta(\mathbf{r}). \tag{5}$$

The matrix which represents operator $(\mathbf{S}\cdot\mathbf{e}_r)^2$ in the basis of singlet/triplet spin states $\{|S, M_S\rangle \,|\, S = 0, 1; M_S = -S, \ldots, S\}$ has quasi-diagonal form

$$(\mathbf{S}\cdot\mathbf{e}_r)^2 = \left(\begin{array}{c|ccc} 0 & 0 & 0 & 0 \\ \hline 0 & \frac{1}{4}(\cos 2\vartheta + 3) & -\frac{\sin 2\vartheta\, e^{i\varphi}}{2\sqrt{2}} & \frac{1}{2}\sin^2\vartheta\, e^{2i\varphi} \\ 0 & -\frac{\sin 2\vartheta\, e^{-i\varphi}}{2\sqrt{2}} & \sin^2\vartheta & \frac{\sin 2\vartheta\, e^{i\varphi}}{2\sqrt{2}} \\ 0 & \frac{1}{2}\sin^2\vartheta\, e^{-2i\varphi} & \frac{\sin 2\vartheta\, e^{-i\varphi}}{2\sqrt{2}} & \frac{1}{4}(\cos 2\vartheta + 3) \end{array}\right), \tag{6}$$

while the corresponding matrix of operator $\mathbf{S}^2$ is diagonal

$$(\mathbf{S}^2)_{SM_S,S'M'_S} = S(S+1)\,\delta_{SS'}\delta_{M_S M'_S}. \tag{7}$$

Thus, the HFS terms do not couple singlet ($S = 0$) and triplet ($S = 1$) states, but $V_{\rm ss}$ couples the triplet states with different values of M_S.

Since the first diagonal element ($SM_S = S'M'_S = 00$) of matrices (6) and (7) is zero, in the singlet case the spin-dependent terms in Eq. (5) vanish and $V_{\rm hfs}$ reduces to

$$V_{\rm hfs}^{(S=0)} = -2\pi\alpha^2\delta(\mathbf{r}). \tag{8}$$

For the triplet case the spin-dependent terms in $V_{\rm hfs}$ are different from zero. Assuming, however, that their contribution is much smaller than the contribution of the term with delta-function, we neglect the M_S-coupling and characterize the lowest state by a definite value of quantum number M_S. In this approximation we keep in the HFS term only diagonal matrix elements $[(\mathbf{S}\cdot\mathbf{e}_r)^2]_{1M_S,1M_S}$ and $(\mathbf{S}^2)_{1M_S,1M_S} = 2$ and apply the expression

$$V_{\rm hfs}^{(S=1)} = \frac{\alpha^2}{2\,r^3}\left[3[(\mathbf{S}\cdot\mathbf{e}_r)^2]_{1M_S,1M_S} - 2\right] + \frac{8}{3}\,\pi\alpha^2\delta(\mathbf{r}). \tag{9}$$

3. RESULTS

The lowest state energy of positronium, calculated using the model without the HFS terms by the WP and CR methods, is shown in Fig. 1(a) in the range of the field strengths from $F = 0$ to 0.25 a.u. ($\approx 1.286\times10^{11}$ V/m). A difference between results obtained by these two methods, which becomes significant at very strong fields ($F \gg F^*$), indicates that the resonance mean energy E obtained by the WP method and the real part of complex energy obtained by the CR method do not have the same meaning, particularly for very broad resonances (see Klaiman, 2010).

The lowest state Ps energy with the HFS, i.e. the p-Ps and o-Ps energies as functions of the field strength, are calculated using the CR method. The calculations show that the term in Eq. (9) which is proportional to $1/r^3$ gives much smaller contribution to the HFS (for about two orders of magnitude) than the term with delta-function. This fact is in agreement with the assumption from the previous section

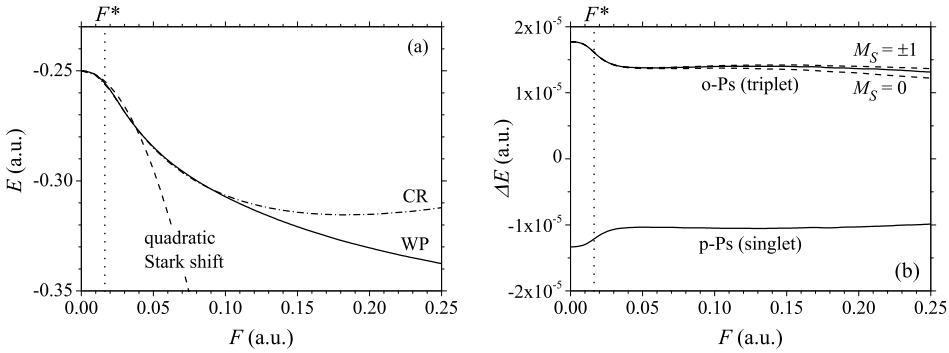

Figure 1: (a) Dependence of the lowest state energy E of positronium on the strength of external electric field F obtained numerically using the wave-packet method (WP) and the complex-rotation method (CR), respectively. For comparison the Stark shift expansion up to the quadratic term is shown (dashed line). The vertical dotted line marks the field strength F^* dividing the tunnelling and OBI domains. (b) Hyperfine splitting of the lowest state energy of Ps in electric field. The p-Ps and o-Ps lowest state energies relative to the unperturbed energy ($\Delta E_{\text{p-Ps,o-Ps}} = E_{\text{p-Ps,o-Ps}} - E$), as functions of the field strength. The dashed lines represent the values for o-Ps which are obtained using the complete expression (9) for $M_S = 0$ and $M_S = \pm 1$ separately, whereas the full line is obtained using only the term with delta-function.

which validates Eq. (9) as a good approximation. The p-Ps and o-Ps energies (the later with and without the term $\sim 1/r^3$), relative to the unperturbed energy shown in Fig. 1(a), are presented in Fig. 1(b). It can be seen that in the tunnelling domain and at the beginning of OBI domain the HFS decreases significantly by increasing the field strength, but for $F > 2F^*$ it changes slowly taking the values which are 20-25% smaller than the field-free value. This behaviour can be explained by the change of form of the lowest state wave function of positronium when it is placed in the field. The HFS in the range $F < 2F^*$ can be estimated by applying the first order perturbation theory, using V_{hfs} (without term $\sim 1/r^3$) as the perturbation. This approach gives $E_{\text{hfs}}(F) \approx \frac{14}{3}\pi\alpha^2|\psi(0;F)|^2$, where $\psi(0;F)$ is the value of the lowest state wave function of Ps in the field of strength F for $r = 0$. This relation indicates that the observed decrease of HFS when F increases is a consequence of the decrease of electron density at the positron position ($|\psi(0;F)|^2$), which can be explained by the shift of the density distribution in electric field towards the barrier.

References

Bunjac A., Popović D. B. and Simonović N. S. : 2017, *Phys. Chem. Chem. Phys.*, **19**, 19829.

Berestetskii, V. B., Liftshitz E. M., Pitaevskii, L. P. : 1982, *Quantum electrodynamics, 2nd ed. (Course of theoretical physics, Vol. 4)*, Butterworth-Heinemann, an imprint of Elsevier, Oxford.

Deutsch, M. and Brown, S. C. : 1952, *Phys. Rev.* **85**, 1047.

Klaiman, S. and Moiseyev, N. : 2010, *J. Phys. B: At. Mol. Opt. Phys.*, **43**, 185205.

Milošević, M. Z. and Simonović, N. S.: 2015, *Phys. Rev. A*, **91**, 023424.

Rich. A. : 1981, *Rev. Mod. Phys.* **53**, 127.

Publ. Astron. Obs. Belgrade No. 99 (2020), 55 -58 *Contributed Paper*

RATES FOR EXCITATION OF THE CO_2 FERMI RESONANCE MEMBERS IN RF ELECTRIC FIELD

V. V. STANKOVIĆ[1], M. M. VOJNOVIĆ[1], M. M. RISTIĆ[2] and G. B. POPARIĆ[1]

[1]*University of Belgrade, Faculty of Physics, Belgrade, Serbia*
[2]*University of Belgrade, Faculty of Physical Chemistry, Belgrade, Serbia*
E-mail violeta.stankovic@ff.bg.ac.rs

Abstract. Rate coefficients for electron impact excitation of the members of the Fermi resonance of CO_2 in non-equilibrium conditions were calculated. Monte Carlo simulation of electron transport trough gas in the presence of radio frequency electric field was employed in order to determine proper electron energy distribution functions (EEDF) for the given parameters – 100 MHz field frequency and the reduced field magnitude of 100 Td.

1. INTRODUCTION

CO_2 gas is extensively used in various devices that generate plasma by radio frequency discharge (Spencer et al. 2011, Srivastava et al. 2010). Electron collisions with CO_2 gas molecules occur frequently inside those devices and influence the further molecular dynamics. Vibrational excitation has great capacity to store energy which is later transferred between excited molecules. This is being used to achieve energy efficient dissociation, which is a key process in CO_2 conversion to ecologically friendly fuels. Rate coefficients are important input data in modeling conditions in discharge devices.

Fermi resonance was first recognized by Enrico Fermi in 1931 (Fermi 1931) as quasi degeneration of two vibrational levels, by which he explained one line in Raman spectra of CO_2, instead of two as then existing theoretical models predicted. Fermi resonances play important role in vibrational energy transfer. CO_2 molecule possesses two groups of nearly degenerate vibrational levels. The first one, called Fermi dyad, includes the lowest symmetrical stretch mode, (100), and the bending mode (020). The second one, named Fermi triad, consists of three modes – (200), (120) and (040). In the present work we are going to show time resolved rate coefficients for electron impact excitation of all these Fermi resonance members, which were obtained by means of a Monte Carlo simulation that treats electrons moving in gas filled space, under the action of a spatially uniform radio frequency

electric field. We chose the reduced electric field, E_R/N (root mean square value), to have magnitude of 100 Td. At this E_R/N value period averaged mean electron energy reaches 3.55 eV.

2. MONTE CARLO SIMULATION

The simulation follows up to 10^7 electrons, which are accelerated by the action of the radio-frequency electric field and subsequently decelerating upon collisions with CO_2 gas molecules, distributed in an infinite space. Electrons are treated one by one and their motion is determined in small time steps by numerical solution of the differential equations of motion. As soon as the steady state is reached, electron energy distribution function is repeatedly sampled, along with other relevant transport parameters, inside one cycle of the electric field and then averaged to acquire better statistics.

Data read from the input cross section database are used to calculate collision probabilities. A collision event is simulated by calling a random number generator.

A significant part of the cross sections for vibrational excitation in our database makes data obtained by coauthors of this paper in the past (Poparić et al. 2010). Those are cross sections for excitation of symmetrical stretch modes (100), (200) and so on up to (800). As it was said in the introduction, Fermi resonance consists of nearly degenerate vibrational modes. Separate contributions of the modes (100) and (020) were obtained after comparing energy loss spectra measured by (Poparić et al. 2010) with spectra reported by (Johnstone et al. 1995) and (Kitajima et al. 2001), whereby their peak deconvolution method and their angular distributions were applied. Cross sections for excitation of (120) and (040) are calculated values originating from (McCurdy et al. 2003).

Since simulation performed for relatively low reduced electric field, superelastic deexcitation from (010) * level to the ground (000) state, which is occuring with non-negligible probability at room temperature (Kato et al. 2008), was taken into account. Cross sections for this process were calculated by using the Klein-Rosseland formula.

2. RESULTS

The simulation shortly described in the previous section was prepared for the electric field parameters of 100 Td (1 Td = 10^{-21} Vm^2) and 100 MHz. The gas pressure was set to 1 Torr (133.3 Pa). EEDFS obtained within one period of oscillation by the simulation were used to determine rate coefficients. Rate coefficients were calculated by applying the formula:

$$K(<\varepsilon>_t, t) = \sqrt{2/m}\int_{\varepsilon_{th}}^{\infty}\sigma(\varepsilon)\sqrt{\varepsilon}f_e(<\varepsilon>_t, \varepsilon, t)d\varepsilon \qquad (1).$$

In the equation above $< \varepsilon >_t$ and $f_e(< \varepsilon >_t, \varepsilon, t)$ represent the mean electron energy and the normalized EEDF, respectively, at the moment of time t, ε is the electron energy, $\sigma(\varepsilon)$ is the cross section for excitation of the given vibrational mode, while the threshold energy is denoted by ε_{th}.

Time resolved rate coefficients for excitation of (100) and (020) modes, belonging to Fermi dyad of CO_2, are shown in figure 1. The results obtained for excitation of the members of Fermi triad, namely of the (200), (120) and (040) modes, are shown in figure 2.

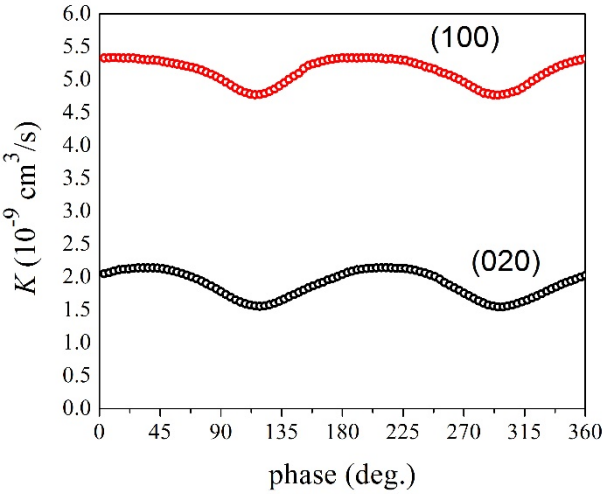

Figure 1: Rate coefficients for excitation of the Fermi dyad members.

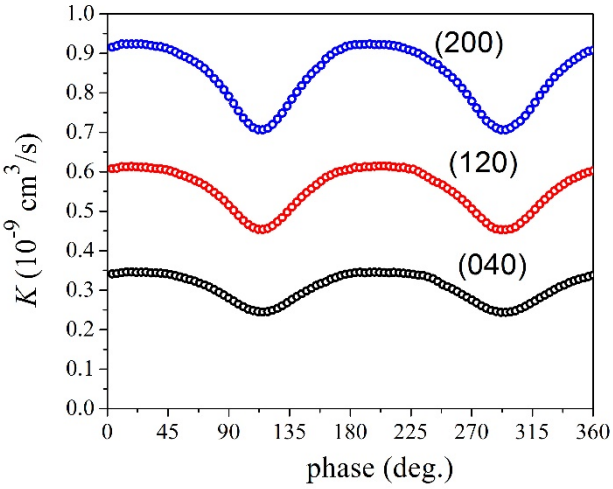

Figure 2: Rate coefficients for excitation of the Fermi triad members.

The obtained results indicate that rates for (100) and (020) are slightly shifted in phase, whereas all shown excitation rates for the members of Fermi triad are in phase. Another difference one may observe when comparing these two figures is that the amplitude of the members of Fermi dyad, shown in figure 1, is the same, but in case of Fermi triad (figure 2) amplitudes differ in magnitude for all three members. The intensity arrangement for these modes follows from the magnitudes of the corresponding cross sections. The time modulation of all these rates can be understood after performing detailed analysis of the position of the effective cross section function for the given mode with respect to the EEDF at the specific moment in time.

Acknowledgments

This work is partly supported by the Ministry of Education, Science and Technological Development of the Republic of Serbia.

References

Fermi, E. : 1931, *Z. Physik*, **71,** 250.

Johnstone, W. M., Akther, P., Newell, W. R. : 1995, *J. Phys. B: At. Mol. Opt. Phys.*, **28**, 743.

Kato, H., Kawahara, H., Hoshino, M., Tanaka, H., Campbell, L., Brunger, M. J. : 2008, *Chemical Physics Letters*, **465**, 31.

Kitajima, M., Watanabe, S., Tanaka, H., Takekawa, M., Kimura, M., Itikawa, Y. : 2001, *J. Phys. B: At. Mol Opt Phys*, **34**, 1929.

McCurdy, C. W., Isaacs, W. A., Meyer, H-D., Rescigno, T. N. : 2003, *Phys. Rev. A*, **67**, 042708.

Poparić, G. B., Ristić, M. M., Belić, D. S. : 2010, *J. Phys. Chem. A*, **114**, 1610.

Spencer, L. F. and Gallimore, A. D. : 2011, *Plasma Chem. Plasma Process.*, **31**, 79.

Srivastava, M.P. and Kobayashi, A. : 2010, *Transactions of JWRI*, **39**, No. 1.

Publ. Astron. Obs. Belgrade No. 99 (2020), 59 - 62 *Contributed Paper*

A DFT STUDY OF DISSOCIATIVE ELECTRON ATTACHMENT TO C_5XH_4N AND $C_4XH_3N_2$ (X=H,Cl,Br) AROMATIC MOLECULES

NATALIA TAŃSKA

Department of Atomic, Molecular and Optical Physics,
Faculty of Applied Physics and Mathematics,
Gdańsk University of Technology,
ul. G. Narutowicza 11/12, 80-233 Gdańsk, Poland
E–mail natalia.tanska@pg.edu.pl

Abstract. Potential energy curves for pyridine (along C-H bond) and 2-bromopyrazine (along C-Br bond) are reported, providing a rough description of a dissociative electron attachment process studied with a simple density functional theory approach. Vertical electron attachment energies for pyridine, pyrazine and their halo derivatives are also presented.

1. INTRODUCTION

Of the many possible electron-molecule interaction processes, dissociative electron attachment (DEA) is one of the most interesting, albeit still not fully described and understood. In this work, we examine the interaction of low-energy electrons with pyridine, pyrazine, and their halo derivatives with a simple density functional theory approach, as well as the applicability of this method to anions in comparison to second order Moller-Plesset perturbation theory (MP2). Pyridine and pyrazine are only briefly discussed in the literature in the context of cross sections for electron scattering [Szmytkowski *et al.*, 2019, Sanz *et al.*, 2013], or temporary anions [Nenner & Schultz 1975, Mathur & Hasted, 1976]. For 2- and 3-bromopyridine and halopyrazines vertical electron attachment energies are reported for the first time.

1. 1. CALCULATIONAL APPROACH

Various parameters of neutral and anion ground states of studied targets in the gas phase have been calculated using the DFT with B3LYP functional and MP2 methods with 6-31G*, 6-31+G*, 6-311++G**, and aug-cc-pVTZ basis sets. Vertical electron attachment energy (VEA) was obtained as the energy difference between neutral and anion ground state, both in optimized neutral geometry. Enthalpies for the following reactions are also evaluated and reported:

$$\mathrm{R{-}H} + \mathrm{e_0^-} \longrightarrow \mathrm{R^-} + \mathrm{H\cdot} \tag{1}$$

for non-substituted hydrocarbons and

$$\mathrm{R{-}X} + \mathrm{e_0^-} \longrightarrow \mathrm{R\cdot} + \mathrm{X^-} \tag{2}$$

for X=Cl, Br, where e_0^- stands for thermal electron (0 eV). Furthermore, the adiabatic potential energy curves, from which the activation energy can be read, obtained in 6-31+G* basis set with B3LYP functional for dissociative processes are presented and discussed. All calculations were performed with Gaussian 16 program suite.

2. RESULTS AND DISCUSSION

2. 1. VERTICAL ELECTRON ATTACHMENT ENERGIES

Calculated VEAs with various basis sets for pyridines compared with available experimental data are shown in Figure 2. As readily seen, the MP2 method either considerably underestimates the results or predicts the wrong anion state. Unfortunately, the problem also arises for DFT with increasing basis set, with the pyridine molecule apparently being the most sensitive for those changes. Moreover, this problem also concerns to pyrazine and its derivatives (not shown). One can notice, that although B3LYP/aug-cc-pVTZ gives the closest results to the experimental values, they are only slightly improved compared to those obtained at 6-31+G* and 6-311++G** level. This has also been confirmed for other molecules, as well as better performance than MP2 if diffuse functions are included [Szarka *et al.* 1998]. Activation energy values (E_0) for pyridine derivatives show that the lowest anion state is almost repulsive along C-X bond, whereas for halo pyrazines they have a slightly higher values. According to DFT calculations, the lowest state of pyrazine anion ($^2B_{3u}$) is bound (with ZPE correction) and so are anions of its derivatives, in contrary to pyridine-like molecules, however the VEA of pyrazie is confirmed to be negative. Values of VEA and ΔH obtained at B3LYP/aug-cc-pVTZ level (and estimated as the best) are listed in Table 1 and 2.

	(1)	2-Cl(1)	2-Br(1)	3-Cl(1)	3-Br(1)	4-Cl(1)	4-Br(1)
VEA (eV)	-0.85	-0.48	-0.42	-0.46	-0.4	-0.44	-0.36
VEA[a] (lit., eV)	-0.72	-0.41	-	-0.35	-	-0.22	-0.19
E_0 (kcal/mol)	-	1.38	≈ 0	1.18	≈ 0	≈ 0	≈ 0
ΔH(eV)	3.26-3.68[b]	≈ 0	-0.40	2.29	1.91	0.13	-0.26

Table 1: E_0 calculated with B3LYP/6-31+G*, ΔH from Eq. (1-2) and VEA, both calculated at B3LYP/aug-cc-pVTZ level for pyridine (1) and halo derivatives. [a]Experimental results of Nenner & Schultz, 1975. [b]Calculated for 3-,4- and 5-hydrogen position, from the lowest to highest value, respectively.

	(2)	2-Cl(2)	2-Br(2)
VEA (eV)	-0.22	0.14	0.2
VEA (lit., eV)	-0.08[c]	-	-
E_0 (kcal/mol)	-	5.78	3.79
ΔH(eV)	3.32	-0.03	-0.42

Table 2: Calculated and literature values for pyrazine (2) and halo derivatives, see Table 1 for further explanation. [c]Mathur & Hasted, 1976.

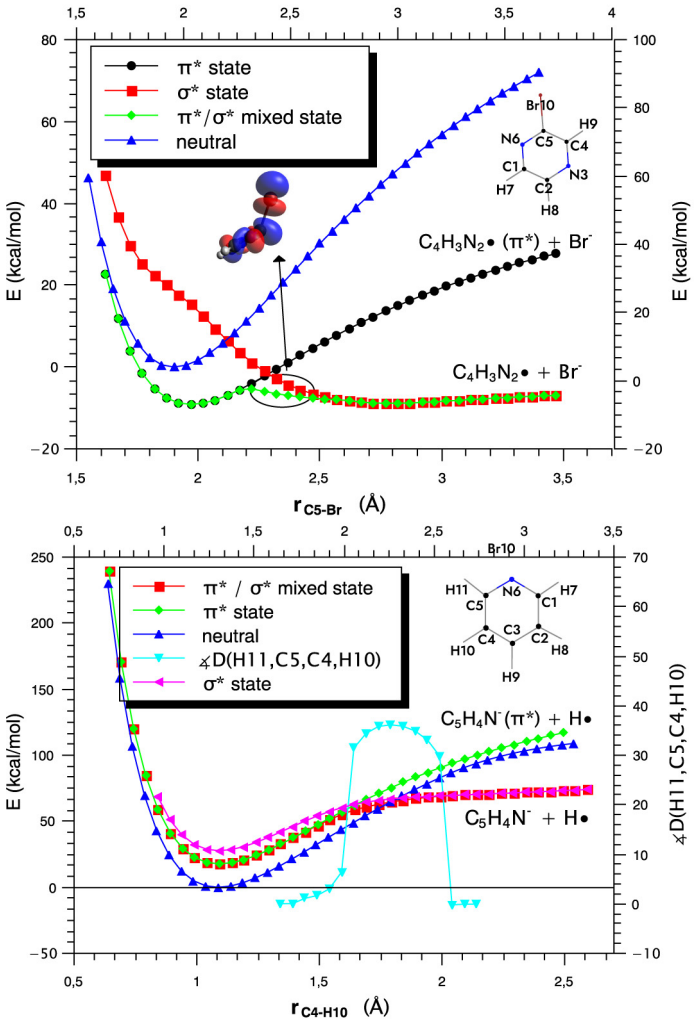

Figure 1: Example adiabatic potential energy curves along indicated bonds for 2-bromopyrazine (upper) and pyridine (lower).

2. 2. ADIABATIC POTENTIAL ENERGY CURVES

Potential energy curves (PECs) for 2-bromopyrazine and pyridine are shown in Figure 1. A similar analysis has been carried out earlier [e.g. Li, Sanche & Sevilla, 2002 and other works of these authors]. For each molecule, four different curves along C_n-X bond are investigated, namely the one of the neutral molecule, relaxed anionic curve (representing π^*/σ^* mixed state), π^* planar state, and pure σ^* state. Further analysis of Mulliken charges and spins suggests that the most energetically favored process for pyridine and pyrazine is the one described with Eq. 1, while for substituted molecules with Eq. 2, with the anionic lowest (ground) state in both cases passing from π^*- to σ^*-type SOMO (singly occupied molecular orbital). During such

a process, the molecule must undergo a symmetry change [e.g. Modelli & Venuti, 2001], which reveals in a rapid change of dihedral angle containing X atom. This reaction is recognized as the electron transfer process. Similar PECs were obtained for the rest of molecules of interest. It should be noted that all pyridines with an excess electron are not stable systems and they are bound artificially. Moreover, in such studies time dependence of reaction dynamics is not taken into account.

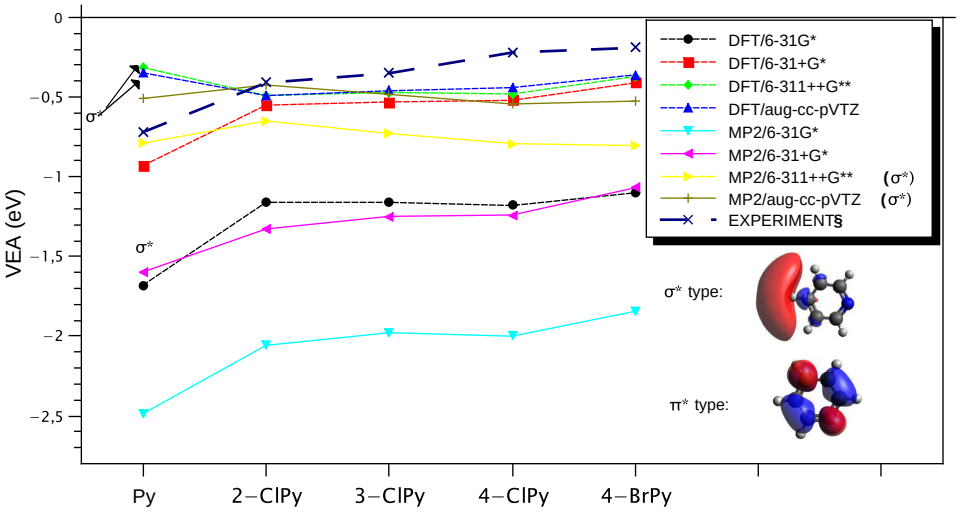

Figure 2: § Nenner & Schultz 1975. The lowest in energy VEAs obtained at given basis set, with an indication of which of them relate to σ^* states. It should be noted that all the results obtained with MP2/6-311++G** and aug-cc-pVTZ basis sets concern σ^* states.

3. ACKNOWLEDGEMENTS

This work was supported by a computational grant of the Academic Computer Center in Gdańsk (TASK).

References

Frish, M. J., Trucks, G. W., Schlegel, H. B. *et al.* Gaussian 16, Revision C.01, Gaussian, Inc.: Wallingford, CT, 2019

Li, X., Sanche, L., Sevilla, M. D. : 2002, *J. Phys. Chem.* **106**, 11248-11253.

Mathur, D., Hasted, J. : 1976, *J. Chem. Phys.* **16**, 347-352.

Modelli, A., Venuti, M. : 2001, *J. Phys. Chem.* **105**, 5836-5841.

Nenner, I., Schultz, G. : 1975, *J. Chem. Phys.*, **62**, 1747-1758.

Sanz, A. G. et al.: 2013, *J. Chem. Phys.*, **139**, 184310-1-184310-9

Szarka, A., Curtiss, L., Miller, J. R. : 1998, *J. Chem. Phys.* **246**, 147-155.

Szmytkowski, Cz., Stefanowska, S., Tańska, N., Żywicka, B., Ptasińska-Denga, E., Możejko, P.: 2019, *J. Mol. Phys.*, **117**, 395-403

Publ. Astron. Obs. Belgrade No. 99 (2020), 63 - 66 *Contributed Paper*

EXCITATION OF THE (001) MODE OF CO_2 IN 2.45 GHz MICROWAVE E FIELD AND DC B FIELD

M. M. VOJNOVIĆ[1], V. V. STANKOVIĆ[1], M. M. RISTIĆ[2] and G. B. POPARIĆ[1]

[1]*University of Belgrade, Faculty of Physics, Belgrade, Serbia*
[2]*University of Belgrade, Faculty of Physical Chemistry, Belgrade, Serbia*
E-mail mvojnovic@ff.bg.ac.rs

Abstract. This paper presents rate coefficients for excitation of the (001) mode of CO_2, determined for microwave electric field crossed at right angle with static magnetic field. The rate coefficient data were obtained for the reduced electric field amplitude of 50 Td and frequency of 2.45 GHz. Both time dependent behavior and time averaged results are analyzed. Rate coefficients were calculated on the basis of electron energy distribution functions, provided by our Monte Carlo simulation.

1. INTRODUCTION

The ever increasing danger of the global warming calls for immediate actions to be taken in order to reduce carbon dioxide emission in the atmosphere. Scientists are faced to a great challenge to find the fastest and the most cost effective response. Carbon dioxide conversion to ecologically friendly fuels stands out among the most promising research directions. As CO_2 splitting is crucial for the conversion process, different technologies are being developed in order to achieve energy efficient plasma assisted CO_2 dissociation. It is already established that highest energy efficiency is achieved in non-thermal plasma produced in a microwave discharge device that usually operates at 2.45 GHz with the reduced electric field, E_R/N (root mean square value of the electric field reduced to number density), having the magnitude of 50 Td (1 Td = 10^{-21} Vm^2) (Britun and Silva 2018). The secret lies in low energy excitation of the first asymmetrical stretch level (001) of CO_2.This process is followed by energy transfer between different vibrational levels (V-V transfer); higher vibrational states are being populated, which eventually leads to dissociation. The described dissociation mechanism requires less energy than it is required in electronic excitation (Bogaerts et al. 2016).

Due to necessity of rate coefficient data for plasma modeling and the importance of (001) excitation for CO_2 dissociation, it is mandatory to determine, as reliable as possible, (001) excitation rate coefficients. In our recent paper

(Vojnović et al. 2019), we published the results obtained for orthogonal DC electric and magnetic fields. The increase of rates with application of the magnetic field in a wide range of E_R/N was observed and explained. Since microwave discharge is mostly used in CO_2 conversion for the reasons already mentioned, we continue our study for the conditions of the presence of 2.45 GHz electric field and static magnetic field. In these conditions, electrons will move in elliptical path. This kind of motion is caused by the Lorenz force and it is done with cyclotron frequency, f_c, whereby:

$$2\pi f_c = \mathrm{e}B/m_e \qquad (1).$$

In this equation e, B and m_e denote the electron charge, the magnetic induction and electron mass, respectively. Electrons will absorb energy from the alternating electric field. With increase of the magnetic field, more and more energy is absorbed up to a certain point, after which the absorbed energy begins to decline. This is the well known electron cyclotron resonance (ECR) effect with resonance condition that cyclotron frequency equals the field frequency, f. For 2.45 GHz this condition is fulfilled at B = 875 G. In this study we will follow the rise of the (001) rates with increasing magnetic field, showing the time resolved data and the increase/decrease of the period averaged rates with the increase of the magnetic field.

2. SIMULATION

In the simulation electrons are traveling through a space uniformly filled with gas molecules under the influence of the forces of the present alternating electric and static magnetic fields. Numerical solving of the differential equation of motion provides the electron position and velocity in each small time step in the simulation. Random number generator is used to simulate the collision event and angular distribution of electrons after scattering. The probabilities of these events rely on the cross section database, which was successfully tested by comparison of the obtained transport parameters with data from different experimental groups (Vojnović et al. 2019). Since study is performed for low E_R/N, superelastic collisions for the transition $(010)^* \rightarrow (000)$ were added to the simulation database (population of the (010) level is non-negligible at room temperature (Kato et al. 2008)). Cross sections for superelastic collisions were calculated by using the Klein-Rosseland relation.

After steady state is reached, electron transport data start being sampled within a period of the field oscillation. The simulation procedure independent on the gas species was tested by comparing transport parameters with benchmark values for model gases (White et al. 1999, Nolan et al. 1997).

3. RESULTS AND DISCUSSION

Rate coefficients were calculated by using the formula:

$$K(<\varepsilon>_t, t) = \sqrt{2/m}\int_{\varepsilon_{th}}^{\infty}\sigma(\varepsilon)\sqrt{\varepsilon}f_e(<\varepsilon>_t, \varepsilon, t)d\varepsilon \qquad (2),$$

where $<\varepsilon>_t$ and $f_e(<\varepsilon>_t, \varepsilon, t)$ are the mean electron energy and the normalized EEDF, respectively, at time *t*, ε is the electron energy, $\sigma(\varepsilon)$ is the cross section for excitation of the (001) mode and ε_{th} is the threshold energy. Calculations were performed for the commonly used microwave field frequency of 2.45 GHz and for the reduced electric field magnitude of 50 Td, since at this value of E_R/N vibrational level excitations are shown to be the dominant process in plasma (Fridman 2008). The value of the reduced DC magnetic field, *B/N*, was varied from 0 up to 5000 Hx.

Figure 1 shows the time-modulated rates for excitation of the first asymmetric stretch mode, (001), for different values of *B/N* in the range from 0 to 3000 Hx. The amplitude of oscillation is gradually growing with the rise of the magnetic field, until it is damped at 3000 Hx, which is the point very close to the *B/N* value corresponding to ECR conditions (2720 Hx). It is interesting to note that this behavior is contrary to the situation with the electron mean energy, for which oscillation amplitude is highest at the point of resonance, as expected.

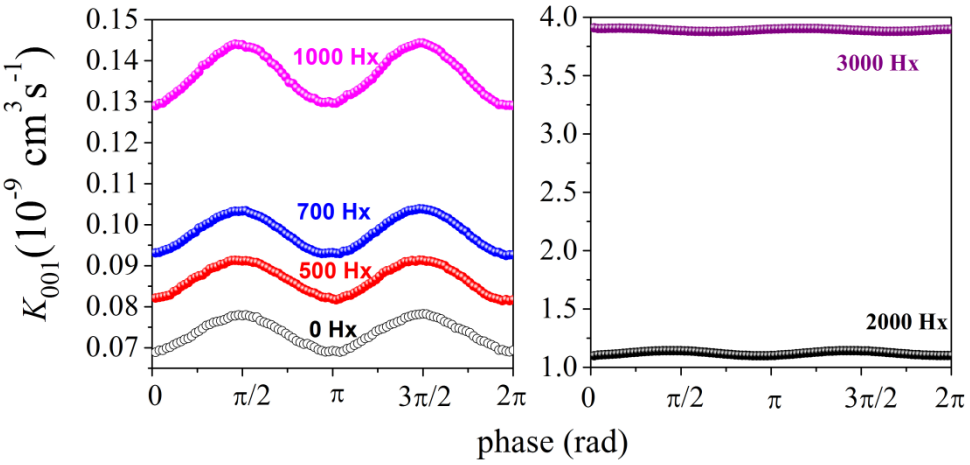

Figure 1: Time modulated (001) mode excitation rates for different *B/N*.

The fast increase of the rates with increasing magnetic field is also noticeable. To illustrate how fast these rates are rising, we plotted the function of the period averaged rates vs. *B/N* in the interval from 0 to 5000 Hx (figure 2). In the inset of the figure 2, we also show the dependence of the period averaged mean energy on *B/N*. It comes as no surprise that the maximal value of the both functions is reached at 2720 Hx, which, for the number concentration *N* of $3.22 \cdot 10^{22} m^{-3}$, set in our

simulation, corresponds to B = 875 G. Interestingly, the maximal value of the averaged (001) rates that equals $4.52 \cdot 10^{-9} cm^3 s^{-1}$ is very close to the value we obtained for zero *B* field conditions in DC electric field at 50 Td (Vojnović et al. 2019). The obtained data are nearly perfectly fitted by the Gaussian function.

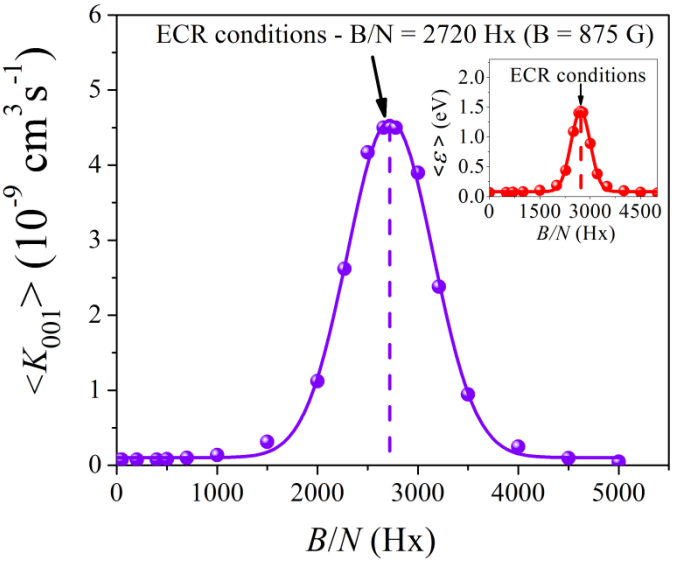

Figure 2: Period averaged rates vs. *B*/*N* – the simulation results (sphere), Gaussian function fit to data (full line), the position of ECR conditions (dash line); the inset: period averaged mean energy vs. B/N

Acknowledgments

This work is partly supported by the Ministry of Education, Science and Technological Development of the Republic of Serbia.

References

Bogaerts, A., Wang, W. Berthelot, A., Guerra, V., *Plasma Sources Sci. Technol.*, **25** (2016) 055016.

Britun, N., Silva, T. : 2018*, Plasma Chemistry and Gas Conversion, IntechOpen, London*.

Fridman, A.: 2008, *Plasma Chemistry*, Cambridge university press, New York.

Kato, H., Kawahara, H., Hoshino, M., Tanaka, H., Campbell, L., Brunger, M. J., *Chemical Physics Letters*, **465** (2008) 31.

Nolan, A. M., Brennan, M. J., Ness, K. F., Wedding, A. B., *J. Phys. D: Appl. Phys*, **30** (1997) 2865.

Vojnović, M. M., Ristić, M. M., Stanković, V.V., Poparić, G. B. : 2019*, Phys. Rev. E*, **99**, 063211.

White, R. D., Ness, K. F., Robson, R. E., Li, B., *Phys. Rev. E*, **60,** (1999) 2231.

Publ. Astron. Obs. Belgrade No. 99 (2020), 67 - 70 *Contributed Paper*

CROSS SECTIONS CALCULATIONS FOR ELECTRON SCATTERING FROM RHODANINE AND CYANOACETIC ACID

BOŻENA ŻYWICKA[1] and PAWEŁ MOŻEJKO[2]

[1]*Nicolaus Copernicus High School No. I,*
ul. Wały Piastowskie 6, 80-855 Gdańsk, Poland
E-mail bozena.zu.zywicka@gmail.com

[2]*Department of Atomic Molecular and Optical Physics,*
Faculty of Applied Physics and Mathematics,
Gdańsk University of Technology,
ul. Gabriela Narutowicza 11/12, 80-233 Gdańsk, Poland
E-mail paw@pg.edu.pl

Abstract. Cross sections for electron-impact ionization and for elastic electron scattering for rhodanine ($C_3H_3NOS_2$) and cyanoacetic acid ($C_3H_3NO_2$) have been calculated in wide impinging electron energy range.

1. INTRODUCTION

New accurate experimental data on electron interactions with matter, including collisional cross sections are still crucial and desired for understanding a wide variety of natural and technological processes occurring and carried on in complex environments (see e.g. Szmytkowski and Możejko 2020). Recent interest in electron interaction with rhodanine ($C_3H_3NOS_2$), its derivatives and cyanoacetic acid ($C_3H_3NO_2$) is connected with their potential use in solar cells. Especially, the process of electron attachment to dye-sensitized solar cell components have been studied by Modelli *et al*. 2010 and Modelli and Burrow 2011.

In this contribution we report cross sections calculations for two different collisional processes i.e. elastic electron scattering (ECS) and electron-impact ionization (ICS). These cross sections have been computed for rhodanine ($C_3H_3NOS_2$) and cyanoacetic acid ($C_3H_3NO_2$) in a wide collisional energy range spanned between the ionization threshold and 4 keV. The geometrical structure of the studied molecules is shown in figure 1. Rhodanine is a 5-membered

heterocyclic organic compound possessing a thiazolidine core while cyanoacetic acid contains two functional groups, a nitrile NC and a carboxylic acid.

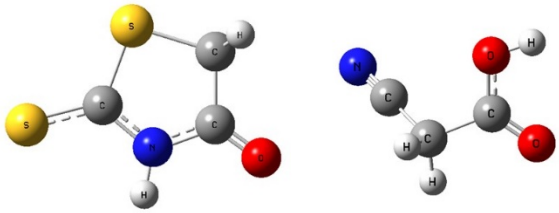

Rhodanine
$C_3H_3NOS_2$

Cyanoacetic acid
$C_3H_3NO_2$

Figure 1: Geometrical structure of the studied molecules.

2. THEORETICAL METHODS

The electron-impact ionization cross section of a given molecular orbital can be calculated using the binary-encounter-Bethe method (BEB) see e.g. Kim and Rudd 1994 and Hwang *et al.* 1996:

$$\sigma^{BEB} = \frac{S}{t+u+1}\left[\frac{\ln t}{2}\left(1-\frac{1}{t^2}\right)+1-\frac{1}{t}-\frac{\ln t}{t+1}\right], \tag{1}$$

where $u=U/B$, $t=T/B$, $S=4\pi a_0^2 NR^2/B^2$, $a_0=0.5292$ Å, $R=13.61$ eV, and T is the energy of the impinging electron. The total cross section for electron-impact ionization can be obtained as a sum of ionization cross sections calculated for all molecular orbitals:

$$\sigma^{ION} = \sum_i^{n_{MO}} \sigma_i^{BEB}, \tag{2}$$

where n_{MO} is the number of the given molecular orbital. It is extremely important that in the BEB method there is no free parameter. All quantities have well defined physical meaning and can be quite precisely evaluated. The electron binding energy, B, kinetic energy of the given orbital, U, and orbital occupation number, N, have been calculated for the ground state of the geometrically optimized molecules with the Hartree-Fock method using quantum chemistry computer code GAUSSIAN (Frisch *et al.* 2003) and 6-31G+d Gaussian basis set. Obtained that way, ionization energies are not precise enough and are usually higher, even more than 1 eV, from experimental ones. For this reason, to include into account the

effect of electron correlations within molecule, we have performed also outer valence Green function (OVGF) calculations of ionization potentials using the GAUSSIAN code see e.g. Zakrzewski and Niessen 1994. It is worth to notice that the BEB method usually provides ionization cross sections which are in quite good agreement (within ±15%) with experimental data see e.g. Karwasz *et al.* 2014.

Elastic electron scattering from the studied molecules has been investigated on the static plus polarization level with well known, additivity rule (Raj 1991), in which the total elastic cross section can be calculated from cross sections for elastic electron scattering from constituent atoms of the target molecule.

3. RESULTS AND DISCUSSION

Figure 2 shows electron-impact ionization cross section for rhodanine molecule calculated for energies ranging from the ionization threshold at 8.59 eV up to 4 keV. The cross section maximum of 12.98×10^{-20} m^2 is located at 85 eV.

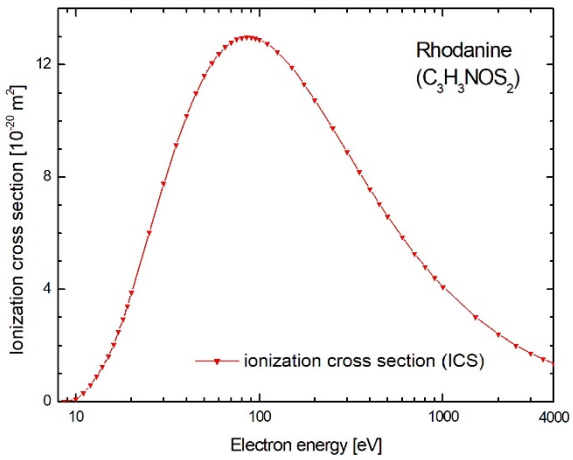

Figure 2: Electron-impact ionization cross section (ICS) calculated for rhodanine.

Figure 3 shows comparison of ICS and ECS cross sections calculated for cyanoacetic acid. The calculated ionization threshold for cyanoacetic acid is 11.464 eV. ICS maximum for this target reaches maximum of 10.57×10^{-20} m^2 at 90 eV. It can be easily seen that in the case of cyanoacetic acid contribution of elastic collisions and electron-impact ionization into overall electron scattering efficiency is almost equal for collisional energies higher than 1 keV.

The sum of the computed ECS and ICS can be used as approximation of total electron scattering cross section (TCS) for cyanoacetic acid. Basing on our

previous works the agreement between evaluated in such way TCS and measured one is quite satisfactory (see e.g. Szmytkowski et al. 2005, Szmytkowski et al. 2007, Szmytkowski et al. 2018).

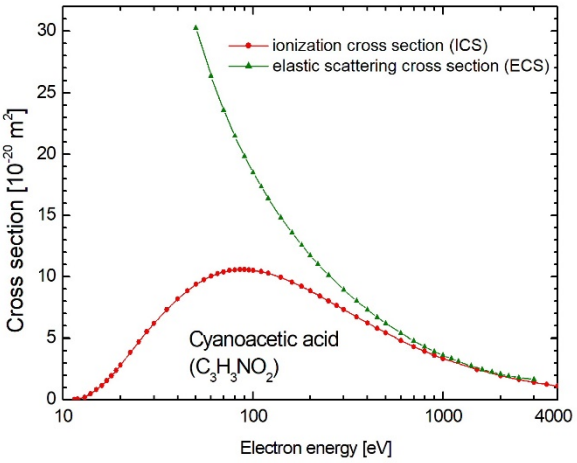

Figure 3: Cross section for elastic electron scattering (ECS) and electron-impact ionization cross section (ICS) calculated for cyanoacetic acid.

Numerical calculations have been performed at the Academic Computer Center (TASK) in Gdańsk.

References

Frisch, M. J. *et al* : 2003, *GAUSSIAN 03, Revision B.05*, Gaussian, Pittsburgh.
Hwang, W., Kim, Y.-K., Rudd, M.E. : 1996, *J. Chem. Phys.*, **104**, 2956.
Karwasz, G. P., Możejko, P., Song, M.-Y. : 2014, *Int. J. Mass Spectrom.*, **365-366**, 232.
Kim, Y.-K., Rudd, M. E. : 1994, *Phys. Rev. A*, **50**, 3954.
Modelli, A., Burrow, P. D. : 2011, *J. Phys. Chem. A*, **115**, 1100.
Modelli, A., Jones D., Pshenichnyuk, S.A. : 2010, *J. Phys. Chem. C*, **114**, 1725.
Raj, D. : 1991, *Phys. Lett. A*, **160**, 571.
Szmytkowski, Cz., Domaracka, A., Możejko, P., Ptasińska-Denga, E., Kwitnewski, S. : 2005, *J. Phys. B*, **38**, 745.
Szmytkowski, Cz., Domaracka, A., Możejko, P., Ptasińska-Denga, E. : 2007, *Phys. Rev. A*, **75**, 052721.
Szmytkowski Cz., Możejko, P. : 2020, *Eur. Phys. J. D*, **74**, 90.
Szmytkowski, Cz., Stefanowska, S., Ptasińska-Denga, E., Możejko, P. : 2018, *J. Electron Spectrosc. Relat. Phenom.*, **222**, 24.
Zakrzewski, V.G., von Niessen, W. : 1994, *J. Comp. Chem.*, **14**, 13.

Publ. Astron. Obs. Belgrade No. 99 (2020), 71 - 74 *Contributed Paper*

SINGLE-ELECTRON CAPTURE IN $p - \mathrm{He}^+$ COLLISIONS

DANILO DELIBAŠIĆ, NENAD MILOJEVIĆ and IVAN MANČEV
Department of Physics, Faculty of Sciences and Mathematics, University of Niš, P.O. Box 224, 18000 Niš, Serbia
E–mail danilo.delibasic@pmf.edu.rs

Abstract. Single-electron capture in collisions between fast protons p and helium ions $\mathrm{He}^+(1s)$ in the ground state is studied in the framework of the three-body boundary-corrected first Born approximation (CB1-3B). State-summed total cross sections are calculated by summing up the state-resolved total cross sections for principal quantum number values $n \leq 4$ according to the Oppenheimer scaling law. The obtained theoretical results are found to be in satisfactory agreement with the available experimental data.

1. INTRODUCTION

Electron capture processes in collisions between fast ionic projectiles with atomic targets have been a subject of non-diminished interest for decades. Computations of their corresponding cross sections carry both a fundamental, as well as a practical value. Electron capture cross sections play a crucial role in estimating the energy losses of ions during their passage through matter of varying kinds. As such, these cross sections databases find useful applications in both pure physics areas, such as plasma physics, astrophysics and heavy ion transport physics, as well as interdisciplinary areas, such as fusion energy research and medical physics.

In this work, we are interested in the process of single-electron capture in collisions between fast protons p and helium ions $\mathrm{He}^+(1s)$ in the ground state. This is a genuine three-body process, and as such poses a critical test to the validity of three-body theories. The cross sections are calculated in the framework of the boundary-corrected first Born approximation, often abbreviated as CB1-3B, which was first developed in the work of Belkić et al. 1979. The CB1-3B method represents the first order term in the perturbation expansion of the exact eikonal transition amplitude. Note that since the CB1-3B method employs the eikonal hypothesis, it is essentially a high energy theory. This method was successfully applied to a plethora of electron capture processes (Belkić et al. 1986, Belkić et al. 1987, Belkić et al. 1987b), as well as extended to a four-body theory, with the development of the four-body boundary-corrected first Born approximation, abbreviated as CB1-4B (Mačev et al. 2012). A systematic agreement with available measurements at intermediate and high energy values was found. The CB1-3B and CB1-4B approximations are fully quantum-mechanical approaches, which strictly preserve the correct boundary conditions in both the entrance and exit collision channels. In ion-atom collisions, boundary conditions should

fully be taken into account, whenever the aggregates are charged in the asymptotic channels (Belkić 2004, Belkić 2008). Charge exchange in $p + \mathrm{He}^+(1\mathrm{s})$ collisions has been investigated by means of various methods, such as the hidden crossing theory within the framework of dynamical adiabatic approach (Grozdanov et al. 2018), the wave-packet convergent close-coupling method (Faulkner et al. 2019), the continuum distorted-wave approximation (Mukherjee et al. 1980), the boundary-corrected continuum intermediate state approximation (Samanta et al. 2010). Atomic units will be used throughout unless otherwise stated.

2. THEORY

We consider single-electron capture in collisions between fast protons and helium ions in the ground state according to process:

$$p + \mathrm{He}^+(1\mathrm{s}) \rightarrow \mathrm{H}(\Sigma) + \mathrm{He}^{2+}, \tag{1}$$

which can also be written in the following form:

$$Z_P + (Z_T, e)_{1s} \rightarrow (Z_P, e)_\Sigma + Z_T, \tag{2}$$

where $Z_P = 1$ and $Z_T = 2$ are the respective charges of the projectile P and target T, while the symbol Σ denotes the capture into all final states of the projectile. In order to actually calculate the state-summed total cross sections Q_Σ for process (2), we will first need to calculate the state-resolved total cross sections Q_{nlm} for capture into arbitrary final states, with $\{n, l, m\}$ being the usual triplet of quantum numbers. We first consider the following process:

$$Z_P + (Z_T, e)_{1s} \rightarrow (Z_P, e)_{nlm} + Z_T. \tag{3}$$

The prior form of the transition amplitude in the CB1-3B approximation for process (3) can be written in the following form:

$$T_{if}(\vec{\eta}) = Z_\mathrm{P} \int\int \mathrm{d}\vec{s}\mathrm{d}\vec{R}\varphi^*_{nlm}(\vec{s}) \left(\frac{1}{R} - \frac{1}{s}\right) \varphi_i(\vec{x})\mathrm{e}^{i\vec{\beta}\cdot\vec{R} - i\vec{v}\cdot\vec{s}}(vR + \vec{v}\cdot\vec{R})^{i\xi}, \tag{4}$$

where $\vec{\beta} = -\vec{\eta} - \beta_z\hat{\vec{v}}$ is the momentum transfer (with $\beta_z = v/2 + \Delta E/v$), while $\Delta E = E_i - E_f$ is the difference between the initial (target and electron) and final (projectile and electron) bound state energies, and $\vec{v}$ is the projectile velocity. The transverse momentum transfer vector is denoted by $\vec{\eta} = (\eta\cos\phi_\eta, \eta\sin\phi_\eta, 0)$, and has the property $\vec{\eta}\cdot\vec{v} = 0$ for $\vec{v}$ along the $z-$axis. The position vectors of the electron relative to the projectile and target are denoted by $\vec{s}$ and $\vec{x}$, respectively, while $\vec{R}$ denotes the relative position vector of the projectile to the target. One-electron wave functions $\varphi_i(\vec{x})$ and $\varphi_{nlm}(\vec{s})$ are, respectively, the bound state wave functions of the target system $(Z_T, e)_{1s}$ before the collision (i.e. the He^+ ground state wave function), and the projectile system $(Z_P, e)_{nlm}$ after the collision (i.e. the H arbitrary state wave function). Finally, we also introduced the following symbol $\xi = (Z_P - Z_T)/v$.

The original six-dimensional integral for the transition amplitude matrix elements T_{if} from Equation (4) can be reduced to a one-dimensional integral over a real variable in the interval $[0, 1]$. The state-resolved total cross sections become:

$$Q_{nml} \equiv Q_{if}(a_0^2) = \frac{1}{2\pi v^2}\int_0^\infty d\eta\eta|T_{if}(\vec{\eta})|^2. \tag{5}$$

Numerical integration of the two-dimensional integral in Equation (5) over the two real variables is performed using Gauss-Legendre quadrature. Our general program can calculate the state-resolved total cross sections for capture from the ground state $(1s)$ of the target into arbitrary final states (n, l, m) of the projectile. The state-summed total cross sections for capture into all final states are then obtained by applying the Oppenheimer n^{-3} scaling law (Oppenheimer 1928) as:

$$Q \equiv Q_\Sigma = Q_1 + Q_2 + Q_3 + 2.561 Q_4, \tag{6}$$

where the state-resolved total cross sections Q_n and Q_{nl} are, respectively, calculated according to:

$$Q_n = \sum_{l=0}^{n-1} Q_{nl}, \quad Q_{nl} = \sum_{m=-l}^{+l} Q_{nlm}. \tag{7}$$

A preassigned convergence of at least two decimal places is achieved, with a total of 96 integration points along each of the two integration axes being used.

3. RESULTS AND DISCUSSION

The present theoretical results in the CB1-3B method, as well as the comparison with the available experimental data, are given in Figure 1. Theoretical results are

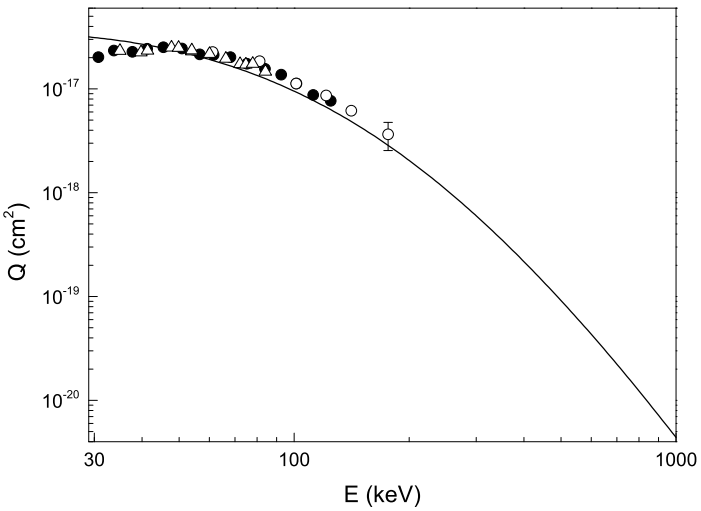

Figure 1: State-summed total cross sections as a function of impact energy E (keV) in the laboratory frame of reference for single-electron capture into all final bound states H(Σ) from the ground state of the helium ion $He^+(1s)$ by protons. The full curve is present result in the CB1-3B method. Experimental data: △ Peart et al. 1983, • Rinn et al. 1985, ○ Watts et al. 1986.

presented in the energy range from 30 to 1000 keV in the laboratory frame of reference, while the measurements were made for energies up to 176 keV. Note that all experimental data sets Peart et al. 1983, Rinn et al. 1985, and Watts et al. 1986 are in good mutual accord. As can be seen in Figure 1, the present CB1-3B results exhibit a very good agreement with all the available measurements. There is a slight overestimation of the experimental data for energies below 40 keV, as well as a slight underestimation for energies between 60 keV and 140 keV. These discrepancies are, however, very slight, and for the highest energy data point of Watts et al. 1986 at $E = 176$ keV, the theory approaches the experimental value within the measurement error. Moreover, having in mind that CB1-3B is a high energy theory, and the available measurements are all in the intermediate energy range, some discrepancy was indeed natural. The agreement is nevertheless good, and is expected to improve even further for higher energy values.

4. CONCLUSION

The value of this work, besides providing us with useful total cross section values for the process of single-electron capture in collisions between protons p and helium ions He^+, is that it also represents a further critical test of the validity of the CB1-3B approximation. The CB1-3B method has provided very accurate reproductions of experimental results for many electron capture processes. After contrasting it with the experimental data for this genuinely three-body single-electron capture process (1), we can conclude that the agreement is indeed good, and the validity of the CB1-3B method is now even more strongly confirmed.

Acknowledgements Authors thank the Ministry of Education, Science and Technological Development of the Republic of Serbia for support under Contract No. 451-03-68/2020-14/200124.

References

Belkić Dž., Gayet R. and Salin A. : 1979 *Phys. Rep.* **56**, 279
Belkić Dž., Gayet R., Hanssen J. and Salin A. : 1986 *J. Phys. B: At. Mol. Phys.* **19**, 2945
Belkić Dž. and Taylor H. S. : 1987 *Phys. Rev. A* **35**, 1991
Belkić Dž., Saini S. and Taylor H. S. : 1987b *Phys. Rev. A* **36**, 1601
Mančev I., Milojević N. and Belkić Dž. : 2012 *Phys. Rev. A* **86**, 022704
Belkić Dž. : 2004 *Principles of Quantum Scattering Theory*, Institute of Physics, Bristol
Belkić Dž. : 2008 *Quantum Theory of High-Energy Ion-Atom Collisions*, Taylor & Francis, London
Grozdanov T. and Solov'ev E. : 2018 *Eur. Phys. J. D* **72**, 64
Faulkner J., Abdurakhmanov I. B., Alladustov Sh. U., Kadyrov A. S. and Bray I. : 2019 *Plasma Phys. Control. Fusion* **61**, 095005
Mukherjee S. and Sil N. C. : 1980 *J. Phys. B: At. Mol. Phys.* **13**, 3421
Samanta R., Purkait M. and Mandal C. R. : 2010 *Phys. Scr.* **82**, 065303
Oppenheimer J. R. : 1928 *Phys. Rev.* **31**, 349
Peart B., Rinn K. and Dolder K. : 1983 *J. Phys. B: At. Mol. Phys.* **16**, 1461
Rinn K., Melchert F. and Salzborn E. : 1985 *J. Phys. B: At. Mol. Phys.* **18**, 3783
Watts M. F., Dunn K. F. and Gilbody H. B. : 1986, *J. Phys. B: At. Mol. Opt. Phys.* **19**, L355

Publ. Astron. Obs. Belgrade No. 99(2020), 75 - 78 *Contributed Paper*

INTRODUCING A NEW GUIDED ION BEAM INSTRUMENT - NOVion

IGOR SAVIĆ[1], STEPHAN SCHLEMMER[2] and DIETER GERLICH[3]

[1] *Department of Physics, Faculty of Sciences,*
University of Novi Sad
Trg Dositeja Obradovića 4, Novi Sad, 21000 (Serbia)
E-mail: savke@uns.ac.rs

[2] *I. Physikalisches Institut*
Universität zu Köln
Zülpicher Straße 77, Köln, 50937 (Germany)
E-Mail: schlemmer@ph1.uni-koeln.de

[3] *Physikalisches Institut*
Technische Universität Chemnitz
Reichenhainer Straße 70, Chemnitz, 09107 (Germany)
E-Mail: gerlich@physik.tu-chemnitz.de

Abstract. A new Guided Ion Beam instrument (NOVion) for measuring absolute integral cross sections for collisions between ions and neutrals (molecules and atoms) has been assembled and tested. This apparatus is operational since some time in Novi Sad. Our main goal is to use this instrument for studies to understand elementary processes occurring in any kind of technical or astrophysical low temperature plasmas. Some results are presented in this contribution.

1. INTRODUCTION

During the last decades, a lot of theoretical and experimental work has been performed to obtain information about elementary processes in plasmas or gas discharges. Among many other important parameters, knowing absolute cross sections (or reaction rate coefficients) for ion-neutral collisions is crucial. They are needed for understanding and modeling complex chemical system using sophisticated models. Many data used for modeling, have been measured only at one collision energy (or equivalent temperature) or extrapolated from high energy measurements. A lot of effort has been invested to understand these processes

below room temperature or to understand state to state specific cross sections. At higher energies, many states are involved, and the situation is more complicated. Understanding plasmas is still far from being complete because of many competing processes.

During last decades, many experimental techniques have been developed for studying ion chemistry, (stationary and afterglow, drift and selected ion tube, ion-cyclotron resonance, radio frequency traps, a 2 K drift tube and the CRESU flow system (cinétique de réactions en écoulement supersonique uniforme)). In addition, the versatile, very sensitive and reliable Guided Ion Beam (GIB) technique has been established. In Novi Sad, a new GIB instrument with the name NOVion is available. According to the best of our knowledge, this instrument is one of the 5 instruments of this type operational in the world.

In this paper NOVion is shortly described and some preliminary results are presented.

2. EXPERIMENTAL

The first GIB instrument has been developed in Freiburg and was described in (Gerlich 1971) and later in (Teloy and Gerlich 1974). Improvements of this early instrument as well as detailed description of the universal GIB instrument can be found in (Gerlich 1992).

NOVion is briefly described and schematically shown in (Savić et al. 2020). A publication with more technical details is in preparation. Here, only a short description of the basics of this instrument is given.

Primary ions are produced in a storage ion source (SIS) by electron bombardment of neutral gas or a mixture of gases. In this way a wide variety of different ions can be produced and stored. The ions internal energy can be influenced by changing the storage time, the electron energy, or the number density of primary and buffer gas in the SIS.

Ions produced in the SIS are mass selected using a first quadrupole ($4P_1$) and transferred into the octopole (8P) ion guide. This octopole guides the ions (in inhomogeneous electric radio frequency fields) through the scattering cell (SC).

Collisions between primary ions and neutral target gas occur in the SC. The collision energy can be changed by superimposing a DC potential to the rf voltage of the 8P. The collision energy is not exactly determined by the DC potential differences between SIS and 8P. Space charge effects in the SIS and differences in surface potentials can introduce some energy shift. To determine the laboratory energy of primary ions, two methods are available: retarding potential method described in (Teloy and Gerlich 1974) and time of flight (TOF) method described in (Gerlich 1992). For our energy calibrations both methods are in use in NOVion.

From the 8P, after collisions, the primary and product ions are transferred to the second quadrupole ($4P_2$), mass selected, detected by a Daly type ion detector and counted.

For determining absolute integral cross sections, the absolute pressure in the SC is measured using a membrane manometer (Pfeiffer CMR 375).

Determination of absolute integral cross sections is thoroughly described in (Savić et al. 2020). Knowing absolute effective integral cross sections, it is trivial to convert them into effective reaction rate coefficients.

3. FIRST RESULTS AND CONCLUSIONS

We have measured absolute integral cross sections for the formation of H_3^+ in collisions of H_2^+ with H_2. This reaction has been used as a first tests for the new instrument because many experimental and theoretical data already exist.
The reaction

$$H_2^+ + H_2 \rightarrow H_3^+ + H \qquad (1)$$

is highly exothermic and it is of great importance for hydrogen plasmas. After testing the instrument, reaction (1) has been extensively studied in the collision energy range between 0.1 and 10 eV and the results have been published recently (Savić et al. 2020). Our results and a new analytical function recommended for the energy dependence of the cross section are shown on Figure 1.

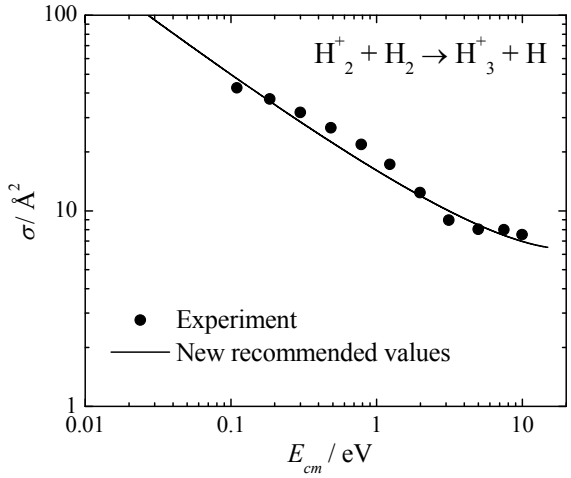

Figure 1: Measured and recommended absolute integral cross sections for reaction $H_2^+ + H_2 \rightarrow H_3^+ + H$ as function on center of mass system collision energy E_{cm}. Previous experimental and theoretical results can be found in (Savić et al. 2020)

Some preliminary results have been measured for the reaction

$$HeH^+ + H_2 \rightarrow H_3^+ + He \qquad (2)$$

at a nominal laboratory energy of E_1 = 84 meV, corresponding (for this mass ratio) to an effective temperature of 300 K. For comparing our result with published data,

we converted the measured effective cross section into an effective reaction rate coefficient *k.* This value is presented in Table 1 together with those obtained with other techniques – see (Anicich 2003) and references therein.

T (K)	*k* ($cm^3 s^{-1}$)	*Technique*
300	$8.6 \cdot 10^{-10}$	GIB (This work)
298	$1.83 \cdot 10^{-9}$	ICR
300	$> 1 \cdot 10^{-9}$	DT
296	$1.5 \cdot 10^{-9}$	SIFT

Table 1: Reaction rate coefficient for reaction $HeH^+ + H_2 \rightarrow H_3^+ + He$. (ICR - Ion Cyclotron Resonance Mass Spectrometry, DT - Drift Tube, SIFT - Selected Ion Flow Tube)

Our value measured with the GIB is almost 2 times lower than literature values and this stimulated us to explore this reaction over a wide range of collision energies. It is interesting to note that the literature data are reached at elevated collision energies, indicating non-thermal conditions, especially in the ICR instrument. The article on this topic is in preparation.

Conclusion of this contribution is that a new versatile and sensitive GIB instrument is operational in Novi Sad and that will successfully contribute to understanding of plasmas.

Acknowledgements

Financial support by the Deutsche Forschungsgemeinschaft (DFG) is gratefully acknowledged, especially via SCHL 341/17-1.

References

Anicich, V. G.: 2003, *JPL Publ.*, **03-19**, Pasadena, California.

Gerlich, D.: 1971, Diplomarbeit, Freiburg, Deutschland.

Gerlich, D.: 1992, *in State-Selected and State-to-State Ion-Molecule Reaction Dynamics. Part 1: Experiment, Advances in Chemical Physics Series,* **Vol. LXXXII**, *eds.: Ng C.Y., Baer M.*, J. Wiley & Sons, New York.

Savić, I., Schlemmer, S., Gerlich, D.: 2020, ChemPhysChem, accepted article https://doi.org/10.1002/cphc.202000258.

Teloy, E., Gerlich, D.: 1974, *Chem. Phys.,* **4**, 417.

Publ. Astron. Obs. Belgrade No. 99 (2020), 79 – 82 *Contributed Paper*

RATE COEFFICIENTS FOR Ar^+ IN Ar/BF_3 MIXTURES

Ž. NIKITOVIĆ[1], M. GILIĆ[2], J. MITRIĆ[3] and Z. RASPOPOVIĆ[4]

[1,2,3,4]*Institute of Physics, University of Belgrade, Pregrevica 118, 11080 Belgrade, Serbia*

[1]zeljka@ipb.ac.rs
[2]martina@ipb.ac.rs
[3]jmitric@ipb.ac.rs
[4]zr@ipb.ac.rs

Abstract. In this paper we present most probable reactions of Ar^+ ion with Ar/BF_3mixtures. Appropriate gas phase enthalpies of formation for the products were used to calculate scattering cross section as a function of kinetic energy. These data are needed for modeling in numerous applications of technologically important BF_3discharges. Results for transport coefficients as a function of *E/N* (*E* -electric field; *N*-gas density), specially rate coefficients were obtained by using the Monte Carlo technique.

1. INTRODUCTION

Cold plasmas are frequently used in new technologies where they open up the possibilities of non-intrusive production or modification of various substances (Makabe et al. 2006.). These plasmas have a high electron temperature and low gas temperature so non-equilibrium behavior of a large number of species becomes important (Robson et al. 2005.). Current computer resources allow studies of complex global models (Murakami et al. 2013.) which describe the behavior of such plasmas by taking into account a very large number of particles. The knowledge of ion-neutral reactions is generally available (see https://nl.lxcat.net/data/set_type.php) although the effects of reactions on transport parameters of particular ions are much less studied due to non-detectability of rapidly vanishing ionic fluxes. This especially holds for ions whose transport is affected by fast reactions (Stojanović et al. 2014. andNikitović et al. 2016.).

In this paper we firstly selected the most probable reactions of Ar^+ with BF_3 gases for thermodynamic threshold energies below about 15 eV.

2. CROSS SECTION SETS

Complete cross section sets for ion transport are scarce in spite of a broad range of specific methods relevant for quantification of particular cross sections. The main problem in heavy particle scattering, easily and precisely selecting the state of the projectile and target before the collision, is still very complicated for a range of conditions, so databases for ion scattering (Murakami et al. 2013. and https://nl.lxcat.net/data/set_type.php) are still devoid of such data. Phelps established the first worldwide accessible database with cross section sets (see https://nl.lxcat.net/cache/5b33772b61cf9/) tested for each particular case either for swarm conditions of spatially resolved measurements of emission or ion mobility values. In order to focus on effects of reactive processes introduced by BF_3 we neglected all but these two components of the Ar^+ + Ar cross section set. Complete cross section sets used in this work are shown in Figure 1.

Appropriate gas phase enthalpies of formation for the products (Table 1) were used to calculate thermodynamic thresholds.

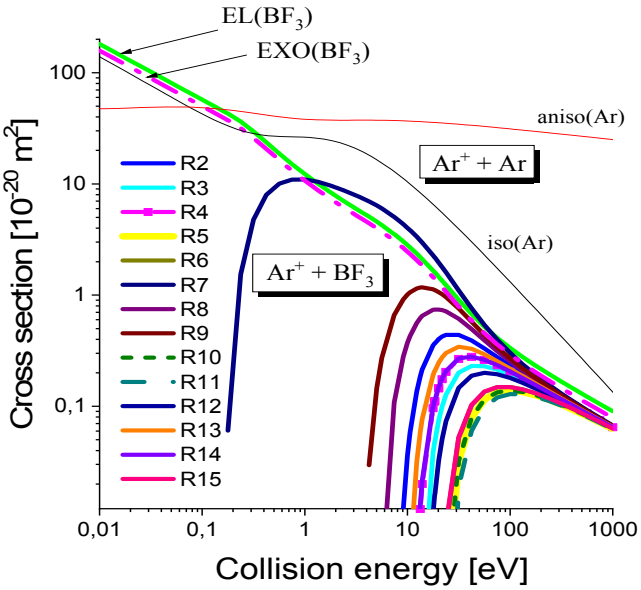

Figure 1: Cross section sets for Ar^+in BF_3.

Ion/neutral	ΔH_f(ion) kJ/mol (room temperature)	ΔH_f(neutral) kJ/mol (room temperature)
Ar^+/Ar	1520.57	0
Ar_2^+/ Ar_2	1398.1	-1.01
B^+/B	1363.3	562.7
BF^+/BF	957	-115.8
BF_2^+/BF_2	314	-589.9
BF_3^+/BF_3	364.3	-1137.0
F^+/F	1760.2	79.4
F_2^+/F_2	1514.5	0

Table 1: Heats of formation $\Delta_f H^0$ at 298 K (kJ/mol).

3. DISCUSSION AND RESULTS

Monte Carlo Simulations (MCS) have many applications for analysis of the transport of charged particles in plasmas. MCS provide swarm data with the only the uncertainty due to statistical fluctuations and uncertainties in the cross sections. In addition, MCS is the basis of hybrid models of plasmas allowing easy and accurate representation of the end effects and of the non-local high energy groups of particles which are essential in production of plasmas and treatment of surfaces.The MC code used in our analysis is based on the null collisions method.

In Figure 2 we show rate coefficients for reactions of Ar^+ ions with Ar/BF_3 mixtures at T=300K, calculated by Monte Carlo simulations. Rate coefficients are important for applications of the global model to Ar/BF_3 mixtures. We are presenting reaction products and thermodynamic thresholds for Ar^+ + BF_3(Nikitović et al. 2019.)formation a) total attachment and b) attachment for endothermic and exothermic reaction products.

4. CONCLUSION

In addition to presenting the data we show here the effects of non-conservative collisions to ion transport. Data for swarm parameters for ions are needed for hybrid and fluid codes and the current focus on liquids or liquids in the mixtures with rare gases dictates the need to produce data compatible with those models.

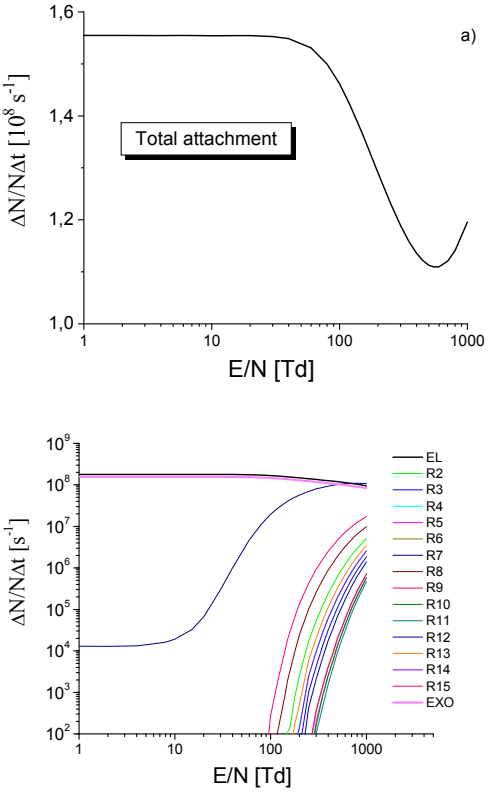

Figure 2: Rate coefficients of Ar^+ in Ar/BF_3 mixtures.

References

Makabe, T., Petrović, Z. : 2006, *Plasma Electronics: Applications in Microelectronic Device Fabrication Taylor and Francis*, New York: CRC Press.

Murakami, T., Niemi, K., Gans, T., O'Connell, D., Graham, W. G. : 2013, *Plasma Sources Sci. Technol.,***22,** 015003.

Nikitović, Ž.,Gilić, M., Raspopović, Z.,Stojanović, V. : 2016,*EPL*,**116,** 15002.

Nikitović, Ž., Raspopović, Z., Stojanović,V. : 2019, *EPL*, **128**, 15001.

Robson, R. E., White, R. D., Petrović, Z. Lj. : 2005, *Rev. Mod. Phys*., **77,** 1303.

Stojanović, V., Nikitović., Ž., Raspopović, Z., Jovanović, J. : 2014, *Acta Physica Polonica,***A125,** 46.

Section 2.

PARTICLE AND LASER BEAM INTERACTION WITH SOLIDS

MATERIALS PROCESSING WITH LOW PRESSURE PLASMA: PRESENT ISSUES AND POSSIBLE SOLUTIONS

MASAHARU SHIRATANI and KAZUNORI KOGA

Department of Electronics, Kyushu University,
744 Motooka, Fukuoka 819-0395, Japan
E-mail siratani@ed.kyushu-u.ac.jp

Abstract. Among various materials processing, we focus on thin film fabrication for integrated circuits using low pressure plasma. Present issues of thin film fabrication in semiconductor industry include film deposition at lower temperatures, film stress management, and coverage improvement in trenches. Because of maturities in materials processing using low pressure plasma, there is little room to meet the demands by optimizing processing conditions using conventional plasma reactors. Most conventional thin film fabrication for integrated circuits predominantly employs surface reactions. The elementary surface chemical reactions inherently are described by the Arrhenius equation, and hence lowering the surface temperature easily reduces surface reaction rates by a few orders of magnitude, leading to undesirable changes of compositions, structures, and properties of films. One possible approach to overcome this surface reaction limited bottleneck is to employ gas phase reactions in a sophisticated way. By using this approach, we have realized 1) SiNx films at 100 ºC, whose qualities are comparable to SiNx films at 350 ºC deposited by conventional plasma CVD, 2) stress reduction of DLC films, and 3) coverage improvement of SiOx films in trenches. The results suggest that possible solutions should combined with development of new concept reactors in order to satisfy the aggressive demands in industry. Such challenges will open new era of semiconductor fabrication.

References

Hwang, S. H., et al.: 2019, *Plasma Fusion Res.*, **14**, 4406115.
Kim, Y., et al.: 2020, *Curr. Appl. Phys.*, **20**, 191.
Fang, T., et al.: 2018, *Thin Solid Films*, **660**, 891.
Kojima, T., et al.: 2018, *Plasma Fusion Res.*, **13**, 1406082.
Shiratani, M., et al.: 2011, *J. Phys. D*, **44**, 174038.

MULTIPLE ELECTRON SCATTERING IN ATOMIC AND SURFACES COLLISIONS

KÁROLY TŐKÉSI

Institute for Nuclear Research, ATOMKI, Debrecen, Hungary
E-mail tokesi@atomki.mta.hu

Abstract. Double differential spectra of electrons ejected in ion-atom or ion-solid collisions are in the focus of general interest for a long time. These spectra are relatively easy to measure, and they show many fine details relevant for the collisions dynamics. In the past decade special effort has been devoted to understand the high energy part of the electron spectra. Significantly enhanced emission of fast electrons far above the so-called binary encounter energy was observed in both ion-atom and ion-solid collisions. In some cases, fast electrons have been identified from double, triple and quadruple scattering by the projectile and target cores. The ejected electron gains energy in every encounter with the projectile in such processes [Sulik et al. 2002, Sulik and Tőkési 2007]. This mechanism is often referred to as Fermi-shuttle acceleration. After a brief history of the study of Fermi-shuttle acceleration mechanisms in atomic collisions, we present classical trajectory Monte-Carlo results of various projectile and target combination to analyze and identify the multiple scattering components of the ejected electron spectra.

We also present a theoretical description of the spectra of electrons elastically scattered from various samples [Tőkési and Varga 2018]. The analysis is based on very large scale Monte Carlo simulations of the recoil and Doppler effects in reflection and transmission geometries. Besides the experimentally measurable energy distributions the simulations give many partial distributions separately, depending on the number of elastic scatterings (single, and multiple scatterings of different types). Furthermore, we present detailed analytical calculations for the main parameters of the single scattering, taking into account both the ideal scattering geometry, *i.e.* infinitesimally small angular range, and the effects of the real, finite angular range used in the measurements. The effect of the multiple scattering on intensity ratios, peak shifts and broadening, are shown. We show results for multicomponent and double layer samples. Our Monte Carlo simulations are compared with experimental data. We found that our results are in good agreement with the experimental observations.

Acknowledgement: The work was support by the National Research, Development and Innovation Office (NKFIH) Grant KH126886.

References

Sulik, B., Koncz, Cs., Tőkési, K., Orbán, A., Berényi, D.: 2002, *Phys. Rev. Lett.*, **88**, 073201.

Sulik, B., Tőkési, K.: 2007, *Advances in Quantum Chemistry,* **52**, 253.

Tőkési, K., Varga, D.: 2018, *Frontiers in Nuclear and Particle Physics*, **1**,132.

SIMULATING PLASMA-WALL INTERACTION IN FUSION REACTORS WITH BEAM-SURFACE EXPERIMENTS

RÉGIS BISSON

Aix-Marseille Université,CNRS, PIIM, Marseille, France
E-mail regis.bisson@univ-amu.fr

Abstract. Fusion fuel (deuterium and tritium) trapping at the divertor of tokamaks is one major concern in fusion devices such as ITER or DEMO because of fuel recycling issues as well as nuclear safety regulation related to tritium radioactivity. We developed an approach that couples dedicated experimental studies with modeling at relevant scales, from microscopic elementary steps to macroscopic observables, in order to build reliable and predictive fusion reactor wall models. This integrated approach is applied to ITER divertor material (tungsten) and advances in the development of wall models are presented.

The fundamental mechanisms behind deuterium trapping from pristine tungsten have been studied combining a multi-scale experimental and theoretical approach. Polycrystalline samples were implanted at 300 K with 500 eV D_2^+ ions. The experimental sample characterization included bulk microstructure (FIB-SEM), deuterium bulk profile (NRA), deuterium release kinetics (TPD) and surface chemical composition (AES). These experimental results are complemented by Density Functional Theory (DFT) inputs to initialize a Macroscopic Rate Equations (MRE) wall model describing all elementary steps of experiments: implantation of fuel, fuel diffusion in the bulk, fuel trapping on defects and release of trapped fuel during temperature variation of samples. We show that the DFT-based MRE model can account for all experimental observables only if two types of defects are taken into account, namely grain boundary sites and a defective tungsten oxide surface layer, see Hodille *et al.* 2017. These two type of defects can be highlighted thanks to their different fuel detrapping kinetics, as demonstrated by Laser Induced Desorption (LID) experiments using a high power infrared laser beam simulating transient thermal loads at power densities relevant for ITER.

References

Hodille, E.A., Ghiorghiu, F., Addab, Y., Založnik, A., Minissale, M., Piazza, Z., Martin, C., Angot, T., Gallais, L., Barthe, M.-F., Becquart, C.S., Markelj, S., Mougenot, J., Grisolia, C., Bisson, R. : 2017, *Nuclear Fusion*, **57**, 076019.

Publ. Astron. Obs. Belgrade No. 99 (2020), 89 - 92 *Contributed Paper*

CHANNELING POTENTIAL THROUGH RADIAL DEFORMED TRIPLE WALL CARBON NANOTUBES

D. BORKA and V. BORKA JOVANOVIĆ

Department of Theoretical Physics and Condensed Matter Physics (020), Vinča Institute of Nuclear Sciences - National Institute of the Republic of Serbia, University of Belgrade, P.O. Box 522, 11001 Belgrade, Serbia
E–mail dusborka@vinca.rs
E–mail vborka@vinca.rs

Abstract. In this study we presented a theoretical investigation of the channeling interaction potential between proton and the radial deformed (12, 0)@(8, 0)@(4, 0) triple-wall carbon nanotubes (TWNTs). Multi-wall nanotubes (MWNTs) can be technically realised with better channeling performance than the single-wall nanotubes (SWNTs) and that is why we believe that these investigations can be useful for guiding of nanosized ion beams. Obtained results show that the channeling potential is strongly influenced of level of radial deformation of nanotube.

1. INTRODUCTION

After the discovery of the carbon nanotubes, a lot of theoretical groups started to work on theoretical modeling and computer simulation of ion channeling through carbon nanotubes, see Artru et al. 2005 and Borka et al. 2011 and references therein. The experimental advancement in this area is still in the very beginning (Zhu et al. 2005, Chai et al. 2007). The both mentioned experiments are performed with the well aligned MWNTs, and that is why we study MWNTs in this paper.

Carbon nanotube can be radially deformed if we apply external mechanical stress (Hasegawa & Nishidate 2006, Imtani & Jindal 2007) or external electric field (Shtogun & Woods 2009, Kan et al. 2010) or if we use atomic force microscope (Shtogun & Woods 2009). The presence of deformations influence strongly on the nanotube's channeling properties (Abu-Assy & Soliman 2016). This work is continuation of our previous investigation (Borka Jovanović et al. 2017, Borka & Borka Jovanović 2019, Borka & Galijaš 2019). In this work we have presented a theoretical investigation of the channeling potential with the radial deformed TWNTs(12, 0)@(8, 0)@(4, 0).

2. THEORY

In this work we assumed the continuum model approximation (Lindhard 1965, Gemmel 1974). We calculate the proton nanotube interaction potential $U(x, y)$ as a function of the proton-atom distance r. We used the Molière's approximation of

the Thomas-Fermi interaction potential (Molière 1947) $V(r)$ in the following form: $U(x,y) = \sum_{k=1}^{J} \frac{1}{d} \int_{-\infty}^{\infty} V\left(\sqrt{\rho_k^2 + z^2}\right) dz$, where the k-th term in the sum represents the continuum interaction potential of the proton and the k-th atomic string, with the distance d between average centres of two adjacent carbon atoms along the row, while the ρ_k is the distance between the proton and k-th string. The total number of atomic strings in the nanotube is indicated by J and in our case it is 48 (see Figure 1).

3. RESULTS AND DISCUSSION

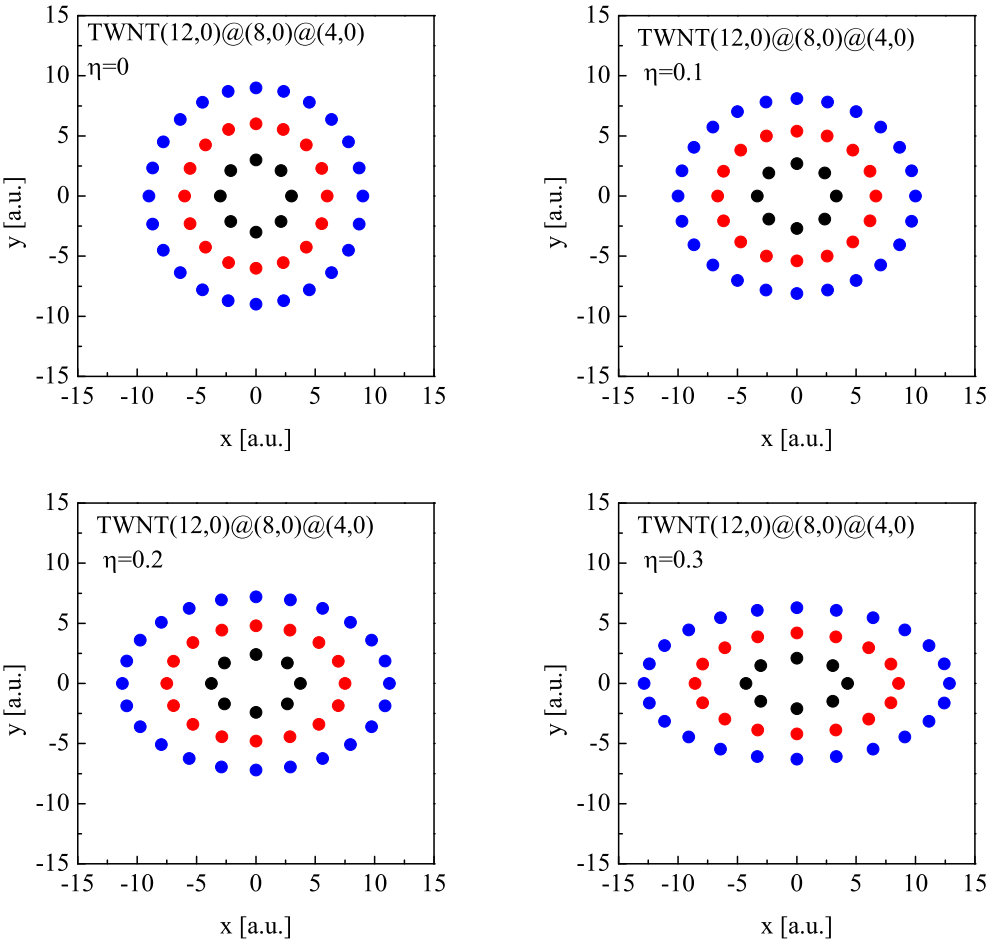

Figure 1: The view along axes of short TWNTs(12, 0)@(8, 0)@(4, 0) under different radial strains: (left top) $\eta = 0$ (perfect nanotube); (right top) $\eta = 0.1$; (left down) $\eta = 0.2$; (right down) $\eta = 0.3$, respectively.

Here, we have analyzed from theoretical aspect the channeling interaction poten-

tial of protons and the radial deformed TWNT(12, 0)@(8, 0)@(4, 0). We take into account the effect of the radial deformation because majority of nanotubes are radially deformed. Radial deformation is characterized by the dimensionless parameter $\eta = (R - R_y)/R$, where R_y is semi-minor axis and R is the radius of underfomed nanotube (Shtogun & Woods 2009). Also, we can express the semi-axis as a function of the radius R and the parameter η: $R_x = R(1-\eta)^{-1}$ and $R_y = R(1-\eta)$.

We study 4 different cases of short TWNT(12, 0)@(8, 0)@(4, 0): for perfect nanotube ($\eta = 0$) and under three different radial strains: $\eta = 0.1$, 0.2 and 0.3. From Figure 1 we can see that the intersection of the nanotube with the transverse plane gives an ellipse with semi-major axis R_x and semi-minor axis R_y. We can conclude that the radial cross section of the nanotube can take different elliptical shapes depending on the values of parameter η.

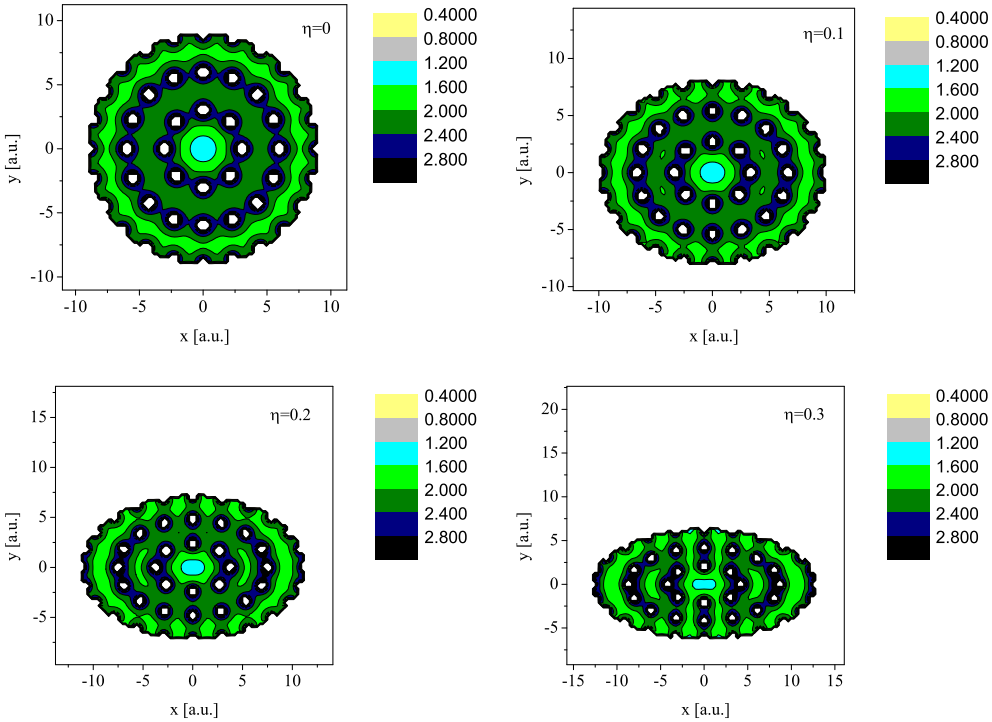

Figure 2: Contour plot of the channeling interaction potential $U(x, y)$ in the xy plane between proton and TWNTs(12, 0)@(8, 0)@(4, 0) under different radial strains: (left top) $\eta = 0$; (right top) $\eta = 0.1$; (left down) $\eta = 0.2$; (right down) $\eta = 0.3$, respectively. Values for potential U(x,y) within nanotube are presented in atomic units.

The radius of carbon nanotube R is: $R = l\sqrt{3}(2\pi)^{-1}\left(n^2 + nm + m^2\right)^{1/2}$, where the (n, m) represents chiral index and l represents interatomic length (the bond length between carbon atoms ≈ 0.144 nm (Saito et al. 2001)). The position of the carbon atom of the k-th atomic string in a plane perpendicular to the nanotube axis is determined by the angle: $\theta_k = \arctan\left(\frac{R_y}{R_x}\tan\left(2\pi(k-1)/N\right)\right)$, rel-

ative to the semi-major axis and the distance from the nanotube center: $R_k = \left(R_x^{-2} - \sin^2\theta_k \left(R_x^{-2} - R_y^{-2}\right)\right)^{-1/2}$.

The interaction potential can be calculated using following equation: $U(x,y) = \frac{4Z_1Z_2e^2}{d} \times \sum_{k=1}^{N} \sum_{j=1}^{3} a_j K_0 \left(b_j \sqrt{x^2+y^2+R_k^2 - 2\sqrt{x^2+y^2}R_k\cos\theta_k}\right)$, where $Z_1 = 1$ and $Z_2 = 6$ are the atomic numbers of the proton and carbon atom, respectively, e is the elementary charge, $a_1 = 0.35$, $a_2 = 0.55$, $a_3 = 0.1$, $b_1 = 0.3/a_{tf}$, $b_2 = 1.2/a_{tf}$, $b_3 = 6/a_{tf}$, where $a_{tf} = (9\pi^2/(128Z_2))^{1/3}a_0$ is the screening Thomas-Fermi radius, and a_0 is Bohr radius.

We can notice that the TWNT(12, 0)@(8, 0)@(4, 0) consists of SWNT(12, 0), SWNT(8, 0) and SWNT(4, 0). We can calculate the total interaction potential like: $U(x,y)_{TWNT} = U(x,y)_{SWNT(12,\ 0)} + U(x,y)_{SWNT(8,\ 0)} + U(x,y)_{SWNT(4,\ 0)}$.

Figure 2 shows contour plots of the channeling interaction potential $U(x,y)$ in the xy plane of proton and TWNT(12, 0)@(8, 0)@(4, 0) for perfect straight nanotube ($\eta = 0$) and for nanotubes under three different radial strains. Values for potential U(x,y) within nanotubes are presented in atomic units. The potential is changing very quickly close to atomic rows and the changing of potential is very slowly near the nanotube center where is the minimum value of potential. We can conclude that the nanotube channeling potential depends strongly on the radial strain.

Acknowledgments. This work is supported by Ministry of Education, Science and Technological Development of the Republic of Serbia.

References

Abu-Assy, M. K. & Soliman, M. S.: 2016, *Nucl. Instrum. Meth. Phys. Res. B* **384**, 93.
Artru, X. et al.: 2005, *Phys. Rep.* **412**, 89.
Borka, D., Petrović, S., Nešković, N.: *Channeling of protons through carbon nanotubes*, Nova Science Publishers, ISBN 978-1-61122-050-6, New York (2011).
Borka Jovanović, V., Borka, D., Galijaš, S. M. D.: 2017, *Phys. Lett. A* **381**, 1687.
Borka, D. & Borka Jovanović, V.: 2019, *Atoms* **7**, 88.
Borka, D. & Galijaš, S. M. D.: 2019, *Rom. Rep. Phys.* **71**, 207.
Chai, G., Heinrich, H., Chow, L., Schenkel, T.: 2007, *Appl. Phys. Lett.* **91**, 103101.
Gemmell, D. S.: 1974, *Rev. Mod. Phys.* **46**, 129.
Hasegawa, M. & Nishidate, K.: 2006, *Phys. Rev. B* **74**, 115401.
Imtani, A. N. & Jindal, V. K.: 2007, *Phys. Rev. B* **76**, 195447.
Kan, B. et al.: 2010, *Nanoscale Res. Lett.* **5**, 1144.
Lindhard, J. K.: 1965, *Dan. Vidensk. Selsk., Mat.-Fys.Medd.* **34, No. 14**, 1.
Molière, G.: 1947, *Z. Naturforsch. A* **2**, 133.
Saito, R., Dresselhaus, G., Dresselhaus, M. S.: *Physical Properties of Carbon Nanotubes*, Imperial College Press, London (2001).
Shtogun, Y. V. & Woods, L. M.: 2009, *J. Phys. Chem. C* **113**, 4792.
Zhu, Z. et al.: 2005, *Proc. of the Int. Conf. on Charged and Neutral Particles Channeling Phenomena*, **5974** (Bellingham, Washington: SPIE) pp 1-13.

Publ. Astron. Obs. Belgrade No. 99 (2020), 93 - 96 *Contributed Paper*

POTENTIAL ENERGY CALCULATIONS OF A CHARGED PARTICLE OUTSIDE A REAL METAL SURFACE

S. M. D. GALIJAŠ, G. B. POPARIĆ and V. MILOSAVLJEVIĆ

University of Belgrade, Faculty of Physics, P. O. Box 368, 11000 Belgrade, Serbia
E–mail galijas@ff.bg.ac.rs

Abstract. In this work we consider a more complex system with the point charge located between the real metal covered with thin dielectric film and multiply charged ion. In many cases, precise knowledge of the potential energy of a charge particle outside a real planar surface is very important for deep understanding many transfer processes. For metal-vacuum interface, the charge transfer play a significant role especially for photo and thermionic-emission and also in a different ion beam processes. Furthermore in electron diffraction and positron diffraction spectroscopy as well as in scanning tunneling microscopy, charge transfer between a metal and the vacuum is also involved.

1. LIMITATIONS OF THE CLASSICAL CHARGE-METAL SURFACE INTERACTION

The method of image charges is a basic problem-solving tool in electrostatics, see Jennings et al. 1988. The name originates from the replacement of certain elements in the original layout with imaginary charges, which replicates the boundary conditions of the problem.

Let's take a look at the potential energy of a point charge outside a planar surface. By using the method of mirror charges, we get the following expression for the potential energy of a charge q located at a distance d ($d > 0$) from the metal vacuum interface:

$$V(d) = -\frac{q^2}{16\pi\varepsilon_0 d}. \tag{1}$$

There are several problems. From the above equation we will see that for $d \to 0$, classical image potential diverges to $-\infty$. This has no physical meaning since the potential energy inside a grounded metal is finite. That is obviously a huge problem because the description becomes unrealistic in the region which is very important for investigation of all surface processes. The use of appropriate models, like surface barrier model, is one of the ways to overcome the limitation of the classical approach.

Here we point out, that there is a big difference between short range electron-metal surface interaction and large ions-metal surface interaction, see Aumayr et al. 2011. Namely, large ions slowly approaching the metal surface interface feel the potential well because of the short range repulsion from the ion cores as the constituent elements

of the crystal lattice. Also, from the standpoint of classical physics, the precise determination of the metal surface position is not so important, but if we investigate for instance the charge transfer processes, knowledge about the position of the image plane relative to the layers of metal atoms, is of crucial importance. Moreover, we do not take into account electron-electron interaction, which means that we consider external electrons to be physically distinguishable from the electrons contained in metal under consideration. So, the classical electrodynamics can not specify which of the barrier models should be taken into account for appropriate interaction between incoming or outgoing charge with electrons in the considered metal. In that way, we need strict quantum mechanical calculations of interaction.

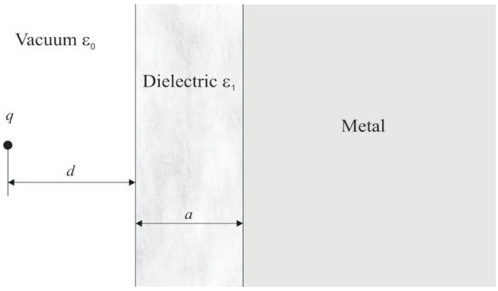

Figure 1: A point charged particle q at a distance d from the metal surface covered with a thin oxidized film. The thickness a reaches several nanometers.

2. THE METAL SURFACE COVERED WITH A THIN OXIDIZED FILM

Advantage of the image method is reflected in the fact that it can be applied not only in the case when we have a charge particle outside a metal or dielectric surface but also in the most realistic case of the interaction between a charged particles with real (oxidized) surface (see Fig. 1) effectively using analogy with optics. In this approach, after collision of the incident plane electromagnetic wave with real metal surface, the amplitude of the transmission and reflection coefficients are discussed.

For a point charged particle q positioned at a normal distance d from the metal covered by a very thin oxidized dielectric film with permittivity ε_1 (see Lake et al. 2011.), the potential energy can be expressed in the following form

$$V(d) \approx -\frac{q^2}{16\pi\varepsilon_0}\frac{1}{d+\frac{a}{\chi}}, \tag{2}$$

introducing dielectric constant of the thin oxidized film $\chi = \varepsilon_1/\varepsilon_0$ (under the condition $a \ll d$). The thickness a reaches several nanometers.

3. APPLICATION

As an illustrative example of the above analysis, we consider the population or partial neutralization of the Rydberg states of multiply charged ions interacting with

solid surfaces. That is, obviously, typical electron transfer process from solid structure to the ion. Considering the population of the Rydberg states ($n_A \gg 1$) of highly charged ions ($Z \gg 1$) interacting with solid surfaces, two aspects of the process can be analyzed. The first one is devoted to the intermediate stages of the population dynamics. These stages are characterized by the neutralization rates and the neutralization distances R_c^N, see Galijaš et al. 2019. The final population probabilities represent another important aspect of the process. Namely, from the population distributions one can recognize the Rydberg states $\mid n_A, l_A, m_A >$ with principal quantum number n_A and angular momentum quantum number l_A, that are dominantly populated. The both aspects of the population process have been considered in the last twenty years and still represent an open theoretical problem, see Nedeljković et al. 2012, Nedeljković et al. 2014. In order to find appropriate neutralization distances for example, or any other values which characterized the population process, we have to estimate the potential energy function, i.e., to estimate the electron potential energy at any point between real metal surfaces and approaching or outgoing ion subsystem (in our case in normal direction related to the metal surface).

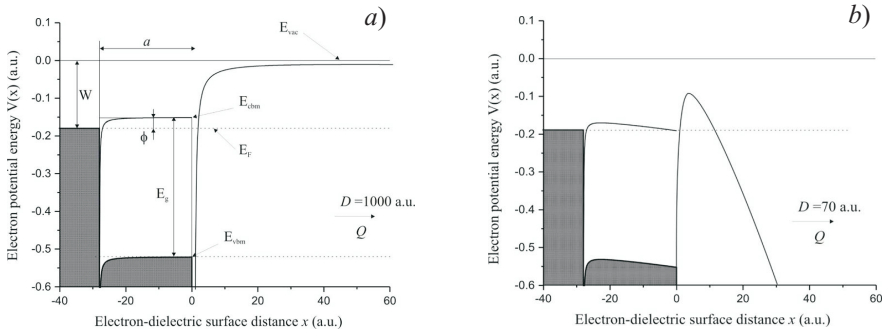

Figure 2: The electron potential energy inside metal Co, inside dielectric Al_2O_3 and between the dielectric surface and ion charge $Q = 44$ for a) $D = 1000$ a.u. and b) $D = 70$ a.u.

The potential energy V for an active charge q located in the region between the surface under consideration and the ion with charge Q is composed of three contributions: attraction between the charge q and its own image V_{qS}, direct interaction between the charge q and the ion V_{qQ} and interaction between the charge q and the ions self-image because of the existence of the metal-dielectric V_{qIQ}. If we restrict our consideration to the ionic states with large eccentricities, i.e. with low values of angular momentum quantum number, only a narrow cylindrical area around the ion trajectory participate in electron exchange process from real metal to ion during the neutralization process or in opposite way, during the reionization process. In that case we get

$$V \approx \frac{q^2}{16\pi\varepsilon_0}\left[\frac{-\eta}{d} + \frac{(1-\eta^2)}{\eta}\sum_{k=1}^{\infty}\frac{(-\eta)^k}{d+ka}\right] + \frac{1}{4\pi\varepsilon_0}\frac{qQ}{D-d} + \frac{qQ}{4\pi\varepsilon_0}\left[\frac{-\eta}{D+d} + \frac{(1-\eta^2)}{\eta}\sum_{k=1}^{\infty}\frac{(-\eta)^k}{D+d+ka}\right], \tag{3}$$

where $\eta = (\varepsilon_1 - \varepsilon_0/\varepsilon_1 + \varepsilon_0)$ denotes the dielectric function while the ion with charge Q is positioned at a normal distance D from the metal covered by dielectric film.

Inside the dielectric, the image potential V_{in} is screened by the dielectric media as ε^{-1}. Additionally, within the dielectric film, the reference energy becomes the conduction band E_{cbm} instead of the vacuum level. Along these lines, the potential energy of the point charge q inside the dielectric is given by

$$V_{in} = E_{cbm} - \frac{q^2}{16\pi\varepsilon_0\varepsilon(d+a)} + \frac{qQ}{4\pi\varepsilon_0\varepsilon(D-d)} - \frac{qQ}{4\pi\varepsilon_0\varepsilon(D+d+2a)}. \tag{4}$$

The last two terms in Eq. (4) represent the additional contribution of the ion in our system.

4. DISCUSSION

In Fig. 2 we present the potential for an electron when an ion ($Q = 44$) is far away from dielectric surface at $D = 1000$ a.u. As an example we have considered Co, whose Fermi level is 5 eV (≈ 0.18 a.u.) below the vacuum level, covered with Al_2O_3. The dielectric layer has thickness $a = 1.5$ nm (≈ 28a.u.) with fixed band gap $E_g = 9.9$ eV (≈ 0.36a.u.) and dielectric permittivity $\varepsilon_1 = 9$ ($\eta = 0.8$). Electrons in the solid are restricted from entering the vacuum region by the barrier ϕ from $-a < x < 0$, and the work function W outside the dielectric. With E_{cbm} and E_{vbm} we denote the bottom of the conduction and the top of the valence band described through functions $V_{cbm}(x)$ and $V_{vbm}(x)$, respectively. E_F is Fermi level and E_{vac} is the vacuum level.

In the case when the ion charge Q comes close to the dielectric surface ($D =$ 70a.u.), the potential curve changes in a way presented in Fig. 2b. Figs. 2a and 2b show the evolution of the barrier heights in the vacuum and in the dielectric regions as the ion (Q = 44) approaches the surface.

Acknowledgement. This work is supported by the Ministry of Education, Science and Technological Development of the Republic of Serbia.

References

Aumayr, F., Facsko, S., El-Said, A. S., Trautmann, C., Schleberger, M. : 2011, *J. Phys: Condens. Matter*, **23**, 393001.

Galijaš, S. M. D., Poparić, G. B. : 2019, *Phys. Scr.*, **94**, 025401.

Jennings, P. J., Jones, R. O. : 1988, *Adv. Phys.*, **37**, 341.

Lake, R. E., Pomeroy, H., Grube, H., Sosolik, C. E. : 2011, *Phys. Rev. Lett.*, **107**, 063202.

Nedeljković, N. N., Majkić, M. D., Galijaš. S. M. D. : 2012, *J. Phys. B: At. Mol. Opt.*, **45**, 215202.

Nedeljković, N. N., M. D., Galijaš. S. M. D., Mirković, M. A. : 2014, *J. Quant. Spectrosc. Radiat. Transfer*, **134**, 46.

Publ. Astron. Obs. Belgrade No. 99 (2020), 97 - 100 *Contributed Paper*

INTERACTIONS OF IONS WITH GRAPHENE-SAPPHIRE-GRAPHENE COMPOSITE SYSTEM: STOPPING FORCE AND IMAGE FORCE

A. KALINIĆ[1,2], I. RADOVIĆ[2], L. KARBUNAR[3], V. DESPOJA[4] and Z. L. MIŠKOVIĆ[5]

[1]*School of Electrical Engineering, University of Belgrade, Bulevar Kralja Aleksandra 73, Belgrade 11120, Serbia*
E-mail ana.kalinic@vin.bg.ac.rs

[2]*Vinča Institute of Nuclear Sciences - National Institute of the Republic of Serbia, University of Belgrade, P.O. Box 522, Belgrade 11001, Serbia*
E-mail iradovic@vin.bg.ac.rs

[3]*School of Computing, Union University, Knez Mihailova 6, Belgrade 11000, Serbia*
E-mail lkarbunar@raf.rs

[4]*Institute of Physics, Bijenička 46, Zagreb 10000, Croatia*
E-mail vito@phy.hr

[5]*Department of Applied Mathematics, and Waterloo Institute for Nanotechnology, University of Waterloo, Waterloo, Ontario N2L 3G1, Canada*
E-mail zmiskovi@uwaterloo.ca

Abstract. We derive general expressions for the stopping and image forces on an external charged particle moving parallel to a sandwich-like structure consisting of two doped graphene sheets separated by a layer of Al_2O_3 (sapphire).

1. INTRODUCTION

In nanoscale devices graphene typically appears in stacks separated by insulating layers (Yan et al. 2012), which usually support strong Fuchs-Kliewer or optical surface phonon modes (Fischetti et al. 2001). Those phonon modes are active in the terahertz (THz) to mid-infrared (mid-IR) frequency range and can hybridize with the Dirac plasmon in doped graphene which operates in the same frequency range (Fei et al. 2011). As a prototype of layered heterostructures involving doped graphene sheets, in our previous publication (Despoja et al. 2017) we studied a

graphene-sapphire-graphene composite system. We derived an expression for its effective dielectric function using two complementary methods for graphene's electronic response, based on the massless Dirac fermions method and the *ab initio* approach, and found that the structure supports a variety of interesting plasmon-phonon hybrid modes in the THz to mid-IR frequency range. In our recent publication (Despoja et al. 2019) we derived an expression for the total potential in the plane of the upper graphene sheet (the wake potential) and studied the impact of plasmon-phonon hybridization on the wake effect in the interaction of moving external charge with the graphene-Al_2O_3-graphene composite. In this work we derive general expressions for the stopping and image forces on an external charged particle moving parallel to the graphene-Al_2O_3-graphene composite system in order to study the effects of plasmon-phonon hybridization on those forces. Note that we use Gaussian electrostatic units, set $\hbar = 1$ and denote the charge of a proton by $e > 0$.

2. BASIC THEORY

We use a Cartesian coordinate system with coordinates $\{\vec{R}, z\}$, where $\vec{R} = \{x, y\}$ is a two-dimensional (2D) position vector in the xy-plane and z the distance from it, and assume that two graphene sheets are placed in the planes $z = a/2$ and $z = -a/2$, as shown in Fig. 1, with the space between them being a layer of Al_2O_3 (sapphire) of thickness a. The sapphire layer is approximated by a homogeneous dielectric slab described by local dielectric function $\varepsilon_s(\omega)$ (Ong et al. 2012), whereas graphene sheets are described by 2D response functions, $\chi_1(q, \omega)$ and $\chi_2(q, \omega)$, for their non-interacting electrons. Furthermore, we assume that an incident particle with charge Ze moves at the velocity v parallel to a graphene-Al_2O_3-graphene composite at distance b from the closest surface.

In our previous publication (Despoja et al. 2017) we derived an expression for the screened Coulomb interaction $W(\vec{q}, \omega, z, z')$ between the points in Fig. 1 with $z, z' \geq a/2$ as $W(\vec{q}, \omega, z, z') = (2\pi/q)e^{-q|z-z'|} + W_{ind}(\vec{q}, \omega, z, z')$, where

$$W_{ind}(\vec{q}, \omega, z, z') = \frac{2\pi}{q}\left[\frac{1}{\varepsilon(\vec{q},\omega)} - 1\right] e^{-q(z+z'-a)} \tag{1}$$

is the induced Coulomb interaction with $\vec{q} = \{q_x, q_y\}$ being the momentum transfer vector parallel to the xy-plane and $q = \sqrt{q_x^2 + q_y^2}$, whereas the effective 2D dielectric function $\varepsilon(\vec{q}, \omega)$ may be written as:

$$\varepsilon(q, \omega) = \frac{1}{2}\left[1 + \varepsilon_s(\omega)\coth(qa) + \frac{4\pi e^2}{q}\chi_2\right] - \frac{1}{2}\frac{\varepsilon_s^2(\omega)cosech^2(qa)}{1+\varepsilon_s(\omega)\coth(qa)+\frac{4\pi e^2}{q}\chi_1} \tag{2}$$

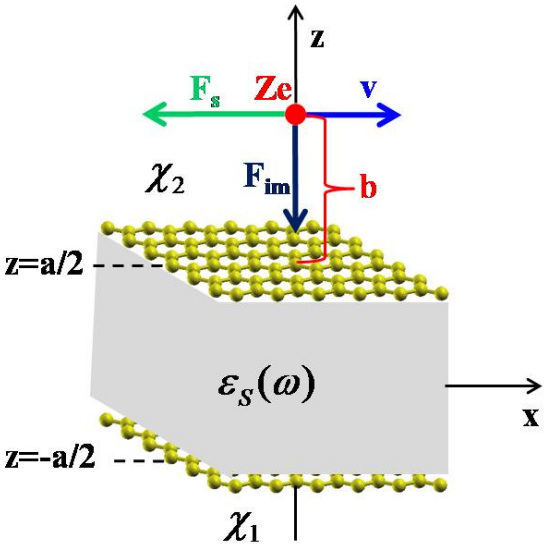

Figure 1: Diagram of the stopping force F_s and the image force F_{im} that act on the point charge Ze moving parallel to the x axis with constant speed v at a fixed distance b above the graphene-Al_2O_3-graphene composite system.

3. RESULTS FOR STOPPING AND IMAGE FORCES

For an external point charge Ze moving parallel to a graphene-Al_2O_3-graphene composite at a fixed distance b above the top graphene layer placed in the $z = a/2$ plane with a constant velocity $\vec{v}$, so that its charge density may be written as $\rho_{ext}(\vec{R}, z, t) = Ze\delta(\vec{R} - \vec{v}t)\delta[z - (a/2 + b)]$, the induced potential in the region above the upper graphene sheet, $z \geq a/2$, may be expressed as:

$$\Phi_{ind}(\vec{R}, z, t) = \frac{Ze}{(2\pi)^2} \int W_{ind}(\vec{q}, \vec{q} \cdot \vec{v}, z, a/2 + b)\, e^{i\vec{q}\cdot(\vec{R}-\vec{v}t)} d^2\vec{q} \qquad (3)$$

Substituting Eq. (1) into Eq. (3) and assuming that a point charge moves along the x axis with the speed v, one obtains an expression for the induced potential as:

$$\Phi_{ind}(x, y, z, t) = \frac{Ze}{2\pi} \int \frac{e^{-q(z-a/2+b)}}{q} \left[\frac{1}{\varepsilon(q, q_x v)} - 1\right] e^{i[q_x(x-vt)+q_y y]} dq_x dq_y \qquad (4)$$

The stopping and the image forces on the moving charge Ze are defined in terms of the induced potential $\Phi_{ind}(x, y, z, t)$, respectively, as follows (Marinković et al. 2015):

$$\mathrm{F}_s = -Ze\,\frac{\partial \Phi_{ind}(x,y,z,t)}{\partial x}\Big|_{x=vt,y=0,z=a/2+b} \tag{5}$$

$$\mathrm{F}_{im} = -Ze\,\frac{\partial \Phi_{ind}(x,y,z,t)}{\partial z}\Big|_{x=vt,y=0,z=a/2+b} \tag{6}$$

By using these definitions along with Eq. (4), it is easy to obtain:

$$\mathrm{F}_s = \frac{2(Ze)^2}{\pi}\int_0^\infty\int_0^\infty \frac{q_x e^{-2qb}}{q}\, Im\left[\frac{1}{\varepsilon(q,q_x v)}\right] dq_x dq_y \tag{7}$$

$$\mathrm{F}_{im} = \frac{2(Ze)^2}{\pi}\int_0^\infty\int_0^\infty e^{-2qb}\, Re\left[\frac{1}{\varepsilon(q,q_x v)} - 1\right] dq_x dq_y \tag{8}$$

where we used the symmetry properties of the real and imaginary parts of the dielectric function $\varepsilon(q,\omega)$ from Eq. (2).

Note that the stopping force is the negative of the usual stopping power S, $\mathrm{F}_s = -S$, whereas the image force is related to the familiar image potential V_{im} via $F_{im} = -\,dV_{im}/db$.

Acknowledgments

This research is funded by the Ministry of Education, Science and Technological Development of the Republic of Serbia, Serbia-Croatia bilateral project (Grant No. 337-00-205/2019-09/28), the QuantiXLie Center of Excellence, a project cofinanced by the Croatian Government and European Union through the European Regional Development Fund - the Competitiveness and Cohesion Operational Programme (Grant No. KK.01.1.1.01.0004), and the Natural Sciences and Engineering Research Council of Canada (RGPIN-2016-03689).

References

Despoja, V., Djordjević, T., Karbunar, L., Radović, I., Mišković, Z. L.: 2017, *Phys. Rev. B*, **96**, 075433.

Despoja, V., Radović, I., Karbunar, L., Kalinić, A., Mišković, Z. L.: 2019, *Phys. Rev. B*, **100**, 035443.

Fei, Z., Andreev, G. O., Bao, W., Zhang, L. M., McLeod, A. S., Wang, C., Stewart, M. K., Zhao, Z., Dominguez, G., Thiemens, M., Fogler, M. M., Tauber, M. J., Castro-Neto, A. H., Lau, C. N., Keilmann, F., Basov, D. N.: 2011, *Nano Lett.*, **11**, 4701.

Fischetti, M. V., Neumayer, D. A., Cartier, E. A.: 2001, *J. Appl. Phys.*, **90**, 4587.

Marinković, T., Radović, I., Borka, D., Mišković, Z. L.: 2015, *Plasmonics*, **10**, 1741.

Ong, Z.-Y., Fischetti, M. V.: 2012, *Phys. Rev. B*, **86**, 165422.

Yan, H., Li, X., Chandra, B., Tulevski, G., Wu, Y., Freitag, M., Zhu, W., Avouris, P., Xia, F.: 2012, *Nat. Nanotechnol.*, **7**, 330.

Publ. Astron. Obs. Belgrade No. 99 (2020), 101 - 104 *Contributed Paper*

IONIC VELOCITY AS A MEASURE OF AN INTERPLAY OF THE NEUTRALIZATION ENERGY AND THE DEPOSITED KINETIC ENERGY IN THE SURFACE NANOSTRUCTURE CREATION

M.D.MAJKIĆ[1], N.N. NEDELJKOVIĆ[2], and M.A. MIRKOVIĆ[3]

[1] *University of Pristina, Faculty of Technical Sciences, Kneza Milosa 7, 38220 Kosovska Mitrovica, Serbia*
E–mail milena.majkic@pr.ac.rs

[2] *University of Belgrade, Faculty of Physics, P.O. Box 368, 11001 Belgrade, Serbia*
E–mail hekata@ff.bg.ac.rs

[3] *University College of Civil Engineering and Geodesy, Hajduk Stankova 2, 11050 Belgrade, Serbia*
E–mail mirkovicmarko@vggs.rs

Abstract. We consider the role of the ionic velocity in the nanostructure creation during the interaction of highly charged Xe^{Z+} ions with solid surface.The quasi-resonant two-state vector model and the micro staircase model are used for the analysis of the neutralization process accompanied by the surface modification. For very low ionic velocity, the neutralization energy gives the main contribution in the surface nanostructuring, while for large ionic velocity the nanofeatures are created due to the kinetic energy loss (nuclear and electronic stopping power). The existence of the critical velocity, which separates these two regions, is discussed.

1. INTRODUCTION

In recent years, the highly charged ions (HCI) have been widely used as an effective tool for surface modifications. Depending on the solid type, ionic charge and velocity, different surface nanofeatures can be created, such as craters, hillocks or caldera like structures etc., see Aumayr et al. 2011. For very low ionic velocities ($v < 0.1$a.u.) the surface nanofeatures are created due to deposition of the ionic neutralization energy. For moderate ionic velocities the energy necessary for the nanostructure creation, consists both of the neutralization energy and the deposited kinetic energy (nuclear and electronic stopping power), see Lake et al. 2011 and Majkić et al. 2019.

The aim of the present contribution is to present the role of the ionic velocity in the surface modifications. For that purpose we extend our previous analysis of the HCI neutralization in the interaction with solid surface, see Majkić et al. 2017. We analyze the intermediate Rydberg state population by employing the quasi-resonant

two-state vector model (TVM) and use the micro staircase model for the cascade neutralization.

2. CRITICAL VELOCITY

We consider the HCI of initial charge $Z \gg 1$ impinging upon a metal surface (MV-system) perpendicularly at very low to moderate velocity v. The ionic Rydberg states are populated by the quasi-resonant electron tunnelling through the potential barrier formed between the ion and solid surface. The initial ionic charge $Q = Z$

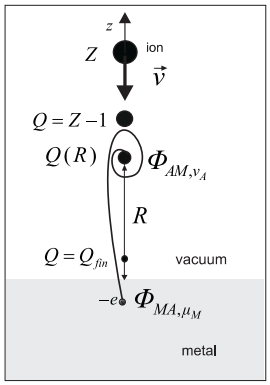

Figure 1: Cascade neutralization of HCI with initial charge Z within the MV-system.

decreases in time, $Q = Q(R)$, approaching the final value $Q = Q_{fin}$ at ion-surface distance $R = R_{min}$ (see Fig. 1). This process is known as cascade neutralization: $Q = Z \to Q = Z - 1 \to ... \to Q_{fin}$; by using the micro-staircase model, we take into account the fine structure of the population process in each macro-cascade. The neutralization process is accompanied by the release of the neutralization energy and its deposition into the surface, which leads to the nanofeatures creation.

Within the framework of the TVM the state of the active electron is described by two wave functions $\Psi_1(\vec{r}, t)$ and $\Psi_2(\vec{r}, t)$, evolving simultaneously in two opposite directions in time: see Nedeljković et al 2007 and Majkić et al. 2019. These functions can be considered as the space-time modifications of the eigenfunctions Φ_{MA,μ_M} and Φ_{AM,ν_A} of the in-Hamiltonian and out-Hamiltonian, respectively, where $\mu_M = (\gamma_M, n_{1M}, m_M)$ and $\nu_A = (n_A, l_A, m_A)$ are the metallic parabolic and atomic spherical quantum numbers, respectively, see Fig. 1. The functions $\Psi_1(\vec{r}, t)$ and $\Psi_2(\vec{r}, t)$ constitute the intermediate two-state of the active electron at the ion-surface distance R, and the corresponding mixed flux $I_{\mu_M,\nu_A}(R)$. The transition probability density is expressed via relation $T_{\mu_M,\nu_A}(t) = \left|\int_R^\infty I_{\mu_M,\nu_A}(R)dR\right|^2 / v^2$; the intermediate Rydberg state population probability is given by $P_{\nu_A}(R) = \int \sum_{n_{1M},m_M} T_{\mu_M,\nu_A}(t)d\gamma_M$. The micro-staircase model for the multielectron neutralization is based on the knowledge of the probabilities $P_{\nu_A}(R)$ and the corresponding neutralization distances. By employing this model we estimate the final ionic charge $Q = Q_{fin}$, see Majkić et al. 2019. The charges Q_{fin} increases with increasing of the ionic velocity v due to the increasing of the population probabilities maxima.

The ion with the initial charge Z (before the neutralization begins) is characterized by the initial potential energy $W_{Z,pot}$. After neutralization cascade, in front of the solid surface at minimal ion-surface distance R_{min}, within the MV-system, the ionic potential energy is given by: $W_{Q_{fin}^{MV},pot}$. The neutralization energy in the considered MV-system is (see Majkić et al. 2019)

$$W^{(Z,MV)} = W_{Z,pot} - W_{Q_{fin}^{MV},pot}. \tag{1}$$

The velocity-behaviour of the neutralization energy is the same as the behaviour of the population probabilities.

For very low ionic velocity, the neutralization process is complete ($Q_{fin} \approx 0$) and the neutralization energy $W^{(Z,MV)} = W_{Z,pot}$ is almost sufficient for the surface nanostructuring. In the case of moderate ionic velocity, due to incompleteness of the neutralization process ($Q_{fin} \neq 0$), both the deposited kinetic energy $E_{k,dep}$ and the neutralization energy $W^{(Z,MV)}$ provide the energy necessary for the nanofeatures formation. These facts indicate the existence of the area of the ionic velocities where the neutralization energy gives the main contribution to the nanofeatures creation, and the complementary one where the kinetic energy loss has to be taken into account. The velocity for which the neutralization and the deposited kinetic energy equally contribute to the nanostructure creation separates these two regions. We denote this value as critical velocity v_c:

$$W^{(Z,MV)}(v_c) = E_{k,dep}(v_c) \tag{2}$$

3. RESULTS

The results obtained in the MV-system we can apply in the analysis of the neutralization process and surface modification in the metal-dielectric-vacuum system (MDV-system) by employing the concept of the effective ionic charge Z_{eff}. That is, we use the expression $W^{(Z,MDV)} = W^{(Z_{eff},MV)}$, see Majkić et al. 2017. It is important to note here that Z_{eff} is a velocity independent quantity.

We analyse the process of the nanocrater formation by impact of slow highly charged Xe^{Z+} ions on the Co surface covered with a thin Al_2O_3 film, see Lake et al. 2011. The experimental values of the ionic velocities are in the region $v \in [0.25, 0.33]$ a.u., so that one expect that both the neutralization energy and the deposited kinetic energy participate in the process of the surface modification. Considering the neutralization cascade in the MDV-system, we take into account that the dielectric film is strongly perturbed during the ionic motion and the process of the nanostructure formation. For that reason we use the value for dielectric constant $\epsilon = 2$ for Al_2O_3 film instead of its optical value $\epsilon = 8$. The corresponding effective ionic charges are calculated in Majkić et al. 2017, and presented in the Table 1.

The kinetic energy $E_{k,dep}$ deposited in the thickness of the film $s_0 = 27$ a.u. are calculated by Lake et al., 2011 for the velocities used in experiment, i.e. for $E_k = 8.1 \cdot Z$ keV. These values can be used to estimate the quantity $E_{k,dep}$ for other velocities assuming the simple proportionality $E_{k,dep} = \kappa E_k$. We get the value $\kappa = 0.03$ for all considered ionic charges $Z \in [25, 45]$. In Fig. 1 we present the neutralization energy and the deposited kinetic energy for the Xe^{Z+} ions within the

Z	25	30	35	40	45
Z_{eff}	18.7	23	27.5	31.4	35
v_c (a.u.)	0.18	0.21	0.23	0.25	0.26

Table 1: Effective core charges Z_{eff} and critical velocities v_c in the case of the crater formation in the MDV-system (Co + Al_2O_3 film) by the impact of Xe^{Z+} ions.

considered MDV-system. The critical velocities v_c are obtained in the intersection of these curves; the corresponding values are presented in Table 1. We note that the calculated values for the critical velocities are in the region of the experimentally used velocity values. This is in accordance with the prediction that the nanocraters are formed by the participation of both the neutralization and the kinetic energy.

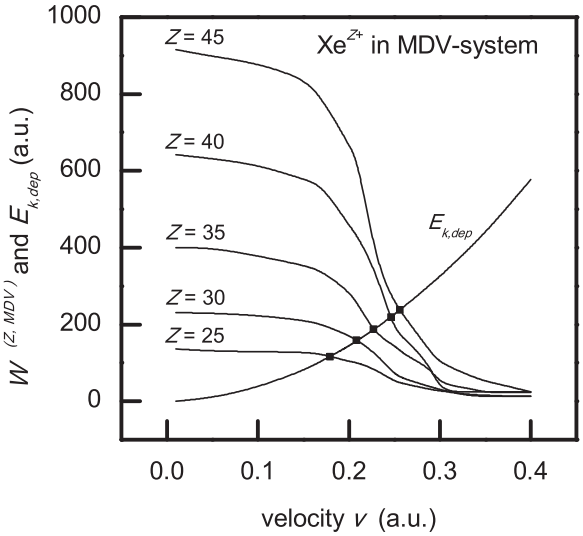

Figure 2: Neutralization energy $W^{(Z,MDV)}$ and deposited kinetic energy $E_{k,dep}$ for Xe^{Z+} ions within the MDV-system (Co + Al_2O_3 film) via ionic velocity v. By symbols we denote the critical velocities v_c for the craters formation.

Acknowledgments

This work was supported in part by the Ministry of Education, Science and Technological Development of the Republic of Serbia (Project 171016, 171029).

References

Aumayr, F., Facsko, S., El-Said, A. S., Trautmann, C., Schleberger, M.: 2011, *J. Phys.: Condens. Matter*, **23**, 39.
Lake, R., Pomeroy, J. M., Grube, H., Sosolik, C.E.: 2011, *Phys. Rev. Lett.*, **107**, 063202.
Majkić, M. D., Nedeljković, N.N., Mirković, M. A.: 2019, *Vacuum*, **165**,62-67.
Majkić, M. D., Nedeljković, N.N., Dojčilović, R. J.: 2017, *Mater. Res. Express*, **4**, 095027.
Nedeljković, N.N., Majkić, M. D.: 2007, *Phys. Rev. A*, **76**, 042902.

Publ. Astron. Obs. Belgrade No. 99 (2020), 105 - 108 *Contributed Paper*

STATE-SELECTIVE CHARGE EXCHANGE CROSS SECTIONS IN Be^{4+} + H(1s) COLLISION

I. ZIAEIAN and K. TŐKÉSI

Institute for Nuclear Research (Atomki), 4026 Debrecen Bem tér 18/c, Hungary

Abstract. Charge exchange *nl* partial cross sections have been calculated for collision of Be^{4+} with ground state hydrogen using the 3-body classical trajectory Monte Carlo method and quasiclassical trajectory Monte Carlo method of Kirschbaum and Wilets. The cross sections have been obtained for projectile n=1, 2, 3, 4 and 5 states and for corresponding allowed l quantum numbers. Calculations are carried out in the impact energy range between 1 and 1000 keV/au. Our results are compared to existing previous results. We showed that the calculations by QTMC-KW model improve the calculated cross sections.

1. INTRODUCTION

Beryllium is typically considered as the armor material for Plasma Facing Components (PFCs) of fusion devices and it is the first wall of the International Thermonuclear Experimental Reactor (ITER) (see Pitts et al. 2011). The inelastic collision processes between Be^{q+} ions and H are particularly important when energetic neutral hydrogen is injected into the plasma for heating and diagnostic purposes (see Hackman et al. 1984). Therefore the accurate description and knowledge of these interactions are extremely important for fusion research. The state-selective cross sections for charge exchange in collision between Be and hydrogen atom has been studied in the past using different theoretical approaches such as; MOCC method (see Harel et al. 1998, 1997), AOCC method (see Fritsch et al. 1984), OEDM (see Errea et al. 1982, 1998) and GTDSE method (see Jorge et al. 2016). The quasiclassical trajectory Monte Carlo method of Kirschbaum and Wilets (QTMC-KW) model (see Kirschbaun et al. 1980) is one step further for a better description of the classical atomic collisions. For atoms, a necessary condition for stability is that the electrons are not allowed to collapse to the symmetry point, i.e., to the nucleus. The effective potential enforcing this condition is motivated by the Heisenberg uncertainty principle $rp \geq \xi_H \hbar$, where r and p are the distance and momentum of an electron with respect to a nucleus and ξ_H is constant. For the H atom, this condition is equivalent to the de Broglie description of the hydrogen atom.

In this work we present state selective charge exchange cross sections in collision between Be^{4+} and ground state hydrogen atom using the 3-body classical trajectory Monte Carlo method (CTMC) and quasiclassical trajectory Monte Carlo method of Kirschbaum and Wilets (QTMC-KW). Our results are compared to existing previous results.

2. THEORY

In the present work, the CTMC simulations were made in the three-body approximation. The three particles (p; projectile, e; electron, T; target) are characterized by their masses and charges. For the description of the interaction among the particles, Coulomb potential is used. Figure 1 shows the relative position vectors of the three-body collision system.

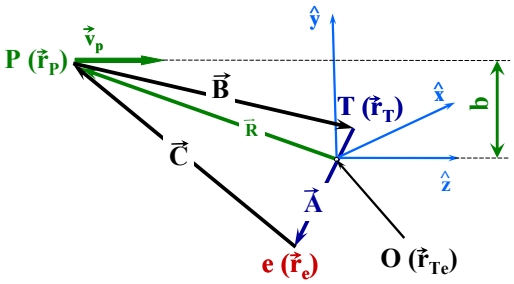

Figure 1: The relative position vectors of the particles involved in 3-body collisions. $\vec{A} = \vec{r}_e - \vec{r}_T$, $\vec{B} = \vec{r}_T - \vec{r}_p$ and $\vec{C} = \vec{r}_p - \vec{r}_e$, in such way that $\vec{A} + \vec{B} + \vec{C} = 0$. Also, $\vec{r}_{\mathrm{Te}}$ is the position vector of the center-of-mass of the target system, and b is the impact parameter.

For the more accurate classical simulation results, we must also consider the rule of Heisenberg and Pauli principles. This approach was proposed by Kirschbaum and Wilets (KW) as a fermion molecular dynamic model (FMD). According to this model the effective potential, V_H motivated by the Heisenberg principles, is added to the pure Coulomb inter-particle potentials describing the classical atom. Thus

$$H_{FMD} = H_0 + V_H \tag{1}$$

where H_0 is the usual Hamiltonian containing the total kinetic energy of all bodies and Coulomb potential terms between all pairs of electrons and between the nucleus and electrons, respectively. The extra term is

$$V_H = \sum_{n=a,b} \sum_{i=1}^{N} f\left(r_{ni}\,, p_{ni}; \xi_H\,,\, \alpha_H\right), \tag{2}$$

where a and b denote the nuclei and the i, j index the electrons. Also, $r_{\alpha\beta} = r_\beta - r_\alpha$ and relative momenta are:

$$p_{\alpha\beta} = \frac{m_\alpha p_\beta - m_\beta m_\alpha}{m_\alpha + m_\beta} \tag{3}$$

The constraining potential can be written in the following form

$$f\left(r_{\lambda\nu}, p_{\lambda\nu}; \xi, \alpha\right) = \frac{\xi}{4\alpha r_{\lambda\nu}^2 \mu_{\lambda\nu}} exp\left\{\alpha\left[1 - \left(\frac{r_{\lambda\nu} p_{\lambda\nu}}{\xi}\right)^4\right]\right\} \quad (4)$$

In this work, α_H=4 and ξ_H= 0.9428 are used in Eq. 4 for the description of the Heisenberg constrain, respectively.

3. RESULTS

To study the collision between Be^{4+} and hydrogen atom we used both the standard 3-body classical trajectory Monte Carlo (CTMC) and quasiclassical trajectory Monte Carlo method of Kirschbaum and Wilets (QTMC-KW) methods. We performed a classical simulation with an ensemble of 1×10^6 primary trajectories for each energy. The calculations were carried out in the projectile energy range between 10 and 1000 keV/au, relevant to the interest of the fusion research when the target hydrogen atom is in the ground state. We estimate uncertainties in our calculation as 0.6% error. It is worth nothing that, this is the first time to present state–selective cross section data using the QTMC-KW method for Be^{4+} + H(1s) system.

The accurate knowledge of the charge exchange cross sections in fusion plasma is very important. For example, the charge exchange recombination spectroscopy (CXRS) measurements using Be^{4+} provide a high quality determination of the plasma parameters. The quality of such concentration measurements relies on the accuracy of the charge exchange cross sections. We have calculated the state-selective charge exchange cross section to the projectile bound state (see Eq. 5.) according to CTMC and QTMC-KW methods.

$$Be^{4+} + H(1s) \rightarrow Be^{3+}(nl) + H^{+} \quad (5)$$

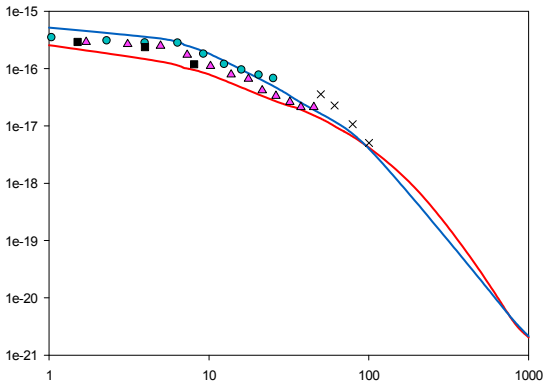

Figure 2 : State-selective charge exchange cross section into the 3s state of the projectile in Be^{4+} + H(1s) collision, as a function of the impact energy. CTMC (solid red line), QTMC-KW (solid blue line), MOCC (Harel) (●), AOCC (Fritsch) (■), OEDM (Errea) (▲), BCCIS (Das) (×).

Figure 2 shows the state-selective charge exchange cross section into the 3s state of the projectile in Be^{4+} + H(1s) collision. According to Fig 2., we found improvement in the cross section using QTMC-KW method compared to the standard CTMC model. We also found excellent agreement between our QTMC-KW results and the previous data.

Acknowledgement

The work was support by the National Research, Development and Innovation Office (NKFIH) Grant KH126886. This work has been carried out within the framework of the EURO fusion Consortium and has received funding from the Euratom research and training program 2014-2018 under grant agreement No 633053. The views and opinions expressed herein do not necessarily react to those of the European Commission.

References

Errea, L., M´endez, L., Riera, A. : 1982, *Phys. Lett. A*., **92**, 231.
Errea, L. F., Harel, C., Jouin, H., M´endez, L., Pons, B., Riera, A. : 1998*, J. Phys. B.,* **31**, 3527.
Fritsch, W., Lin, C. D. : 1984, *Phys. Rev. A*., **29**, 3039.
Hackman, J., Uhlenbusch, J. : 1984, *J. Nucl. Mater.,* **128/129**, 418.
Harel, C., Jouin, H., Pons, B., Errea, L. F., M´endez, L., Riera, A. : 1997, *Phys. Rev. A*., **55**, 287.
Harel, C., Jouin, H., Pons, B. : 1998, *At. Data. Nucl. Data Tables*., **68**, 279.
Jorge, A., Su´arez, J., Illescas, C., Errea, L. F., M´endez, L. : 2016, *Phys. Rev. A*., **94**, 032707.
Kirschbaun, C. L., Wilet, L. : 1980, *Phys. Rev. A.*, **21**, 834.
Pitts, R. et al.: 2011, *J. Nucl. Mater*., **415**, S957.

Publ. Astron. Obs. Belgrade No. 99 (2020), 109 - 112 *Contributed Paper*

CHARACTERIZATION OF PLASMA DEPOSITED CARBON-SILICON OXIDE THIN FILMS

C. CARRA[1], R. BARNI[1], D. DELLASEGA[2], A. NATALELLO[3], M. FANCIULLI[4], A. MEDVIDS[5] and C. RICCARDI[1]

[1] *Dipartimento di Fisica "Giuseppe Occhialini", Università degli Studi di Milano-Bicocca Piazza della Scienza 3 Milan I-20126, Italy*
E–mail c.carra@campus.unimib.it

[2] *Dipartimento di Energia, Politecnico di Milano, Via Ponzio 34/3, I-20133 Milan, Italy*

[3] *Dipartimento di Biotecnologie e Bioscienze, Università degli Studi di Milano-Bicocca, Piazza della Scienza 2, I-20126 Milan, Italy*

[4] *Dipartimento di Scienza dei Materiali, Università degli Studi Milano-Bicocca, Via Cozzi 53, I-20125 Milan, Italy*

[5] *Department of Semiconductor Physics, Riga Technical University, 3/7, Paula Valdena Str., LV-1048 Riga, Latvia*

Abstract. An experimental study of plasma enhanced chemical vapor deposition technique is presented. Low-pressure radiofrequency inductive plasma discharges of argon, oxygen and hexamethyldisiloxane are employed to deposit silicon oxycarbide thin films. The effect of working gas mixture, total processing pressure and deposition time on film composition has been investigated. The characterization of deposits is performed by means of Attenuated Total Reflectance-Fourier Transform Infrared Spectroscopy (ATR-FTIR), Electron Paramagnetic Resonance (EPR), Raman spectroscopy and Scanning Electron Microscopy (SEM).

1. INTRODUCTION

Silicon-based thin films and nanostructures hold great interest for applications as diverse as microelectronics, photonics, MEMS and catalysis (see Stabler et al. 2018). The development of materials gifted with satisfactory characteristics, such as controlled chemistry and morphology, can benefit a variety of applications. Plasma sources are of great interest in industrial applications and processing technology; in particular, inductively coupled plasma (ICP) discharges are one of the most efficient yet cost effective way to produce dense plasma by low power input and are also able to process both conducting and dielectric materials (see Conrads et al. 2000).
This paper wants to illustrate an instance for the deposition of carbon-containing silicon thin films employing Plasma Enhanced Chemical Vapour Deposition (PECVD)

and a comprehensive characterization of the deposited materials, for the purpose of understanding how plasma parameters influence the growth processes.

2. EXPERIMENTAL SET-UP

The PECVD reactor configuration is displayed in Figure 1. The deposition chamber is a cubic box with 40 cm per side and the vessel is connected to the main pumping line, composed by a rotary and a turbomolecular pump in series. The plasma source is placed inside a cap on the top of the chamber. It is an ICP commercial antenna by CCR Technologies Gmbh, it is composed of a 65 x 2.5 mm strip electrode cylindrically bent with a 17 cm diameter. The antenna is coupled to a RF 13.56 MHz power generator (Dressler RF Generator, Cesar 1310) through a manual matching box with two variable capacitors and equipped with a cooling water system. Approximately, the RF voltage as well as the current are uniformly distributed all along the antenna surface (see Weiler et al. 1998). A narrow injector inlets the gases for the plasma discharge directly above the antenna.

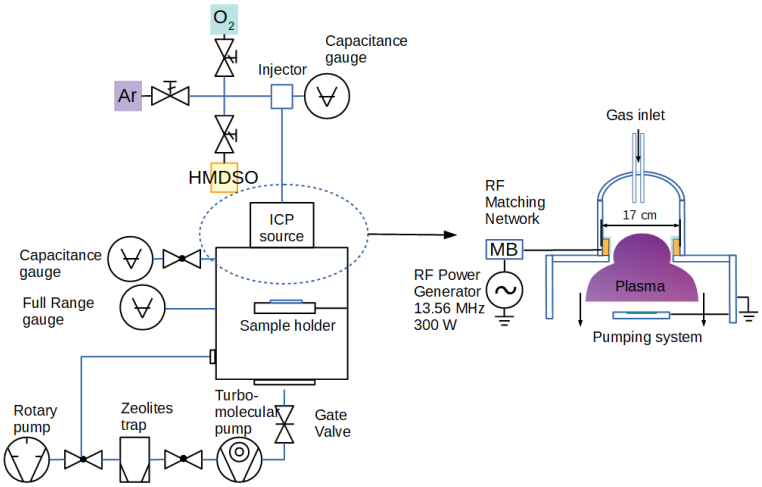

Figure 1: Schematic diagram of the deposition system and the ICP plasma source.

The vacuum vessel and the sample holder, and consequently the substrates, are grounded. In steady state operations, the RF generator supplies 300 W to the system, which it is the maximum allowed by the antenna heat dissipation system. The backward power is in the range of 10-15%, depending on the total pressure inside the chamber. A sheath is formed between the plasma and the sample holder and the sheath potential is 5-10 V lower than the plasma potential, while the electron temperature is 1-2 eV (see Barni et al. 2007).
The gas carriers of the discharge are argon and oxygen, and the precursor is hexamethyldisiloxane (HMDSO, Fulka ≥98%), a volatile organosilicon compound which, having a high vapour pressure (43 mbar at 20°C), easily evaporates and can sustain high flow rates under vacuum. The source gases are flowed through micrometer valves into the plasma chamber and partial pressures are monitored using a capacitance pressure gauge and a full range vacuum gauge. The partial pressures of the

ingoing gases determine the composition of the starting mixture for the deposition process, HMDSO has been varied from 10 to 40% of the total treatment pressure and the O_2:Ar ratio from 3:1 to 0:1. The estimated hydrodynamic conditions assure that the mixture is well-mixed in the flow direction. The depositions are performed varying the starting gas mixture, the total processing pressure ($3{\cdot}10^{-2}$-$3{\cdot}10^{-1}$ mbar) and deposition time (10-30 min). The substrate are Si(001) wafers, aluminium foils and alumina slabs, they are placed directly within the diffuse plasma region.
Post deposition thermal treatments are performed in order to allow desorption of interstitial species and induce crystallization of the amorphous layer. The films are annealed for 1h at 1050°C in controlled atmosphere, with a nitrogen flux of 8 L/min.

3. RESULT AND DISCUSSION

Operating parameters during deposition processes have been varied in order to evaluate the films composition and morphology. The substrates have been partially masked to measure the films thickness by means of a mechanical profilometer. The average deposition rate was about 20 nm/min, with the maximum being 72 nm/min at the highest pressure and precursor concentration considered.

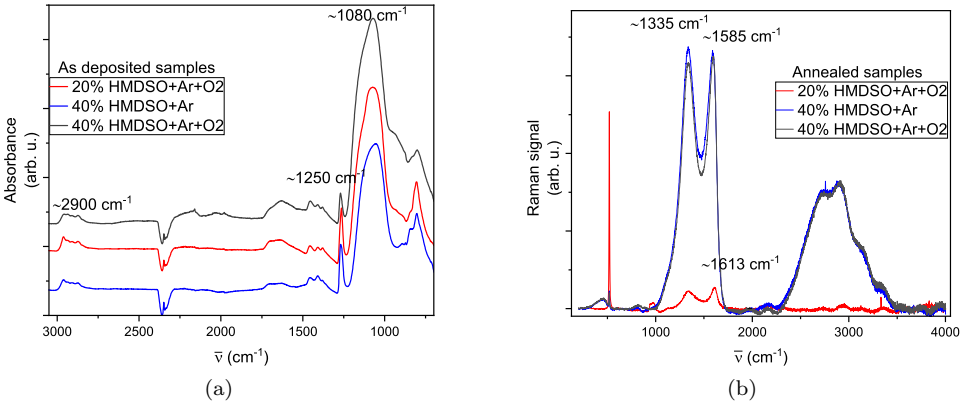

Figure 2: Normalized ATR-FTIR spectra in the 3050-700 cm^{-1} spectral region of the as-deposited films (a panel) and Raman spectra of the respective annealed samples irradiated at 514.5 nm (b panel).

ATR-FTIR spectroscopy in Figure 2(a) reveals several bonding arrangements in the as-deposited SiC_xO_y giving insight in their chemical structures (see Wavhal et al. 2006). The characteristic peaks of carbosilane and carbidic groups are present at 800 cm^{-1}. The strongest absorption band in the range 1000-1150 cm^{-1} is assigned to the asymmetric stretching vibrational modes of SiOSi and SiOC functional groups. Due to its broad structure, the deconvolution into Gaussian peaks of the absorption band and a study of the second derivative spectra are performed, the frequency shift of spectral components is attributed to changes in the SiOSi bonding angle. The $(CH_3)_3Si$-group is easily recognized by a sharp band at 1260 cm^{-1}. At higher wavenumbers, the typical stretching bands of sp^3 hydrogen coordinated carbon atoms in a linear aliphatic compound appear centred at 2900 cm^{-1}.

Electron Paramagnetic Resonance spectroscopy has been carried out in an X band ($\sim$ 9.4 GHz) spectrometer equipped with a high Q-factor cylindrical cavity (Bruker ER4122SHQ). The signal is unaffected upon sample rotation, it follows that the g-factor is isotropic. The experimental data are consistent with a g = 2.0055$\pm$0.0002, it is assigned to bulk silicon dangling bonds in $^{\bullet}$Si$\equiv$ Si configuration, called D center (see Pantelides 1986). The presence of amorphous silicon suggests the oxides deposits to have Si-rich domains. Annealing treatments are demonstrated to induce the phase separation between Si and the amorphous films (see Yi et al. 2002) leading to the segregation into silicon nanocrystals, whose size depends on the overabundance of Si atoms in the deposit. Post-annealing EPR measurements have confirmed the saturation of Si DBs, but still the optimal annealing conditions need to be met since further investigations do not confirm the presence of nanocrystals.
Micro-Raman spectroscopy has been employed to study the structural properties of SiC_xO_y annealed samples. In Figure 2(b) the spectra reveal a typical diamond-like-carbon structure confirming that graphite crystallites are formed (see Bokobza et al. 2014). The spectra display the characteristic G peak at 1582 cm^{-1}, corresponding to the LO phonon at Γ, and the defect-activated D and D' peaks at $\sim$1350 and $\sim$1620 cm^{-1}. The second-order of D peak, at higher wavenumber, suggests a great degree of disorder in the carbon structures. Data indicate that oxygen in the plasma mixture brings no significant differences in samples composition. The low wavenumber region of Raman spectra identifies silica or quartz components in the film, showing a broad and asymmetric band at 450 cm^{-1} assigned to SiOSi bending vibrations and its overtone at about 800 cm^{-1} (see Smit et al. 2003). The band deconvolution is not final in discerning the exact structure. It is possible to appreciate that in the 20% HMDSO+Ar+O_2 sample these bands are not present.
SEM images show that films are composed of quasi-spherical nanoparticles with the size in the range of 20 nm, determining a nodular surface which is a typical result of ballistic aggregation. At high total treatment pressure, mushroom-shaped extrinsic nodular defects begin to grow at the substrate interface.

4. CONCLUSION

The effect of working conditions on films composition has been investigated by means of different and complementary diagnostic techniques. Future approaches will be to develop electrical and optical plasma diagnostics to better understand the role of plasma parameters in deposition processes and devise an ad hoc post-deposition annealing to control crystallization. Additionally, new precursors will be tested.

References

Barni, R., Zanini, S., & Riccardi, C. : 2007, *Vacuum*, **82**(2), 217-219.
Bokobza, L., Bruneel, J.-L., Couzi, M. : 2014, *Vibrational Spectroscopy*, **74**, 57–63.
Conrads, H., Schmidt, M. : 2000, *Plasma Sources Science and Technology*, **9**(4), 441.
Pantelides, S. T. : 1986, *Physical review letters*, **57**(23), 2979.
Smit, C., et al. : 2003, *Journal of applied physics*, **94**(5), 3582-3588.
Stabler, C. et al. : 2018, *Journal of the American Ceramic Society*, **101**(11), 4817-4856.
Wavhal, D. S., et al. : 2006, *Plasma Processes and Polymers*, **3**(3), 276-287.
Weiler, M., et al. : 1998, *Applied Physics Letters*, **72**(11), 1314–1316.
Yi, L. X., et al. : 2002, *Applied Physics Letters*, **81**(22), 4248-4250.

Publ. Astron. Obs. Belgrade No. 99(2020), 113 - 116 *Contributed Paper*

NUMERICAL INVESTIGATION OF THE PLASMA FORMATION IN SKIN TISSUE BY NANOSECOND Nd: YAG LASER PULSE

HRISTINA DELIBAŠIĆ [1], VIOLETA PETROVIĆ [1], IVAN PETROVIĆ [2], CARLOS MOLPECERES [3] and SARA LAUZURICA [3]

[1] *Faculty of Science, University of Kragujevac, Radoja Domanovića 12, 34000 Kragujevac, Serbia*

[2] *Technical Collage of Applied Studies, University of Kragujevac, Kragujevac, Serbia*

[3] *Centro Láser, Universidad Politécnica de Madrid, C/ Alan Turing, 1. 28031, Madrid, Spain*

Abstract. A numerical analysis is performed to investigate the comparative contribution of the mechanisms responsible for electron gain and losses in laser-induced breakdown of the skin and underlying tissues. In this regard we adopted a simple theoretical formulation relying on the numerical solution of a rate equation that describes the growth of the electron density due to the joined effect of multiphoton, cascade and chromophore ionization processes. Here, the rate also includes the effect of electron loss due to diffusion and recombination processes. The analysis considered skin tissue irradiated by a Nd:YAG laser radiation in the 200 – 550 nm wavelength range with 6 ns pulse duration full-width half-maximum (FWHM).

1. INTRODUCTION

Since its first discovery in the 1980s (Anderson et al. 1981, Nakagawa et al. 1985), laser-induced skin tissue breakdown has been extensively studied due to its potential and promising applications in different fields, such as molecular and cellular biophysics and bioengineering. As the pulsed laser technologies continued to advance, the fundamental knowledge of laser-skin interaction mechanisms has become of vital importance in the development of modern medicine. Parallel to the investigations related to medical progress in the field, laser-induced breakdown (LIB) phenomena has been extensively studied by several researchers to determine theoretically, as well as experimentally, breakdown thresholds and free electrons density distribution of the formed plasma. Although the breakdown of skin tissues induced by nanosecond laser pulses has attracted active attention, complete and

detailed modeling of the mechanism involved in this phenomenon is still an open question.

In the present work, a modified model previously developed by Hoseinimotlag et al. 2014 based on the solution of the free electron density rate equation is proposed to numerically investigate laser-driven plasma formation in skin tissue induced by a Gaussian pulse with a full width at half the maximum (FWHM) of 6 ns at wavelengths in the range 200 nm to 550 nm. The model takes into account the generation of free electrons due to the combined effect of multiphoton, cascade and chromophore ionization processes. These processes are opposed by the loss of electrons within the interaction region through diffusion out of the focal volume and recombination. Thus, in this work, the computations focus on studying the separate contribution of each of the gain and loss processes.

2. THEORETICAL MODEL

The skin tissue is a composite structure containing the inclusions of different type and dimension (blood vessels, nerve endings, sweat glands, and hair follicles), which essentially makes it difficult in the understanding of the processes that occur under the interaction of laser with skin. According to Rogov et al. 2014 the main constituent of the skin is water (~70 %) and that is why, in a first approximation, the human skin can be considered as water-like tissue media.

Laser-induced breakdown in water-like tissue media has attracted wide attention for its significance in the fundamental research on laser-matter interaction and as a baseline model for studying ablation of skin tissues (Fanjul-Vélez et al. 2014). The prime mechanism of the optical ablation we are dealing with in the present study is plasma induced ablation, and hence the description of the process requires the consideration of multiphoton ionization and ionization by light absorption. All these effects can be included in the rate equation that describes the free electron density as a function of time (Hoseinimotlag et al. 2014):

$$\frac{d\rho}{dt} = \left.\frac{d\rho}{dt}\right|_{mpi} + \left.\frac{d\rho}{dt}\right|_{ch} + W_{casc}\,\rho - W_{diff}\,\rho - W_{rec}\,\rho^2, \tag{1}$$

where the first three terms describe the evolution of the electron density generated by the combined effect of multiphoton, chromophore (the contribution through light absorption by chromophores in the skin tissue), and cascade ionization, respectively. The multiphoton rate, $(d\rho/dt)|_{mpi}$, is obtained by Eq. (29) of (Kennedy 1995), while for the cascade rate, W_{casc}, we used Eq. (16) of (Kennedy 1995). The second $(d\rho/dt)|_{ch}$, i.e. the free-electron density due to chromophore ionization is estimated as in (Fang and Hu 2004). As indicated by the minus sign, the loss of high-energy electrons due to diffusion and recombination proceeds at the rates, W_{diff} and W_{rec}. The values of loss rates can be found in (Kennedy 1995).

Assuming a Gaussian profile for the temporal distribution of the laser pulse, a Runge–Kutta method with adaptive step size is used to numerically solve Eq. 1 for the time-varying electron density. As suggested by (Fang and Hu, 2004) in our

analysis we assumed that pre-existing free electron density is negligible at the start of the laser pulse, $\rho(0) = 0$.

3. RESULTS AND DISSCUSION

To get a deeper insight into the exact contribution of the physical processes to the electron density growth rate, the free electron density equation (Eq. 1) is numerically solved for two laser wavelengths, particularly 355 nm and 532 nm with a focal spot diameter of 10.6 µm and laser pulse intensity of 0.5×10^{10} W/cm^2. Accordingly, Figs. 1(a) and 1(b) represent the time evolution of electron density, when the laser pulses are centered at $t = 20$ ns. It should be noted that when electron density is greater than a critical value (Vogel et. al 2005): ρ_{cr} [cm^{-3}] $\cong 1.1 \times 10^{21}/\lambda^2[\mu m]$, the plasma become highly reflective, and the incoming laser light leads to growth of the plasma volume rather than the free electron number. Therefore, in our analysis, the critical free-electron density is calculated to be $I \sim 8.7 \times 10^{21}$ cm^{-3} at 355 nm (Fig. 1(a)) and $\sim 3.8 \times 10^{21}$ cm^{-3} at 532 nm (Fig. 1(b)).

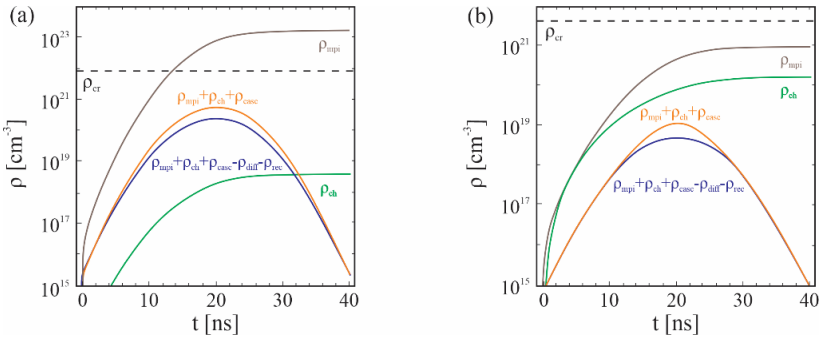

Figure 1: Evolution of the free-electron density for different gain and loss processes at wavelength: (a) 355 nm and (b) 532 nm. The dashed curve is the critical electron density ρ_{cr}.

For skin tissue ablation by nanosecond pulses, the characteristics of the LIB model need to be further elucidated. Acceptance of this model is far from ubiquitous, especially when tissue absorption becomes significant as the light wavelength approaches the ultraviolet region. Given this fact, the effect of the laser wavelength on the free electron density, numerically evaluated via Eq. 1, have been studied. The results are shown in Fig. 2. Calculations were performed for $I \sim 0.35 \times 10^{10}$ W/cm^2 in the wavelength range $200 - 550$ nm. The remaining parameters are the same as those of Fig. 1.

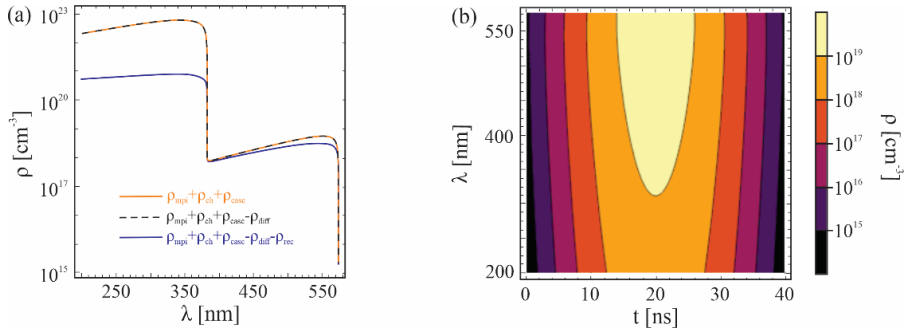

Figure 2: (a) wavelength dependence of electron density for electron creation and loss processes participating in the electron density equation, (b) contour representation of free electron density as a function of time and laser wavelength.

4. CONCLUSION

In summary, we analyzed the time evolution of the free electron density in the absence and presence of each gain and loss process included in the rate equation describing the time evolution of the free electron density in LIB. Beside standard multiphoton and cascade ionization rates, in this paper we incorporated chromophore ionization pathway to explain the skin tissue ablation by nanosecond laser pulses. The presented results verified that in the nanosecond regime, the losses of the free electrons via recombination and diffusion can be neglected (especially when the wavelength exceeds 532 nm) because of the relatively long lifetime and diffusion time of those electrons. Such statement is also confirmed by other researchers (Vogel et. al 2005). We also observed the wavelength dependence of the free electron density and analyzed contribution of each gain and loss mechanisms on this dependence. Our results indicated that shorter wavelengths lead to enhanced electron densities and, hence, the optical breakdown becomes possible at lower laser intensities.

Acknowledgements. This work was supported by the RS MESTD, Project No. OI 171020, COST Action CA17126 "Towards understanding and modelling intense electronic excitation" and Madrid Regional Government project BIOPIELTEC-CM (S2018/BAA-4480) .

References

Anderson R. R., Parrish J. A. : 1981, *J. Invest. Dermatol,*. **77**, 13–19.
Fang Q. and Hu X. H. : 2004, *IEEE J. Quantum Electron*, **40**(1), 71.
Fanjul-Vélez F., Salas-García I. and Arce-Diego J. L. : 2014. *Laser Phys.*, **25**(2), 025606.
Hoseinimotlag S. N., Sharifi M. S. and Shoja K. : 2014, *IJFPS*, **4**(1), 28.
Kennedy P. K. : 1995, *IEEE J. Quantum Electron*, **31**(12), 2243-2244.
Nakagawa H., Tan O. T. and Parrish, J. A. : 1985, *J. Invest. Dermatol*, **84**(5), 396-400.
Rogov P. U., Smirnov S. V., Semenova V. A., Melnik M. V. and Bespalov V. G. : 2016, *J. Phys. Conf. Ser.*, **737** (1), 012047.
Vogel A., Noack J., Huttman G. and Paltauf G.: 2005, *Appl. Phys. B*, **8**1, 1020.

Publ. Astron. Obs. Belgrade No. 99 (2020), 117 - 120 *Contributed Paper*

PRINCIPAL COMPONENTS ANALYSIS OF PRINTED CIRCUIT BOARD LIBS DATA

D. SEVIC[1], M. S. RABASOVIC[1], P. GREGORČIČ[2], M. D. RABASOVIC[1] and B. P. MARINKOVIC[1]

[1] *Institute of Physics, University of Belgrade, Pregrevica 118, 11080 Zemun, Serbia*
E–mail sevic@ipb.ac.rs

[2] *Faculty of Mechanical Engineering, University of Ljubljana, Aškerčeva 6, 1000 Ljubljana, Slovenia*

Abstract. One of the ways to achieve rapid prototyping of printed circuit boards is by using the laser ablation. The laser-induced breakdown spectroscopy (LIBS) is a convenient method for monitoring the selective removal of thin layers by laser. In this paper the obtained LIBS data are analyzed by using principal component analysis (PCA).

1. INTRODUCTION

Laser ablation has many applications. Main aim of our research presented in Rabasovic et al. 2016. was rapid prototyping of printed circuit board. We have used the laser-induced breakdown spectroscopy (LIBS) as a convenient method both for ablation and for monitoring the selective removal of thin layers by laser. In Rabasovic et al. 2016 the LIBS data were analyzed by using correlation coefficients. Nowadays, availability of more and more fast computers, capable of machine learning, moves the analysis algorithms from simple numerical calculation towards the more sophisticated artificial intelligence methods. Interesting applications of machine learning algorithms for analysis of LIBS data are presented in Boucher et al. 2015, Moros et al. 2013, Serranoa et al. 2014. In this paper we study the spectral data obtained in Rabasovic et al. 2016. by using the Principal Component Analysis (PCA).

2. PRINCIPAL COMPONENT ANALYSIS

One of the basic machine learning techniques is based on using the principal component analysis. The method is proposed long ago, see Hoteling 1933, Karhunen 1947, Loeve 1948. However, because of their low computing efficiency, the PCA and other, more sophisticated, machine learning algorithms become extensively used only recently.

The data set of certain structure is used to "train" the machine to learn some specific characteristics of input data. Then, machine could be used to recognize and identify these characteristics in newly presented data of similar structure and nature.

If X is a data matrix with m rows and n columns, each variable being a column and each sample a row, PCA decomposes X as the sum of r t_i and p_i, where r is the rank of the matrix X:

$$X = t_1 p_1^T + t_2 p_2^T + ... + t_k p_k^T + ... + t_r p_r^T \qquad r \leq \ min\{m, n\} \tag{1}$$

In the PCA decomposition, the p_i vectors are eigenvectors of the covariance matrix; it holds:

$$cov(X) = \lambda_i p_i \tag{2}$$

where λ_i is the eigenvalue associated with the eigenvector p_i.

The t_i, p_i pairs are ordered by the amount of variance captured. The t_i vectors are known as scores and contain information on how the samples relate to each other. The p_i vectors are known as loadings and contain information on how the variables relate to each other. Generally, the PCA model is truncated after k components.

3. EXPERIMENTAL SET-UP AND METHODS

Our experimental setup is and its applications for elemental analysis using LIBS, including several ways of processing spectra, are described in detail in Rabasovic et al. 2012, Rabasovic et al. 2014, Rabasovic et al. 2019, Sevic et al. 2011. The data analyzed here were obtained by experimental setup described in Rabasovic et al. 2016; at that time we have calculated the correlation coefficients of measured spectra to identify the moment of achieving the full removal of copper layer by laser ablation. Here, we implement the PCA to achieve automatic recognition of the instant when laser ablation of copper layer has been finished and the laser starts damaging the composite substrate of printed circuit board. We use Solo software package (Version 8.8, Eigenvector Research Inc, USA) for computing the PCA.

4. RESULTS AND DISCUSSION

Streak images of plasma breakdown optical spectra of printed circuit board at the start, when only copper is ablated; and when the substrate is fully exposed, are shown in Fig. 1. Their differences could be seen by a naked eye.

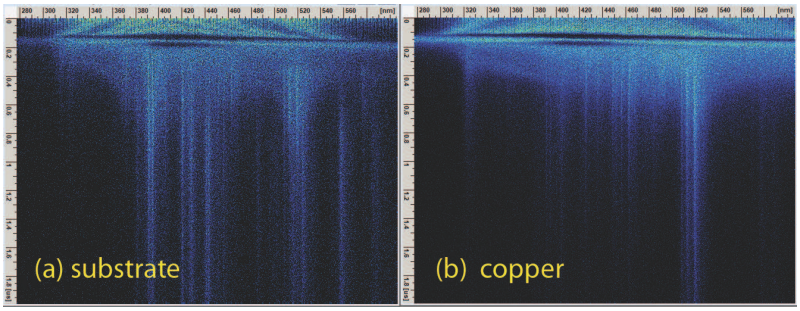

Figure 1: Streak images of plasma breakdown optical spectra of (a) copper conductor and (b) a printed circuit board substrate.

The first two principal components of LIBS data are shown in Figure 2. The plots justify our decision in Rabasovic et al. 2016. to calculate correlation coefficients of spectra in the range between 370 nm and 500 nm. In that range, the principal components look the least noisy.

Scores plot of first two principal components is shown in Fig 3. As expected, the scores corresponding to spectra at start of ablation and at the end of ablation are spaced widely apart, enabling automatic recognition of the moment when the useful ablation ends. The spectra corresponding to partial ablation are somewhere in between on PC1 axis, and widely apart on PC2 axis.

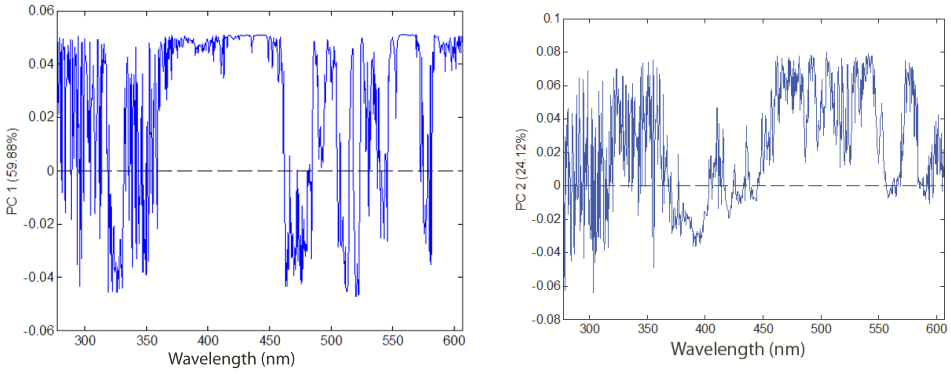

Figure 2: The first two principal components of LIBS data.

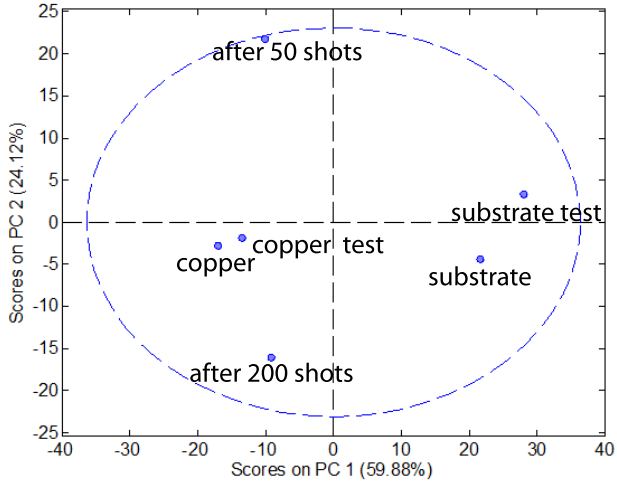

Figure 3: Scores plot of first two principal components.

5. CONCLUSION

The laser ablation is one of the ways to achieve rapid prototyping of printed circuit boards. We have analyzed the LIBS data of printed circuit board by using machine learning algorithm. In our previous analyses we have used the correlation coefficients to identify the moment when laser ablation reaches the composite substrate of printed circuit board. Now, we have proved that it is possible to automatically detect the instant when the copper layer is fully ablated by PCA.

Acknowledgment

This work was financially supported by the Institute of Physics Belgrade, through the grant by the Ministry of Education, Science, and Technological Development of the Republic of Sebia

References

Boucher T.F., Ozanne M.V., Carmosino M.L., Dyar M.D., Mahadevan S., Breves E.A., Lepore K.H., Cleggc S.C. : 2015 *Spectrochimica Acta Part B* **107** 1.

Hoteling, H. : 1933 *Journal of Educational Psychology* **24** 417.

Karhunen, K. : 1947 "ber lineare Methoden in der Wahrscheinlich-keitsrechnung". *Ann. Acad. Sci. Fennicae. Ser. A. I. Math.-Phys.* **37** 1.

Loeve, M. : 1948 *Processus stochastiques et mouvements Browniens, Paris: Gauthier-Villars.*

Moros J., Serrano J., Gallego F.J., Macas J., Laserna J.J : 2013 *Talanta* **110** 108.

Serranoa J., Moros J., Snchez C., Macas J., Laserna J.J : 2014 *Analytica Chimica Acta* **806** 107.

Rabasovic M.S., Sevic D., Pejcev V., Marinkovi B.P. : 2012 *Nucl. Instrum. Meth. B* **279**, 61.

Rabasovic M.S., Marinkovi B.P., Sevic D. : 2014 *IEEE Transactions on Plasma Science* **42**, 2388.

Rabasovic M.S., Sevic D., Lukac N., Jezersek M., Mozina J., Gregorcic P. : 2016 *Appl. Phys. A* **122**, 186.

Rabasovic M.S., Rabasovic M.D., Marinkovic B.P., Sevic D. : 2019 *Atoms* **7**, 6.

Sevic D., Rabasovic M.S., Marinkovic B.P. : 2011 *IEEE Trans. on plasma science* **39**, 2782.

Publ. Astron. Obs. Belgrade No. 99 (2020), 121 - 124 *Contributed Paper*

APPEARANCE OF Be II 436.1 nm LINE WITH FORBIDDEN COMPONENT IN LIBS PLASMA

B. D. STANKOV[1], M. R. GAVRILOVIĆ BOŽOVIĆ[2] and M. IVKOVIĆ[1]

[1] *Institute of Physics, University of Belgrade, 11080 Belgrade, P.O. Box 68, Serbia*
E-mail biljanas@ipb.ac.rs

[2]*Faculty of Engineering, 34000 Kragujevac*
E-mail marijana.gavrilovic@kg.ac.rs

Abstract. In this work study of LIBS on BeO target in low pressure gas mixture of Ar (97 %) and H_2 (3%) using a nanosecond pulsed laser with 266 nm wavelength is presented. The appearance of forbidden component of Be II 436.1 nm was observed and presented in comparison with the previously acquired results for pulsed gas discharge plasma.

1. INTRODUCTION

The results of the experimental study of the singly charged beryllium spectral line 436.1 nm, transition $3p^2\ P^o$- $4d^2\ D$, and its forbidden component, transition $3p^2\ P$-$4f^2\ F^o$, were previously reported, e.g.: see Stankov et al. 2018.a In this paper beryllium lines were recorded from gas discharge running in pulsed regime, after ablation of beryllium oxide (BeO) discharge tube. The plasma source was described in detail, e.g.: see Stankov et al. 2018.b.

The reason for the necessity of devising another experiment, to examine Be II with forbidden line, is twofold: a) there were dust particles in the pulsed discharge plasma observed, e.g.: see Stankov et al. 2018.b.; b) published experimental results can not be used for testing of the overall line shape modeling because the influence of the allowed line optical thickness and additional electric field has not been accounted for, e.g.: see Stankov et al. 2018.a.

LIBS stands for Laser Induced Breakdown Spectroscopy technique that uses a short laser pulse to create plasma on the sample surface. Analysis of this plasma enables determination of material's elemental composition, without sample preparation and with simple experimental setup. Difficulties that arise during analysis are mainly associated with the fast evolving plasma which demands well temporally and spatially resolved measurements.

This paper explores the possibility of recording Be II line with forbidden component in LIBS plasma. As a comparative study, LIBS method was chosen because it is assumed there will be no dust particles production. Besides, experimental setup used for LIBS plasma creation gives the possibility for spatially resolved measurements and experimental testing of self-absorption, which could not be performed in gas discharge experiment. Aim of this study is to check the possibility of spatially and temporally resolved measurements of Be line with forbidden component in dust free environment.

2. EXPERIMENT

Experimental apparatus for pulsed gas discharge plasma recordings, e.g.: see Stankov et al. 2018.b, was set up as for the standard end-on linear discharge plasma observation. Axial image of the plasma source was projected onto the entrance slit of a spectrometer (Andor Technology, Shamrock 303), by the use of a focusing mirror and achromatic lens. For line shape recordings the imaging spectrometer was equipped with iCCD camera (Andor Technology, model DH734). Line shape recordings were performed with full vertical binning and gate width of 50 ns at various delay times.

For the LIBS method, the fourth harmonic of Nd:YAG Q-switched laser (Quantel, Q-smart 450) at 266 nm, with repetition rate of 10 Hz, was used. The pulse energy at 266 nm was 70 mJ, on the average. The laser beam was focused perpendicular to the BeO target by the means of biconvex achromatic lens L1 (f1 = 100 mm), see Figure 1.

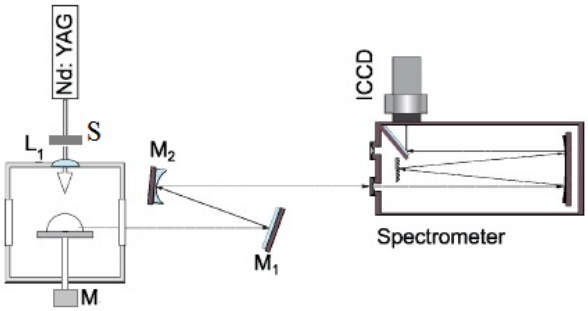

Figure 1: LIBS setup

Target made from BeO ceramics was glued to the carrier, which was rotated by the motor (M), in the low pressure chamber. 1 : 1 image of the plasma plume was projected by optical mirrors M1 and M2 on the entrance slit (20 μm wide) of a 0.5 m Ebert-type spectrometer (f/8.6 equipped with a grating of 1180 grooves per mm). The spectrometer was mounted with an iCCD camera (Andor Technology, model DH734I-18U-03, with 1024 x 1024 pixels, 13 x 13 μm size, 18 mm intensifier diameter). The iCCD camera was operated in the image mode and controlled using a pulse generator (DDG 535, Stanford Research Systems) triggered optically by the occurrence of plasma on the BeO target. Fast photodiode placed towards the target was used to convert the light signal. The shatter (S), placed between the laser and the lens L1, was changing open/close position for every 16 laser shots. Images of the plasma were accumulated over 16 laser shots and the final signal was the product of 10 such accumulations. Accumulation of the signal was performed to exclude the influence of the eventual shot-to-shot changes in the signal. The acquisition gate width was 100 ns.

3. RESULTS AND DISCUSION

Diagnostics of plasma parameters, the electron number density, *Ne,* and electron temperature, *Te,* was used for characterization of two experimental methods.

For optimal conditions in the pulsed discharge plasma electron number density, *Ne,* was determined from the peak separation $\Delta\lambda ps$ of the H_β line using formula (6) from e.g.: see Ivković et al. 2015. *Te* was estimated from the ratio of Be II 467.3 nm/Be I 457.3 line intensities, using formula (1):

$$\frac{I_1}{I_2} = \frac{h^3}{2(2\pi mk)^{3/2}} \frac{(gA)_1 \lambda_1 N_e}{(gA)_2 \lambda_2 T_e^{3/2}} exp\left(\frac{E_2 - E_1 + E_1^{ion} - \Delta E}{kT_e}\right), \quad (1)$$

where $E_1{}^{ion}$ is ionization potential and ΔE is ionization potential lowering.

After several iterations *Ne* and *Te* were determined, and presented in Table 1, e.g.: see Stankov et al. 2018.a. Maximum values of *Ne* and *Te* are measured to be $9.3 \cdot 10^{22}$ m^{-3} and 16800 K.

For LIBS method, the chamber was filled with 10 mbar of Ar (97%) and H_2 (3%) mixture. The previously mentioned experimental conditions were chosen in order to achieve maximum Be and H line intensity.

Experimental profile of the Hα line fitted with Voigt function was used for determination of *Ne* in LIBS plasma. Stark halfwidth, w_S, is determined by assuming $w_S = w_L$ and introducing this result in Eq. (12), e.g.: see Konjević et al. 2012. Instrumental line profile was measured at several wavelengths using Oriel penlight calibration lamp. *Te* was estimated from the ratio of Be II 467.3 nm/Be I 457.3 line intensities, equation (1). The electron density and plasma temperature are displayed in Figure 2a as functions of time. Temporal evolution of Be II nm with forbidden component is presented in Figure 2b. Forbidden component, transition $3p^2$ P- $4f^2$ F^o, is easily seen on the blue wing of Be II, transition, $3p^2$ P^o-$4d^2$ D.

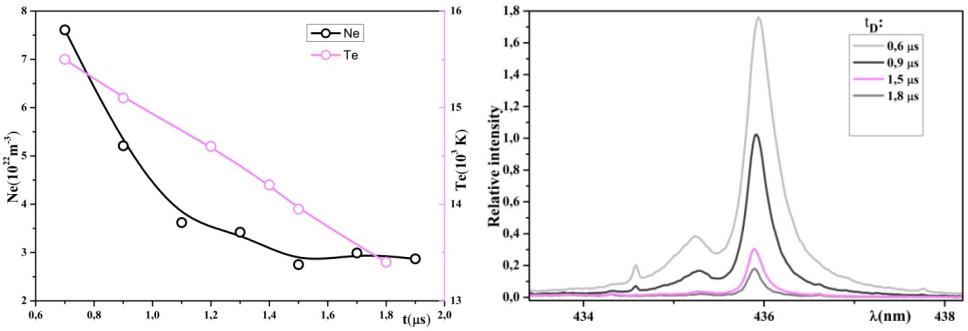

Figure 2: a-Temporal evolution of Ne and Te for LIBS on BeO target, b-Temporal evolution of Be II with forbidden component for LIBS on BeO target

The dependence of wavelength peaks separation *s* and peaks intensity ratio *F/A* upon *Ne* for Be II allowed and forbidden component is shown in Figure 3.

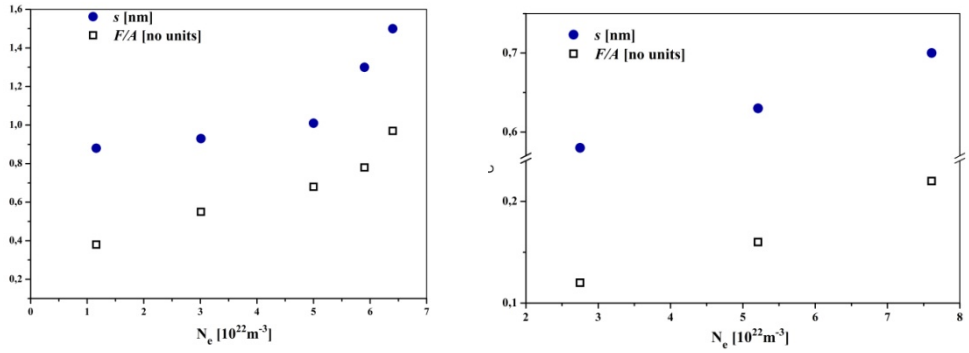

Figure 3: wavelength peaks separation *s* and peaks intensity ratio *F/A* dependence upon *Ne* for Be II Line with forbidden component for: a) pulsed discharge plasma b) LIBS plasma

Slight discrepancy between s[nm] values for two experimental setups exists. More notable discrepancy is observed for F/A values. Reason for this may be presence of self-absorption and spatial inhomogenity in both experimental setups. The example of spatially resolved Be II 436.1 nm line is presented in Figure 4.

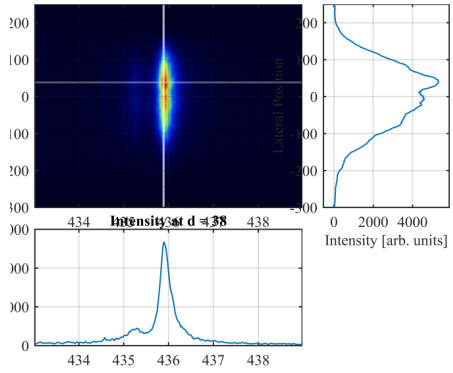

Figure 4: Spatially resolved Be II 436.1 nm line in LIBS plasma

In the next step of investigation, *Ne* and *Te* will be determined using spatially resolved measurements of Be and H lines. Since there were no dust particle observed, as assumed, results obtained from LIBS experiment may be used to evaluate the effect of dust particles on Be line parameters obtained from gas discharge.

References

Ivković, M., Konjević, N., Pavlović, Z.: 2015, *J. Quant. Spectrosc. Radiat. Transfer*, **154** (2015) 1.

Konjević, N., Ivković, M., Sakan, N.: 2012, *Spectrohemica Acta Part B*, **76**, 16.

Stankov, B. D., Ivković, M., Vinić, M., Konjević N.: 2018a, *EPL*, **123**, 63001.

Stankov, B. D., Vinić, M., Gavrilović Božović, M. R., Ivković, M.: 2018b, *Rev. Sci. Instrum.*, **89**, 053108.

Publ. Astron. Obs. Belgrade No. 99 (2020), 125 - 128 *Contributed Paper*

TREATMENT OF STEEL SURFACES BY PLASMA FLOW GENERATED IN MAGNETOPLASMA COMPRESSOR

NORA TRKLJA BOCA[1], ŽARKO MIŠKOVIĆ[2], BRATISLAV OBRADOVIĆ[1], RADIVOJE MITROVIĆ[2] and MILORAD KURAICA[1]

[1] *Faculty of Physics, University of Belgrade, Studentski trg 12, Belgrade, Serbia*
E-mail nora@ff.bg.ac.rs

[2] *University of Belgrade, Faculty of Mechanical Engineering, Kraljice Marije 16, Belgrade, Serbia*

Abstract. Steel (type 100Cr6) samples have been treated with plasma pulses, using helium with 5% of hydrogen as a working gas. Plasma is formed within electrode system of magnetoplasma compressor, a type of magnetoplasma accelerator which accelerates and compresses plasma. Every plasma shot deposits 9 J/cm^2 of energy to the surface of the treated material. The surface modification was monitored by optical microscopy, hardness measurement, roughness measurement, and X-ray diagnostics. The experimental setup enables spectra recording at the position where plasma-material interaction is realized. Improvements in physical properties of samples were achieved after plasma treatments.

1. INTRODUCTION

Magnetoplasma compressor (MPC) is a type of magnetoplasma accelerator, it has semi-transparent electrode system, it operates in an ion current transfer regime and produce quasi-stationary compression plasma flows (CPF) [Puric et al. 2003.]. The lifetime of the compressed plasma flow is around 150 μs, plasma velocity is up to 100 km/s, electron density and temperature are close to 10^{23} m^{-3} and 2 eV, respectively.

The topic of the present paper is investigation of interaction between plasma formed within MPC and steel 100Cr6 samples. Steel 100Cr6 is mainly used for small and medium sized bearing components. It is also regularly used for other machine components that require high tensile strength and high hardness.

2. EXPERIMENTAL SETUP

In the MPC, plasma is formed within the electrode system during the process of capacitor discharge. The presented research project has been realized in the residual gas regime, using helium with 5% of hydrogen. The position of the steel samples is fixed at z = 4.5 cm, where every plasma shot deposits 9 J/cm^2 of energy to the surface of the treated samples (Trklja et al. 2019.). Scheme of the experimental setup is shown in Fig.1

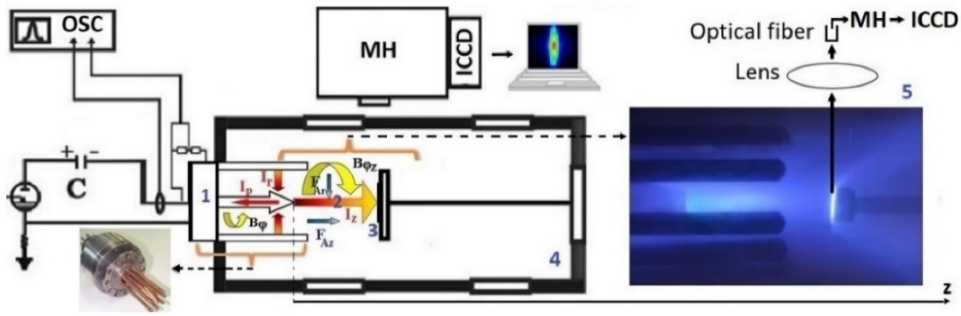

Figure 1: Experimental setup: 1. Magnetoplasma compressor, 2. Compressed plasma flow, 3. Sample, 4. Vacuum chamber, 5. Surface (steel 100Cr6) treatment by CPF.

Steel samples (1 cm x 1 cm) were mechanically cut, polished and prepared for treatment in MPC device. The general picture of the surface changes is obtained using optical microscope. Hardness and roughness of steel surfaces have been measured before and after plasma treatments using Zwick Mic 10 Hand Hardness Instrument and MarSurf XR 1 Surface Roughness Tester, respectively.

The X-ray diffraction (XRPD) investigation was conducted on automated multipurpose Rigaku Smartlab X-ray Diffractometer in Θ – Θ geometry.

Spectral investigation of the plasma-surface interaction area is realized using one meter spectrometer and PIMAX1 ICCD camera.

3. EXPERIMENTAL RESULTS AND DISCUSSION

Values of electron density and temperature in the plasma layer next to the sample surface are $2.4 \cdot 10^{22}$ m^{-3} and 0.5 eV, respectively. Electron density is calculated using distance between allowed and forbidden component of helium 447.1 nm line (Czernichowski et al., 1985.). The electron temperature is calculated using relative intensity ratio of Fe I and Fe II spectral lines.

Optical microscope images of the treated samples indicate the formation of vortex structures. Fig. 2. represents the surface of one steel sample treated with five plasma shots (which is not positioned on the center of the CPF, but it is useful for the present description) obtained by an optical microscope. There are three areas on

this surface: the right part is the untreated region where the plasma hasn`t interact with the surface; the left part of this sample is the region where CPF hits the sample directly; the middle area represents the peripheral zone of plasma – sample interaction in which material from the central area of plasma - surface interaction is blown and smooth area is formed.

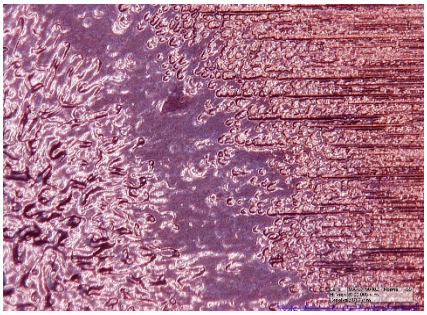

Figure 2: Untreated and treated steel 100Cr6 samples (optical microscope)

From the results of the roughness measurement it can be seen that after treatment with three and more plasma shots, the peripheral region of the treated surface becomes noticeably flat. The central area of the treated surface become significantly rough after several treatments because during each plasma-target interaction, the surface material is again melted and mixed.

Plasma shots make steel target firmer after just one plasma treatment. Three plasma shots lead to a hardness value of 350 HV and after more than three plasma shots, it comes to saturation.

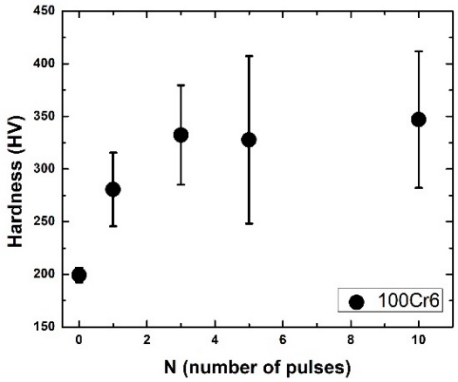

Figure 3: Hardness of the steel 100Cr6 samples depending on the number of plasma treatments

Result of x-ray analysis of the sample treated with ten plasma shots is represented in Fig.4. Starting sample (steel 100Cr6) is solely composed from α-Fe.

Treatments with plasma shots leads to partially transformation to γ-Fe of thin surface layer of sample.

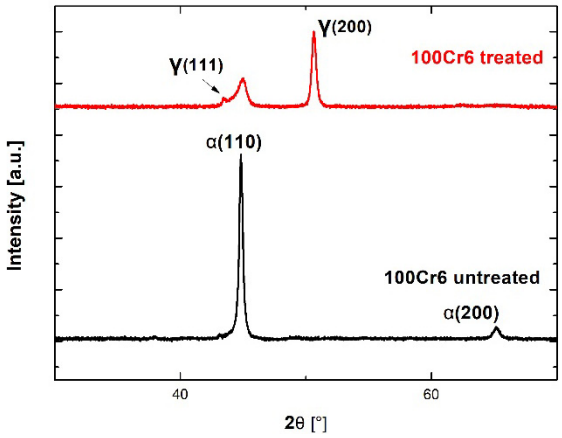

Figure 4: Hardness of the steel 100Cr6 samples depending on the number of plasma treatments

4. CONCLUSIONS

Modifications of steel 100Cr6 samples treated by a plasma produced within MPC have been monitored depending on the number of plasma treatments. Significant improvement of hardness has been achieved. Presented type of experimental investigation is useful for industry application and it is of interest for fusion related experiments concentrated on material treatment within plasma accelerators and analysis of the surface modification under high thermal loads.

References

Czernichowski, A., Chapelle, J.: 1985, *JQSRT*, **33**, 427.

Purić, J., Dojcinovic, I. P, Astashynski, V. M., Kuraica, M. M., Obradovic, B. M.: 2003, *Plasma Sources Sci. Technol.*, **13**, 74.

Trklja, N., Iskrenovic, P. S., Miskovic, Ž. Z., Krstić, I. B., Obradovic, B. M., Mitrović, R. M., Kuraica, M. M.: 2019, *JINST*, **14**, C09041.

Publ. Astron. Obs. Belgrade No. 99 (2020), 129 - 132 *Contributed Paper*

TUNGSTEN AND ODS STEEL BEHAVIOR AT HIGH INTENSITY, 10^{15} W/cm^2, LASER IRRADIATION IN AIR AND VACUUM AMBIENCE: COMPARATIVE STUDY

M. TRTICA[1], J. STASIC[1], J. LIMPOUCH[2] and P. GAVRILOV[2]

[1]*VINCA Institute of Nuclear Sciences - National Institute of the Republic of Serbia, University of Belgrade, Belgrade, Serbia. E-mail: etrtica@vinca.rs*

[2]*Faculty of Nuclear Sciences and Physical Engineering, Czech Technical University in Prague, CZ-115 19 Prague, Czech Republic*

Abstract. The effects of high intensity, 10^{15} W/cm^2, laser radiation on tungsten (W) and oxide dispersion-strengthened (ODS) steel in ambiences of air and vacuum were studied. In both samples and mediums high intensity laser radiation induced morphological and chemical variations. Surface features and phenomena depend on the material characteristics and the ambience applied. Thus, crater depth was larger in vacuum then in air for ODS steel sample - ~55 μm vs. ~9 μm. Irradiation was accompanied with the appearance of plasma which can emit X-ray radiation. Chemical surface changes, particularly oxidation, were registered as well.

1. INTRODUCTION

The study of laser-material interaction is of particular interest in the last decade, primarily owing to modern applications, see Aliofkhazraei 2016. The use of intense ultrashort lasers, like femtosecond (fs) laser applied in this work, is essential due to creation of specific surface features. W and ODS steel considered here have extraordinary characteristics making them attractive for various applications, including nuclear complex (construction of fission and fusion reactors). In inertial fusion (IF) reactor both metals are serious candidates as the First Wall Materials (FWM), see Trtica 2018. FWMs are exposed to various fluxes like electromagnetic and thermal, thus the action of high intensity laser radiation can, in one approximation, simulate behavior of these materials inside the reactor, Montanari et al. 2017 and Trtica et al. 2020. The goal of this paper is to study the behavior of W and ODS steel under conditions of high laser intensity - 10^{15} W/cm^2 in air and vacuum. Variations of morphological features and chemical surface content were the primary aim.

2. EXPERIMENTAL

Tungsten sample (disc, diameter 25 mm, 3 mm thick) was produced by sintering process, with the grain size ~20-80 μm, using Ni/Cu and Ni/Fe binders. ODS steel (square, 10 mm × 10 mm, 0.4 mm thick) was synthesized by mechanical alloying and hot isostatic pressing in Ar, with composition (wt%) Cr(16):Al(3):W(1.5)-Y_2O_3(0.35) and Fe (balance). Average sizes of Y_2O_3 and pre-alloyed powders were 40 nm and 50 μm, respectively. Experimental setup is the same as in works Trtica 2018 and Trtica et al. 2020 - laser beam with 15 mm diameter was focused through lens (f=150 mm) perpendicularly on the sample. The fs laser was Ti:sapphire (PULSAR, Amplitude Technologies), wavelength 804 nm; pulse 60 fs; pulse energy ≤12 mJ; TEM_{00} mode; linearly, vertically polarized beam. Irradiations were performed at 1013 and ~1×10^{-4} mbar pressure in air and vacuum, respectively. Characterization was done by optical microscope, scanning electron microscope (SEM) with energy dispersive analyzer, and optical interferometric profilometry.

3. RESULTS AND DISCUSSION

Material surface changes by laser depend on various irradiation parameters - laser parameters (wavelength, pulse length, pulse count, intensity, etc.), as well as material properties (e.g. absorptivity) and ambience. Experimental work was focused on morphological and chemical effects induced on W and ODS steel surface in air and vacuum by fs-laser after the action of 100 pulses.

3. 1. IRRADIATION IN AIR AMBIENCE

The effects of fs laser on W and ODS steel at the pulse energy of ~5.2 mJ and intensity ~10^{15} W/cm^2 are shown in Fig. 1. Generally, complex effects were detected: (a) crater like features in both samples, more prominent in ODS steel (Fig.1 A1-3 and B1-3); (b), surface cracking in the central zone, with additional grain fusion in case of W; (c) cross section of the craters was conical in both targets with similar depth, ~9 μm; (d) at the peripheral region more intense lifting of the material detected in W. Only in case of ODS steel laser induced periodic surface structures (LIPSS) were recorded. Also, hydrodynamic (HD) effects were much more prominent in case of W (Fig. 1 A3). Fundamentally, the process of fs-laser-metal interaction is complex and starts with free electrons absorbing the incident radiation, see Trtica et al. 2020. Further, the hot electrons cool down by diffusion and electron-phonon interaction leading to thermal equilibrium between lattice and electron subsystems. The dynamics of the system prior to this equilibrium can be described by two-temperature model. Finally, after several ps, laser-metal interaction can be considered a thermal process. If the initial laser intensity is sufficient, the ablation can take place on a time scale ≥100 ps. The ablated material cools rapidly in a space close to the target, and it can build up unique structures on the surface. Ablation mechanisms are diverse and they can comprise phase

explosion, fragmentation, etc. Creation of LIPSS recorded in this experiment is a complex process as well, and one explanation includes the interference of incident laser beam with the so-called surface waves, scattered off the imperfections on the material and running along its surface.

At high laser intensities plasma was formed above the samples and it was expected to emit x-ray radiation. Chemical surface changes (central zone) were more prominent in case of ODS steel, i.e. [O] was 2.6% against 1.0% in W.

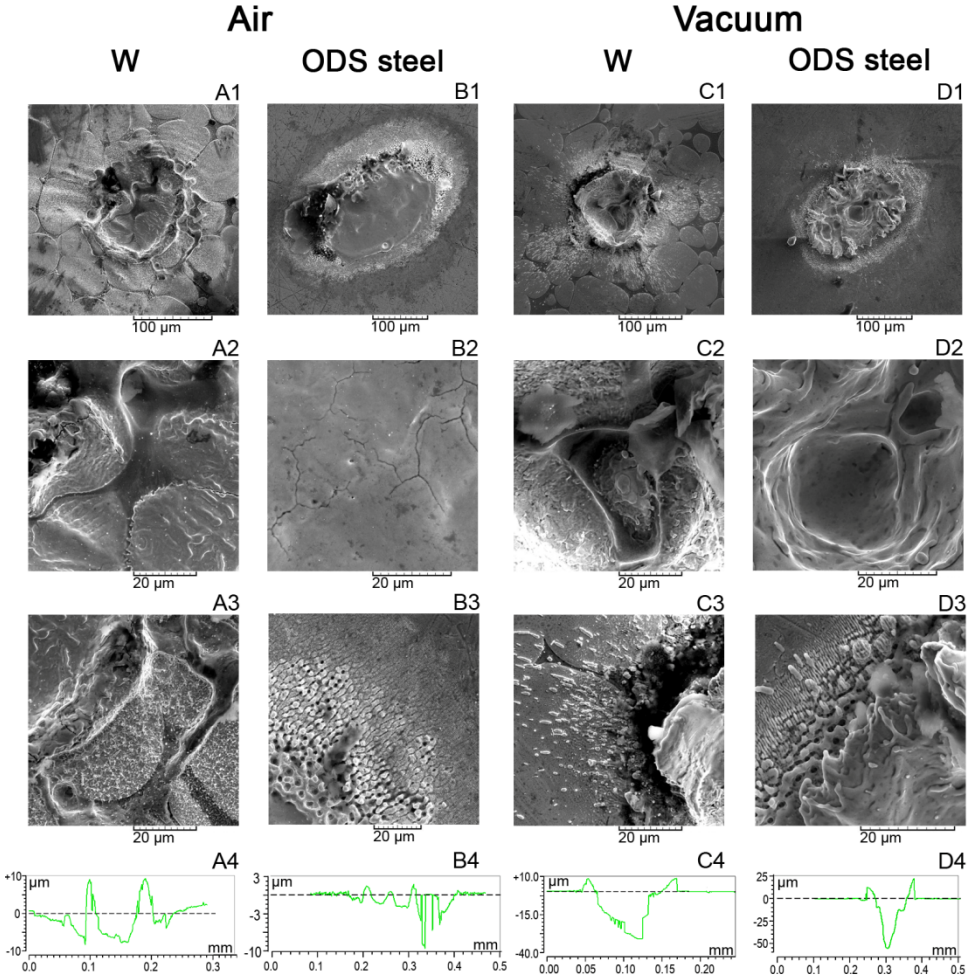

Figure 1: SEM and 2D profilometric analysis of W and ODS steel after action of laser pulses in air and vacuum. Energy ~5.2 mJ, intensity ~10^{15} W/cm^2.

3.2. IRRADIATION IN VACUUM AMBIENCE

In the main, modifications of both targets in vacuum are more pronounced than in air which is explained by better coupling of laser radiation with the surface.

Changes are as follows: (a) in the central zone, grain fusion is present in W - Fig. 1 C2, while violent structure was obtained in ODS steel (Fig. 1 D2). Crater depth was more prominent in steel, i.e. ~55 μm vs. ~33 μm in W; (b) lifting of the material on the periphery was more prominent in steel, while HD effects were dominantly observed in W. LIPSS are registered only on steel. Also, in vacuum ambience, at the intensity used, plasma was generated above both samples. Chemical analysis (central zone) showed that oxidation was absent in case of W while at ODS steel surface it was strong, in the interval from ~2 to ~36%, probably caused by redistribution of oxygen which is initially present in the sample.

4. CONCLUSION

Study of fs laser-target (W and ODS steel) interaction in air and vacuum was presented. It was shown that applied laser pulse energy of ~5.2 mJ, intensity 10^{15} W/cm^2, induced distinguishing surface features and phenomena. Generally, they are in strong correlation with sample type and ambience: (i) in both targets crater like damages were registered with crater depth larger in ODS steel, ~55 μm, vs. ~33 μm for W in vacuum. Also, damages were always more prominent in vacuum. In the peripheral area specific changes were registered such as HD effects, LIPSS; (ii) irradiation was accompanied with the appearance of plasma which can emit x-ray radiation; (iii) chemical surface changes, particularly oxidation, were registered in air as well as in vacuum but only in ODS steel. The results could contribute to better understanding of the behavior of nuclear reactor materials under high fluxes that can be simulated by laser intensities applied here.

Acknowledgements: The research was sponsored by the: (i) Ministry of Education, Science and Technological Development of the Republic of Serbia, project 172019; (ii) IAEA project "Pathways to energy from inertial fusion: Materials beyond ignition"; (iii) ESIF and the Czech Republic, the Project Center of Advanced Applied Science [CZ.02.1.01/0.0/0.0/16_019/0000778] - through The Operational Program. Research, Develop. and Education and, (iv) Czech Ministry of Education, Youth and Sports [project LTT17015].

References

Aliofkhazraei, M. (Ed.), 2016, *Handbook of Nanoparticles*, Springer Int. Pub., Switzerland.

Montanari, R., Pakhomova, E., Pizzoferr., R., Richetta, M., Varone, A.: 2017, *Metals*, **7**, 454.

Trtica, M.: 2018 (December), *IAEA Final Report for Contract 20636 (period: 2016-2018)* within CRP F13016, "Pathways to energy from inertial fusion: Materials beyond ignition".

Trtica, M., Stasic, J., Limpouch, J., Gavrilov, P., Chen, X., Ciganovic, J.: 2020, *Fusion Engin. and Design*, **150**, 111360.

Section 3.

LOW TEMPERATURE PLASMAS

Publ. Astron. Obs. Belgrade No. 99 (2020), 135 *Invited Lecture*

HIGH-RESOLUTION SPECTROSCOPY OF CATION-HELIUM COMPLEXES AT LOW TEMPERATURE

OSKAR ASVANY and STEPHAN SCHLEMMER
I. Physikalisches Institut, Universität zu Köln
E–mail asvany@ph1.uni-koeln.de

Abstract. To date, one of the most successful approaches for the elucidation of molecular ions is action spectroscopy, in which typically infrared radiation is applied to a mass selected ensemble of trapped (or guided) ions. Its very high sensitivity derives from counting ions as the spectroscopic signal, and not detecting light as in conventional methods. For weakly bound ionic complexes such as $H^+(H_2O)_n$, $CH_5^+(H_2)_n$ or $H_3^+(H_2)_n$, the action spectroscopic method called vibrational predissociation has been the standard technology for decades (Okumura et al. 1985, Bieske and Dopfer 2000). More recently, there is also increasing interest in weakly bound cation-helium complexes which can be conveniently investigated in modern cryogenic ion trap environments.

The research group in Köln set out to investigate the complexes HHe_n^+, $H_2He_n^+$ and H_3^+-He_n, being very fundamental ions and consisting of the two most abundant elements in the universe. HHe^+ has been detected in space recently by Güsten at al. 2019. On this conference, new vibrational work on the fundamental complexes HHe_n^+, $n = 2-6$, is presented. As seen in the Figure below, these complexes consist of the strongly bound chromophore He-H^+-He ($n = 2$), surrounded by more loosely bound He atoms. With a $^1\Sigma$ ground state, this chromophore has a simple vibrational spectrum consisting of the IR active asymmetric stretching mode and the degenerate bending mode. The weakly bound He atoms in the complexes with $n = 3 - 6$ allow to probe the chromophore by predissociation spectroscopy. Using various IR sources, we have localized these vibrational features for the first time (Asvany et al. 2019). Very recently, also high-resolution information for the fundamental three-nucleus-four-electron molecule He-H^+-He has been obtained.

The final aim of this research project will be high-resolution rotational spectroscopy for those species which possess a permanent dipole moment, as e.g. HHe_3^+, H_2He^+ and potentially H_3^+-He. This can be achieved via a double resonance, consisting of a rotational excitation followed by a predissociating transition. The feasibility of such a double-resonance scheme has already been demonstrated for CH_3^+-He (Töpfer et al. 2018).

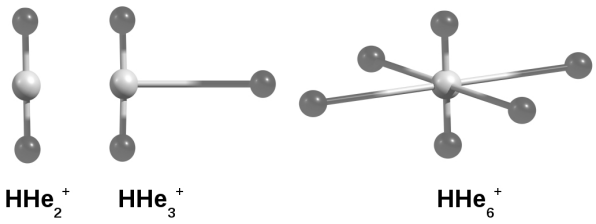

References

Asvany, O. et al. : 2019, *J. Phys. Chem. Lett.* **10**, 5325.
Bieske, E. and Dopfer, O. : 2000, *Chem. Rev.* **100**, 3963.
Güsten, R. et al. : 2019, *Nature* **568**, 357.
Okumura, M., Yeh, L.I., Lee, Y.T. : 1985, *J. Chem. Phys.* **83**, 3705.
Töpfer , M. et al. : 2018, *Phys. Rev. Lett.* **121**, 143001.

A NEW LOOK AT OXYGEN PLASMAS - QUANTITATIVE SPECTROSCOPY FOR RIGOROUS TESTING OF MODELS

JEAN-PAUL BOOTH[1]

ABHYUDAY CHATTERJEE[1], OLIVIER GUAITELLA[1], DMITRY LOPAEV[2], SERGEY ZYRYANOV[2], TATYANA RAKHIMOVA[2], DMITRY VOLOSHIN[2], NELSON DE OLIVEIRA[3] and LAURENT NAHON[3]

[1]*Laboratoire de Physique des Plasmas, CNRS/Ecole Polytechnique/Sorbonne Universités, 91128 Palaiseau, France*

[2]*Skobeltsyn Institute, Lomonosov Moscow State University, Russia*

[3] *Synchrotron SOLEIL, Saint-Aubin, Gif-sur-Yyette ,France 91192*
E-mail jean-paul.booth@lpp.polytechnique.fr

Abstract. Despite many decades of study, models of discharges in molecular gases still lack accurate data on many key collisional processes, even for such "simple" and ubiquitous gases as O_2. Good data is lacking for near-threshold electron-impact dissociation, surface recombination, the role of metastables, of gas heating, of vibrational excitation, of energy transfer and surface thermal accommodation. Direct measurement of the rate constants of individual processes is a fastidious process, where it is even possible. As an alternative approach, we compare comprehensive measurements of internal plasma parameters to simulations for a plasma with relatively simple chemistry, namely a DC positive column discharge in pure O_2. This well-characterized, stable and uniform discharge is optimal for experiment-model comparison. Although it has been studied for a very long time, new experimental methods, including synchrotron Vacuum ultraviolet absorption spectroscopy and laser cavity ringdown absorption spectroscopy (CRDS), allow the densities of all the major species (atomic, molecular, in ground and excited states), as well as the gas translational temperature to be measured, with much-improved absolute accuracy, and with time resolution.. Applied to (partially- and fully-) modulated discharges, these measurements provide unprecedented insight into the kinetic processes occurring (in the gas phase and at surfaces), and a profound test of the models. Whereas a model can be adjusted to fit a set of steady state measurements at one given set of operating conditions, trends with pressure and discharge current, and especially the temporal response to current modulation, are much harder to reconcile with an incorrect model. In practice, model failures often result from omission of key processes, or to neglect of their temperature-dependence. With the relatively simple chemistry occurring in pure O_2, with measurements of all principal species as well as the gas temperature, it is possible to identify the missing reactions, and even estimate their rates (and/or activation energies) by adjusting the model to fit the measurements.

PHYSICAL APPLICATIONS IN LIFE SCIENCE

K.-D. WELTMANN, T. GERLING, J. F. KOLB and Th. von WOEDTKE

Leibniz Institute for Plasma Science and Technology e. V. (INP Greifswald), Germany
E-mail weltmann@inp-greifswald.de

Abstract. The properties of plasma and its generated cocktail of physical and chemical compounds leads to significant microbial inactivation on various specimens and offers a wide range of possible applications for decontamination purposes. Actually e.g. caused by Covid-19, an increasing demand also for new and sufficient decontamination methods offers the chance for selected plasma based applications of surfaces. Further selected components of the plasma influence cell signalling, apoptosis and other cellular processes. Studies on the decontamination of surfaces, gases, liquids, on the treatment of seeds and plants as well as the experience and knowledge acquired in the new field plasma medicine are the starting point and basis of several new disciplines like "Plasma Agriculture", “Plasma Cosmetics”, “Plasma Pharmacy/Pharmacology”, “Plasma Oncology” just to mention the most actual research activities. Applications for healing of chronic wounds and cancer treatment become a more and more important and clinically relevant research field in plasma medicine (Metelmann et al. 2018, Schuster et al. 2016). The sophisticated biomedical applications of plasmas require atmospheric pressure plasma sources, which are now available in many different designs and configurations (von Woedtke et al. 2013). First devices especially for wound healing are certified as medical products class II. Because of other devices, which enter the market partly without clinical trials or with poor physical and biological characterization, there is clearly a need for standard parameters. With the help of standards, plasma sources can be perfectly adapted to dermatological and other medical applications and will achieve higher acceptance. Such a pre-selection criteria ensure the safety of investigators, patients and therapists. A well-known and applicable standard also guarantees the identification of devices that are not suitable as medical plasma sources, DIN 2014. One focus of the contribution – besides medicine - will be agriculture. The lecture also discusses different plasma sources and applications and shows selected results with regard to the current state of application.

References

DIN SPEC 91315:2014-06, 2014, *General requirements for plasma sources in medicine*, DIN Deutsches Institut für Normung e.V., Beuth Verlag Berlin (in German).

Metelmann, H. R. et al. (eds): 2018, *Comprehensive Clinical Plasma Medicine, Springer Nature.*

Schuster, M. et al.: 2016, *Visible Tumor Surface Response to Physical Plasma and Apoptotic Cell Kill in Head and Neck Cancer. J. Cranio. Maxill. Surg.*, **44***,* 1445.

von Woedtke, Th., Reuter, S., Masur, K., Weltmann, K.-D.: 2013, *Plasmas for medicine. Phys. Rep.*, **530**, 291-320 (a).

NUMERICAL SIMULATION-BASED OPTIMISATION OF PLASMA SOURCES FOR MEDICAL APPLICATIONS

ANDREW R. GIBSON[1,2]

[1]*Research Group for Biomedical Plasma Technology, Ruhr-Universität Bochum, Universitätsstraße 150, 44801 Bochum, Germany*

[2]*Institute of Electrical Engineering and Plasma Technology, Ruhr-Universität Bochum, Universitätsstraße 150, 44801 Bochum, Germany*

E-mail gibson@aept.rub.de

Abstract. Plasma technology has potential to generate significant societal benefits through a range of biomedical applications. In terms of widespread use in real-word scenarios, plasma applications span the entire spectrum from early stage proof-of-concept (e.g. cancer therapy) to emerging clinical tools (e.g. chronic wound treatment) to proven, indispensable clinical interventions (e.g. electrosurgery). A common thread in all biomedical applications is the interaction between a complex plasma system, typically containing a range of biologically active components such as photons, reactive species, electric fields and currents, and a complex biological system. In such systems, optimization of application outcomes requires optimization of the plasma properties that drive the relevant biological effects. Given the wide variety of active components that may play a role, and the experimental difficulties in measuring these components, optimization through experiment alone is a significant challenge. A promising approach to overcome this challenge is the use of experimentally validated numerical simulation approaches for plasma and device optimization. Here, various simulation approaches are used to demonstrate the potential for simulation-based optimization of plasma sources for cancer therapy and disinfection of surfaces. In the context of cancer therapy, a combined approach utilizing experimentally validated plasma-chemical kinetics modelling (Schröter *et al.* 2018, Wijaikhum *et al.* 2017) and computational fluid dynamics is used to determine design parameters for the scaling of reactive oxygen species delivery via needle-like plasma sources at atmospheric pressure for prostate cancer therapy. In the context of plasma disinfection, 2D hybrid plasma simulations (Tian and Kushner 2015) are used to predict photon fluxes incident on different surfaces of an object placed inside a low-pressure plasma reactor to assess the optimum plasma operating conditions for the disinfection of complex structures.

Acknowledgements. The author would like to thank Prof. Mark J. Kushner for providing the GlobalKin and HPEM codes used in this work, and for continued collaboration. Ongoing collaboration with colleagues from the University of York (Dr. Sandra Schröter, Prof. Deborah O'Connell and Prof. Timo Gans) and the Ruhr-Universität Bochum (Dr. Marcel Fiebrandt and Prof. Peter Awakowicz) are also gratefully acknowledged.

References

Schröter, S. et al: 2018, *Phys. Chem. Chem. Phys.*, **20**, 24263.
Tian, P. and Kushner, M. J.: 2015, *Plasma Sources Sci. Technol.*, **24**, 034017.
Wijaikhum, A. et al.: 2017*, Plasma Sources Sci. Technol.*, **26**, 115004.

TRANSIENT SPARK DRIVING CIRCUIT OPTIMIZATION FOR ENHANCED GENERATION OF NITROGEN OXIDES

MARIO JANDA[1], KAROL HENSEL[1] and ZDENKO MACHALA[1]

[1] *Division of environmental physics, Faculty of mathematics, physics and informatics, Comenius University, Mlynska dolina F2, 84248 Bratislava, Slovakia*
E–mail janda1@uniba.sk

Abstract. Nitrogen fixation in atmospheric air plasma discharges becomes an emerging application due to great potential in agriculture. We are testing N-fixation by Transient Spark (TS): a dc-driven self-pulsing discharge with a repetition frequency of 1-10 kHz. Generated sparks (Figure 1) are of very short duration (∼10 ns) and the energy delivered to plasma is limited to ∼1 mJ per pulse, because the spark is formed only by discharging of the internal circuit capacitance (20-30 pF). This makes TS an efficient plasma source for nitrogen oxides (NOx) generation (Janda et al. 2016). The density of NOx increases with increasing repetition rate, but the increase of frequency also leads to the transition to less efficient high pressure glow discharge (GD) regime (Figure 1).

Large ballast resistor (R = 5-10 MΩ) is used to eliminate TS to GD transition. However, this approach causes decreasing energy efficiency of TS at higher frequency due to the growing losses on R. For this reason, we tested various driving circuit modifications using additional coils and capacitors to keep discharge in spark regime even with R below 5 MΩ. We were able to maintain the discharge in spark regime with R = 2.3 MΩ using additional capacitance C = 70 pF. Moreover, we succeeded to increase the NOx generation efficiency approximately by factor 2. There was no benefit from using even higher external capacitance (tested up to C = 500 pF). The sparks during the active discharge phase were more intense, but the charging of C during the relaxation phase (see Figure 1) was much longer, i.e. the repetition frequency of current pulses decreased.

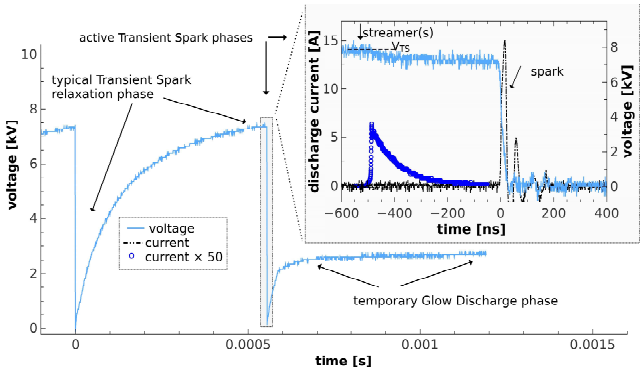

Figure 1: TS current and voltage waveforms.

Acknowledgements: Supported by Slovak Research and Development Agency APVV-17-0382, and Slovak Grant Agency VEGA 1/0419/18.

References

Janda, M., et al. : 2016, *Plasma Chem. Plasma Proc.*, **36**, 767.

CAVITY RING-DOWN SPECTROSCOPY AS A TOOL FOR PLASMA DIAGNOSTICS

NIKŠA KRSTULOVIĆ

Institute of Physics, Bijenička cesta 46, 10000 Zagreb, Croatia
E-mail niksak@ifs.hr

Abstract. Cavity Ring-Down Spectroscopy (CRDS) is one of most sensitive absorption based technique for detection and diagnostics of elements in gaseous phase. It is based on measuring of photons lifetime in a resonator (decay time of oscillating photons traversing the optical cavity), not on light intensity, which allows very good stability of the system (low level of noise). When the wavelength of photons is tuned to some resonant transition of absorbing feature the photon lifetime decreases while by comparison with non-resonant lifetime one can get absorption coefficient (in cm^{-1}) as a function of wavelength – it is optical absorption spectrum in absolute units. From such spectral line-profiles, CRDS technique allows calculation of species concentrations in particular quantum state. Data analysis and experimental features allow complete 3D + temporal monitoring of sample of interest including underlying physical or chemical processes (dissociation or association of molecules, de-excitation processes, ionization, collisions) (see Labazan et al. 2003, Labazan et al. 2006 and Krstulović et al. 2006). CRDS is sensitive, versatile and robust analytical technique to study species in gaseous or plasma phase. This work briefly describes the basic principles of CRDS and summarizes our achievements related to applications for studying of atmospheric pressure plasma jets (APPJ) (see Zaplotnik et al 2015) and single and double laser produced plasmas (LPP) (see Krstulović et al. 2008, Krstulović et al. 2009). Emphasis is given to the temporal resolution and pulsed character of the plasma sources.

References

Labazan, I., Krstulović, N., Milošević, S. : 2003, *J. Phys. D: Appl. Phys*., **36**, 2465.
Labazan, I., Krstulović, N., Milošević, S. : 2006, *Chem. Phys. Lett.*, **428**, 13.
Krstulović, N., Labazan, I., Milošević, S. : 2006, *Eur. Phys. J. D*, **37,** 209.
Krstulović, N., Čutić, N., Milošević, S. : 2008, *Spectrochim. Acta B*, **63**, 1233.
Krstulovic, N., Čutić, N., Milošević, S. : 2009. *Spectrochim. Acta B*, **64**, 271.
Zaplotnik, R., Bišćan, M., Krstulović, N., Popović, D., Milošević, S. : 2015, *Plasma Sources Sci. Technol*., **24**, 054004.

PROBING NEUTRAL OXYGEN ATOMS BY LASER-OPTIC CATALYTIC SENSOR

GREGOR PRIMC[1,2]

[1]*Jozef Stefan Institute, Department for Surface Engineering, Jamova cesta 39, 1000 Ljubljana, Slovenia*
E-mail gregor.primc@ijs.si

[2]*Plasmadis Ltd., Teslova ulica 30, 1000 Ljubljana, Slovenia*
E-mail gregor.primc@plasmadis.com

Abstract. Europe is facing the fourth industrial revolution, referred to as Industry 4.0. Concepts of Industry 4.0 include smart automation, virtualization, advanced prediction with artificial intelligence and general robotization and automation. Many processes, as well as devices, are not ready for such a big leap in automation, one of them being plasma devices, which are, from a user perspective, regarded as "black boxes". Typical plasma devices have measurable and adjustable discharge parameters (electrical voltage, current, frequency, gas inlet, pressure). On the other hand, plasma parameters, such as fluxes of reactive species on the plasma-treated products and temperature of reactive species, which are crucial information in precise and reliable plasma process control, are not monitored, let alone controlled. Complying with the Industry 4.0 standards, processes have to be monitored by numerous advanced sensors that are coupled to into a smart control system. We have made a first step in developing a laser-optic catalytic sensor that is capable of measuring neutral oxygen atom density in a low-pressure gaseous plasma with low ion-to-neutral-atom ratio. Next challenge is the development of smart industrial reactors that will be able to self-regulate plasma parameters sustaining homogeneous plasma throughout the whole production process.

References

Mozetič, M., Vesel, A., Primc, G., Zaplotnik, R.: 2019, Introduction to plasma and plasma diagnostics, Thomas, Sabu (ed.), Mozetič, Miran (ed.), Cvelbar, Uroš (ed.). Non-thermal plasma technology for polymeric materials: applications in composites nanostructured materials, and biomedical fields., Amsterdam: Elsevier. cop. pp. 23-65.

Primc, G. et al.: 2019, Method and device for detection and measuring the density of neutral atoms of hydrogen, oxygen or nitrogen, EP 3146327(B1), granted 11. 6. 2019, Munich: European Patent Office.

A DETAILED REACTION MECHANISM SET FOR VIBRATIONAL CHEMISTRY IN CO_2 PLASMAS

T. SILVA and V. GUERRA

Instituto de Plasmas e Fusão Nuclear, Instituto Superior Técnico, Universidade de Lisboa, Portugal
E-mail tiago.p.silva@tecnico.ulisboa.pt

Abstract. This contribution is devoted to the modelling of CO_2-containing discharges. The presented work is supported by a zero-dimensional chemistry model coupled with the homogenous electron Boltzmann equation which has been validated by isolating different aspects of the complex kinetics, namely through the: (i) study of the time-resolved evolution of the lower vibrationally excited CO_2 levels during the afterglow of CO_2 discharges (Silva 2018) (ii) investigation of the effect of electrons on the distribution of the lower vibrationally excited CO_2 levels obtained in pulsed and continuous glow discharges (Grofulovic 2018), (iii) investigation of the influence of N_2 on the CO_2 vibrational distribution function and dissociation yield in pulsed glow discharges (Terraz 2020), (iv) validation of the electron-impact dissociation cross sections of CO_2 (Morillo-Candas 2020) and (v) study of the gas heating in the afterglow of pulsed CO_2 glow discharges (Silva 2020). Herein we address different theories and scaling laws to describe the CO_2 decomposition and the vibrational excitation involving highly excited states. Special attention is devoted to the difference between state-to-state and single- or multi-temperature approximation methods. The influence of different reaction rate coefficients on important plasma parameters, namely the gas temperature, vibrational distribution functions and dissociation rates is analyzed in detail. In order to complement this study and validate our kinetic model, the simulation results are compared against experimental data obtained in pulsed DC glow discharges, with special interest on the understanding of the mechanisms leading to oxygen and CO production.

Acknowledgments

This work was partially funded by Portuguese FCT - Fundação para a Ciência e a Tecnologia, under projects UIDB/50010/2020 and UIDP/50010/2020

References

Grofulovic, M et al.: 2018, *Plasma Sources Sci. Technol.,* **27**, *115009*
Morillo-Candas A et al.: 2020, *Plasma Sources Sci. Technol.,* **29**, *01LT01*
Silva, T et al.: 2018, *Plasma Sources Sci. Technol.,* **27**, *015019*
Silva, T et al.: 2020, *Plasma Chem. Plasma P,* **40**, 713-25
Terraz L et al.: 2020, *J. Phys. D: Appl. Phys.,* **53***, 094002*

PLASMA JETS AND MULTIJETS IN CONTACT WITH LIQUIDS IN BIOMEDICAL EXPERIMENTS: ELECTRO FLUID DYNAMIC AND REACTIVE SPECIES DISTRIBUTION

A. STANCAMPIANO[1], A. VALINATTAJ OMRAN[1], F. TAMPIERI[2], S. DOZIAS[1], E. SZILI[3], J.-M. POUVESLE[1], P. ESCOT BOCANEGRA[1], CRISTINA CANAL[2] and E. ROBERT[1]

[1] *GREMI, CNRS UMR 7344, Université d'Orléans, 45000 Orléans, France*

[2] *Universitat Politècnica de Catalunya, Biomaterials, Biomechanics & Tissue Engineering Group, 08019 Barcelona, Spain*

[3] *Future Industries Institute, University of South Australia, Adelaide, SA5095, Australia*

E-mail augusto.stancampiano@univ-orleans.fr

Abstract. Plasma jets are being intensively studied for biomedicine applications but their fine control remains challenging due to the mutual interactions between plasma and target. Even considering perhaps one of the simplest scenario in a research laboratory, using a plasma jet to treat a 2D culture of cells in a plastic multi-well plate, it is not known in detail how the physical environment of the micro-well may influence the nature of the plasma jet treatment. This study aims to shed light on this topic by investigating how electro fluid dynamic (EFD) flows influence the delivery of the bioactive plasma-generated RONS when a plasma jet is used to treat a biologically-relevant liquid (i.e. PBS) in a standard tissue culture grade 24-well plate. The results show how the formation of complex EFD flows in the liquid induce a non-uniform distribution of the RONS. Shortly after the ignition of the plasma jet an initial rapid liquid stream can reach the bottom of the well, whereas a stable vortex mixing is observed few seconds later. Electric charge accumulation on the liquid surface and plasma induced gas swirling could be the causes of the liquid motions. Furthermore, the liquid depth/volume and the voltage polarity are found to be critical parameters in controlling the delivery of the RONS to the bottom of the well.

References

Mohades, S., Lietz A., Kruszelnicki, J., Kushner, M. J. : 2020, *Plasma Processes and Polymers*, **17**, 3

Stancampiano, A., Chung, T.-H., Dozias, S., Pouvesle, J.-M., Mir, L. M., Robert, E. : 2019, *IEEE Trans. Radiat. Plasma Med. Sci*., **4**, 3

PIC MCC AND FLUID SIMULATION OF PROCESSING PLASMAS: COLLISION RADIATIVE MODELS AND ION ENERGY DISTRIBUTION FUNCTIONS

D. VOLOSHIN

Skobeltsyn Institute of Nuclear Physics Lomonosov Moscow State University (SINP MSU), 1(2), Leninskie gory, GSP-1, Moscow 119991, Russian Federation
E-mail dvoloshin@mics.msu.su

Abstract. Argon based low-temperature plasmas are widely used both for fundamental process research and in technology applications. The long-lived Ar excited species act as energy reservoirs and have an influence on the discharge structure through the energy transfer to other species and surfaces. VUV photons from the Ar resonance states can substantially influence the properties of the processing materials, both in positive and negative ways. In this sense the simulation of plasma processing ICP (Kropotkin et al. 2020) and CCP discharges should correctly predict the Ar excited states densities in the plasma using collision-radiative model (Kovalev et al. 2019). Material modification on the atomic layer scale requires precise control of the ion flux and ion energy distribution function at the electrode. The experimental research combined with numerical simulations could provide better diagnostics for RF discharges. Such approach was used to determine the plasma density from the ion current to the Langmuir probe: with the PIC MCC simulation for a cylindrical (Voloshin et al. 2015) and a flat (Voloshin et al. 2016) probes. The relation between the ion flux and plasma density in an RF CCP discharge was studied both experimentally and with the 2D PIC MCC simulation (Bogdanova et al. 2018). The ion composition and energy spectra was studied both experimentally and numerically with PIC MCC model in Ar-H2 plasma of RF CCP discharge: see Bogdanova et al. 2019. The results of fast model for IEDF calculation in pure gases: Ar, Xe and N2 are presented in comparison with experimental measurements. Results in a pulsed CCP plasma: measurements of metastable and resonance states in the afterglow and application of CRM for the afterglow phase are also shown.

References

Bogdanova, M. et al. : 2018, *Plasma Sources Sci. Technol.*, **27**, 025003.
Bogdanova, M. et al. : 2019, *Plasma Sources Sci. Technol.*, **28**, 095017.
Kovalev, A.S. et al.: 2019 *Phys. Plasmas*, **26**, 123501.
Kropotkin, A. N., Voloshin, D. G. : 2020, *Phys. Plasmas*, **27**, 053507.
Voloshin, D. et al. : 2015, *Eur. Phys. J. D*, **69**, 23.
Voloshin, D. et al. : 2016, *Plasma Sources Sci. Technol.*, **25**, 015018.

EFFECTS OF IONIZING RADIATIONS ON THE REACTIVITY INSIDE CLUSTERS OF LINEAR HYDROCARBONS: POLYMERIZATION VS. CYCLIZATION

S. INDRAJITH[1*], J. KOCISEK[2], A. DOMARACKA[1], C. NICOLAFRANCESCO[1], P. ROUSSEAU[1], J. FEDOR[2], M. FARNIK[2] and B. A. HUBER[1]

[1] *Normandie Univ., ENSICAEN, UNICAEN, CEA, CNRS, CIMAP, 14000 Caen, France*
*E-mail * indrajith@ganil.fr*

[2] *J. Heyrovský Institute of Physical Chemistry v.v.i., The Czech Academy of Sciences, 18223 Prague, Czech Republic.*

Abstract. Recently, Cassini-Huygens mission brought interesting results concerning one of Saturn's biggest satellites, Titan. In fact, it has been shown that this moon's typical orange-brownish haze layers could be due to the presence of aerosols which are essential for it's climate, radiation balance and atmosphere chemistry. However, since it is mainly composed of nitrogen, methane and a small amount of more complex hydrocarbons, understanding the way such PAHs are formed is mandatory (see Zhao L. 2009 and Brown H.R. 2009). Collisions of low energy ions with loosely bound clusters of molecules are studied in the gas phase with the aim to analyze either fragmentation processes, which occur due to the transfer of energy and charge, or, at the opposite, growth processes leading to molecular growth and the formation of new of larger covalently bound molecules. It has been shown that this triggers reactivity, as observed in C60 clusters (see Delaunay R. 2018) or PAH ones (see Delaunay R. 2015). When several atoms are kicked out along the ion trajectory in the cluster large covalently bound systems can be formed. We present results on cluster systems containing linear chain molecules like butane and butadiene. We will discuss the possible formation of ring structures and the path to aromatic molecules. The irradiation of hydrocarbons clusters using different radiation sources (electrons and ions) allows to determine the balance between ionization induced reactivity and collision induced one.

References

Brown H.R., et al.: 2009*, Springer*, 'Titan from Cassini-Huygens', **214**, 79.
Delaunay R et al.: 2018, *Carbon*, **129**, 766-774
Delaunay R et al.: 2015, *J. Phys. Chem. Lett.*, **6(9)**, 1536-1542.
Zhao, L., et al.: 2018, *Nature Astronomy*, **2**, 973-979.

ATMOSPHERIC PRESSURE MICRODISCHARGES AND JETS FOR AN INACTIVATION OF MICROBIOTA

ALIAKSANDRA KAZAK and LEANID SIMONCHIK

Institute of Physics of NAS of Belarus, Nezalezhnasci ave. 68-2, 220072 Minsk, Belarus

E-mail a.pavlova@ifanbel.bas-net.by

Abstract. Among a variety of plasma sources, particular attention is focused on the development and application of plasma jets due to their ability of surface treatment outside of a closed discharge volume (see K.H. Schoenbach). The dc microdischarge is only one type of discharges used for plasma jet generation. This discharge is the main studied object in given report. The discharge parameters are following: the gas temperature is 1600–2000 K, the typical electron density is ~ 10^{12}–10^{13} cm^{-3}, and the average electron energy is 1 eV (see V.I. Arkhipenko). It is shown, that the basic results obtained for this discharge are applicable to microdischarges with ripple and pulsing voltages.

Investigations of plasma jets are under consideration as well. It has been shown that ozone is the main bioactive component of jets in mixtures of helium with oxygen and argon with oxygen, and nitrogen-containing molecules (NO, NO_2, N_2O, HNO_2) for air and nitrogen plasma jets. The plasma chemistry in both the discharge and jet is discussed. Concentrations of long-living bioactive molecules are determined. It is shown the ways to control the jets compositions using different current modes of discharge.

An attention to the application of the obtained plasma structures for biomedical applications is paid. The effect of various bactericidal factors on samples contaminated with microbiological cells is under consideration. This observation allows to choose the most effective mode of microdischarge generation for applications. The inactivation of microbiota of various levels of organization is demonstrated.

References

Schoenbach, K. H. and Becker, K.: 2016, *Eur. Phys. J. D.*, **70**, 29.
Arkhipenko, V. I. et al.: 2018, *High Temp. Mater. Process*., **22**, 273–278.

SPECTROSCOPIC INVESTIGATION OF DISCHARGE AND AFTERGLOW PHASE OF MICROSECOND PULSED GLOW DISCHARGE

IVAN B. KRSTIĆ

Faculty of Physics, University of Belgrade, Studentski trg 12, 11000 Belgrade, Serbia
E-mail ivan@ff.bg.ac.rs

Abstract. This work focuses on the spatial and temporal characteristics of a pulsed Grimm-type glow discharge operated with 30 – 60 μs power pulses in argon (Krstić et al. 2020) with frequency of 5 kHz and currents of 20, 40 and 60 mA. The emission characteristics of the discharge are studied to obtain insight into the excitation and recombination processes of atoms and ions of argon fill gas and copper sputtered material. Properties of representative line emissions during the discharge and the afterglow periods of the discharge pulse were analyzed. Two groups of lines can be differentiated according to the time development. Atomic lines with the low energy of the upper level have a strong initial peak at the beginning of the discharge pulse, and a small afterpeak, see Fig. 1. Lines from high energy levels show the opposite behavior: small initial peak and a strong afterpeak. For the more detailed investigations of the energy and charge transfer processes, hydrogen has been added to the argon with different percentages.

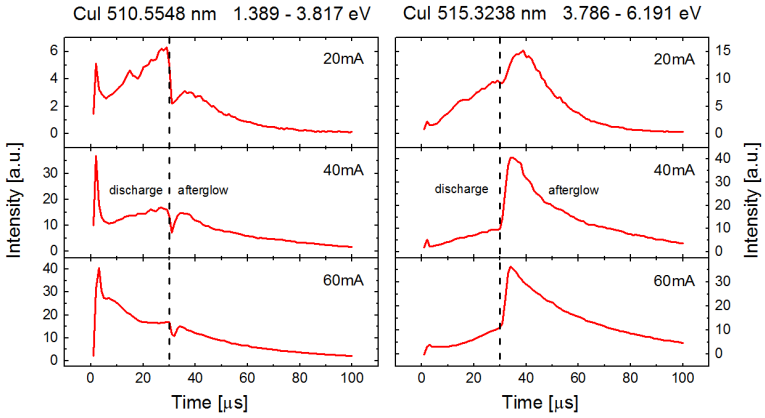

Figure 1: Time dependent emission of representative Cu I lines.

References

Krstić, I.B., Obradović, B.M., Kuraica, M.M.: 2020, *J. Instrument.*, 15 (1) C01006.

BREAKDOWN AND CHARACTERISTICS OF NON-EQUILIBRIUM LOW-PRESSURE DC DISCHARGES IN VAPOURS OF LIQUIDS

JELENA MARJANOVIĆ[1], DRAGANA MARIĆ[1], GORDANA MALOVIĆ[1] and ZORAN LJ. PETROVIĆ[1,2]

[1]*Institute of Physics, University of Belgrade, Pregrevica 118, 11080 Belgrade, Serbia*
[2]*Serbian Academy of Sciences and Arts, Kneza Mihaila 35, 11001 Belgrade, Serbia*
E-mail sivosj@ipb.ac.rs

Abstract. The study of non-equilibrium discharges in liquids and their vapors have become very popular due to a variety of possible applications, such as in nanoscience for the synthesis of nanographene layers and fast growth of carbon nanotubes (Hagino et al. 2012), for the treatment of materials and surfaces (Fumagalli et al. 2012), in biomedicine (Stalder et al, 2006), for polymerization processes and thin-film synthesis (Brunet et al. 2017), in fuel industry - sources of hydrogen (Petitpas et al. 2007), for purification and decontamination (Kitano et al. 2006), etc. However, emergence of new devices demands knowledge on elementary processes and their balance in discharge that can be obtained from studies of breakdown and electrical characteristics of discharges. Here we present results of the comprehensive experimental investigation of breakdown properties, spectra, spatial and spectrally resolved emission and V-A characteristics in low-pressure discharges in vapours of methanol, ethanol, isopropanol, n-butanol and water that provide sets of data for different operating regimes (Sivoš et al. 2015, 2019). Furthermore, we performed a detailed analysis of unusual behaviour of the discharge observed at the transition from normal to abnormal glow regime in methanol and ethanol vapour and the existence of double channels of the discharge observed in Townsend and normal glow regime in water vapour. Therefore, this paper aims to give an overview of breakdown data and data for Volt-Ampere (V-A) characteristics of discharges in vapours of studied liquids; and to emphasize some of the issues that can be important in the analysis and interpretation of results.

References

Brunet, P., Rincón, R., Martinez, J. M., Matouk, Z., Fanelli, F., Chaker, M., Massines, F. : 2017, *Plasma Process Polym*., **14**, e1700049.

Fumagalli, F., Kylian, O., Amato, L., Hanus, J., Rossi, F. : 2012, *J. Phys. D: Appl. Phys.,* **45**, 135203.

Hagino, T., Kondo, H., Ishikawa, K., Kano, H., Sekine, M., Hori, M. : 2012, *Appl. Phys. Express*, **5**, 035101.

Kitano, K., Aoki, H., Hamaguchi, S. : 2006, *Japan. J. Appl. Phys*., **45**, 8294.

Petitpas, G., Rollier, J. D., Darmonb, A., Gonzalez-Aguilar, J., Metkemeijer, R., Fulcheri, L. : 2007, *Int. J. Hydrogen Energy*, **32**, 2848C.

Sivoš, J., Škoro, N., Marić, D., Malović, G., Petrović Z. Lj. : 2015, *J. Phys. D: Appl. Phys*., **48**, 424011.

Sivoš, J., Marić, D., Škoro, N., Malović, G., Petrović Z. Lj. : 2019, *Plasma Sources Sci. Technol*,. **28**, 055011.

Stalder, K. R, Nersisyan, G., Graham, W. G. : 2006, *J. Phys. D: Appl. Phys*., **39**, 3457.

A REACTION MECHANISM FOR VIBRATIONALLY COLD CO_2 PLASMAS

A. F. SILVA[1,2,3], A. S. MORILLO-CANDÁS[2], O. GUAITELLA[2] and V. GUERRA[3]

[1]*DIFFER, Eindhoven, the Netherlands*

[2]*LPP, École Polytechnique, Sorbonne Université, France*

[3]*IPFN, Instituto Superior Técnico, Universidade de Lisboa, Portugal*

E-mail a.f.sovelasdasilva@differ.nl

Abstract. The use of plasmas for CO_2 utilization has been under investigation in recent years following a wave of environmental awareness. In this work we research this topic using a bottom-up strategy to study fundamental CO_2 plasma processes. For this we rely on modelling and on dedicated experiments with which a reaction mechanism for vibrationally cold CO_2 plasmas can be validated in a relatively large range of experimental conditions. The simulation tool we use, LoKI (see Tejero-del-Caz *et al.* 2019), couples a Boltzmann and a chemistry solver. The simulated results obtained with the mechanisms proposed are validated against CO_2 glow discharge measurements at pressures lower than 5 Torr, reduced electric fields ranging from 50 to 100 Td and flowing at few sccm (see Morillo-Candás *et al*. 2019). The model can reproduce the measured values of product formation as well as discharge power and electric field. Although vibrational populations are low, we show them to have a significant effect on the electron properties. The shape of the EEDF is also significantly dependent on the dissociation degree. Moreover, we discuss the role of electronically excited states on CO_2 dissociation, showing that the first electronic excited state of CO can have beneficial effect in further producing CO and O in the discharge.

This work was partially funded by Portuguese FCT - Fundação para a Ciência e a Tecnologia, under projects UIDB/50010/2020 and UIDP/50010/2020, by NWO, in the framework of the CO2-to-products program, and by the french national funding agency under the project number ANR-16-CE06-0005.

References

Morillo-Candás, A. S., Drag, C., Booth, J. P., Dias, T., Guerra, V. Guaitella, O.: 2019, *Plasma Sources Sci. Technol.*, **28**.

Tejero-del-Caz, A., Guerra, V., Gonçalves, D., Lino da Silva, M., Marques, L., Pinhão, N., Pintassilgo, C.D., Alves, L. L.:2019, *Plasma Sources Sci. Technol.,* **28**.

MONTE CARLO FLUX SIMULATIONS OF ELECTRONS IN CO_2

L. VIALETTO[1], P. VIEGAS[1], S. LONGO[2] and P. DIOMEDE[1]

[1] *DIFFER – Dutch Institute for Fundamental Energy Research, De Zaale 20, 5612 AJ Eindhoven, the Netherlands*
E-mail l.vialetto@differ.nl

[2]*Dipartimento di Chimica, Università degli Studi di Bari, via Orabona 4, 70126 Bari, Italy*

Abstract. A boost in the investigation of CO_2 plasmas has been recently motivated by a possible application to carbon capture and utilization. Numerical models describing the interplay between electron and heavy particles kinetics require accurate and fast computational approaches. In particular, in CO_2, deviations from a two-term solution of the electron Boltzmann equation (EBE) are expected already at low/moderate reduced electric fields (*E/N*). Moreover, a common assumption is to avoid the accurate description of excited states or to neglect the velocity distribution of the background gas (or both). In this work, approximations that are usually employed in the study of electron kinetics in CO_2 are analyzed, together with strategies to overcome them.

Electron kinetics in CO_2 is described by means of a fully native Monte Carlo Flux (MCF) code. The MCF method provides detailed calculations of the Electron Velocity Distribution Function through a highly efficient variance reduction technique. In this work, the MCF code takes into account the thermal velocity distribution function of gas molecules. This extension, together with an accurate description of rotational and vibrational excited states, provides a better agreement with measured transport coefficients at low *E/N*. At moderate *E/N*, MCF calculations are benchmarked against multi-term solutions of the EBE, showing excellent agreement and limitations of the two-term approximation.

References

Bongers, W, et al. : 2017, *Plasma Process.. Polym.*, **14**, 1600126.
Longo, S., Diomede, P. : 2004, *Eur. Phys. J. Appl. Phys.,* **26**, 177-85.
Schaefer, G., Hui, P. : 1990, *J. Comp. Phys.*, **89**, 1-30.
Vialetto, L., Longo, S., Diomede P. : 2019, *Plasma Sources Sci. Technol.*, **28**, 115015.

ANALYTICAL CAPABILITIES OF TEA CO_2 LASER BASED LIBS SETUP

SANJA ŽIVKOVIĆ, JELENA PETROVIĆ, JOVAN CIGANOVIĆ and MILOŠ MOMČILOVIĆ

VINČA Institute of Nuclear Sciences
- National Institute of the Republic of Serbia,
University of Belgrade, PO Box 522 11351 Belgrade, Serbia
E-mail sanjaz@vinca.rs

Abstract. Laser-Induced Breakdown Spectroscopy (LIBS) has become a very popular analytical method given some of its unique features such as applicability to any type of sample, practically no sample preparation, stand-off sensing capability, speed of analysis, and a possibility to analysis even the light elements. In this paper, we present a unique laboratory LIBS setup developed in our research group. This system uses infrared TEA CO_2 laser as the excitation source and time-integrated spatially resolved (TISR) signal detection. In our recent publications, we have demonstrated the potential of using the cost-effective TEA CO_2 based LIBS system not only for the fast elemental analysis but also for the simultaneous determination of hardness of materials.

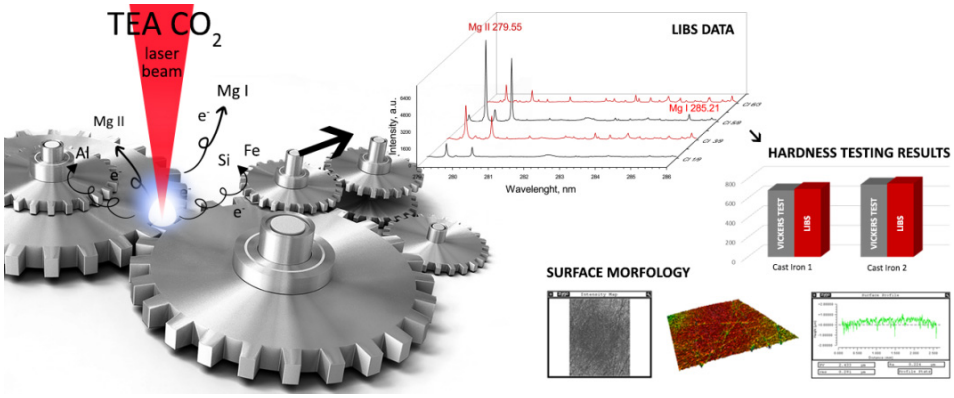

Figure 1: Graphical illustration of LIBS analysis

Acknowledgments: This research was supported by the Ministry of Education, Science and Technological Development of Republic Serbia.

References

Momcilovic, M., Petrovic, et al.: 2020, *Plasma Chem Plasma Process* **40**, 499–510.
Zivkovic, S., Savovic, J., et al.: 2017, *J. Alloys Compd.*, **700**, 175–184.

Publ. Astron. Obs. Belgrade No. 99 (2020), 153 - 156 *Contributed Paper*

OPTICAL EMISSION SPECTROSCOPY OF H_2 IN A TOROIDAL MAGNETISED PLASMA

RUGGERO BARNI,[1] PRINCE ALEX,[1] ESMAT GHORBANPOUR[2] and CLAUDIA RICCARDI[1]

[1]*Dipartimento di Fisica G.Occhialini, Università degli Studi di Milano-Bicocca, piazza delle Scienza 3 Milano I-20126, Italy*

E-mail: claudia.riccardi@mib.infn.it

[2]*Department of Physics, Faculty of Science, University of Guilan, P.O. Box 41335-1914, Rasht, Iran*

Abstract. A noninvasive diagnostic technique relying on optical emission spectroscopy is used for studying plasma confined in a purely toroidal magnetic field. Visible emission lines of molecular hydrogen were specifically targeted. Bi-dimensional structures and poloidal plasma profiles were reconstructed from the emissivity distribution of hydrogen Fulcher system using tomographic method. A few details concerning the methods employed to capture different emission viewlines, data reduction and tomographic reconstruction techniques are also addressed.

1. INTRODUCTION

The quest for finding new sources of energy have generated large interest in magnetized plasmas where plasma is confined in toroidal device such as tokamaks and stellarators aiming to produce energy through controlled thermonuclear fusion (see Wagner 2007). In particular, there is an ongoing effort aimed to better understand the effect of anomalous particle transport in reducing the confinement in magnetized plasma (see Wagner 2007). This phenomenon is quite general and related to the dynamical effects due to turbulence, which arise naturally in magnetized plasmas (see Tynan et al. 2009). In particular there is evidence of drift-wave turbulence in magnetically confined plasmas and, associated to that, the appearance and build-up of large amplitude density fluctuations in the edge region of plasmas, strongly contributing to turbulent cross-field particle and energy fluxes (see Tynan et al. 2009). The turbulence measurements are generally more complicated in plasmas than in fluids due to the faster time scales and to the difficulties in measuring locally microscopic parameters such as the plasma density and temperature (see Dudok de Wit et al. 2013). Another approach is related to the use of the electromagnetic radiation emitted by the plasma state. This usually

escapes from the plasma and could be collected from outside, without a direct disturbance of the system. As a tool for the study of plasma turbulence, optical diagnostics could be demanding too (see Donne' 2006). Since in plasma turbulence the associated autocorrelation times are in the range of a few microseconds to tens of microseconds, the diagnostics should be faster than these time scales. Optical emission spectroscopy (OES) is usually fast enough. For instance, in a hydrogen plasma, the lifetime of hydrogen n=3 state, emitting the H_α line, is about 10 ns. However, even in a simple hydrogen low temperature plasma, OES reveals many features arising from the complex plasma gas phase. Although atomic hydrogen dominates emission, it is common to spot emission also from the rich structure of excited levels of the H_2 molecules (see Barni et al. 2018). Such features in the emission spectra are suitable to study particular phenomena happening in the plasma, be it those arising due to presence of minority ions, the recombination or the dynamical effects induced by the collisions with neutrals (see Pierre et al. 2004). The continuous improvement in radiative collisional models also opens up the concrete possibility to relate spectroscopical data to constrain or even to measure more fundamental plasma parameters (see Capitelli et al. 2013). Here we present the application of an OES passive optical diagnostics to the study of emissivity in a simply magnetized toroidal (SMT) device using a low resolution visible spectrometer. In particular our aim will be to reconstruct the 2D pattern of emissivity of H_2 molecular states of the so-called Fulcher-α band system, the $3p\pi\ d\ ^3\Pi_u\ [3c] \rightarrow 2s\sigma\ a\ ^3\Sigma_g^+\ [2a]$ transitions (see Aguilar et al. 2008).

2. EXPERIMENTAL SETUP

Layout of the experimental setup is shown in figure 1. The Thorello device consists of four 90° curved and corrugated stainless steel sectors joined together to form a complete torus with a major radius of 40 cm and a minor radius of 8.75 cm. A set of 56 number of water-cooled circular coils surrounding the chamber enable us to apply a purely toroidal magnetic field (a simply magnetized torus, SMT configuration) of intensity up to 0.2 T using a 600 A DC stabilized current supply. Base pressure of less than $1x10^{-4}$ Pa is achieved using a couple of turbomolecular pumps backed by two rotary pumps. Experiments were normally performed by filling high purity hydrogen gas up to a pressure of a few 10^{-2} Pa. Plasma is produced by thermionic emission of three intertwined thoriated tungsten filaments bent in a 13 turns spiral shape (diameter 7 mm and length of 3 cm), placed with the axis aligned to the magnetic field about the center of the poloidal cross section. The filament is heated by passing a current of tens of ampere and discharge is struck between the hot filament (cathode) and the grounded vacuum vessel (anode) by applying a potential difference of about 150 V. More precisely a limiter, a hollow disk of 15 cm diameter, short-circuits the vertical electric field. Typical plasma parameters estimated using Langmuir probes at the radial center of the device are given by Te ~ 4 eV, Ti ~ 0.2 eV, Ne ~ 10^{11} cm^{-3} (see Barni et al. 2009).

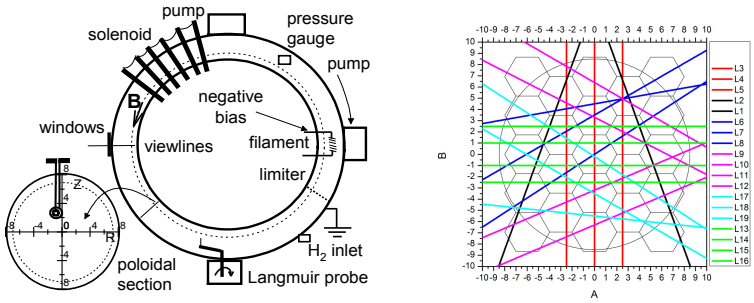

Figure 1: Left: experimental layout of the Thorello device. Right: viewline system of measurement and relation with the 2D poloidal section map of the device.

3. RESULTS AND DISCUSSION

In order to demonstrate the capabilities of the proposed diagnostics we have performed a few measurement in our magnetized plasma device. We take advantage of the steady state stable conditions of the SMT plasma. To reduce statistical uncertainty we measure three times the full set of 19 viewlines, each set with a different random order, to mitigate effects due to plasma parameters drift. Spectrometer acquisition times were optimized to each viewline, and spectra were cleaned by subtracting the relevant dark spectra (see Barni et al. 2018). The average intensity of each viewline was then evaluated, together with a statistical error. The discharge OES spectra we are discussing about were taken from plasma driven by a 70 A filament current and a 150 V cathode bias, with a magnetic field of 70 mT, starting from a 0.1 Pa pure hydrogen gas. A typical spectrum measured is shown in Figure 2. Apart from the more prominent Balmer lines, it is possible to spot the lines corresponding to the Fulcher-α diagonal bands. They are the more bright ones, at 602.0, 612.3, 622.6 and 632.9 nm [(n,n)-Q1 with n=0…3], corresponding to the transitions from subsequent excited vibrational levels of the 3c state. The reconstruction of the 2D pattern of emissivity in the SMT poloidal cross-section is then undertaken from the 19 viewline average dataset, as we have discussed in our previous works (see Barni et al. 2018). In figure3 we report the results for the first of the Fulcher-α diagonal band lines, compared with the Balmer H_α. It could be noticed that, contrary to naive expectations, the molecular line pattern is more concentrated in the central region, around the filament magnetic shadow in the poloidal cross-section.

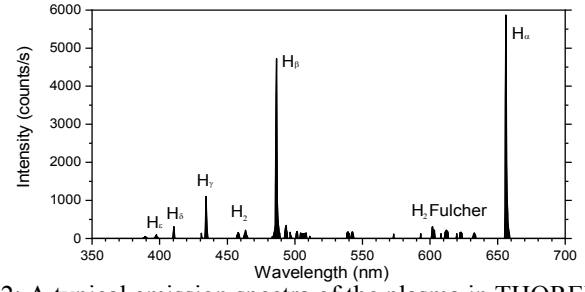

Figure 2: A typical emission spectra of the plasma in THORELLO.

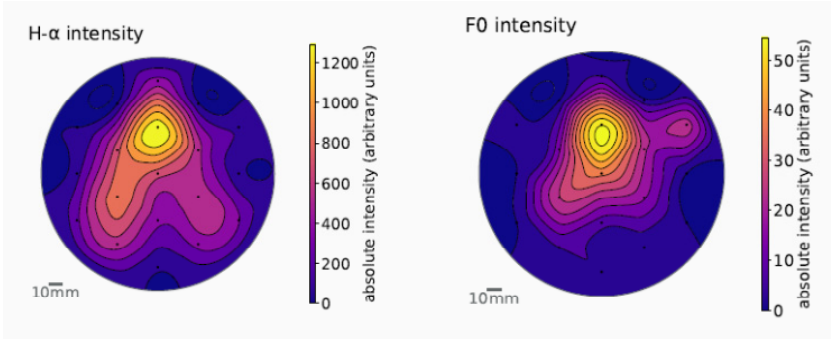

Figure 3: A reconstructed map of emissivity of the first H_2 Fulcher-α diagonal bands, compared with the Balmer H_α from the plasma.

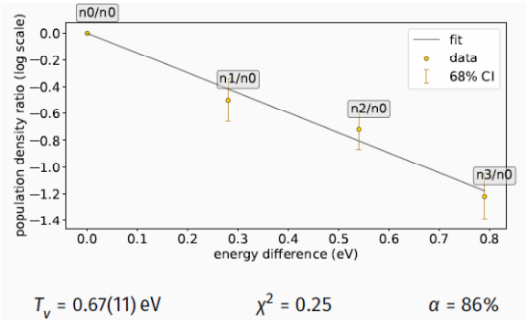

Figure 4: Extraction of the excitation temperature of the H2 3c state in the cell corresponding to the brighter spot of the plasma column.

Finally, from the reconstructed intensities of the diagonal bands, using the relevant lifetimes and branching ratios (see Fantz et al. 2006) it is possible to estimate the relative population of the first four vibrational levels of the excited H2 3c state. As it could be seen from figure 4, their distribution is roughly by a Boltzmann factor, from which it is possible to extract an effective excitation temperature or, as it sometimes referred to, a vibrational temperature, in this case T_{exc}=0.67±0.11 eV. It should be compared with a central electron temperature of 4.4 eV.

References

Aguilar, A., et al. : 2008, *Astrophys. J. Suppl. Series*, **177**, 388.
Barni, R., et al. : 2009, *Plas. Phys. Control. Fus.,* **51,** 085010.
Barni, R., et al. : 2018, *Plas. Sci. Tech.,* **20,** 025102.
Capitelli, M., et al. : 2013, *Spectr. Acta B,* **83-84,** 1.
Donnè, A.J.H. : 2006 *Plas. Phys Control. Fusion,* **48,** B483.
Dudok de Wit, T., et al. : 2013, *Space Science Review,* **178**, 665
Fantz, U., Wunderlich, D. : 2006, *Atomic Nuclear Data Table,* **92**, 853.
Pierre, T., et al. : 2004, *Phys. Rev. Lett.,* **92,** 065004.
Tynan, A., et al. : 2009, *Plas. Phys. Control. Fusion.,* **51,** 113001.
Wagner, F. : 2007, *Plas. Phys. Control. Fusio*n, **49**, B1

Publ. Astron. Obs. Belgrade No. 99 (2020), 157 - 160 *Contributed Paper*

INVESTIGATION OF A MICROSECOND-PULSED COLD PLASMA JET

N. CVETANOVIĆ[1], M. A. SHAHRIAR[2], B. M. OBRADOVIĆ[3], Z. LIU[2], K. YAN[2] and M. M. KURAICA[3]

[1]*University of Belgrade, Faculty of Transport and Traffic Engineering, 11000 Belgrade, Serbia*

E-mail nikola@ff.bg.ac.rs
[2]*Institute of Industrial Ecology and Environment, Zhejiang University, Hangzhou 310007, China*
[3]*University of Belgrade, Faculty of Physics, 11001 Belgrade, Serbia*

Abstract. This work presents initial results of studying a pulsed cold plasma jet with a fast voltage rise-time. The aim of the experiment is a spectroscopic investigation to the purpose of attaining the jet streamer space-time development and plasma parameters near the target. Results show a comparably fast streamer progression with strong electric field in the period of maximum current.

1. INTRODUCTION

In the last decade nonthermal; atmospheric pressure discharges have been adopted as the future of plasma application due to their many advantages, see for instance Fridman et al. 2008, Branderburg et al. 2019. A subtype of this type of plasma are low temperature plasma jets, usually obtained in the flow of inert gases Winter et al. 2015, Weltmann et al. 2017, Reuter et al. 2018. In a number of publications helium plasma jets are especially investigated as candidates for treatment of biomedical and other samples, see for instance Weltmann et al. 2017, Reuter et al. 2018, Yan et al. 2017, Nastuta et al. 2011, Teschner et al. 2019. They have also been studied from the standpoint of plasma characterization, both through modeling and experiment, Boeuf et al. 2013, Sretenović 2014, Winter et al. 2015.

One of such sources with and accompanying power supply has been developed at the Zhejiang University, Zheng et al. 2016, Deng et al. 2018. This cold plasma jet has so far been used for treatment of various bio-samples. It operates with a microsecond voltage pulse characterized with a fast rise-time. In this work, the primary aim was a spectroscopic investigation to the purpose of studying the jet streamer space-time development and plasma parameters near the target. Here we present only the initial results of a planned detailed study.

2. EXPERIMENT

The pulsed power supply and a dielectric barrier discharge (DBD) jet reactor are combined into a single device, Deng et al. 2018. The grounded electrode is a metal nozzle with its inner surface covered by a quartz tube, 6 mm in diameter. Inside the nozzle, at its center axis, a smaller quartz tube is placed, 4 mm in diameter. The high-voltage wire electrode is inserted in the smaller quartz tube. In this way a barrier discharge is formed between the two quartz tubes having 0.5 mm thickens. The low-temperature plasma jet then protrudes form the nozzle width the diameter of ~4 mm and length of 1-7 cm depending on the voltage. In this experiment a copper plate was used as a grounded target to increase the jet stability. The target was placed at a distance of 13.5 mm from the jet nozzle.

The electrodes are supplied by a pulsed power source with a pulse width of 0.8 μs, voltage of 2.6 kV and a repetition rate of 21 kHz. The rise time of the voltage pulse is 400 ns. Helium flow of 99.996% purity was controlled by means of a mass flow controller at rate of 3 l/min. The voltage was measured using the Tektronix P6015A high voltage probe, and current is determined from voltage drop over 200 Ω non inductive resistor connected in series with the discharge.

A quartz lens was used to project the jet image onto the entrance of the spectrometer. The overall time–space unresolved emission spectra in a wide range of 300–900 nm, was recorded using a low resolution spectrometer Ocean Optics USB4000. The spatiotemporally resolved measurements were done using the Solar MSDD 1000 spectrometer with the focal length of 1 m and the grating of 1200 grooves/mm. At the exit of the monochromathor the light was detected using the ICCD camera (PI-MAX2, Princeton Instruments) with 1024×1024 pixels. The camera was triggered using a time-delayed pulse signal, initially generated by the rising slope of the discharge voltage pulse. The delay camera triggering system enabled precise setting of the gate width and the delay time for the recording. This spectrometer system has an instrumental width FWHM=0.04 nm.

3. RESULTS

Several spectroscopic methods, typical for examining atmospheric pressure discharges, were employed in this experiment. Namely, axial distribution of various species emissions was used to examine the jet spatial structure. Helium and oxygen atomic line emission was used to examine the discharge axial development in time. By measuring the transverse light intensity distribution and applying the Abel inversion, the radial distribution of light intensity was obtained. The N_2^+ first negative system emission band was used to measure the molecule rotational temperature. Stark polarization spectroscopy of He I 492.2 nm line was used to estimate the electric field at the target.

Figure 1 shows the time-space development of He I 706 nm line. Since this line is exited via electron impact, this graph can be taken as development of the jet streamer. As can be seen, the graph shows typical features of the positive guided

streamer, Gerling et al. 2011, Sretenović et al. 2014. Specifically, one can see the bullet-like progression towards the cathode till the time of 160 ns. The streamer travels from the nozzle to the cathode target during the current rise and reaches it at the moment of current maximum. After reaching the target, a weak back-streamer is formed towards the jet nozzle. During the strong current a long-lived atmospheric pressure glow discharge above the target is formed.

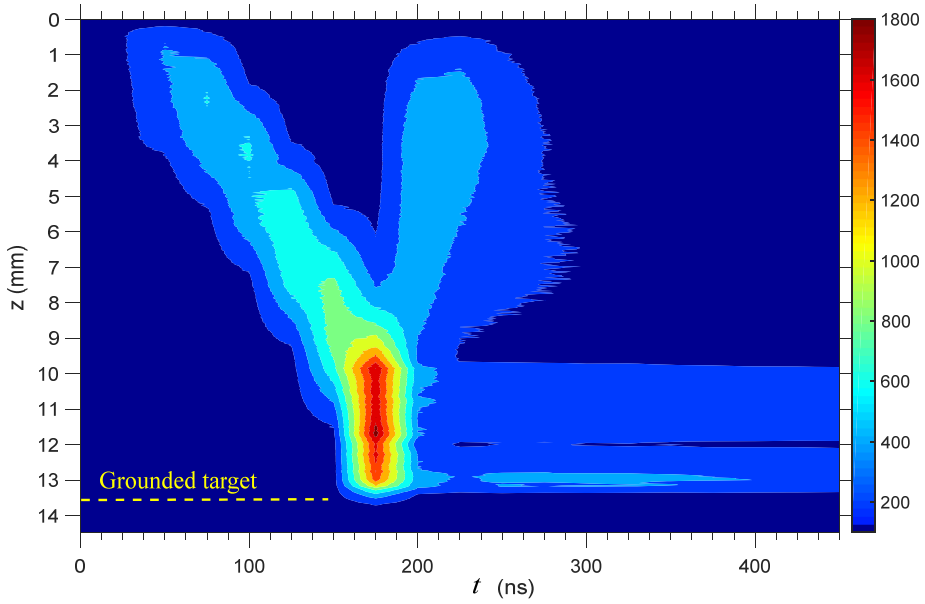

Figure 1: Contour plot of He I 706.5 nm emission, gate width 25 ns.

From the graph, the average velocity is estimated at $8.4 \cdot 10^4$ m/s which is much higher than typical jet bullet velocity, see for instance Sretenović et al. 2014, Gerling et al. 2012. This can be explained by the short rise-time of the voltage in our case. Namely, it was shown in Lu et al. 2014, that the short voltage rise-time crucially increases the streamer velocity. The velocity obtained here agrees with the trends given in the mentioned paper.

Figure 2 shows the spatial distribution of different species in the time when the streamer has reached the target and a stable atmospheric pressure discharge lasts for several hundreds of nanoseconds. The light emissions of different species show similar patterns. Especially interesting is the formation of light and dark zones, similar to the glow discharge, in the vicinity of the target. The exception to the shape of the distribution is hydrogen H_β line. It is well known that at atmospheric pressure the hydrogen Balmer lines have a delayed excitation due to the necessity of molecule dissociation and excitation from helium metastables, see Navratil et al. 2006.

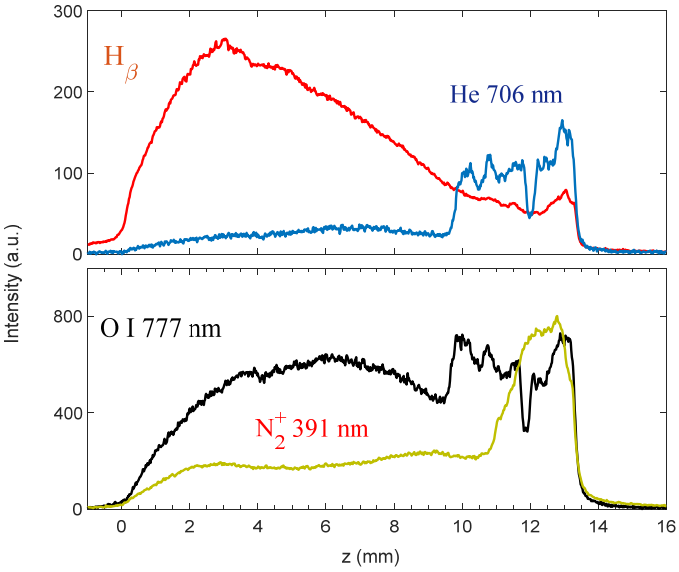

Figure 2: Axial distribution of emission from different species after *t*=200 ns.

The jet gas temperature near the target, estimated form the rotational temperature of nitrogen molecule ion was T=340±30 K. Stark spectroscopy showed interesting the features of the spectral line profile near the target. Specifically, strong electric fields ~25 kV/cm were observed, with the field inhomogeneity in the observed region.

References

Brandenburg, R., Bogaerts, A., et al., 2019, *Plasma Process Polym.,* **16** :e1700238

Fridman, G., Friedman, et al., 2008, *Plasma Process. Polym.*, **5**, 503–533.

Gerling, T., Nastuta, A. V., Bussiahn, R, Kindel, E, Weltmann, K-D, 2012, *Plasma Sources Sci. Technol.* **21** 034012

Lu, X., Naidis, G.V., Laroussi, M., Ostrikov, K., 2014, Physics Reports, **540**, 123

Navratil, Z., Brandenburg, R., Trunec, D., et al. 2006, *Plasma Sources Sci. Technol.*, **15,** 8

Nastuta, A. V., Topala I., Grigoras C., et al., 2011, *J. Phys. D: Appl. Phys.*, **44**, 105204

Reuter, S., vod Woedtke, Th, Weltmann, K-D, 2018, *J. Phys. D: Appl. Phys.*, **51** 233001

Sretenović, G.B., Krstić, B., Kovačević, V., Obradović, B. M., Kuraica, M. M., 2014, *J. Phys. D: Appl. Phys.*, **47,** 102001

Teschner, T.; Bansemer, R.; Weltmann, K.-D.; Gerling, T., 2019, *Plasma*, **2**, 348-359.

Winter, J., Brandenburg, E, Weltmann, K-D, 2015, *Plasma Sources Sci. Technol.*, **24,** 064001

Weltmann, K-D, vod Woedtke, Th, 2017, *Plasma Phys. Control. Fusion*, **59** 014031

Yan, D, Sherman, J. H., Keidar, M., 2017, *Oncotarget*, **8**, 15977.

Publ. Astron. Obs. Belgrade No. 99 (2020), 161 - 164 *Contributed Paper*

COMPARISON OF EXPERIMENTAL AND SEMI-CLASSICAL RESULTS FOR Ar II STARK BROADENING PARAMETERS FOR (^{3}P) 4s ^{2}P – (^{3}P) 4p ^{2}D^o MULTIPLET

S. DJUROVIĆ[1], B. BLAGOJEVIĆ[2] and N. KONJEVIĆ[3]

[1]*University of Novi Sad, Faculty of Sciences, Department of Physics, Trg Dositeja Obradovića 4, 21000 Novi Sad, Serbia*
E-mail djurovic@uns.ac.rs

[2]*NASA Goddard Space Flight Center, Greenbelt, MD 20771, USA*
E-mail branimir.blagojevic@nasa.gov

[3]*University of Belgrade, Faculty of Physics, Studentski trg 12, 11001 Belgrade, Serbia*
E-mail nikruz@ff.bg.ac.rs

Abstract. Comparison of experimental and calculated data for Stark broadening parameters for the Ar II 4726.87 Å, 4879.86 Å and 4965.08 Å spectral lines from multiplet (^{3}P) 4s ^{2}P – (^{3}P) 4p ^{2}D^o is presented in this work.

1. COMPARISON OF THE EXPERIMENTAL AND THEORETICAL DATA

During the testing new set of semi-classical theoretical results by Blagojević and Konjević 2017, 2020 for singly ionized non-hydrogenic atom lines, we have located set of experimental Stark shift data for Ar II multiplet 14, (the transition (^{3}P)4s ^{2}P - (^{3}P)4p ^{2}D^o) with number of experimental shifts showing similar temperature trend, see Fig.1 (data for some multiplet lines are so close that they are irresolvable in this figure). The reported shifts in Fig.1 were measured by various groups of authors using different plasma sources and plasma diagnostic techniques. The measured experimental line shifts indicate different low electron temperature trend and much smaller absolute shift values, see Fig 1. As expected, two sets of semi-classical results Blagojević and Konjević 2017 and Jones et al. 1971 for line shift and widths, see Figs.1 and 2 and Table 1, agree very well, because present calculations (in figures and Table 1 denoted with Tw) are essentially identical with Jones et al. 1971. The exception is improved numerical procedure used by Blagojević and Konjević 2017, 2020 in comparison with Jones et al. 1971. Another difference between Blagojević and Konjević 2017, 2020 and Jones et al. 1971: the

energy level data are taken mainly from Moore 1971 while transition probabilities (TP) were calculated using Coulomb approximation Bates and Damgaard 1949 method. For our calculations, Tw in Figs 1 and 2 and Table 1, both, the energy levels data and TP were taken from NIST data base using small program for automatic data acquisition.

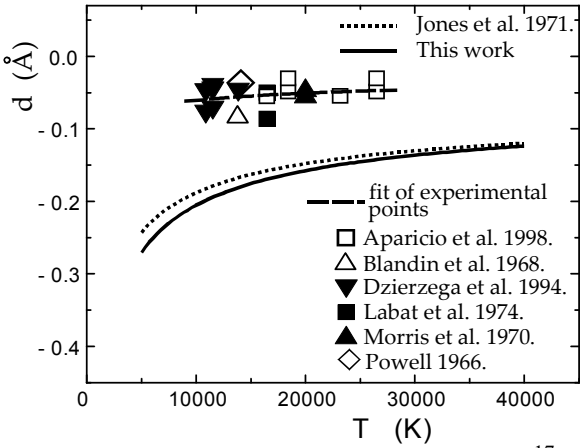

Figure 1: Stark shifts at electron density $N_e = 10^{17}$ cm^{-3} versus electron temperature.

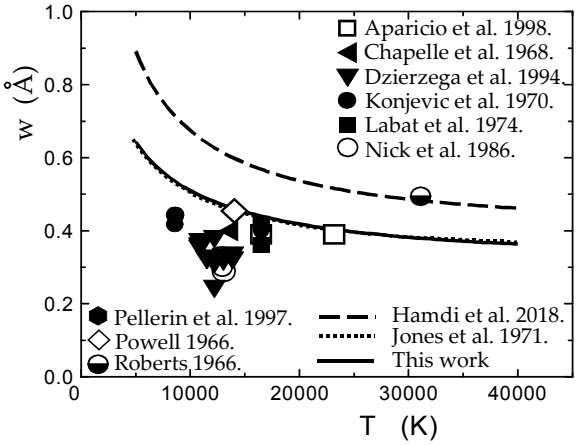

Figure 2: Stark full widths at half maximum (FWHM) at electron density $N_e = 10^{17}$ cm^{-3} versus electron temperature.

The results for Stark widths in Fig. 2 and Table 1 denoted by Hamdi et al. 2018 are calculated by another semi-classical approach while energy levels and TP

Ar II Multiplet (^{3}P) 4s ^{2}P – (^{3}P) 4p ^{2}D^o					
	Jones et al. 1971.		This work		Hamdi et al. 2018
	Mult. 4898 Å		Mult. 4898.6811 Å		Line 4879.86 Å
T (K)	*Halfwidth* (Å)	*Shift* (Å)	*Halfwidth* (Å)	*Shift* (Å)	*Halfwidth* $w_e + w_i$ (Å)
5000	0.644	- 0.243	0.645	- 0.271	0.891
10000	0.502	- 0.188	0.506	- 0.204	0.677
20000	0.416	- 0.148	0.423	- 0.1581	0.535
30000					0.485
40000	0.368	- 0.120	0.362	- 0.1231	0.464
60000			0.310	- 0.1021	0.441

Table 1: Theoretical Stark widths FWHM and shifts for electron density $N_e = 10^{17}$ cm^{-3} and temperatures in the range (5000 – 60000) K.

are calculated as well, see details in Hamdi et al. 2018. Further notes: the theoretical results in figures and table by Jones et al. 1971 and Tw are reported for the average wavelength of the multiplet 14 while results by Hamdi et al. 2018 are for the single line quoted in Table 1. The results for shifts and widths from Jones et al. 1971 and this work are electron impact values while Hamdi et al 2018 data are electron + ion impact Stark widths.

Finally, on the basis of the comparison of experimental and theoretical data for Ar II multiplet 14 one can conclude that this is rather well documented Stark shift case, which offers interesting possibility for theoretical study of electron temperature dependence and magnitude of shift values.

Acknowledgements

Djurović, S. and Konjević N. thanks for financial support of the Ministry of Education, Science and Technological Development of the Republic of Serbia (Grant No. 451-03-68 / 2020-14 / 200125).

References

Aparicio, J. A., Gigosos, M. A., Gonzalez, V. R., Perez, C., de la Rosa, M. I., Mar, S.: 1998, *J. Phys. B*, **31**, 1029.

Bates, D. R., Damgaard A.: 1949, *The calculation of the absolute strengths of spectral lines. Phil Trans R Soc Lond A242:101*.

Blagojević, B., Konjević, N.: 2017, *J. Quant. Spectrosc. Radiat. Transfer*, **198**, 9.

Blagojević, B.: 2020, *Software tools for modeling the atomic spectral line shapes of laboratory, industrial and astrophysical plasmas,* https://www.researchgate.net/publication/338864209

Blandin, J., Sahal-Bréchot, S., Chapelle, J., Sy, A.: 1968, *Phys. Lett.*, **26A**, 487.

Chapelle, J., Sy, A., Cabannes, F., Blandin, J.: 1968, *J. Quant. Spectrosc. Radiat. Transfer*, **8**, 1201.

Dzierzega, K., Musiol, K.: 1994, *J. Quant. Spectrosc. Radiat. Transfer*, **52**, 747.
Hamdi, R., Ben Nessib, N., Sahal-Bréchot, S., Dimitrijević, M. S.: 2018, *Month. Not. Roy. Astron. Soc.*, **488**, 2473.
Jones, W. W., Benett, S. M., Griem, H. R.: 1971, *Tehnical Report 71-128, University of Maryland, College Park*.
Konjević, N., Labat, J., Ćirković, Lj., Purić, J.: 1970, *Z. Phys.*, **235**, 35.
Labat, J., Djeniže, S., Ćirković, Lj., Purić, J.: 1974, *J. Phys. B*, **7**, 1174.
Morris, J. C., Morris, R. V.: 1970, *Aerospace Research Laboratories Report No. ARL 70-0038*.
Moore, C. E.: 1971, *Atomic Energy Levels*, *Vol. I, Nsrds-NBS 35*.
Nick, K. P., Helbig, V.: 1986, *Phys. Scr.*, **33**, 55.
NIST Atomic Spectroscopy Database, https://www.nist.gov/pml/atomic-spectra-database.
Osterbrock, D. E.: 1989, *Astrophysics of Gaseous Nebulae and Active Galactic Nuclei*, Mill Valley, California. S.
Pellerin, S., Musiol, K., Chapelle, J.: 1997, *J. Quant. Spectrosc. Radiat. Transfer*, **57**, 377.
Powell, W. R.: 1966, *Dissertation, John Hopkins University*.
Roberts, D. E.: 1966, *Phys. Lett.*, **22**, 417.

Publ. Astron. Obs. Belgrade No. 99 (2020), 165 - 168 *Contributed Paper*

STARK LINE BROADENING WITHIN SPECTRAL SERIES OF POTASSIUM ISOELECTRONIC SEQUENCE

IVAN P. DOJČINOVIĆ, NORA TRKLJA BOCA, IRINEL TAPALAGA and JAGOŠ PURIĆ

University of Belgrade, Faculty of Physics, P. O. Box 44, 11000 Belgrade, Serbia

Abstract. Stark line broadening within potassium-like emitters was investigated, using regularity approach. Available Stark data for ns-np, np-ns, np-nd, nd-np and nd-nf spectral series within potassium isoelectronic sequence present input data for regularity analysis. Formulas expressing Stark widths dependence on the value of the upper-level ionization potential and the rest core charge of the emitter, for analyzed spectral series have been established and can be used for calculation of Stark widths for transitions within spectral series of any potassium-like emitter.

1. INTRODUCTION

In the presented paper Stark widths of transitions within ns-np, np-ns, np-nd, nd-np and nd-nf spectral series of potassium like emitters are investigated using regularity approach.

Stark broadening data for emitters within potassium isoelectronic sequence are of great interest for astrophysics and fusion physics. For example, potassium lines are important for investigation of chemical evolution of stars; Ca II lines are used for opacity research of young stellar object; Sc III lines are present in the spectra of Am Fm stars. Ti IV and V V Stark widths data are of interest for first-wall problem in fusion physics. Data for Cr, Mn and Fe are of interest for fusion physics, too.

The ground state of K I and Ca II has [Ar]4s electronic configuration, with term ^{2}S, while Sc III, Ti IV, V V, Cr VI, Mn VII, Fe VIII,… have [Ar]3d electronic configuration of ground state, with term ^{2}D. Except this difference in configuration of ground states, all members of potassium isoelectronic sequence have similar excited states, so regularity behavior of atomic parameters within spectral series are expected. In the present research, just one-electron transition processes have been analyzed.

2. THEORETICAL BACKGROUND

The regularity approach used in present investigation is based on equation (1) (Trklja et al. 2018).

$$\omega^* = \frac{\omega}{Z_e^c} = a \cdot \log \chi^{-b} \tag{1}$$

ω^* is the reduced Stark width, χ is the electron binding energy on the upper level of analyzed transition, Z_e is the rest core charge of the emitter; $a = const \cdot N_e \cdot f(T_e)$, b is a fitting coefficient. Parameter c can be found by analyzing the quality of the fit which is determined by factor R^2 (Dojčinović et al. 2019.).

Temperature normalization is done according to equation (2) (Purić et al. 1999).

$$\omega = A + B \cdot T^{-C} \tag{2}$$

Normalization of electron density is done using the approximation of linear dependence of Stark widths on electron density which has been found as appropriate.

3. RESULTS AND DISCUSSION

Regularity analysis within potassium like emitters include 148 spectral lines: K I (46), Ca II (56), Sc III (10), Ti IV (10), V V (26). Stark width data used in the present study are taken from Stark B data base (Sachal-Brechot et al. 2018). And complemented with available experimental data of Stark widths. χ values are taken from NIST atomic database (Kramida et al. 2018). Data were complemented with available experimental data of Stark widths.

Dependence of R^2 on c for the potassium isoelectronic sequence is presented in Fig. 1. Parameter c is approximately equal to 2.8.

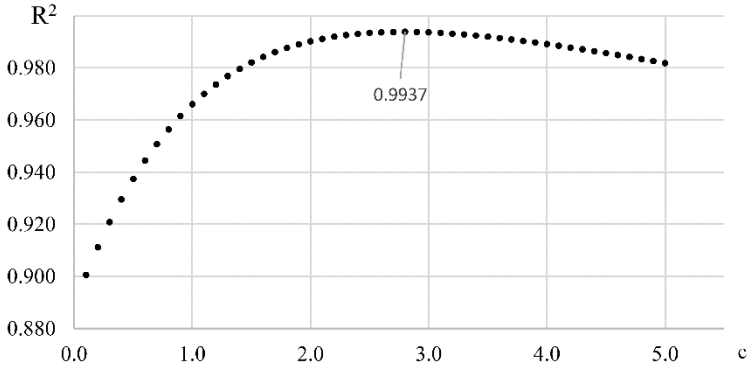

Figure 1: Determination of parameter c

All Stark widths used in the present investigation are normalized at electron density $N_e=10^{22}$ m^{-3} and temperature T=100000 K. Temperature normalization is done using parameters A, B and C (equation (2)) which are results of fitting process. Each transition has its own A, B and C parameters. As example of fitting procedure, dependence of Stark width on temperature has been presented for 4s-4p transition within K I (Fig. 2).

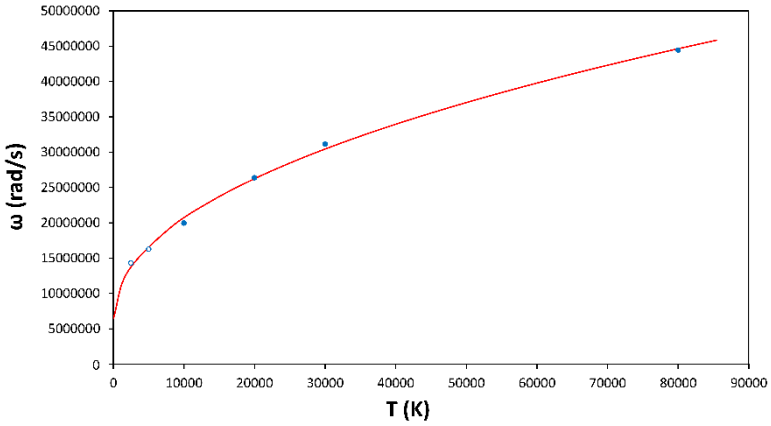

Figure 2: Stark width dependence on temperature for 4s-4p transition within K I

Fig. 3. represents dependence of the reduced Stark width on ionization potential of the upper level of transition, for np-nd spectral series of the potassium isoelectronic sequence, fitted according to equation (1).

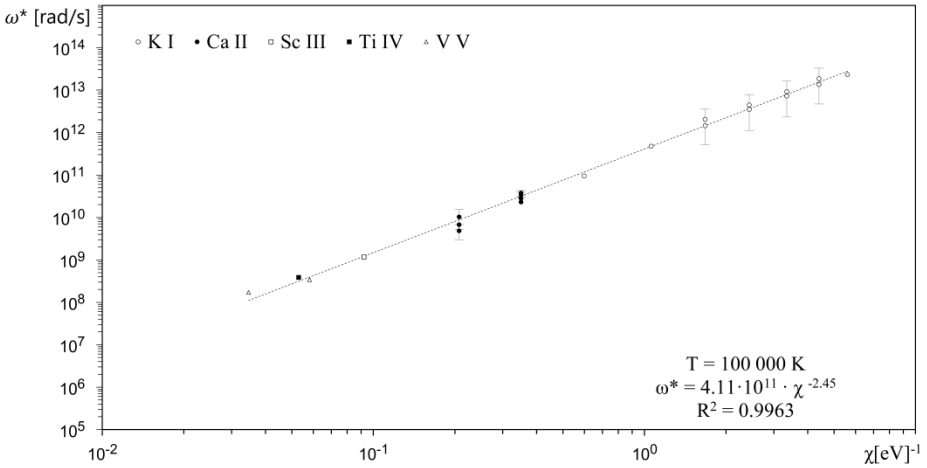

Figure 2: Dependence of ω^* on χ for the np-nd transition within potassium isoelectronic sequence ($N_e=10^{22}$ m^{-3}, T=100000 K)

According to fitting parameters, Stark widths for any transition within ns-np, np-ns, np-nd, nd-np and nd-nf spectral series of potassium isoelectronic sequence can be calculated using formula (3):

$$\Delta\lambda = p \cdot 10^{-20} \cdot \frac{Z_e^{2.8} N_e}{\chi^q} \lambda^2 \qquad (3)$$

Values of parameters p and q are given in Table 1. In equation (3) λ and Δλ are expressed in [m], N_e is expressed in [m^{-3}] and χ is expressed in [eV].

Spectral Series	p	q
ns-np	2.00	2.39
np-ns	1.87	2.39
np-nd	4.11	2.45
nd-np	3.87	2.34
nd-nf	3.61	2.54

Table 1: Values of parameters p and q in equation (3) for analyzed spectral series

4. CONCLUSIONS

Results of presented regularity analysis enable calculation of Stark widths for any transitions within ns-np, np-ns, np-nd, nd-np and nd-nf spectral series of the potassium isoelectronic sequence. Calculation of Stark widths of potassium-like ions is of interest for astrophysics and plasma physics.

References

Dojčinović, I.P., Trklja, N., Tapalaga, I., Purić, J. : 2019*, MNRAS*, **489**, 2997

Kramida, A., Ralchenko, Yu., Reader, J., and NIST ASD Team, *NIST* Atomic Spectra Database (ver. 5.5.6), [Online]. Available: https://physics.nist.gov/asd [2018, Jun 27]. National Institute of Standards and Technology, Gaithersburg, MD.

Sahal-Brechot, S., Dimitrijević, M.S., Moreau, N. : 2018. STARK-B database, [online]. Available: http://stark-b.obspm.fr [February 14, 2018]. Observatory of Paris, LERMA and Astronomical Observatory of Belgrade

Trklja, N., Tapalaga, I., Dojčinović, I.P., Purić, J. : 2018*, New Astron.*, **59**, 54

Publ. Astron. Obs. Belgrade No. 99 (2020), 169 - 172 *Contributed Paper*

THE ELECTRON NUMBER DENSITY MEASUREMENT FROM PULSED NEEDLE-TO-CYLINDER GAS DISCHARGE SOURCE AT ATMOSPHERIC PRESSURE IN HELIUM

J. JOVOVIĆ

University of Belgrade, Faculty of Physics, Studentski trg 12-16, P.O Box 44, Belgrade, Serbia
E-mail jjovica@ff.bg.ac.rs

Abstract. The novel atmospheric pressure gas discharge source is constructed. The source is driven by pulsed power generator in pure helium. The electron number density N_e=(0.55±0.11) × 10^{15} cm^{-3} is measured by means of He I 447.2 nm line fitting procedure. The similar N_e results are obtained from He I 492.2 nm line using the same diagnostics procedure. However, the N_e measured from the hydrogen Balmer H_β line is three times lower, probably due to the H I emission from the outer discharge region. In case of plasma-water drop interaction, analyzing the H_β line, N_e=0.55 × 10^{15} cm^{-3} is obtained at the beginning of treatment. During the water drop treatment, the spectrum of Fe I lines as a consequence of oxides formation on the cathode surface, is recorded as well.

1. INTRODUCTION

The He I spectral lines originating from a matrix gas are previously used for N_e diagnostics purposes (Jovović and Šišović 2015, Jovović and Konjević 2014). Due to the presence of an electric field induced by quasistatic ions, the He I 447.1 nm and He I 492.2 nm lines are asymmetrically broadened in atmospheric pressure glow discharge source (Jovović and Šišović 2015). Near the cathode wall, the He I red wing asymmetry is even more pronounced, which is the consequence of a strong DC electric field. The diagnostics procedure based on fitting the He I lines (see Jovović and Šišović 2015), is applied here as well for the characterization of novel atmospheric pressure gas discharge source. Additionally, the fitting of the H_β line is performed and the N_e results discussed.

The novel gas discharge source operating in helium (99.999 %) comprises stainless steel cathode (C) and graphite anode (A), see Figure 1. The source is driven by homemade pulsed voltage generator (2-999 μs pulse width, 0.1 % - 100 % duty cycle). The discharge gap and gas flow were 2 mm and 0.45 l/min, respectively. The optical emission spectroscopy (OES) is performed using Ebert type spectrometer (focal length 2 m, reflection grating 651 grooves/mm, dispersion

0.74 nm/mm) and TE cooled CCD camera (2048 × 506 pixels, pixel size 12 × 12 μm).

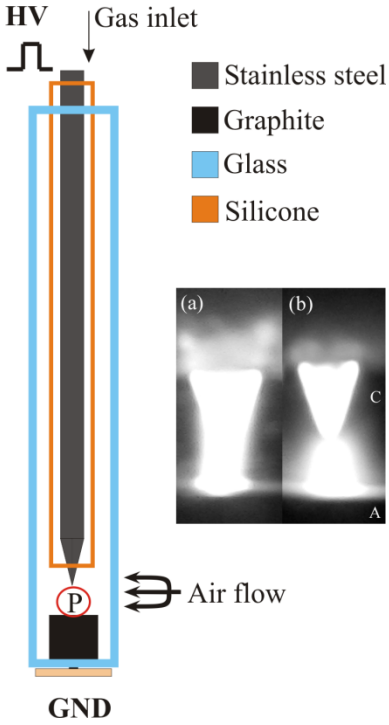

Figure 1: The cross-section of atmospheric pressure gas discharge source. The photos of discharge burning in pulsed (a) and DC regime (b) are given in the inset (C – cathode, A – anode).

2. RESULTS AND DISCUSSION

The 2D contour plots showing the spatial distribution of the H_β line and He I 447.2 nm line recorded by means of the CCD camera area scanning mode are shown in Figure 2. One may notice that in the pulsed regime, both near cathode region and plasma column exist. In the region near cathode, the broadening of both studied lines are evident, see the upper part of Figure 2. The best fit of the H_β line and He I 447.2 nm line, emitted from the plasma column, are presented in Figure 3. The experimental conditions are given in figure captions. The N_e values obtained as a result of the fitting procedure are the following: $(0.16\pm0.03) \times 10^{15}$ cm^{-3} (H_β), $(0.55\pm0.11) \times 10^{15}$ cm^{-3} (He I 447.2 nm) and $(0.48\pm0.1) \times 10^{15}$ cm^{-3} (He I 492.2 nm). The 3 times lower N_e is measured from the H_β line probably due to the H I emission from the outer discharge region.

In the frame of this study, we tested the possibility of using needle-to-cylinder plasma source for decomposition of small volume liquid samples. Hence, the distillated water drop (volume of 0.013 – 0.02 ml) placed on the top of anode was used. Interestingly, $N_e = (0.55\pm0.11) \times 10^{15}$ cm^{-3} is measured from the H_β but

exclusively at the beginning of plasma-water treatment (0-35 s). It is a time period when the water vapor partial pressure is significant in the discharge gap P and H I lines emitted from the central plasma region. In the same time period, Fe I lines originating from the cathode material are present in the spectrum, see e.g Figure 4. At the end of plasma-water treatment, $N_e \sim (0.16 \pm 0.03) \times 10^{15}$ cm^{-3} is measured and Fe I lines vanish from the spectrum. Concerning the N_e determined after the analysis of He I lines, no significant change is detected.

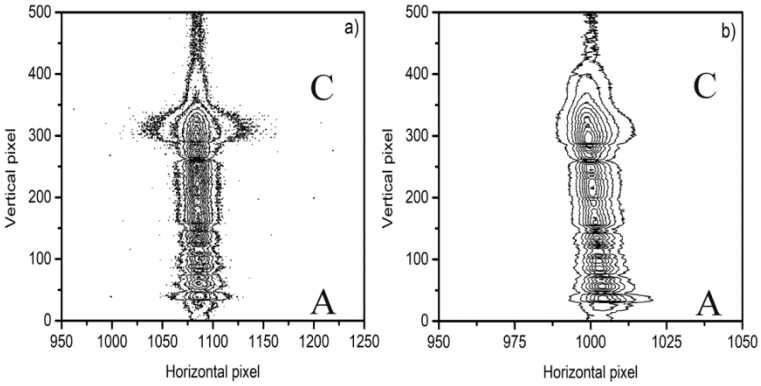

Figure 2: The H_β line (a) and He I 447.2 nm line (b) recorded in the pulsed regime using the imaging mode of CCD camera. Experimental conditions: pulse width 800 μs, duty cycle of 5 %, *I*=20 mA, *U*=435 V.

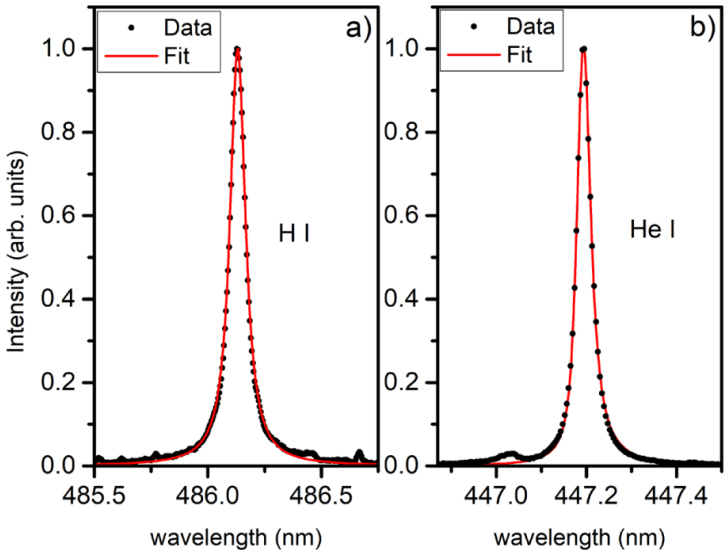

Figure 3: The best fit of the H_β line (a) and He I 447.2 nm line (b), both recorded in the second order of diffraction grating. Experimental conditions: pulse width 800 μs, duty cycle of 5 %, gap 2 mm, *I*=20 mA, *U*=434 V.

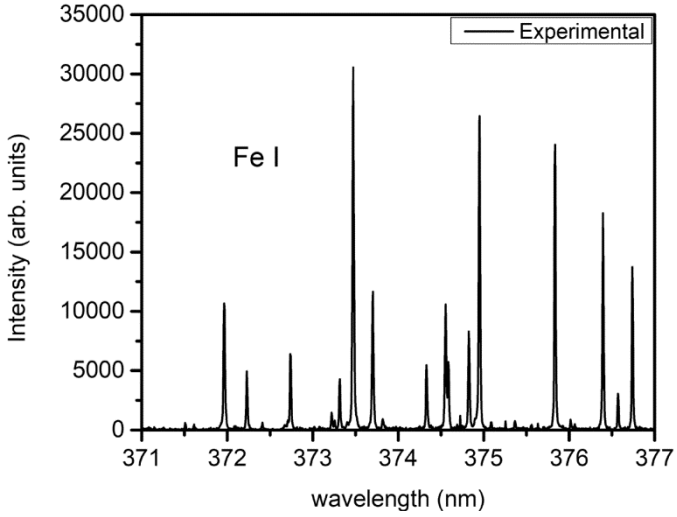

Figure 4: The spectrum of Fe I lines in the range 371-377 nm (*I*=20 mA, pulse width 800 μs). The diffraction grating operated in the second diffraction order.

The tentative explanation for the presence of Fe atoms in plasma is related to the formation of iron-oxide layers on the cathode surface during the plasma–water interaction. The potential application of the presented needle-to cylinder atmospheric pressure gas discharge source operating in pulsed regime is foreseen for the analytical study of conductive liquid samples. In addition, the spectra of cathode material may be used for plasma diagnostics purposes as well. The knowledge of plasma science, fluid dynamics, heat and mass transfer, photolysis, multiphase chemistry, etc., is required for the full understanding of plasma-liquid interaction (Vanraes and Bogaerts 2018).

Acknowledgement

This work is supported by the Ministry of Education, Science and Technological Development of the Republic of Serbia (Project No. 171014).

References

Jovović, J., Konjević, N. : 2004*, Eur. Phys. J. D*, **68**, 60.
Jovović, J., Šišović, N. M. : 2015, *J. Phys. D: Appl. Phys.*, **48**, 365202.
Vanraes, P., Bogaerts, A. : 2018, *Appl. Phys. Rev.*, **5**, 031103

Publ. Astron. Obs. Belgrade No. 99 (2020), 173 - 176 *Contributed Paper*

DIAGNOSTICS OF PLASMA PRODUCED BY LASER ABLATION OF CARBON-BASED POLYMER MATERIAL

M. KUZMANOVIC[1], D. RANKOVIC[1], J. SAVOVIC[2], V. KIRIS[3], A. NEVAR[3], M. NEDELKO[3] and N. TARASENKO[3]

[1]*Faculty of Physical Chemistry, University of Belgrade, Studentski trg 12-16, 11000 Belgrade, Serbia*
E-mail miroslav@ffh.bg.ac.rs

[2]*Department of Physical Chemistry, VINCA Institute of Nuclear Sciences - National Institute of the Republic of Serbia, University of Belgrade, Mike Alasa 12-14, 11001 Belgrade, Serbia*
E-mail lelas@vin.bg.ac.rs

[3]*B. I. Stepanov Institute of Physics, National Academy of Sciences of Belarus, 68-2 Nezavisimost' Ave., Minsk, 220072, Belarus*
E-mail yavasya@yandex.ru

Abstract. Carbon-based polymer materials such as fluoroplastic (Teflon) are commonly used as the inert substrate in laser-induced breakdown spectroscopy (LIBS) analysis of dry residues of liquid samples whether they are inorganic, organic or biological materials. Alongside the emission of analyte atoms, the induced plasma often involves the emission from the substrate material. Strong atomic and ionic carbon lines as well as C_2 and CN molecular bands emitted from Teflon plasma are suitable for plasma diagnostics. In this work, optical emission spectroscopy of TEA CO_2 laser-induced plasma on a Teflon target was applied for the estimation of plasma parameters, temperature, and electron number density. Estimated plasma parameters may be used to correct shot-to-shot variations of the measured intensities of analyte emission.

1. INTRODUCTION

Applications of LIBS for quantitative analysis of liquid solutions are still challenging and suffer from low sensitivity and poor repeatability of measurements. One of the available methods for improvement of analytical performance is to convert liquid to a solid matrix, for example by depositing micro-drops of analyte solutions on a substrate and drying. Commonly, inert material is chosen as a substrate in order to reduce a portion of the laser energy that is spent on substrate vaporization, i.e. to ensure that the induced plasma mainly involves the deposited material. Carbon-based polymer materials such as Teflon are often used

for this purpose: see De Giacomo et al. 2016. Teflon molecules contain only carbon and fluorine and because of the low excitation efficiency of fluorine, the spectral contribution from the substrate is practically limited to carbon. In case the LIBS analysis is carried out in the ambience air, along with carbon atomic and ionic lines molecular bands of diatomic species such as CN and C_2 could be registered in the plasma. In this work, emission from the laser-induced Teflon plasma was utilized for diagnostics of plasma, i.e. estimation of plasma temperature and electron number density. Estimated plasma parameters may be used for correction of the measured intensities of analyte lines whose variations are caused by fluctuations of signal intensities (shot-to-shot variations).

2. EXPERIMENTAL

The experimental setup was based on the Transversely Excited Atmospheric pressure carbon dioxide (TEA CO_2) laser. The laser simultaneously operates at two wavelengths, 10.5709 and 10.5909 μm, with pulse repetition rate up to 2 Hz, in a multimode regime. Laser pulse has initial peak (~100 ns) followed by a decaying tail (~2 μs), with approximately 35% of total pulse energy in the initial spike. The laser beam was focused by ZnSe lens on the target. In most measurements, the laser pulse energy of 150 mJ was used and the beam was focused 5 mm in front of the target. The corresponding fluence and intensity were 10 J/cm^2 and 35 MW/cm^2, respectively. Image of plasma was projected on the entrance slit of a Carl Zeiss PGS2 spectrograph by an achromatic quartz lens. Spatially resolved measurements were provided by moving the target along the laser beam direction. Spectral emission was time-integrated using a scientific grade deep cooled CCD camera, with high quantum efficiency in the UV and VIS spectral region. A Czerny Turner spectrograph was equipped with two plane reflective diffraction gratings with 650 rules/mm blazed at 330 and 590 nm. Linear dispersion in the first spectral order was about 0.7 nm/mm, and the FWHM of the instrumental profile was 0.027 nm for the entrance slit of 25 μm. For the applied spectral dispersion, spectral region captured by a CCD was about 9 nm.

3. RESULTS AND DISCUSSION

When the TEA CO_2 laser beam was focused on the Teflon target surface reproducible plasma could not be obtained even with the highest attainable laser pulse energy of 170 mJ. On the contrary, spectrochemically usable plasma was obtained by focusing the laser beam 5 mm in front of the target. In that case the threshold energy for plasma creation on the Teflon was 130 mJ. Teflon plasma emits strong atomic and ionic carbon lines and C_2 and CN molecular bands, suitable for plasma diagnostics.

The electron number density was determined from Stark width of carbon ionic C II 283.67 nm line. Figure 1a shows the profiles of C II spectral lines obtained using laser pulse energy of 150 mJ focused 5 mm in front of the Teflon target, emitted from a part of the plasma 1 mm from the target surface. The estimated

electron number density was in the range $1.9 \cdot 10^{17}$ to $9.4 \cdot 10^{17}$ cm^{-3}, depending on the plasma observation zone (1 to 3 mm from the target). The carbon lines, C II 250.91 nm and C I 247.86 nm (Figure 1b) were used for determination of the ionization temperature using the ion-to-atom spectral line integral intensities ratios. The estimated plasma temperature was in the range of 16500 K (0.9 mm) to 20500 K (0.3 mm).

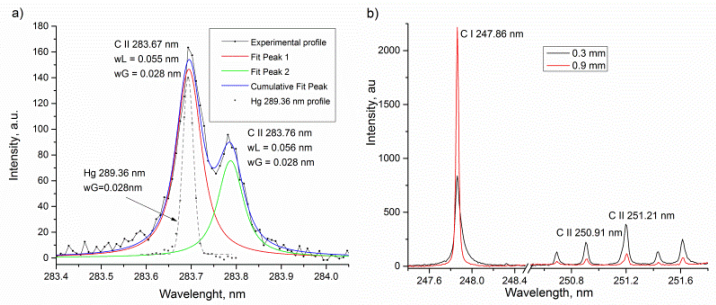

Figure 1: (a) Profile of C II 283.67 nm line used for determination of n_e; (b) Part of LIBS spectra recorded at 0.3 and 0.9 mm from target surface.

The emission spectra of C_2 and CN molecules were used for determination of the rotational (T_{rot}) and vibrational (T_{vib}) temperatures, by comparing the experimentally obtained and synthetic molecular spectra. Because of high dissociation energy of these molecules, relatively low excitation energy of the first excited electronic state, and the favorable value of the transition probabilities their emission intensities are high and suitable for plasma diagnostics: see Kuzmanovic et al. 2019. The emission of the Swan system of C_2 molecules could be obtained only from the plasma region close to the target surface, Figure 2.

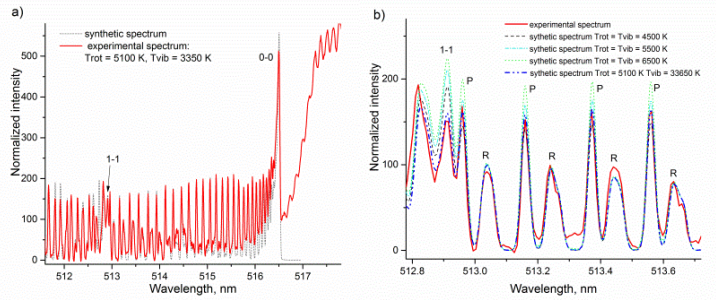

Figure 2: (a) Part of spectrum of sequence $\Delta v=0$ of C_2 Swan system. The spectrum was recorded at a distance of 0.3 mm from the target; (b) the P and R components of the 0-0 band spectrum.

On the contrary, the intensive emission of the $\Delta v = 0$ sequence of B-X violet system of CN molecule could be detected at distances up to 2 mm from the target surface, Figure 3. This is understandable as the CN molecule is formed by the reaction of carbon ablated from the target and nitrogen from the air.

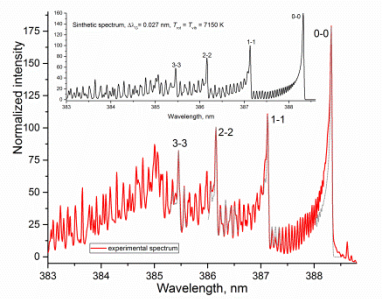

Figure 3: The spectrum of Δv=0 sequence of CN B-X violet system. Laser pulse energy 150 mJ, laser beam focused 5 mm in front of the target. The spectrum was recorded from a slice of plasma parallel to the target, at a distance of 0.3 mm from the target.

From the C_2 spectra, the best matching was obtained for T_{vib} = 3350 K, and the T_{rot} = 5100 K, while from the CN bands, T_{rot} = T_{vib} = 7150 K. The most intense band of the CN violet system showed strong self-absorption and led to overestimated temperature values.

4. CONCLUSIONS

Diagnostics of the TEA CO_2 laser induced Teflon plasma was performed using the emission spectroscopy. The plasma parameters, electron density and temperature, were estimated using emission spectra of neutral and singly charged carbon atoms. Depending on the plasma observation zone, the electron number density and temperature were in the range $1.9 \cdot 10^{17}$ to $9.4 \cdot 10^{17}$ cm^{-3}, and 16500 to 20500 K, respectively. Additional information was obtained from the rotational-vibrational structure of C_2 and CN band intensities. The most intense bands of C_2 emission spectra had more distinct band heads and a better resolved rotational structure than bands of CN violet system, thus, they were more convenient for determination of temperature.

Acknowledgements: The research was funded by the Ministry of Education, Science and Technological Development of the Republic of Serbia (contract no. 451-03-68/2020-14/200146; 451-03-68/2020-14/200017). The Belarusian authors acknowledge the financial support of the Belarusian Foundation for Fundamental Researches under Grant No. BRFFR F20SRBG-001.

References

De Giacomo, A., Koral, C., Valenza, G., Gaudiuso, R., Dell'Aglio, M.: 2016, *Anal. Chem.*, **88**, 5251.

Kuzmanovic, M., Rankovic, D., Trtica, M., Ciganovic, J., Petrovic, J., Savovic, J. : 2019, *Spectrochim. Acta* B, **157**, 37.

Publ. Astron. Obs. Belgrade No. 99 (2020), 177 - 180 *Contributed Paper*

RADIAL DISTRIBUTION OF PLASMA ELECTRON DENSITY AND TEMPERATURE IN ATMOSPHERIC PLASMA JET

Z. MIJATOVIĆ, S. DJUROVIĆ, I. SAVIĆ, L. GAVANSKI and T. GAJO

University of Novi Sad, Department of Physics, Faculty of Sciences,
Trg Dositeja Obradovića 4, Novi Sad, Serbia
E-mail mijat@uns.ac.rs

Abstract. Radial distribution of plasma electron density and temperature of atmospheric argon plasma jet were measured by applying spectroscopic method.

1. INTRODUCTION

Various methods can be applied for plasma jets formation. One of them is based on electrical arc, see for example Snyder et al.1994. Such kinds of jets are used for welding, cutting and coating. They usually work in DC regime with high electrical current (up to 1000 A) and high gas flow (several tens of l/min). At the exit of such sources the plasma temperature can reach 20000 K while the electron density can be around 10^{23} m^{-3}. In this work a DC wall stabilized electrical arc is used. High current pulses were added to the DC current that caused the formation of plasma jet at the exit of the arc column. In this paper results of measurements of plasma electron temperature and electron density along the plasma jet radius are presented.

2. EXPERIMENTAL

Wall stabilized arc working in DC regime is used in this experiment. Argon under atmospheric pressure was the working gas. The Ar gas flow was around 20 l/min. The operating DC current through the arc was 32 A. High current pulses were added to the DC current, so the maximal total current in pulses was 180 A and lasted 4 ms. The pulses were obtained by using civil network and a proper electronic circuit. The frequency of the pulses was 1 Hz. The detailed description of this arrangement can be found in Djurovic et al. 2012 and Gajo et al. 2013.

During high current pulses the plasma jet appeared at the exit of the arc column on the side of the anode. The jet spread into free air through the hole in the anode. The jet was observed side-on close to the exit (about 1 mm from the anode). Radiation from the jet was focused on the entrance slit of 1m-monochromator with 1200 g/mm diffraction grating. At the exit of the monchromator ICCD camera was

placed for spectral line recordings. Image of the plasma jet taken with ICCD is presented in Figure 1. Approximate dimension of the plasma jet is 20 mm in length and 5 mm in diameter close to the arc exit. Spectral recordings were made at the maximum of current pulses about 1 mm far from the arc anode. This is also illustrated in Figure 1.

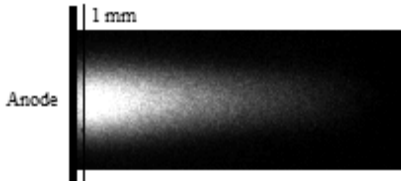

Figure 1: Plasma jet and position of recordings.

The determination of plasma electron densities and temperatures along the radius of the plasma jet was done by applying spectroscopic methods. For plasma electron temperature the Boltzmann plot method was applied using Ar I 415.8, 425.9, 427.2. 430.0, 470.2, 696.5 and 706.7 nm spectral lines. Plasma electron densities were determined from Stark widths of Ar I 430.0 nm spectral line based on theory Griem 1974 with application of correction given in Nikolić 1998. All spectral lines were recorded at 36 positions along the jet diameter. This enabled the application of the Abel inversion procedure. After this procedure these lines were used for plasma diagnostics. Boltzmann plot used for plasma electron temperature determination at the axis of the jet is presented in Figure 2. Example of the recorded profile of Ar I 430.0 nm line, after the Abel inversion procedure, is presented in Figure 3. Estimated errors for temperatures are below 20 %, while for plasma electron densities are below 15 %.

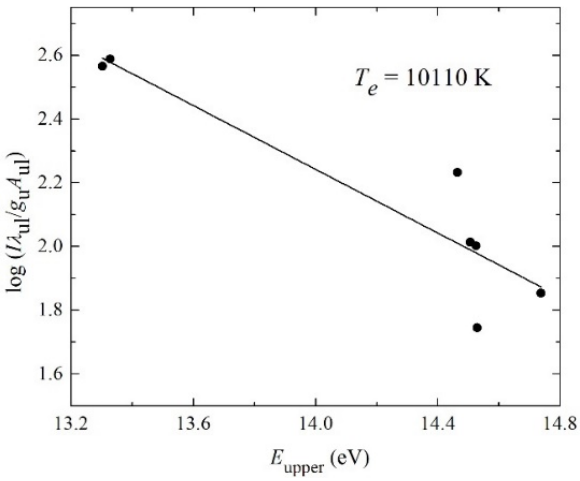

Figure 2: Boltzmann plot using seven Ar I spectral lines.

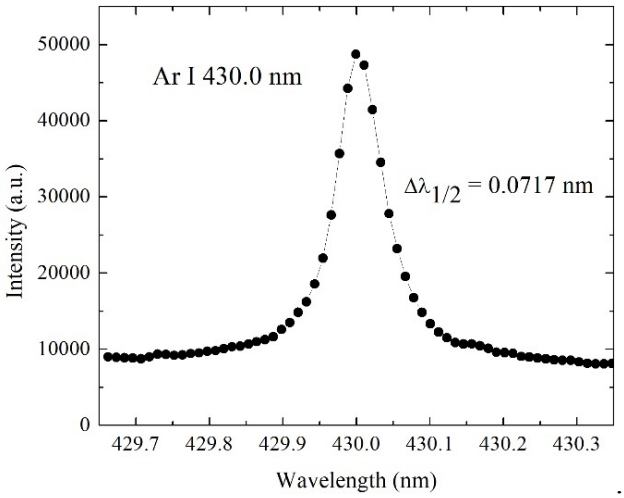

Figure 3: Example of Ar 430.0nm line.

3. RESULTS

Figures 4 and 5 show the distribution of plasma electron temperature and plasma electron density along the radius of the plasma jet at axial position 1 mm far from the exit of the anode.

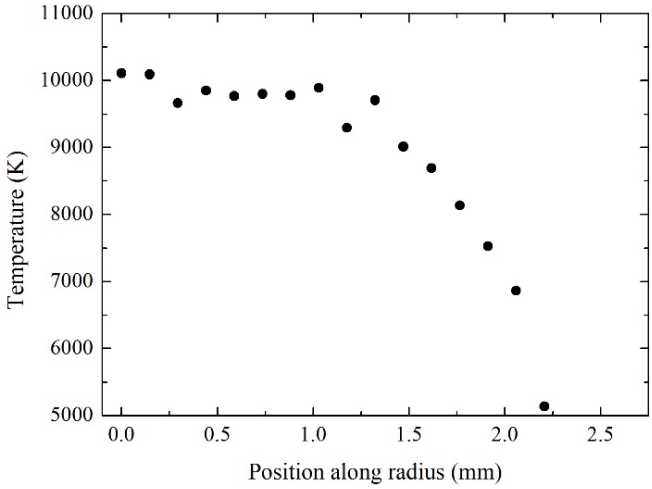

Figure 4: Radial distribution of plasma temperature.

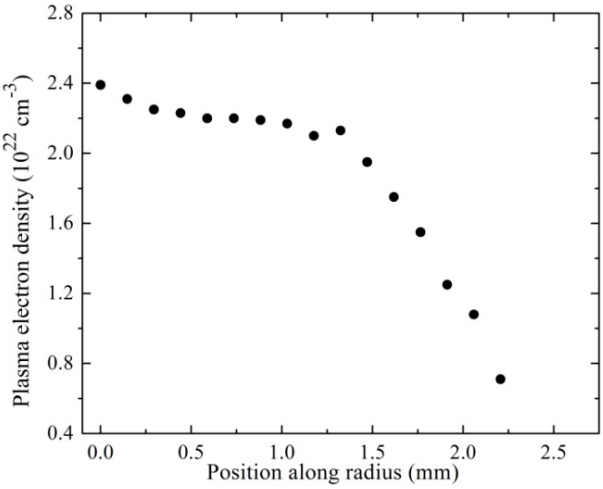

Figure 5: Radial distribution of plasma electron density.

As it can be expected, maximum values of plasma temperature and electron density are around the axis. The temperature profile at around 2 mm from the axis is close to 10000 K. This fact shows that this plasma region, with high plasma temperature, can be used for various plasma applications, like melting materials, powders for coating, plasma reactions, etc. From the comparisons with the values of plasma electron densities and temperatures obtained in Snyder et al. 1994 it can be concluded that they are in reasonable accordance.

Acknowledgement

The coauthors acknowledge financial support of the Ministry of Education, Science and Technological Development of the Republic of Serbia (Grant No. 451-03-68/2020-14/200125).

References

Djurović, S., Mijatović, Z., Kobilarov, R., Savić, I.: 2012, *Plasma Sources Sci. Technol.*, **21**, 1–9 025007.

Gajo, T., Mijatović, Z., Savić, I., Djurović, S., Kobilarov, R.: 2013, *J. Quant. Spectrosc Radiat. Transf.*, **127**, 119.

Griem, H. R.: 1974, *Spectral Line Broadening by Plasmas*, Academic Press, New York.

Nikolić, D.: 1998, *Influence of Plasma Temperature on Argon Spectral Linesw Shape and Shifts*, M. A. Thesis, Faculty of Physics, University of Belrade.

Snyder, S. C., Reynolds, L. D., Fincke, J. R., Lassahn, G. D., Grandy, J. D., Repetti, T. E.: 1994, *Phys. Rev. E*, **50**, 519.

Publ. Astron. Obs. Belgrade No. 99 (2020), 181 - 184 *Contributed Paper*

MEASUREMENT OF ELECTRIC FIELD DISTRIBUTION ALONG THE CATHODE SHEATH OF AN ABNORMAL GLOW DISCHARGE USING Ne I 556.277 nm LINE

N. V. NEDIĆ[1], N. V. IVANOVIĆ[2], Dj. SPASOJEVIĆ[1] and N. KONJEVIĆ[1]

[1]*University of Belgrade, Faculty of Physics, 11001 Belgrade, P.O. Box 44, Serbia*

[2]*University of Belgrade, Faculty of Agriculture, Nemanjina 6, 11080 Belgrade, Serbia*

Abstract. We present the results of an experimental study of the DC Stark shift of the Ne I 556.277 nm line in the cathode sheath region of an abnormal glow discharge in neon with traces of hydrogen. The electric field (of up to 13.4 kV cm^{-1}) is measured in the cathode sheath regionfrom the π-polarized profile of the hydrogen Balmer H_α line using the Stark polarization optical spectroscopy technique. The Ne I 556.277 nm line exhibits a quadratic Stark effect and the values of the coefficients, correlating its Stark shift and electric field strength, were determined. The results are in good agreement with the best-fit formula proposed by Jäger and Windholz indicating in this way that this spectral line can be used for the measurement of electric field strength in the cathode sheath region of an abnormal glow discharges with neon.

1. INTRODUCTION

Investigations of the DC Stark effect of neutral neon lines are numerous and a comprehensive review of relevant publications until 1976 were reported in Ryde (1976). Since then, several authors continued experimental (Jäger and Windholz 1984, Windholz and Neureiter 1988, Jäger et al. 1989) and theoretical (Ziegelbecker and Schnizer 1987) studies of Ne I lines in visible and near UV spectral regions at different electric field strengths, *E*. Recently, Ne I Stark effect studies have been directed towards lower *E* values in experiments carried out in the cathode sheath (CS) region of the Grimm-type glow discharge (GD), using optical emission spectroscopy (OES) with a CCD for spectral lines recording (Majstorović et al. 2013, Šišović et al. 2014). The Stark shift of the studied Ne I line has to be precisely measured in discharge with the distribution of *E* measured by other means (e.g. here from the Stark shifts of the hydrogen Balmer H_α spectral line). In this work, the axial distribution of *E* in the CS is determined in an abnormal glow discharge operated in neon with a small admixture of hydrogen using OES and the Lo-Surdo technique (Ryde 1976, Majstorović et al. 2013) applied to the Ne I 556.277 nm spectral line. The results are compared with those obtained using the

Ne I 520.390 nm spectral line, demonstrated in Ivanović et al. (2017) to be reliable for the measurement of electric field strength.

2. EXPERIMENTAL

In our study, a gas mixture of neon and 0.8% hydrogen is used as the working gas. A modified glow discharge source was laboratory-made after the Ferreira et al. design (Ferreira et al. 1980) described in detail elsewhere (Majstorović et al. 2013, Šišović et al. 2014, Kuraica et al. 1992). Hollow anode (30 mm long with 8 mm inner diameter) has a longitudinal slot (16 mm long and 1.5 mm wide) that serves for side-on observations along the discharge axis. The water-cooled cathode holder has a wolfram electrode (18 mm long and 7.40 mm in diameter) tightly screwed into its holder to ensure good cooling.

Spectroscopic observations of the so-called Grimm GD were performed side-on through an anode slit in translation steps of approximately 1/16 mm. For the H_α experiments, the radiation from the discharge was polarized by a polarizer before entering the spectrometer.

The radiation from the discharge is focused with an achromatic lens (focal length 75.8 mm with unity magnification) through the polarizer onto the 20 μm entrance slit (height restriction 2 mm) of the 2 m focal length Ebert-type spectrometer with 651 g mm^{-1} reflection grating blazed at 1050 nm. For the line shape measurements, the reciprocal dispersion of 0.37 nm mm^{-1} is used throughout this experiment. All spectral measurements were performed with an instrumental profile very close to a Gaussian with the measured full width at half maximum (FWHM) of 8.2 pm in the second diffraction order. Signals from the CCD detector (1 x 3648 pixels, 8 μm pixel width) are collected and processed by a PC.

3. RESULTS

The distribution of the electric field strength in CS region was determined from the π-polarized H_α line profiles by the method explained in (Ivanović et al. 2017).

In Figure 1, we show the profile of the spectral line Ne I 556.277 nm observed at five different axial positions along the discharge axis. The spectral line shapes, recorded in CS region at four distances *d* from the cathode surface, are shown in panels a)–d), and the line shape recorded in the negative glow, panel e).

On the blue and red wings of the examined spectral line, there are two spectral lines, Ne I 556.244 nm and Ne I 556.305 nm, which behave similarly to the Ne I 556.277 nm line in the presence of the electric field. Their relative intensity is low and they have not been analyzed.

The Stark shifts of the Ne I 556.277 nm line were measured relative to the unshifted peak of the W I 370.792 nm line whose profile from the third diffraction order appears in the recorded spectra near the profiles of the studied Ne lines from the second diffraction order, see Figure 1. In the fitting procedure of the experimental Ne I 556.277 nm spectral line profiles,we employed the model function:

$$\mathrm{I}_{\mathrm{mod}}(\Delta\lambda;\Gamma)=\Im*\left[G\left(\Delta\lambda;H_{Ne},c_{Ne},w_{Ne}\right)+G\left(\Delta\lambda;H_{W},c_{W},w_{W}\right)\right]+b \tag{1}$$

where $\Delta\lambda$ is the wavelength shift from the line center, Γ stands for the list $\{H_{Ne},c_{Ne},w_{Ne},H_{W},c_{W},w_{W}\}$ of the model function fitting parameters, and b is the baseline level. The model function (1) is a sum of two Gaussians:

$$G(\Delta\lambda;H,c,w)=H\exp\left[-\left(2\sqrt{\ln 2}\,\frac{\Delta\lambda}{w}\right)^{2}\right], \tag{2}$$

each specified by height H, center c, and FWHM w. In (1),* denotes the convolution with the instrumental profile $\Im$:

$$\Im=\frac{2}{w_{\mathrm{inst}}}\sqrt{\frac{\ln 2}{\pi}}\exp\left[-\left(2\sqrt{\ln 2}\,\frac{\Delta\lambda}{w_{\mathrm{inst}}}\right)^{2}\right] \tag{3}$$

which is in our case the unit-area Gaussianof w_{inst}= 8.2 pm FWHM.

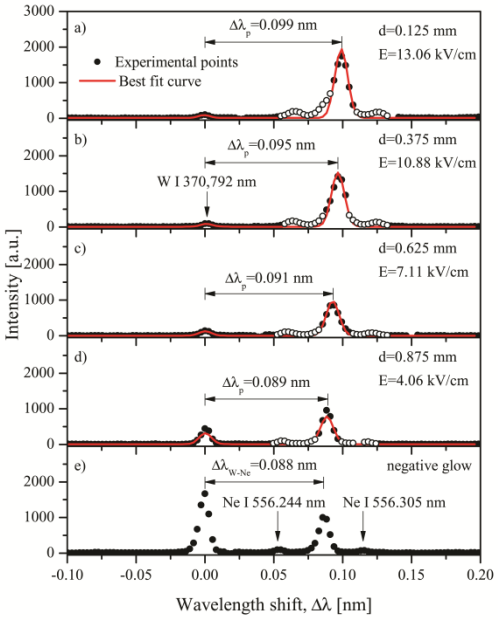

Figure 1: Experimental profiles of the Ne I 556.277 nm spectral line (dots) and their best-fit (red) curves obtained by the model function (1). Hollow experimental points were discarded in the fitting process.

The Stark shifts determined with the foregoing numerical procedure are presented in Figure 2. Our results, depicted by hollow points and red solid line, show reasonable agreement with Jäger and Windholz's prediction for the Ne I 556.277 nm line. The red solid line was obtained by the equation (4) given in Jäger and Windholz (1984), which in the case of small electric fields reduces to Ivanović et al. (2017).

$$\Delta\lambda=-\lambda_{0}^{2}CE^{2}\ , \tag{4}$$

where is $\lambda_0 = 556.277$ nm and $C = -0.0021$ kV^{-2}cm.

The Ne I 556.277 nm spectral line of neon was also observed in the cathode sheath region of an abnormal glow discharge with pure neon. Figure 3. shows the distributions of the CS electric field strength in the pure neon discharge obtained from observed profiles of the Ne I 556.277 nm and Ne I 520.390 nm spectral lines.

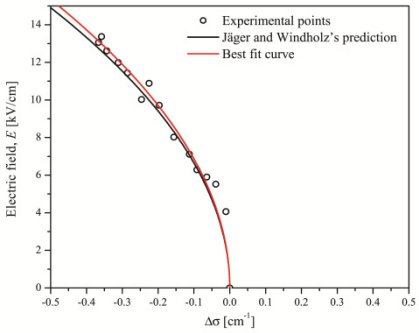

Figure 2: Dependence of the electric field strength E on the Stark shift of the wavenumber $\Delta\sigma$ for the Ne I 556.277 nm spectral line.

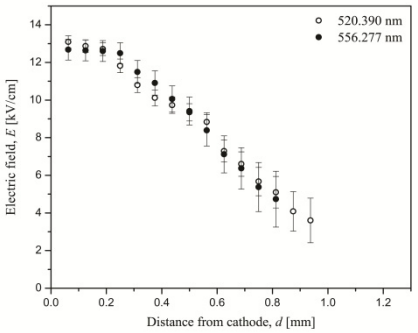

Figure 3. Comparison of the distribution of electric field strength E obtained from observations of Ne I 520.390 nm and Ne I 556.277 nm spectral lines.

4. CONCLUSION

In this work, we showed that the Ne I 556.277 nm spectral line, so far not investigated in our laboratory, is a good candidate for spectroscopic determination of the electric field strength in the cathode sheath region of an abnormal glow discharges with neon. This research expanded the list of the studied Ne I spectral lines, which can be used for reliable electric field strength measurements.

Acknowledgments

This work is supported by the Ministry of Education, Science and Technological Development of the Republic of Serbia (Grant No. 451-03-68 / 2020-14 / 200125).

References

Ferreira N P, Human H G C and Butler L R P 1980 *Spectrochim. Acta Part B* **35** 287

Ivanović N V, Šišović N M, Spasojević Dj and Konjević N (2017), *J. Phys. D: Appl. Phys*.**50**, 125201

Jäger H and Windholz L 1984 *Phys. Scr.* **29** 344

Jäger H, Windholz L and Ziegelbecker R Ch 1989 *Phys. Scr.* **40** 740–4

Kuraica M, Konjević N, Platiša M and Pantelić D 1992 *Spectrochim. Acta Part B* **47**

Majstorović G Lj, Ivanović N V, Šišović N M, Djurović S and Konjević N 2013 *Plasma Sources Sci. Technol.* **22** 045015

Ryde N 1976 *Atoms and Molecules in Electric Fields* (Stockholm: Almqvist & Wiksell)

Šišović N M, Ivanović N V, Majstorović G Lj and Konjević N 2014 *J. Anal. At.Spectrom.***29** 2058–63

Windholz L and Neureiter C 1988 *Phys Rev.* A **37** 1978

Ziegelbecker R Ch and Schnizer B 1987 *Z. Phys.* D **6** 327–35

Publ. Astron. Obs. Belgrade No. 99 (2020), 185 - 188 *Contributed Paper*

LIBS TECHNIQUE BASED ON TEA CO_2 LASER FOR ELEMENTAL ANALYSIS OF IMPURITIES IN GRAPHITE

J. PETROVIC[1*], M. KUZMANOVIC[2], D. RANKOVIC[2], M. TRTICA[1] and J. SAVOVIC[1]

[1]*Department of Physical Chemistry, VINCA Institute of Nuclear Sciences - National Institute of the Republic of Serbia, University of Belgrade, Mike Alasa 12-14, 11001 Belgrade, Serbia*
E-mail jpetrovic@vin.bg.ac.rs

[2]*Faculty of Physical Chemistry, University of Belgrade, Studentski trg 12-16, 11158 Belgrade, 118, PAC 105305, Serbia*

Abstract. Optical emission spectroscopy investigation of plasma induced in air at atmospheric pressure by a transversely excited atmospheric carbon dioxide laser (TEA CO_2) on a pressed graphite (with soil as impurity) target is presented. Despite the softness of the sample, bright and voluminous plasma was obtained, with intensive and well defined spectral emission of atomic and single charge ionic lines of elements contained in the target material. Strong molecular emission bands of CN and C_2 were recorded as well. Good signal to noise ratio provided low values of limits of detection (LODs) for metal elements; in the range of 10 to 100 ppm. Plasma temperature was estimated using a Boltzmann plot method (Fe I and Fe II lines) and rotational structure of the 0-0 band of CN violet system. The obtained temperatures characterize the plasma zones where maximal emission of iron atomic and ionic lines (8200 and 13800 K, respectively), and CN molecular bands (6200 K) could be expected.

1. INTRODUCTION

Laser induced breakdown spectroscopy (LIBS) is a popular analytical technique for rapid and sensitive analysis of most elements, including the ones with low atomic number. Some of the advantages of LIBS are minimal destructiveness and sample preparation, possibility of surface and depth profiling of the chemical composition, remote analysis. A typical LIBS system uses a robust and compact nanosecond Nd:YAG laser, with pulse energy usually less than 200 mJ. However, CO_2 gas lasers were also successfully applied for LIBS analysis of various sample types, with some advantages like eyesight safety and transparency in the air atmosphere. Graphite is very important material in modern technology and there is an interest for rapid and sensitive elemental analysis of its impurities that are usually in the

form of the soil aluminosilicate. In this work, applicability of the LIBS system based on TEA CO_2 laser with low pulse energy, for elemental analysis of pelleted graphite samples was demonstrated.

2. EXPERIMENTAL

A compact, laboratory made IR gas laser was applied to create plasma on pressed graphite sample. The maximal pulse energy of laser was 160 mJ (in multimode), with a cross section of the focused beam of 0.015 cm^2, providing maximal fluence and peak intensity of 10.7 J/cm^2 and 37 MW/cm^2, respectively. The initial peak of the laser pulse contains approximately 35% of total energy (full width at half maximum of 100 ns), followed by a 2 μs long tail. Samples for LIBS analysis were obtained as follows: spectrochemical pure graphite powder was carefully mixed with a powder sample of soil of known composition, and then pelleted under a pressure of 10 tons per cm^2, for 30 min.

Optimal condition to obtain the best signal to noise ratio for metal elements lines was: laser beam focused 5 mm behind the target and plasma observation zone of 1 mm from the target surface. Instead, commonly used time-gated detection, an alternative detection technique was applied; plasma image of the selected plasma slice was focused on the entrance slit of a Cherny-Turner spectrograph (2 m) and recorded in a time-integrated regime using back thinned CCD detector (Apogee Alta F1007).

3. RESULTS AND DISCUSSION

Graphite and coal samples have high absorption in mid-IR spectral range, thus, it was possible to obtain analytically usable plasma and spectral emission by focusing the laser behind the target. The recorded spectra consist of narrow lines with favorable signal to background ratio, without usually very broad O and N lines from air. LODs were estimated as the concentration of analyte that gives a signal that is equal to three times standard deviation of the background intensity. By taking into account known concentration of the elements in graphite pastille, we derived minimal detectable concentration for several elements: Fe II 9.2 ppm, Fe I 67 ppm, Ti I 90 ppm, Ti II 70 ppm, Mn II 10.5 ppm, Mg II 4.5 ppm and Si I 22 ppm. Additionally, improvement of detectability could be obtained by optimization of the experimental conditions and by selecting the optimal spectral line for each element. As an example of typical spectra, spectral intervals containing Fe I and Fe II lines are shown in Figure 1.

Integral intensities of iron spectral lines (Figure 1) were used for Boltzmann plot method, i.e. for estimation of the excitation temperature. As shown in Figure 2a, the estimated temperature was 8200 ± 400 K. Temperature derived from iron ionic lines (Figure 2b) was 13800 ± 500 K. Considering that time-integrated spectral intensities of a plasma slice parallel to the target surface were detected, it is clear that ionic and atomic lines were emitted from different plasma zones and at different time interval during plasma temporal evolution. However, knowledge of

these temperatures is important for estimating the excitation conditions for the observed element and its spectral line, as well as for comparing the line intensities of different elements.

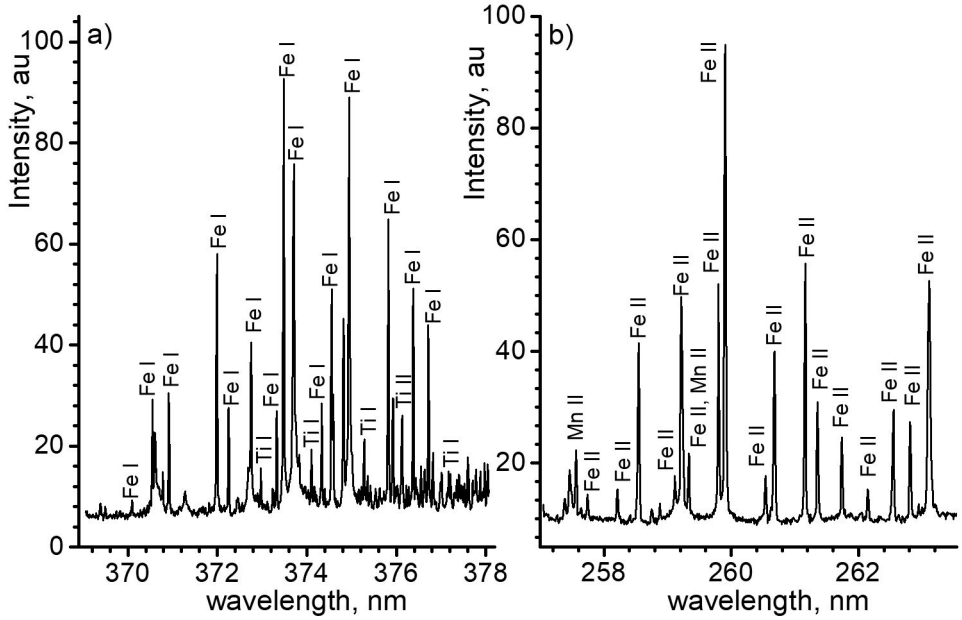

Figure 1: Example of LIBS spectra of pressed graphite with 5% soil.

CN bands of violet system have strong emission even for lower carbon concentration in plasma, especially the 0-0 band. That's why this band could be used for determination of low level carbon content in samples. In case of high carbon concentration in plasma, this band suffers from self-absorption that also reduces its applicability for rotation temperature determination (close to gas temperature). For moderate spectral resolution, rotational structure of 0-0 CN band is unresolved and cannot be used for rotational temperature estimation. In this work, temperature determination by using part of 0-0 band near 1-1 band head, obtained with higher spectral resolution (0.0052 nm FWHM of instrumental profile): as is shown in figure 2b) was demonstrated. The intensity ratios of adjacent components of P and R branches are very temperature sensitive. On the other hand, these rotational components have much lower intensities than band heads, and they are much less perturbed by self-absorption. Experimental and synthetic spectra are normalized with intensities of R components and then fitted to obtain best matching. Best fitting was obtained for T_{rot} = 6200 K, and this result is independent on T_{vib}. The difference in the intensity of the 1-1 band head could be the consequence of two different effects: self-absorption of experimental spectrum and lower value of T_{vib} in comparison with T_{rot}.

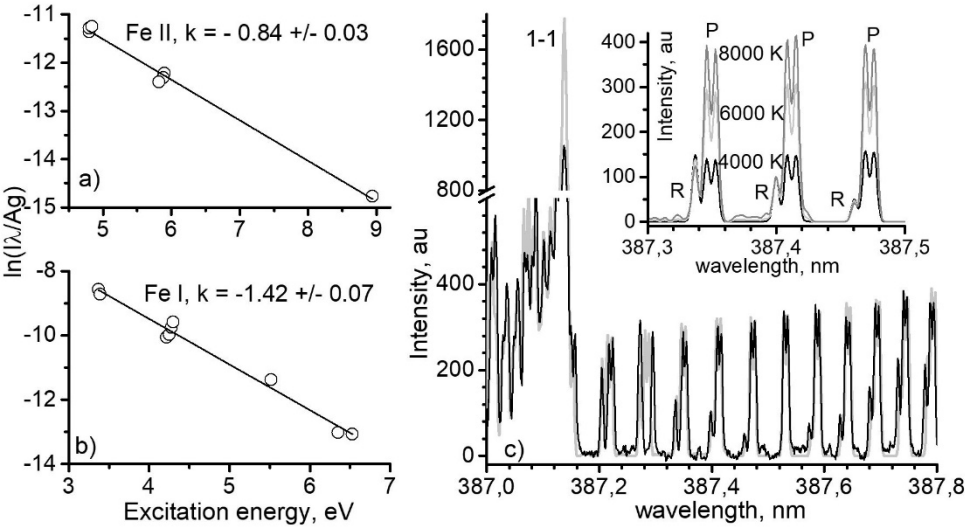

Figure 2: a) and b) Boltzmann plot of ionic and atomic iron lines; c) part of high resolution spectra of 0-0 and 1-1 bands of CN violet system. Grey curve represents a synthetic spectra for $T_{rot} = T_{vib} = 6200$ K. Small graph in figure c) illustrates temperature sensitivity of rotational components of CN band.

4. CONCLUSION

Optical spectroscopy investigation of plasma induced by TEA CO_2 laser on the graphite target was performed to check the applicability of the LIBS technique for elemental chemical analysis of graphite impurities. Low LOD values (in the range of 10 – 100 ppm) were obtained for metal elements from the soil. Plasma temperatures were estimated using a Boltzmann plot method and by analysing CN emission spectral bands. The obtained temperatures are related to the optimal emission zones of different species: 13800 and 8200 K for ionic and atomic emission of iron, and 6200 K for CN molecular emission.

Acknowledgements: The research was funded by the Ministry of Education, Science and Technological Development of the Republic of Serbia (contract numbers: 451-03-68/2020-14/200146; 451-03-68/2020-14/200017).

References

Kuzmanović, M., Ranković, D., Trtica, M., Ciganović, J., Petrović, J., Savović, J.: 2019, *Spectrochim. Acta*, **157B**, 37.

Luque, J., Crosley, D. R.: 1999, *SRI Int. Rep. MP*, **99**, 9.

Savović, J., Stoiljković, M., Kuzmanović, M., Momčilović, M., Ciganović, J., Ranković, D., Živković, S., Trtica, M.: 2016, *Spectrochim. Acta*, **118B**, 127.

Publ. Astron. Obs. Belgrade No. 99 (2020), 189 - 192 *Contributed Paper*

ACCURATE CALCULATIONS OF ENERGY LEVELS AND LIFETIMES OF HE-LIKE OXYGEN

D. E. SALHI[1] and H. JELASSI[1]

[1] *Laboratory on Energy and Matter for Nuclear Sciences Development, LR16CNSTN02, National Centre for Nuclear Sciences and Technologies, Sidi Thabet Technopark, 2020 Ariana, Tunisia*
E–mail salhidhiaelhak@gmail.com

Abstract. Energy levels and lifetimes are calculated for all levels of $1s^2$ and 1snl ($n = 2-8$) configurations of He-like oxygen ion. Multiconfigurational-Dirac-Hartree-Fock (MCDHF) method is adopted for calculating these spectroscopic data. Comparisons are made with similar data obtained with FAC (Flexible Atomic Code) to assess the accuracy of the results. Comparisons were made with the available data in the literature and good agreement was found which confirms the reliability of our results.

1. INTRODUCTION

In the last few years, various theoretical and experimental research for providing atomic data for He-like ions have been carried out. Some data are available at the National Institute of Standards and Technology (NIST) database (see Kramida et al. 2019). In this work, we treat the case of the ion He-like oxygen. This work is a continuous work on the investigation of He-like ions (see Salhi et al., 2017ab, 2019ab).

For our calculations of energy levels and lifetimes, we have adopted the Multiconfigurational-Dirac-Hartree-Fock (MCDHF) method (see Jönsson et al. 2013). Further relativistic corrections arising from the Breit interaction and QED effects have also been included. Additionally, in order to make a rigorous accuracy assessment of our results, we have also performed calculations by the code Flexible Atomic Code (FAC) of Gu (2008). This is also a fully relativistic code which can provide a variety of atomic parameters.

2. RESULTS AND DISCUSSIONS

2. 1. ENERGY LEVELS

The calculated energy levels of $1s^2$, $1s2l$, $1s3l$, $1s4l$, $1s5l$, $1s6l$, $1s7l$ and $1s8l$ configurations for the He-like oxygen generate up to 127 levels. These calculations are performed by means of two codes GRASP2K and FAC. All the calculated energy levels have been compared with the results found in the NIST database (see Kramida et al. 2019). This agreement is shown in Fig. 1. The average difference between the MCDHF/RCI values generated by the code GRASP2K and the NIST values is 0.03% for the states listed in the NIST database while the average difference between

the calculated MBPT values generated by the code FAC and NIST database level energies is 0.04%. Another comparisons were made with a theoretical work (GRASP, FAC mentionned in the Fig. 1.) see Aggarwal et al. 2008, another one with the work see Delahaye et al. 2002 (SS in the Fig. 1.) and the last one with the work of Savukov see Savukov et al. 2003.

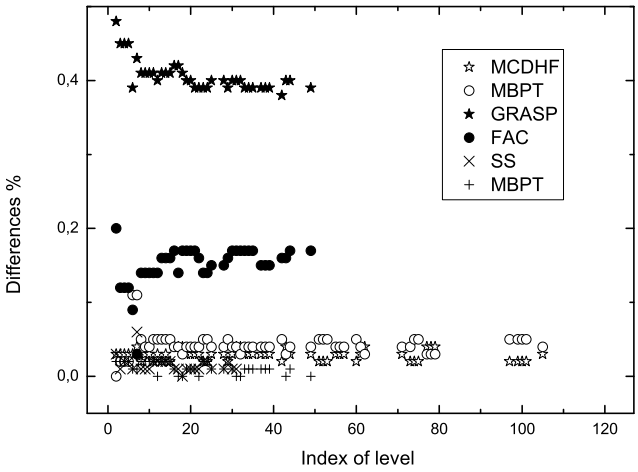

Figure 1: Comparison of our calculated energy levels MCDHF and MBPT data with data of other authors: GRASP and FAC (see Aggarwal et al. 2008), SS (see Delahaye et al. 2002) and MBPT (see Savukov et al. 2003).

Since some of energy levels are not available on NIST, our energy levels of $O\ VII$ from our both methods should be adopted in modelling applications. We may state that overall there is no discrepancy between our results and the other works.

2. 2. LIFETIMES

The lifetime τ for a level j is defined as follows

$$\tau_j = \frac{1}{\sum_i A_{ji}} \tag{1}$$

For brevity, we present in Table 1 the lifetimes of levels up to $n = 4$ calculated by the GRASP2K and FAC codes, which include the contributions from four types of transitions: $E1$, $E2$, $M1$ and $M2$. The two columns (MCDHF/RCI and MBPT) show our work of the calculation for the lifetimes. Just a large difference is found mainly in the level $1s\,3s\ ^3S_1$ with the value published in the NIST database ($(6.5 \pm 0.6)\ 10^{-11} s^{-1}$). However, for the others values the difference is minor.

Index	Configuration	MCDHF/RCI	MBPT	NIST
1	$1s^2\ ^1S_0$			
2	$1s\,2s\ ^3S_1$	1.000E-03		
3	$1s\,2p\ ^3P^o_0$	1.263E-08	1.205E-08	
4	$1s\,2p\ ^3P^o_1$	1.594E-09	1.928E-09	
5	$1s\,2p\ ^3P^o_2$	1.220E-08	1.164E-08	
6	$1s\,2s\ ^1S_0$	3.192E-01	2.231E-02	
7	$1s\,2p\ ^1P^o_1$	3.027E-13	2.926E-13	
8	$1s\,3s\ ^3S_1$	4.453E-11	4.640E-11	(6.5 ± 0.6)E-11
9	$1s\,3p\ ^3P^o_0$	1.888E-11	1.914E-11	(1.92 ± 0.2)E-11
10	$1s\,3p\ ^3P^o_1$	1.883E-11	1.909E-11	(1.92 ± 0.2)E-11
11	$1s\,3p\ ^3P^o_2$	1.892E-11	1.919E-11	(1.92 ± 0.2)E-11
12	$1s\,3s\ ^1S_0$	4.874E-11	4.820E-11	
13	$1s\,3d\ ^3D_1$	6.197E-12	6.180E-12	(7.0 ± 2.0)E-12
14	$1s\,3d\ ^3D_2$	6.203E-12	6.183E-12	(7.0 ± 2.0)E-12
15	$1s\,3d\ ^3D_3$	6.201E-12	6.183E-12	(7.0 ± 2.0)E-12
16	$1s\,3d\ ^1D_2$	6.554E-12	6.550E-12	(8.0 ± 1.5)E-12
17	$1s\,3p\ ^1P^o_1$	1.007E-12	9.561E-13	
18	$1s\,4s\ ^3S_1$	6.747E-11	7.411E-11	
19	$1s\,4p\ ^3P^o_0$	3.203E-11	3.325E-11	(3.12 ± 0.2)E-11
20	$1s\,4p\ ^3P^o_1$	3.197E-11	3.316E-11	(3.12 ± 0.2)E-11
21	$1s\,4p\ ^3P^o_2$	3.209E-11	3.331E-11	(3.12 ± 0.2)E-11
22	$1s\,4s\ ^1S_0$	6.939E-11	6.656E-11	
23	$1s\,4d\ ^3D_1$	1.433E-11	1.435E-11	(1.6 ± 0.15)E-11
24	$1s\,4d\ ^3D_2$	1.434E-11	1.436E-11	(1.6 ± 0.15)E-11
25	$1s\,4d\ ^3D_3$	1.434E-11	1.436E-11	(1.6 ± 0.15)E-11
26	$1s\,4f\ ^3F^o_3$	3.016E-11	3.015E-11	
27	$1s\,4f\ ^3F^o_2$	3.014E-11	3.013E-11	
28	$1s\,4d\ ^1D_2$	1.537E-11	1.528E-11	(1.62 ± 0.15)E-11
29	$1s\,4f\ ^3F^o_4$	3.015E-11	3.014E-11	
30	$1s\,4f\ ^1F^o_3$	3.018E-11	3.018E-11	
31	$1s\,4p\ ^1P^o_1$	2.346E-12	2.208E-12	

Table 1: Lifetimes (τ in s^{-1}) for the lowest 31 levels arising from the $1s^2$ and 1snl with $n = 2 - 4$ configurations of O VII. Two calculations are performed using GRASP2K and FAC codes and compared with other results from the NIST database.

We hope that the present extended results will be useful for future comparisons and may encourage experimentalists to measure their lifetimes.

3. CONCLUSION

In the present study, fine structure energy levels and lifetimes for He-like oxygen are presented. We calculate also the weighted oscillator strengths and transition probabilities but for brevity on the presentation of results, we restrict in this study the presentation of results for energy levels and lifetimes and the other data will be published elsewhere. The self-consistent field approximation and the Breit interaction

Hamiltonian as well as QED effects have been included in the calculations to improve the generated wave functions. The calculated energy levels and lifetimes show a good agreement with other published results from the literature. The present data sets are believed to be the most comprehensive and accurate ones to date for $O\ VII$. The accuracy of the present calculations is high enough to facilitate identification of many observed spectral lines. They are also useful for modeling and diagnosing a variety of plasmas including astronomical and fusion plasma.

References

Aggarwal K. M., Keenan F. P. : 2008, *Astronomy and Astrophysics* **489** 1377-1388.
Delahaye, F., Pradhan, A. K. : 2002 *J. Phys. B* **35** 3377.
Gu, M. F. : 2008, *Canadian Journal of Physics* **86** 5.
Jönsson, P., Gaigalas, G., Bieron, J., Froese Fischer, C., Grant, I. P., : 2013, *Computer Physics Communications* **184** 2197.
Kramida, A., Ralchenko, Yu., Reader, J. and NIST ASD Team (2019) : NIST Atomic Spectra Database. Available : [Online] https://physics.nist.gov/asd
Salhi, D. E., Jelassi, H. : 2017a, *Canadian Journal of Physics* **96**, 3.
Salhi, D. E., Jelassi, H. : 2017b, *Orient. J. Phys. Sciences.* **2** 2.
Salhi, D. E., Jelassi, H. : 2019a, *Atomic Data and Nuclear Data Tables* **126**, 70-157.
Salhi, D. E., Jelassi, H. : 2019b, *Atomic Data and Nuclear Data Tables* **129-130** 101279.
Savukov, I. M., Johnson, W. R., Safranova, U. I. : 2003 *Atomic Data and Nuclear Data Tables* **85** 83.

Publ. Astron. Obs. Belgrade No. 99 (2020), 193 - 196 *Contributed Paper*

TEMPERATURE RELAXATION PROCESS AND EXPANSION OF LASER INDUCED PLASMA

MILOS SKOCIC, DEJAN DOJIC AND SRDJAN BUKVIC

University of Belgrade, Faculty of Physics, Studentski trg 12, 11001 Belgrade, Serbia
E–mail skocic@ff.bg.ac.rs

Abstract. We present results obtained from the hybrid particle-LTE simulation developed by Skocic and Bukvic, 2016. Simulation is conducted for pulsed nanosecond 532 nm Nd-YAG laser for the copper target placed in vacuum. Initial number density of the plasma and temperatures are set to $n_p \approx 1.3 \cdot 10^{27}$ m^{-3}, $T_e \approx 70000$ K, and $T_h \approx 8000$ K, respectively.

Presented results deal with initial moments of LIP temperature relaxation process, with an emphasis on the first couple of nanoseconds. Results indicate that plasma is in thermal equilibrium just after 1 ns for the given initial conditions. Thus, plasma temperature after 1 ns is about $T \approx 55000$ K. After 40 ns number of copper ions and atoms is the same, while after that moment neutral atoms are the most abundant species. Energy transfer to heavy particle is intensive, especially in the first 40 ns.

1. INTRODUCTION

This paper considers energy transfers in plasma created with the interaction of high power nanosecond laser with a metal target. When the target is illuminated by the laser pulse free electrons in metal absorb electromagnetic radiation and immediately transfer energy to the lattice, since the relaxation time for this process is only 10^{-13}s. Due to large amount of absorbed energy, metal melts and evaporates in the surrounding space for the duration of the laser pulse. Temperature of the evaporated material is sufficiently high and provides initial ionization of the vapor while inverse bremsstrahlung ensures direct absorbtion of the laser energy during the remaining time of the laser pulse (Bogaerts et al. 2003, Itina et al. 2002). Electrons lose energy gained from the laser in the excitation and ionization processes as well as in elastic collisions with ions and atoms. After the laser pulse is finished the main process is cooling of the plasma due to fast expansion.

The aim of this paper is to study relaxation of electrons and heavy particles temperature in the early time of plasma lifetime and effects of energy transfer from ionization potential energy and electron kinetic energy on expansion velocity (center of mass velocity) of Laser Induced Plasma (LIP) in later stages of plasma expansion. All results are obtained from the modified simulation developed earlier by Skocic and Bukvic, 2016.

2. MODEL

Our model is a hybrid two temperatures, particle-LTE model and it is intended to describe expansion of LIP created on metal target in vacuum or low pressure ambient gas. Within the simulation heavy particles (atoms and ions) and electrons are considered in a different way. Each heavy particle is represented by its mass, position and velocity vector, at a given time. Movement and *elastic* collisions of heavy particles are monitored in detail. However, details regarding the motion of electrons are ignored completely, the free electrons are represented only by the local density and temperature. Concentrations of the heavy particles are related to the electron density and temperature via the Saha equation, supposing the existence of Local Thermodynamic Equilibrium (LTE). In this way, all *inelastic* collisions are substituted by the Saha equation. *Elastic* collisions of electrons with atoms and ions (e-a and e-i) are maintained separately. Physics of the LIP plasma expansion is described by the kinematics of heavy particles, which is insensitive on details of the plasma state (whether plasma is in LTE or not).

3. RELEVANT PARAMETERS AND INITIAL MOMENT

The most important parameters that must be supplied to simulation at the beginning are density of the heavy particles n_p, average energy per particle E_{av} and temperature of the heavy particles T_h. The temperature of the heavy particles is estimated assuming that metal target (copper) explodes when its temperature approaches critical point temperature. According to Autrique et al, 2013 this temperature is about 8000 K and does not depend on the laser irradiance. n_p is estimated knowing drilling depth and initial volume of plasma, both quantities are available in experiment. Estimation of E_{av} is based on calculated value for fraction of total laser energy absorbed by plasma, see works Bogaerts et al, 2003, 2005. For $I = 5$ GW/cm^2 the average energy is $E_{av} \sim 29$ eV, plasma number density $n_p = 1.3 \cdot 10^{27}$ m^{-3} and T_h=8000 K.

4. RESULTS AND DISCUSSION

Simulation is conducted for pulsed nanosecond 532 nm Nd-YAG laser for the copper target placed in vacuum. In Fig. 1 we present the evolution of plasma parameters in the first 120 ns from the laser pulse. On the left part of the Fig. 1 temperature relaxation among the plasma species for entire plasma life time (120 ns) is given, and on the inset, temperature relaxation in the first 1.0 ns. On the right part of Fig. 1 we present number density evolution of plasma species. Number density change is directly related to plasma expansion and electron temperature decrease.

In the initial moment, estimated average energy is distributed to the potential energy of ionization and to the kinetic energy of the plasma species. We obtained values $T_e \approx 70000$ K, $n_e \approx 1.8 \cdot 10^{27}$ m^{-3}, and $T_h \approx 8000$ K, $n_p \approx 1.3 \cdot 10^{27}$ m^{-3} ($n_{CuI} \approx 8.2 \cdot 10^{25}$ m^{-3}, $n_{CuII} \approx 6.1 \cdot 10^{26}$ m^{-3}, $n_{CuIII} \approx 5.8 \cdot 10^{26}$ m^{-3}). Observing the ionization degree ($x_{Cu_I}/n_p = 0.06$, $x_{Cu_{II}}/n_p = 0.48$, and $x_{Cu_{III}}/n_p = 0.46$) one can see that considerable energy is used in ionization of copper. In the initial moment, T_e is more than 10 times larger than the temperature of the atoms/ions. In the following 1 ns, T_e is reducing while the temperatures of the heavy particles

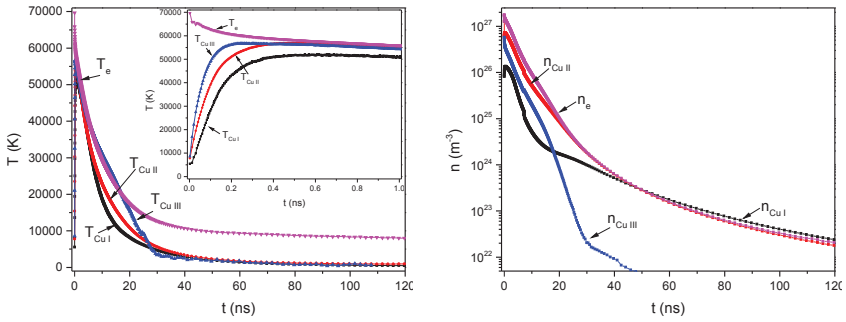

Figure 1: Average values for the plasma species temperatures (Left panel) and number densities (right panel). Inset: Temperatures for the first 1.00 ns after the laser pulse. We present values for Cu atoms (black), singly ionized Cu (red), doubly ionized Cu (blue) and electrons (violet).

are increasing, leading to the common value of ≈ 55000 K. This relaxation process is related to electron-atom and electron-ion elastic collisions (also, electrons loses energy to radiation). It can be observed that in the first ns atoms temperature (T_{CuI}) and ions temperatures (T_{CuII}, T_{CuIII}) are not the same. This effect is due to different electron-atom and electron-ion collision frequencies ($\nu_{e-CuIII} > \nu_{e-CuII} > \nu_{e-CuI}$). The species temperature difference occurs also at later times, and it will be discussed in next paragraph.

After the initial relaxation (thermalisation) plasma starts to expand into the surrounding space. This expansion results in rapid plasma cooling. Plasma temperature evolution is shown on the left part of the Fig. 1. The temperature of the plasma species is different in the entire process of plasma expansion. This could be due to the different processes that influence temperature decrease. Heavy particles are dominantly cooling due to expansion, while electrons are cooling due to collision with the heavy particles and bremsstrahlung radiation. Ionization potential energy is available to particle kinetic energy through the three body recombination process (electrons gain energy in this process). Energy gained in recombination process is transferred to heavy particles via e-i and e-a collisions. At first glance, it is strange that the temperature of atom and ions are not the same. Since atoms and ions have the same mass, the energy relaxation time is much faster than ion-electron or atom-electron relaxation times. The difference between the heavy particle temperatures is only because we present average temperatures while ions and atoms are not evenly distributed in the plasma volume. This is also evident for the temperature of Cu III species in the region between 10 ns to 50 ns.

It is interesting to see how kinetic and potential energy are evolving in time, see Fig. 2. In the initial moment all energy is stored in thermal energy of electrons (blue) and heavy particles (red), and in the potential energy of ionization (violet). In the first ~ 40 ns, energy conversion to E_{cm} (black) is intensive, and heavy particles are predominately accelerating. One can see that after the initial ~ 40 ns, values for E_{cm}, E_{pot}, E_{Th}, and E_{Te} are almost constant. This evidently coincide with curves on Fig.

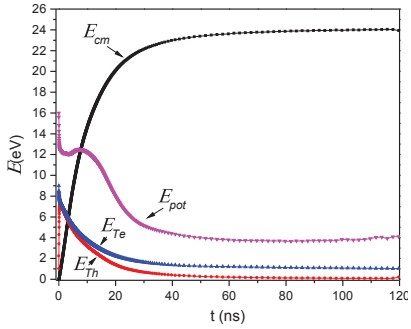

Figure 2: Energy transfer process. Black: the energy stored in expansion velocity (flux) of the heavy particles. Red: thermal energy of the heavy particles. Blue: thermal energy of the electrons. Violet: potential energy of ionization.

1, where after ~ 40 ns the dominant species in the plasma are neutral atoms.

There are several processes responsible for accelerating of the heavy particles. Since plasma is expanding, thermal energy of the heavy particles is directly transferred to the center of mass energy (chaotic movement to directional movement). The potential energy stored ionization energy is transferred to electrons via tree body recombination. Electrons transfer energy to heavy particles in elastic collisions; thus heating/accelerating the heavy particles.

5. CONCLUSION

The presented results are obtained from the simulation conducted for pulsed nanosecond 532 nm Nd-YAG laser for the copper target placed in the vacuum. Simulation is based on hybrid particle-LTE simulation developed by Skocic and Bukvic, 2016. Initial number density of the plasma and temperatures are $n_p \approx 1.3 \cdot 10^{27}$ m^{-3}, $T_e \approx 70000$ K, and $T_h \approx 8000$ K, respectively. Initial volume is set to $r_0^2 z_0 \pi = 100^2 10\pi$ μm^3. Presented results deal with initial moments of LIP temperature relaxation process, with an emphasis on the first couple of ns. Results indicate that plasma is in thermal equilibrium just after 1 ns for given initial conditions. After the initial relaxation, plasma temperature is about $T \sim 55000$ K. After 40 ns number of copper ions and atoms is the same, while after that moment neutral atoms are the most abundant species. Energy transfer to heavy particle is intensive, especially in the first 40 ns.

References

Autrique, D., Clair, G., L'Hermite, D., Alexiades, V., Bogaerts, A. et al., :2013 *J. Appl. Phys.*, **114**, 023301.

Bogaerts, A., Chen, Z., Gijbels, R., Vertes, A., : 2003, *Spec. Acta Part B*, **58**, 1867.

Bogaerts, A., Chen, Z.,: 2005, *Spec. Acta Part B*, **60**, 1280.

Itina, T., Hermann, J., Delaporte, P., Sentis, M., : 2002, *Phys. Rev. E*, **66**, 103.

Skocic, M., Bukvic, S., 2016, *Spec. Acta Part B*, **125**, 103.

Publ. Astron. Obs. Belgrade No. 99 (2020), 197 - 200 *Contributed Paper*

VUV SPECTROSCOPY OF THE He II - LYMAN SERIES FOR ELECTRON DENSITY ESTIMATION

I. TRAPARIĆ[1, 2] and M. IVKOVIĆ[2]

[1]*Faculty of Physics, University of Belgrade, Studentski trg 12, Belgrade, Serbia*

[2]*Institute of Physics, University of Belgrade, Pregrevica 118, Belgrade, Serbia*
E-mail ivke@ipb.ac.rs

Abstract. We report use of the spectral line shapes of the Lyman series of ionized helium for diagnostics of high temperature plasmas. As a light source the low pressure pulsed arc was used. Electron density was determined from width of the He II Pashen alfa line and parameters of the He I 447.1 nm line, while electron temperature was determined from Boltzmann plot of the He II lines. The use of the Inglis-Teller relation on merging of spectral lines along series and on condition for partial local thermodynamic equilibrium was tested as methods for electron density estimation.

1. INTRODUCTION

Vacuum ultra violet, VUV spectroscopy is very important since most intense spectral lines of various elements are in this wavelength region. Special attention was devoted to study of hydrogen and helium lines important for diagnostics of astrophysical and fusion plasmas. Among them, in high temperature plasmas the shape and width of ionized helium Lyman series lines are extensively studied both theoretically, (Kepple, 1971) and experimentally (Wrubel, 2001) and (Mijović, 1989). Since lower members of a series are often highly self-absorbed, in this work methods for plasma diagnostics based on higher member of Lyman series are analyzed.

2. EXPERIMENT

Experimental setup is shown in Figure 1. Plasma source is low pressure pulsed arc, whose inner diameter is 10 mm and distance between electrodes 130 mm. Pressure in the source was set and controlled by needle valve, with the gas flow of 0.2 l/min. One side of plasma source is mounted on VUV spectrometer, and on the other end there is a quartz window. Light emission was obtained by discharging capacitor of Experimental setup is shown in Figure 1. Plasma source is low pressure pulsed arc, whose inner diameter is 10 mm and distance between electrodes 130 mm. Pressure in the source was set and controlled by needle valve, with the gas flow of 0.2 l/min. One side of plasma source is mounted on VUV spectrometer, and on the other end there is a quartz window. Light emission was obtained by discharging capacitor of 5 μF (previously charged using high voltage supply unit) with ignitron switch BK7703. The discharge

process is controlled via automatic trigger unit. Around the source, Rogowski coil was placed, in order to measure current shape and its value. The radiation from this source is projected 1:1 onto the slit of VIS spectrometer using optical mirrors M1 and M2. Mirror M1 is plane mirror, while M2 is focusing mirror (f = 2m). Visible spectrometer is McPherson 2061 Cherny-Turner type spectrometer, who has the slit widths of 15 μm, focal length of 1 m and grating with 1200 grooves/mm. As light detector we used

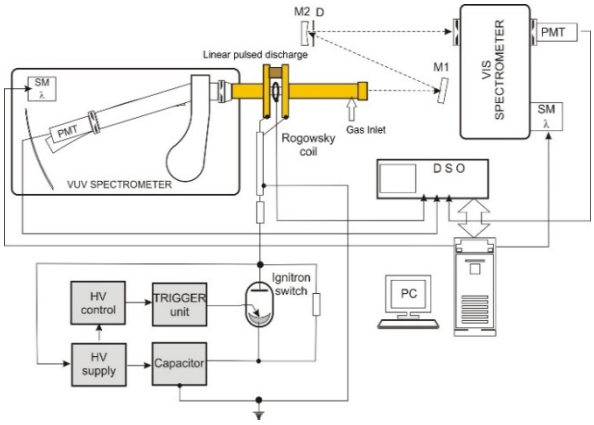

Figure 1: Experimental setup

photomultiplier, PMT mounted on spectrometer exit slit. Wavelength scanning was performed by rotation of diffraction grating with stepper motor, controlled by PC.

As we said above, the other end of plasma source is mounted on VUV spectrometer McPherson 247, which have concave grating of radius 2.2 m and 600 grooves/mm.Wavelength scanning is performed by moving the exit slit around the Rowland circle with help of stepper motor controlled by the PC. Spectrometer is grazing incidence spectrometer (large incidence angle), so we can observe EUV wavelengths from 0 to around 125 nm.

3. RESULTS AND DISCUSSION

In order to compare results obtained by different methods for electron density determination, N_e was determined from spectral lines recorded in visible spectral range. The N_e in early times of plasma evaluation was determined from full width at half maximum, FWHM of He II Pashen alpha line using formula (Busher et al, 1996):

$$N_e[\mathrm{cm}^{-3}] = 3.58 \cdot 10^{17} \cdot \mathrm{FWHM}\ [\mathrm{nm}]^{1.204} \qquad (1)$$

In plasma decay N_e was determined from separation between forbidden and allowed component of the He I using formula (Ivković et al, 2010):

$$\log_{10}(N_e) = 21.5 + \log_{10}\left(\left(\frac{s}{0.1479}\right)^{b(T_e)} - 1\right),\ b(T_e) = 1.46 + \frac{8380}{T_e^{1.2}} \qquad (2)$$

using T_e = 32000 ± 4000 K determined from Boltzmann plot of He II Lyman lines, see Figure 2 and 5. The correction of self-absorption using additional mirror was not possible due to window-less opreration of the discharge tube, since neither air not MgF_2 window are not transparent for radiation at 30 nm and below.

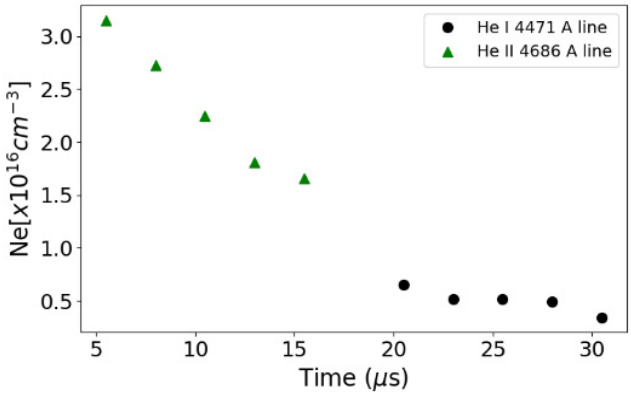

Figure 2: Time dependence of the electron densities in He at 3 mbar and 7 kV

Shapes of the He II lines belonging to the Lyman series were recorded using VUV spectrometer. Recordings were performed at different He gas pressures and different voltages.

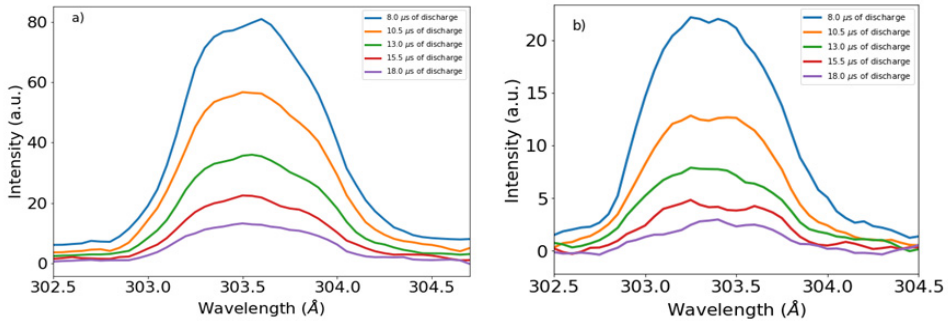

Figure 3: Line shapes of the He II Lyman alpha line at He gas pressure of 3 mbar at discharge voltages V of : a) 7 kV and b) 6 kV

It can be seen that He II Lyman alpha line at 30.2 nm is self-absorbed and becomes even self-reversed, see Figure 3.

Therefore, additional methods based on the recordings of higher members of the He II Lyman series shape for N_e determination were tested. First method is based on relation, see (Inglis-Teller, 1939), between N_e and principal quantum number of the upper level of the last resolved line in series n_{max}:

$$\log_{10}(N_i + N_e\ [cm^{-3}]) = 23.26 - 7.5n_{max} + 4.5\log_{10} Z \qquad (3)$$

The second one is based on determination of n for which partial local thermo-dynamic equilibrium-PLTE criteria, see (Griem, 1963) was satisfied:

$$N_e(cm^{-3}) \geq 7.4 \cdot 10^{18} \frac{Z}{n^{17/2}} \sqrt{\frac{k_B T_e}{E_H}} \qquad (4)$$

Here Z is the nuclear emitter charge, E_H is the hydrogen atom ionization energy and T_e is electron temperature.

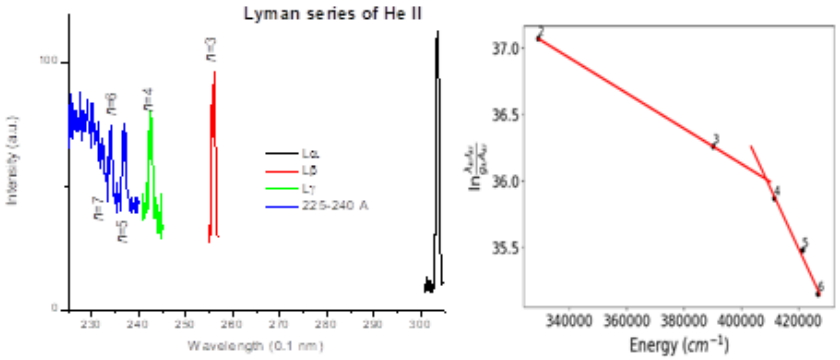

Figure 4. He II Lyman series lines at He gas pressure of 3 mbar at V = 7kV
Spectra recorded (left) and Boltzmann plot (right)

In order to estimate the range of application and accuracy of these methods N_e calculated by these two methods for T_e = 32 000 K is presented in Table 1. It can be seen that both methods can be used only for $N_e < 10^{16}$ cm^{-3}.

Table 1: N_e determined by relation (3) – IT and (4) – PLTE for T_e = 32 000 K

n	2	3	4	5	6	7	8	9
N_e IT [cm-3]	5.02 E20	2.4 E19	2.77 E18	5.2 E17	1.32 E17	4.17 E16	1.53 E16	6.34 E15
N_e PLTE [cm-3]	2.94 E17	9.35 E15	8.11 E14	1.22 E14	2.58 E13	6.97 E12	2.24 E12	8.23 E11

It should be stressed that for He gas pressure of 3 mbar, discharge voltage 7 kV the N_e determined from He II P_α line is 3.15, from IT relation between 1.53 and 4.17 and from PLTE criteria using n = 3.8, see (Konjević et al, 2009) is 0.13 times 10^{16} cm^{-3}. Increasing accuracy of IT method by using envelopes i.e. curves through min and max of series lines proposed by (Vidal, 1966) is under development.

References

Busher S., Glenzer S. and Kunze H.J., 1996, *J.Phys. B, At.Mol.Opt.Phys*. **29**, 4107
Griem H. R., 1963: *Phys. Rev.* **131**, 1170.
Inglis D. and Teller E., 1939, *Astrophys.J.* **90**, 439.
Ivković M. et al., 2010: *Spectrochimica Acta B* **65,** 234.
Kepple P., 1971, *Technical Report University of Maryland* **72-018.**
Konjević N., Jovićević S., Ivković M., 2009, *Physics of plasmas* **16**, 103501.
Mijović S., Pantelić D, Konjević N., Popović M.,: 1989*, Fizika*, **21**, 319.
Vidal C.R., 1966, *JQSRT* **6**, 575.
Wrubel Th. , Buscher S., Kunze H.-J., Ferri S.,2001, *JQSRT* **71,** 739.

Publ. Astron. Obs. Belgrade No. 99 (2020), 201 - 204 *Contributed Paper*

STARK BROADENING OF SPECTRAL LINES WITHIN COPPER LIKE EMITTERS

NORA TRKLJA BOCA, IVAN P. DOJČINOVIĆ, IRINEL TAPALAGA and JAGOŠ PURIĆ

University of Belgrade, Faculty of Physics, P. O. Box 44, 11000 Belgrade, Serbia

Abstract. Regularity analysis of Stark line broadening within copper-like emitters was performed, using available Stark data for Cu I, Zn II, Ge III, Ga IV and Kr VIII. Algorithms for temperature and density normalization were developed. Results are presented for fixed values of electron density and temperature: $N_e=10^{22}$ m^{-3} and T=100000 K. Obtained relations can be used for calculation of Stark widths for transitions within copper-like emitters with lack of Stark broadening data and for quality control of available data.

1. INTRODUCTION

Stark broadening data are significant for the investigation of astrophysical and laboratory plasmas. Years of investigation of the Stark effect phenomena leads to the conclusion of regularity existence within the spectral series of the same isoelectronic sequence. In the presented paper, Stark width regularities within the copper isoelectronic sequence are investigated, using available data for Cu I, Zn II, Ga III, Ge IV and Kr VIII.

Copper is widely used in electrical industry as an electrode material, so Stark data of copper are important for industrial laboratories. Stark widths of zinc, gallium, germanium and krypton are of interest for astrophysics. Spectral lines of zinc are used for determination of metallicity and content of dust in cosmic objects. Gallium is present in hot white drafts, while germanium is found in stellar and interstellar atmosphere. Krypton is a product of s (neutron capture in slow time scale orderly evolution of stellar interiors) and r (neutron capture in fast time scale in type I supernovae) processes (Dimitrijevic et al. 2000).

After regularity analysis using available data, predictions of Stark widths can be done for any transition within the copper isoelectronic sequence.

2. THEORETICAL BACKGROUND

The ground state of neutral copper, as well as all members of copper isoelectronic sequence, has electron configuration of ground state: [Ar]$3d^{10}4s$, with term ^2S, where $3d^{10}$ is energetic stable level. All members of the copper isoelectronic sequence have one uncoupled electron, so they can be treated as quasi-one electron systems and they all have similar excited states. It is expected that atomic parameters within copper-like emitters show some regular behaviour.

The regularity approach used in present investigation is based on the work of Puric et al. 1999. Equation (1) is used for regularity investigation.

$$\log \omega^* = \log \frac{\omega}{Z_e^c} = \log a + b \cdot \log(\chi^{-1}) \quad (1)$$

ω^* is the reduced Stark width, χ is the electron binding energy on the upper level of analyzed transition, Z_e is the rest core charge of the emitter; $a = const \cdot N_e \cdot f(T_e)$, b is a fitting coefficient. Parameter c can be found by analyzing the quality of the fit which is determined by factor R^2 (Tapalaga et al. 2018.).

For each analyzed transition for which there are available Stark width data for different temperatures, the dependence of line width on temperature is fitted according to equation (2) (Purić et al. 1999).

$$\omega = A + B \cdot T^{-C} \quad (2)$$

For transitions analyzed in present investigation, the constancy of the ratio $\Delta\lambda/N_e$ is confirmed and linear dependence of Stark widths on electron density has been found as good approximation.

3. RESULTS AND DISCUSSION

Regularity analysis within copper like emitters include 54 spectral lines: Cu I (11), Zn II (11), Ga III (10), Ge IV (17), Kr VIII (5). Stark width data used in the present study are taken from Stark B data base (Sachal-Brechot et al. 2018). Data were complemented with available experimental data of Stark widths. χ values are taken from NIST atomic database (Kramida et al. 2018). Data were complemented with available experimental data of Stark widths.

Fig. 1. represents dependence of R^2 on parameter c for the copper isoelectronic sequence and it can be concluded that c is approximately equal to 4. Value of R^2 has the same value in the range c=3 to c=5.

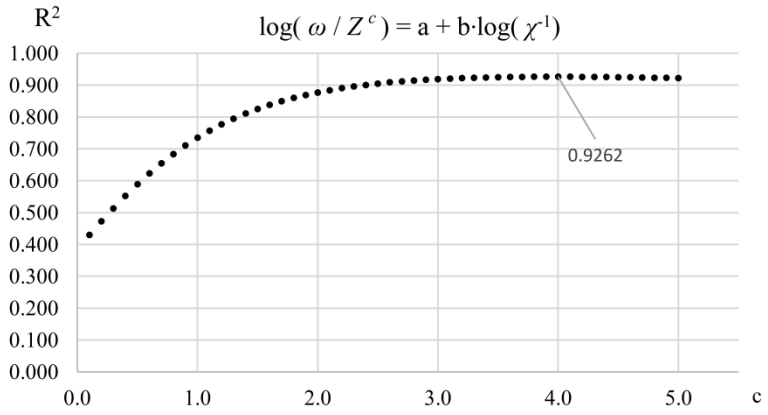

Figure 1: Determination of parameter c

Software for determination of A, B and C parameters has been developed and it enables temperature data normalization. As an example of fitting procedure results, in Table 1, parameters A, B and C are given for 4s-4p transition within analyzed emitters (there is no available Stark width data for 4s-4p transition within Ga III in the database).

Emitter	A	B	C
Cu I	4.08E+07	1.28E+03	75E-02
Zn II	1.08E+09	-9.76E+0.8	83E-04
Ge IV	6.07E+09	6.07E+09	11E-04
Kr VIII	5.31E+07	-8.06E+07	20E-03

Table 1: Parameters A, B and C for 4s-4p transition used for temperature normalization

In the present paper results are presented for $N_e=10^{22}$ m^{-3} and T=100000 K.

Fig. 2. represents dependence of the reduced Stark width on ionization potential of the upper level of transition, for all analyzed spectral lines of the copper isoelectronic sequence, fitted according to equation (1).

According to fitting parameters from Fig. 2, there is an unique formula for Stark width calculation for any line within copper isoelectronic sequence:

$$\Delta\lambda = 1.49 \cdot 10^{-20} \cdot \frac{Z_e^4 N_e}{\chi^{2.62}} \lambda^2 \quad (3)$$

In equation (3) λ and $\Delta\lambda$ are expressed in [m], N_e is expressed in [m^{-3}] and χ is expressed in [eV].

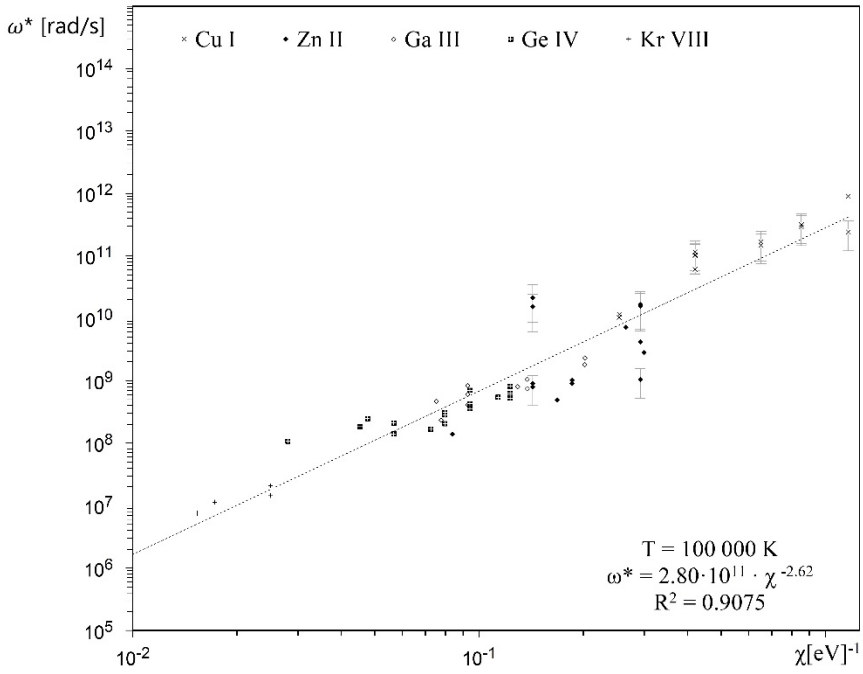

Figure 2: Dependence of ω^* on χ for the copper isoelectronic sequence ($N_e=10^{22}$ m^{-3}, T=100000 K)

4. CONCLUSIONS

Results of presented regularity analysis enable calculation of Stark widths for transitions within copper isoelectronic sequence for which there is no available data in the literature. Also, our results are used as a quality test for experimentally measured Stark broadening values, and for Stark widths calculated using other theoretical methods.

References

Dimitrijevic, M. S., Sahal-Brechot, S.: 2000, *Phys. Scr.*, **61**, 319.

Kramida, A., Ralchenko, Yu., Reader, J., and NIST ASD Team, *NIST* Atomic Spectra Database (ver. 5.5.6), [Online]. Available: https://physics.nist.gov/asd [2018, Jun 27]. National Institute of Standards and Technology, Gaithersburg, MD.

Purić, J., Šćepanović, M.: 1999, *Ap. J.*, **25**, 737.

Sahal-Brechot, S., Dimitrijević, M. S., Moreau, N.: 2018, STARK-B database, [online]. Available: http://stark-b.obspm.fr [February 14, 2018]. Observatory of Paris, LERMA and Astronomical Observatory of Belgrade.

Tapalaga, I., Trklja, N., Dojčinović, I. P., Purić, J.: 2018, *MNRAS*, **474**, 5479.

Publ. Astron. Obs. Belgrade No. 99 (2020), 205 - 208 *Contributed Paper*

DETERMINATION OF THE TEMPERATURE DISTRIBUTION IN THE CATHODE SHEATH REGION OF HYDROGEN GLOW DISCHARGE USING Q-BRANCHES OF FULCHER-α BAND

M. M. VASILJEVIĆ[1], G. LJ. MAJSTOROVIĆ[2] and DJ. SPASOJEVIĆ[1]

[1]*University of Belgrade, Faculty of Physics, Studentski trg 12, 11000 Belgrade, Serbia*

[2]*University of Defence, Military Academy, 11105 Belgrade, Pavla Jurišića Šturma 33, Serbia*

E-mail gordana.majstorovic@va.mod.gov.rs

Abstract. Optical emission spectroscopy (OES) technique is used to measure electric field strength, rotational and gas temperature along the axis of an abnormal glow discharge parallel to the plane copper cathode surface (side-on) operating in hydrogen at low pressure. The rotational temperature of the excited state of H_2 was determined from the rotational structure of the Q branch of Fulcher-α diagonal bands using the Boltzmann plot technique while the obtained ground state temperature is assumed to be equal to the gas temperature. The population of excited energy levels, determined from relative line intensities, was used to derive rotational and gas temperature distributions in the cathode sheat region as well as relative population densities of rotational levels of the $d^3\Pi_u^-$.

1. INTRODUCTION

Glow discharges are extensively used for a wide variety of applications like e.g. as an excitation source for analytical spectroscopy of metal and alloy samples or depth profiling. Most of glow discharge (GD) source applications are based on original Grimm design, described in Grimm 1968., with direct current (DC) and more recently with radio frequency (RF) excitation.

The cathode sheath (CS) region is the most important part of an abnormal GD, therefore it's importance can't be neglected when describing or modeling GD. In this region, a lot of relevant processes for the operation and application of GD occur. All these processes are important in various fields of spectroscopic analysis, for thin film deposition, plasma etching, and depth profiling.

The understanding of plasma fundamentals, phenomena, and plasma applications requires the knowledge of discharge parameters, like the electric field strength distribution, gas, and vibrational temperature of molecules and radicals in the cathode sheath region. Among other plasma parameters, gas (translational) temperature of molecules plays an important role since it determines the rate of chemical reactions.

In this study, an estimation of the rotational and gas temperature, within the CS region will be shown. To evaluate the boundary between the CS and the negative glow (NG) region we used Stark polarization spectroscopy of hydrogen Balmer alpha line. For the gas temperature mapping Fulcher-α diagonal bands are recorded

and analysed in the CS region of the Grimm GDS operating in hydrogen at low pressure by means of OES.

2. EXPERIMENTAL

A detailed description of a modified Grimm GDS source and the experimental setup is given in Majstorović et al, 2013 and Vasiljević et al. 2017. The experiment was realized in hydrogen (purity 99.999%). The axial intensity distribution of radiation has been observed side-on through the anode slot. The discharge tube was translated in approximately 0.125 mm steps. All spectral measurements were performed with an instrumental profile very close to the Gaussian form with measured full width at half maximum (FWHM) of 8.2 pm in the second diffraction order.

For the H_α experiments the radiation from discharge was polarized by a plastic polarizer. The selection of the π - polarized profile was experimentally carried out by orienting the polarizer axis parallel to the discharge axis, whereas the $d^3\Pi_u^-, \nu' \rightarrow a^3\Sigma_g^+, \nu''$ ($\nu'=\nu''=0,1,2$) band lines were observed without the polarizer.

3. RESULTS AND DISCUSSION

The electric field strength distribution in the CS region of the Grimm type GD is determined by fitting the model function (8) fully described in Ivanović et al. 2017, for the experimental profiles of π-polarised H_α line.

The temperature obtained from the Q branch of Fulcher-α band may be considered as the most reliable for the temperature estimation, see Majstorović et al. 2007. Now, we investigate the possibility of using Q branches of the $d^3\Pi_u^-, \nu'=0,1,2 \rightarrow a^3\Sigma_g^+, \nu''=0,1,2$ molecular system for temperature measurement in hydrogen Grimm GD.

The Q branch lines of the electronic transition $d^3\Pi_u^-, \nu' \rightarrow a^3\Sigma_g^+, \nu''$ ($\nu'=\nu''=0,1,2$) are well resolved and have a high signal/noise ratio in the 601-630 nm wavelength region, see Crosswhite, H. M. 1972.

The relative population densities of the rotational levels for $d^3\Pi_u^-$ ($v'=0,1,2$) state, see Fig. 2(a), are in accordance with the Boltzmann function. So, the Boltzmann plot technique, see Majstorović et al. 2007, is used for evaluation of the rotational temperature $T_{rot}(n',v')$ of the excited state. In low-pressure discharges, the number of collisions is not sufficient to redistribute the rotational population. The degree of relation between the rotational population density distribution in n',v' state, and the population of ground electronic state should be proven within the framework of excitation-deactivation balance equations, see Röpcke et al. 1998. According to the model discussed in Astashkevich et al. 1996., the temperature recalculated for the ground vibrational state $X^1\Sigma^+_g, \nu = 0$ can be considered as a valid estimation of the ground state rotational temperature i.e. H_2 gas temperature. Thus, values of the Q branch population of H_2 Fulcher-α band ($\nu'=\nu''=0,1,2$) were

used to determine the rotational temperature of the ground vibrational state T_0 (n', v'), see Fig. 2(b).

In our case, the temperature recalculated for the ground vibrational state $X^1\Sigma^+_g, v = 0$ is two times larger than the rotational temperature of excited states in accordance with the relationship of the rotational constants for the upper $d^3\Pi_u$ and ground $X^1\Sigma^+_g$ (v =0) states, see in Table 1 of Astashkevich et all. 1996. and in Herzberg 1950.

State	T_e (cm^{-1})	B_e (cm^{-1})	α_e (cm^{-1})
$d^3\Pi_u^-$	112753	30.364	0.5520
$a^3\Sigma_g^+$	95980	17.109	0.606
$X^1\Sigma_g^+$	0	60.853	1.0492

Table 1: Molecular constants for hydrogen ground state and Fulcher-α electronic states.

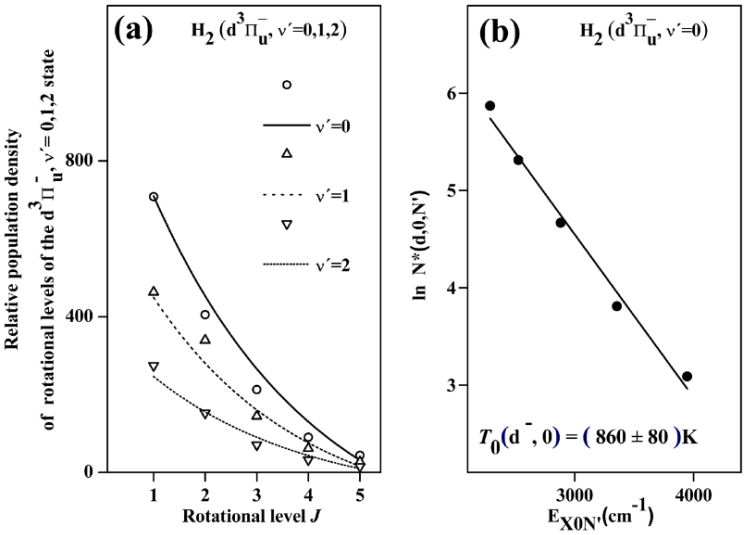

Figure 1: (a) Measured (points) and calculated (lines) values of the rotational population distribution of $H_2(d^3\Pi_u^-)$ levels. Lines represent the function $\exp(-B_vJ(J+1)hc/kT)$ for the corresponding rotational temperatures. (b) Semilogarithmic plot of rotational population densities of $d^3\Pi_u^-$ versus rotational energy of the molecular hydrogen ground states. Experimental conditions: copper cathode; Grimm GD in H_2 at the pressure p = 4.5 mbar; discharge current I = 11 mA; and discharge voltage U = 880V.

The technique mentioned above suggests that the thickness of the CS doesn't exceed 2.25 mm, see F 2(a). The results obtained for the temperature distribution along the CF region, presented in Fig. 2(b), show that both temperatures, T_{rot} (Q-

branch; $\nu' = 0,1,2$) and the rotational temperature of ground vibrational state T_0, change along the cathode fall region Grimm GDS.

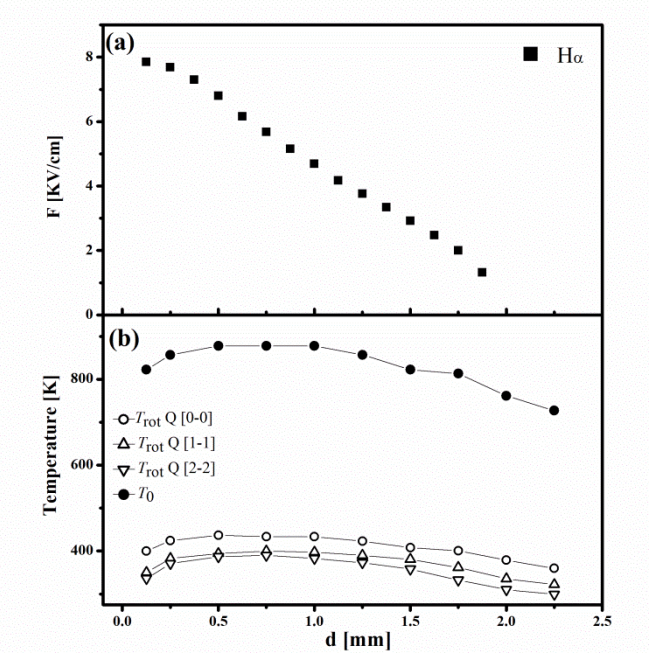

Figure 2: The dependence upon the distance from cathode d of: (a) Electric field strength F and (b) Rotational (T_{rot}) and gas (T_0) temperature distribution of the excited state $H_2(d^3\Pi_u^-)$. Experimental conditions: cooper cathode Grim GD in H_2 at $p = 4.5$mbar, $I = 11$mA, and $U = 880$V.

References

Astashkevich, S. A., Käning, M., Käning, E., Kokina, N. V., Lavrov, B. P., Ohl, A., Röpcke, J.: 1996, *J.Q.S.R.T.*, **56**, 725.

Crosswhite, H. M.: 1972, *The hydrogen molecule wavelength tables,* Gerhard Heinrich Dieke, New York: Wiley-Interscience.

Grimm, W.: 1968 *Spectrochim. Acta B* **23**, 443.

Herzberg, G.: 1950, *Molecular spectra and molecular structure vol I*, New York: Van Nostrand-Reinhold.

Ivanović, N. V., Šišović, N. M., Spasojević, Dj., Konjević, N.: 2017, *J. Phys. D: Appl. Phys.* **50**, 125201

Majstorović, G. Lj., Ivanović, N. V., Šišović, N. M., Djurović, S., Konjević, N.: 2013, *Plasma Sources Sci. Technol*. **22**, 045015.

Majstorović, G. Lj., Šišović, N. M., Konjević, N.: 2007, *Plasma Sources Sci. Technol.***, 16**, 750.

Röpcke, J. , Kaning, M., Lavrov, B. P.: 1998 *J. Phys. IV France* **8,** 207.

Vasiljević, M. M., Spasojević, Dj., Šišović, N. M., Konjević, N.: 2017, *Europhys. Lett.* **119**, 55001.

Publ. Astron. Obs. Belgrade No. 99 (2020), 209 - 212 *Contributed Paper*

NANOSTRUCTURES ASSISTED TEA-CO_2 BASED LIBS: IMPROVEMENT OF THE LIMIT OF DETECTION

SANJA ŽIVKOVIĆ[1], JELENA PETROVIĆ[1], MILOŠ OGNJANOVIĆ[1], JOVAN CIGANOVIĆ[1], DAMJAN BLAŽEKA[2], NIKŠA KRSTULOVIĆ[2] and MILOŠ MOMČILOVIĆ[1]

[1] *VINČA Institute of Nuclear Sciences - National Institute of the Republic of Serbia, University of Belgrade, PO Box 522 11351 Belgrade, Serbia, E-mail sanjaz@vinca.rs*

[2] *Institute of Physics, Bijenička cesta 46, 10000 Zagreb, Croatia*

Abstract. We report preliminary results of an innovative approach based on nanomaterials deposition on the sample surface for the improvement of the limit of the detection of Laser-Induced Breakdown Spectroscopy (LIBS) analysis of trace elements in aluminum alloys. For this purpose, Ag-TiO_2 bimetallic nanoparticles were synthesized and used to enhance the emission signal of laser-induced plasma.

1. INTRODUCTION

Laser-Induced Breakdown Spectroscopy (LIBS) technique has been recognized as a modern, fast, and direct method for multielement material analysis for more than 20 years. Specific advantages of LIBS include a very small amount of the sample required for the analysis with little or no sample preparation and no consumable or waste products. Despite the intrinsic benefits of the LIBS method with respect to other standard analytical techniques (ICP-OES, XRF, AAS), some fundamental limitation in sensitivity and reproducibility of the analytical results has limited the establishment of this method (Zivkovic et al. 2017). Recently, one of the signal enhancement methods has emerged as a possible solution. This promising variant of the LIBS technique, namely Nanoparticle - Enhanced LIBS (NELIBS) is based on the use of metallic nanoparticles which can be determinant in controlling the laser-matter interaction, by directly affecting the coupling of incoming laser electromagnetic field with the irradiated material (Dell'Aglio et al. 2018).

In this work, silver-titanium dioxide bimetallic nanoparticles (NPs) were prepared and used to perform preliminary NELIBS analysis of aluminum alloy samples. Preliminary results have shown that enhancement of the LIBS signal can be achieved using this kind of NPs.

2. EXPERIMENTAL

With the Pulsed Laser Deposition (PLD) method thin film is prepared by the simultaneous ablation of two targets: silver and titanium dioxide. As the thin film substrate pure silica is used. PLD was performed in vacuum using 5 ns Nd:YAG laser operating at 1064 nm, 300 mJ of output energy and repetition rate of 5 Hz. Laser pulses were focused onto the target yielding laser fluence of about 30 mJ/cm^2. PLD setup is shown in (Meljanac *et al.* 2016). Uniformity of the prepared thin layer was tested by LIBS analysis.

Silver-titanium dioxide bimetallic (Ag-TiO_2) nanoparticles were produced by the laser ablation method. A thin layer film obtained by PLD was placed in a glass and covered with 10 ml of bidistilled water. Laser applied was the picosecond Nd:YAG system, operating at 1064 nm with a 150-ps pulse length, pulse energy 40mJ pulse energy, and irradiation time of 30 minutes. The size distribution of the obtained colloid solution of nanoparticles was analyzed by dynamic light scattering (DLS) technique using a *Zetasizer Nano ZS90* (Malvern, UK) with 633-nm He-Ne laser and 90° detection optics. The zeta potential was measured at pH 5 at 25 ± 0.1 °C in a disposable zeta cell (DTS 1070) of a *Nano ZS90* device.

LIBS measurements were conducted using a unique developed LIBS system based on pulsed gas TEA CO_2 laser and time-integrated spatially resolved spectroscopy (TISR). All aluminum alloy samples were mechanically treated with corundum abrasive paper to increase the absorptivity of applied TEA CO_2 laser wavelength. After the samples were clean from the residue of mechanical treatment, samples were coated with a thin layer of nanomaterial dispersion droplets and then were dried. The schematic diagram of the experimental arrangement is shown in Figure 1.

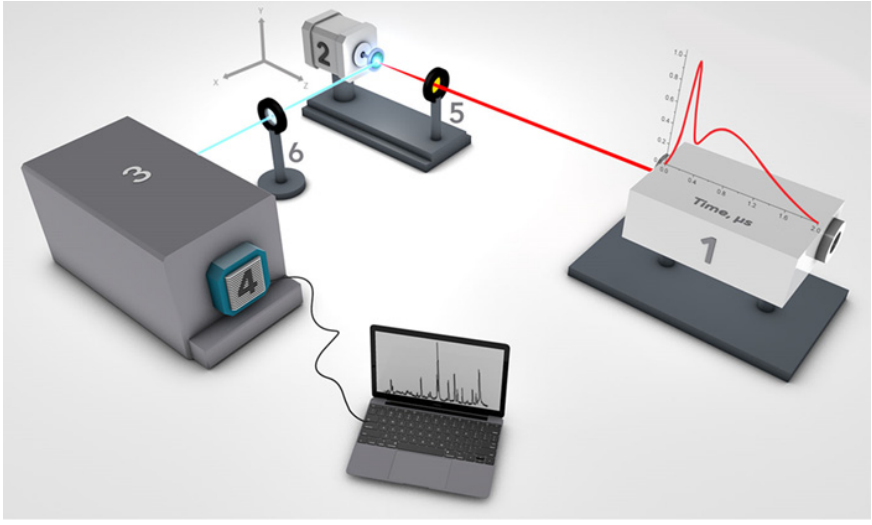

Figure 1: Experimental setup for TEA CO_2 laser-based LIBS

The plasma was generated by focusing a pulsed TEA CO_2 laser that emits at 10.6 μm on the aluminum target with Ag-TiO_2 NPs on the surface at atmospheric pressure. All measurements were taken at the focal point. Applied laser energy was 200 mJ with a repetition rate of 1 Hz and the shot to shot fluctuation of its energy was about 5%. Optical emission from the induced plasma was collected on the entrance slit of a Carl Zeiss PGS2 monochromator by using an achromatic lens with magnification 1:1. LIBS analysis was conducted in time-integrated mode during 10 s using CCD Apogee Alta F1007 camera as a detector. The TISR measurements were performed at the atmospheric pressure in the air. Production of stable and reproducible plasma required fresh area at the target surface which was achieved by target rotation using a continual motor. All measurements were carried out in triplicate and obtained spectra present average values of line intensities from 10 different parts of the sample surface.

3. RESULTS AND DISCUSSION

Uniformity of the PLD thin film was confirmed by the LIBS method. Average spectra consist of several Ti I and Ti II lines and Ag I emission line, Figure 2.

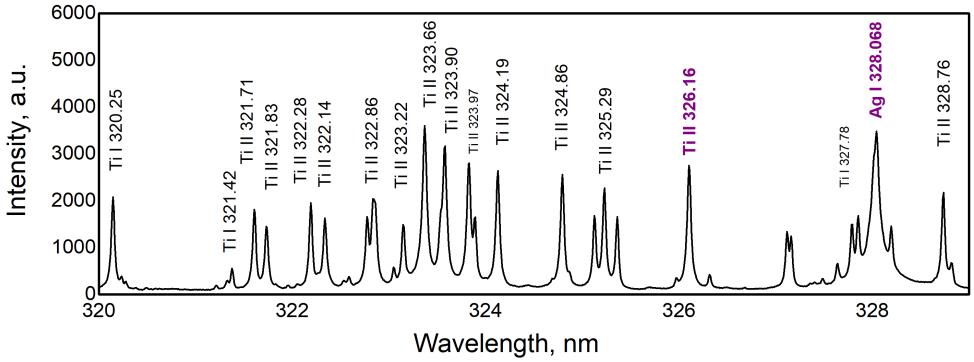

Figure 2: LIBS analysis of Ag:TiO_2 thin film

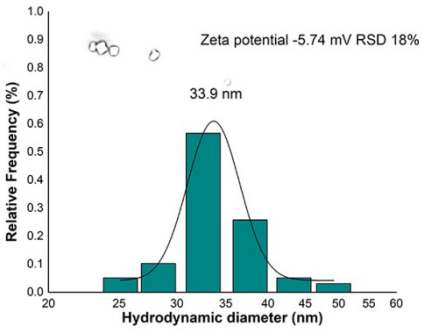

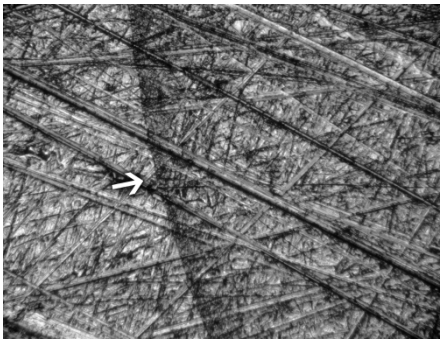

Figure 3: a) Size distribution of NPs; b) Front of NPs dispersion layer applied on a sample surface

The size distribution of synthesized NPs is shown in Figure 3a.

The LIBS spectra segments of the analyzed sample with a focus on the copper line are shown in Figure 4a. Each spectrum represents an averaged spectrum from 10 laser pulses. Considering that TISR method utilizes the fact that intense continuum emission is mostly emitted from a region close to the sample surface, the best signal to background (SBR) value was achieved by changing the viewing position of plasma along its expanding direction of toward the laser beam. Distance between the focusing lens and a target was constant and optimal SBR ratios were obtained at 1 mm in front of the target. For determination limits of detection (LOD) of applied technique, the standard calibration method was chosen. The linear dependency of measured LIBS intensity towards the concentration of Cu in samples was obtained for both LIBS and NELIBS, Figure 4b. The main difference between calibration plots is the incensement of a slope which corresponds to the incensement of method sensitivity. Using a formula $LOD = 3\sigma_B/b$, where σ_B is the standard deviation of background surrounding the selected emission line, and b is the sensitivity defined as the slope of the calibration curve, we estimated that $NELIBS_{LOD}$ is 2.5 times less than $LIBS_{LOD}$.

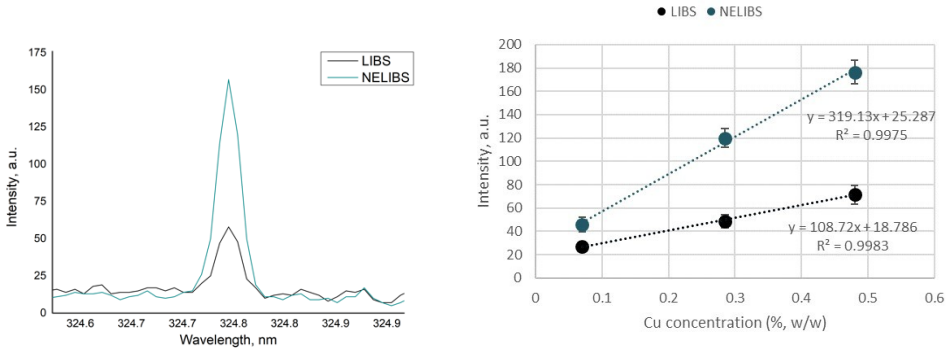

co

Figure 4: a) Segments of LIBS spectra with focus on Cu I 324.754 line; b) Calibration plots for two applied techniques

We believe that some methods could additionally lower the LOD: (1) optimized conditions to obtain thin film by PLD (2) the LIBS spectral characteristics will be improved by optimization dimensions of bimetallic nanoparticles. We will further study the above methods and present the results in our future publications.

Acknowledgments: This research was supported by the Ministry of Education, Science and Technological Development of Republic Serbia, Croatian Science Foundation (under projects HrZZ-PZS-2019-02-5276 and HrZZ-IP-2019-04-6418) and bilateral project between Serbia and Croatia (Project ID 337-00-205/2019-09/15)

References

Dell'Aglio, M.,Alrifai R., De Giacomo A. : 2018, *Spectrochim Acta B* **148**, 105–112.
Meljanac D., et al..: 2016 *J. Vac. Sci. Technol. A* **34** 021514.
Zivkovic S, et al.: 2017, *J Alloys Compd*. **700,** 175-184.

Publ. Astron. Obs. Belgrade No. 99 (2020), 213 – 216 *Contributed Paper*

A NEW LOOK AT SURFACE-WAVE SUSTAINED PLASMA: MAGNETIC CURRENT MODEL TREATED BY A FIXED-POINT METHOD

MILAN S. KOVAČEVIĆ[1],MARKO M. MILOŠEVIĆ[1],
LJUBICA KUZMANOVIĆ[1] and ALEXANDAR DJORDJEVICH[2]

[1]*Faculty of Science, University of Kragujevac, Serbia*

[2]*City University of Hong Kong, Hong Kong*

Abstract. An analytical description and numerical investigation of the cylindrical plasma columns produced and sustained by a weakly damped surface-wave is presented. This paper suggests using a simple magnetic current model in order to obtain a general expression for normalized power of surface-wave. This expression can be deduced theoretically from the full-wave theory already used for such plasmas. The diagrams of normalized power are computed by an iterative procedure known as the fixed-point method. The fixed-point method appears as the natural choice for the numerical treatment of formulae that could arise in a broad class of physical problems usually recognized as guided surface plasma waves.

1. INTRODUCTION

The problem of the propagation of surface-waves along plasma columns had been known for years and has been treated by many authors [Trivelpiece 1967, 1959, Moisan et al 1977, 1979]. Electron waves on a plasma guide attracted the attention of investigators for a long time. A comprehensive review on this topic can be found in [Babovic1999]. We have developed software packets which avoid any starting approximations and successfully calculate expressions in its full-electromagnetic formulations. In this connection, the fixed-point method was completely tested in this paper throughout the calculation of the normalized power of surface-wave in the plasma column.

2. STRUCTURE OF THE LINE

We consider the propagation of an azimuthally symmetric ($m = 0$ mode) surface-wave along cylindrical structure (Figure 1) consisting of a plasma column surrounded by air. Figure 1 shows a sketch of the adopted model. The central part of the line consists of a glass tube of radius b, whose interior is filled with a homogeneous plasma of radius a. Of course, one could imagine plasma is suspended in a glass tube, and we treat the glass wall as a very thin one. The glass tube is a dielectric characterized with permittivity ε_g (in air $\varepsilon_r \approx 1$).

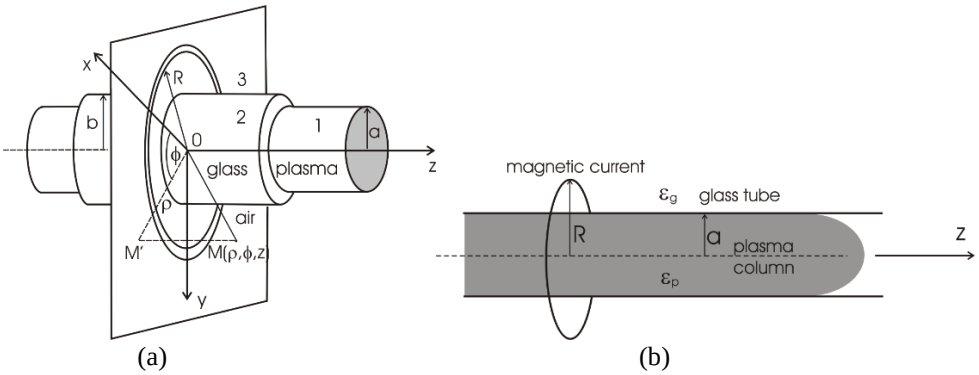

Figure 1: (a) Geometric characteristic and applied cylindrical system, (b) plasma created by the magnetic current.

3. MAGNETIC CURRENT MODEL: FEATURES OF THE FIELD

The mathematical treatment we begin writing Maxwell's equations in a form adapted to our case

$$\nabla \times \vec{H} = \varepsilon_0 \varepsilon \, \partial \vec{E} / \partial t \,, \tag{1}$$

$$\nabla \times \vec{E} = -\mu_0 \partial \vec{H} / \partial t - \vec{J}_m \,. \tag{2}$$

where $\vec{J}_m$ is the magnetic current density which in the cylindrical coordinate system has only azimuthal component and in the form of Dirac delta function is given as

$$J_{m\phi} = U\delta(\rho - R)\delta(z) \,. \tag{3}$$

The components of the electric field $\vec{E}$ are (E_ρ, E_ϕ, E_z) and magnetic field $\vec{H}$ (H_ρ, H_ϕ, H_z). The so-called H (or TE) field is composed of the group E_ϕ, H_ρ, H_z and the E (or TM) field has the components H_ϕ, E_ρ, E_z. The typical method for finding the solution of wave equation connected to the mentioned problem of electromagnetic wave propagation along the plasma waveguide; (first, fairly general case wave equation is formed, and, secondly, the wave equation is solved in plasma, glass and air respectively; at the end, the boundary conditions were applied which is the working framework in [Kovačević 2000]and will be here omitted).

4. RESULTS

We begin with well-known expression for Q [Aliev 1994] which will be the object of our attention:

$$Q = \frac{1}{2} \int_{S_\perp} \sigma |E|^2 dS_\perp \tag{4}$$

where $|E|^2 = |E_\rho|^2 + |E_z|^2$ is the amplitude of the electric field of axial symmetric surface-wave, and $\sigma = -\omega\varepsilon_0\varepsilon_i$ (ε_i is the imaginary part of complex plasma permittivity). The integration would be over the cross-section which is perpendicular to the wave propagation direction. Since we observe two mediums (plasma and the dielectric surrounding plasma), we can write $Q = Q_1 + Q_2$ where the marks 1 and 2 denote the plasma and glass tube respectively (the assumption of infinitely thick dielectric was made). In accordance with the cylindrical system, we have

$$Q_1 = \frac{\sigma_1}{2}\int_0^a |E_1|^2\, 2\pi\rho d\rho = \pi\sigma_1 \int_0^a \left(|E_{1z}|^2 + |E_{1\rho}|^2\right)\rho d\rho \tag{5}$$

$$Q_1 = \frac{\sigma_2}{2}\int_a^\infty |E_2|^2\, 2\pi\rho d\rho = \pi\sigma_2 \int_a^\infty \left(|E_{2z}|^2 + |E_{2\rho}|^2\right)\rho d\rho \tag{6}$$

where $\sigma_1 = -\omega\varepsilon_0\varepsilon_i = \omega\varepsilon_0(\omega_p^2/\omega)(\nu/\omega)$ and $\sigma_2 = -\omega\varepsilon_0\varepsilon_i = -\omega\varepsilon_0\varepsilon_g tg\delta$. Here ν is the collision frequency in the electron-neutral collision, and $tg\delta = \varepsilon_i/\varepsilon_g$ is tangent of loss. The equations (5) and (6) can be written in the form $Q_1 = Q_{1z} + Q_{1\rho}$ and $Q_2 = Q_{2z} + Q_{2\rho}$. Substituting the function E_{1z}, E_ρ, E_{2z} and $E_{2\rho}$ [Kovačević 2000] the following expressions are obtained

$$\frac{Q_{1z}}{Q_0} = \frac{\omega_p^2}{\omega^2}\frac{\nu}{\omega}\frac{(u_1a)^4}{\varepsilon_p^2}\frac{\Delta_1^2}{\Delta'^2}\left[I_0^2(u_1a) - I_1^2(u_1a)\right], \tag{7}$$

$$\frac{Q_{1\rho}}{Q_0} = \frac{\omega_p^2}{\omega^2}\frac{\nu}{\omega}\frac{(\beta a)^2(u_1a)^2}{\varepsilon_p^2}\frac{\Delta_1^2}{\Delta'^2}\left[I_1^2(u_1a) - I_0(u_1a)I_2(u_1a)\right], \tag{8}$$

$$\frac{Q_{2z}}{Q_0} = tg\delta\frac{(u_2a)^4}{\varepsilon_g}\frac{\Delta_2^2}{\Delta'^2}\left[-K_0^2(u_2a) + K_1^2(u_2a)\right], \tag{9}$$

$$\frac{Q_{2\rho}}{Q_0} = tg\delta\frac{(\beta a)^2(u_2a)^2}{\varepsilon_g}\frac{\Delta_2^2}{\Delta'^2}\left[-K_1^2(u_2a) + K_0(u_2a)K_2(u_2a)\right], \tag{10}$$

where $Q_0 = (1/a^4)\left(J^2/8\pi\right)\left(1/\omega\varepsilon_0\right)$, $\Delta' = d\Delta/d(\beta a)$. To make the reading of the text easier, the meaning of individual abbreviations is:

$$\Delta = \begin{vmatrix} u_1aI_1(u_1a) & u_2aK_1(u_2a) \\ (u_1a)^2\varepsilon_g I_0(u_1a) & -(u_2a)^2\varepsilon_p K_0(u_2a) \end{vmatrix},\ \Delta_1 = \begin{vmatrix} u_1aK_1(u_1a) & u_2aK_1(u_2a) \\ -(u_1a)^2\varepsilon_g K_0(u_1a) & -(u_2a)^2\varepsilon_p K_0(u_2a) \end{vmatrix},$$

$$\Delta_2 = \begin{vmatrix} u_1aI_1(u_1a) & u_1aK_1(u_1a) \\ (u_1a)^2\varepsilon_g I_0(u_1a) & -(u_1a)^2\varepsilon_g K_0(u_1a) \end{vmatrix}, u_1 = \sqrt{\beta^2 - k_0^2\varepsilon_p}\ ,\ u_2 = \sqrt{\beta^2 - k_0^2\varepsilon_g}\ .$$

The total normalized power is

$$\tilde{Q} = \tilde{Q}_1 + \tilde{Q}_2 = \tilde{Q}_{1z} + \tilde{Q}_{1\rho} + \tilde{Q}_{2z} + \tilde{Q}_{2\rho}, \qquad (11)$$

The equation (11) was treated by the fixed-point method using the first approximation Y_1 of the dispersion relation [Babović 2002].

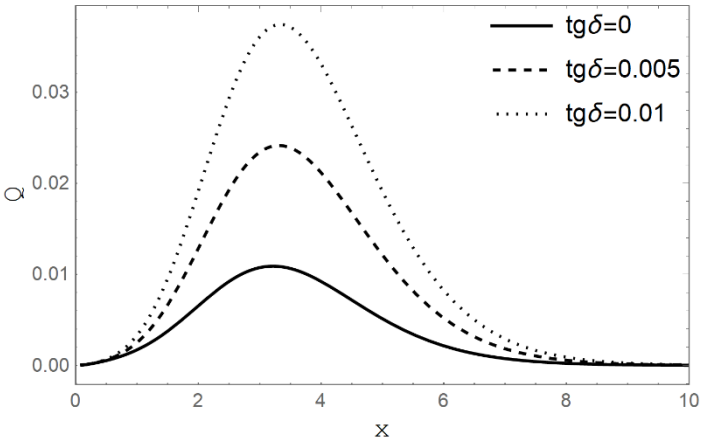

Figure 2: Normalized power $\tilde{Q}$ versus normalized wavenumber $X = \beta a$.

5. CONCLUSION

An analytical model, known as a magnetic current model, for the axialstructure of weakly collisional surface-wave sustained plasma was developed. In order to demonstrate the effectiveness of the fixed-point method, the normalized power vs. normalized wavenumber was calculated. The normalized power per unit length versus normalized phase coefficient for three values of tangent loss was presented. We notice that the absorbance of the power has a clearly expressed maximum around the point $X \sim 3$ for the given parameters; the magnitude of the maximum depends of dielectric losses such that $\tilde{Q}$ in generally increases as $tg\delta$ increases. This characteristic is very important for analyzing surfatron plasma as well as for calculation of the attenuation coefficient α.

References

Aliev, Y. M., Ghanashev, I., Schluter, H., Shivarova A.: 1994, *Plasma S. Scl. Tech.***3**, 216.

Babović, V.: 1999, Excitation of Surface Electron Plasma Waves, Faculty of Sciences Kragujevac, (in Serbian).

Babović, V., Kovačević, M.: 2002, *Journal of research in physics* **29** (1) 5.

Kovačević, M.: 2000, Contribution to study of surfatron plasma sources, MSci thesis, Faculty of Physics, University of Belgrade (in Serbian).

Moisan, M., and Ricard, A.: 1977, *Can. J. Phys.***55** 1010.

Moisan, M. Moisan, M., Zakrzewski, Z., and Pantel, R.: 1979, *J. Phys. D* **12** 219.

Trivelpiece, A.W.: 1967, Slow Wave Propagation in Plasma Waveguides, San Francisco Press, San Francisco.

Trivelpiece, A.W., Gould, R.W.: 1959, *J. Appl. Phys.* **30** 1784.

Publ. Astron. Obs. Belgrade No. 99 (2020), 217 - 220 *Contributed Paper*

PLASMA MODIFICATION OF LIGNOCELLULOSIC TEXTILE MATERIALS

ANA KRAMAR[1*], BILJANA PEJIĆ[1], BRATISLAV OBRADOVIĆ[2], MILORAD KURAICA[2] and MIRJANA KOSTIĆ[1]

[1]*Faculty of Technology and Metallurgy, University of Belgrade, Karnegijeva 4. 11000 Belgrade, Serbia*
E-mail akramar@tmf.bg.ac.rs, biljanap@tmf.bg.ac.rs, kostic@tmf.bg.ac.rs

[2]*Faculty of Physics, University of Belgrade, Studentski trg 12, 11000 Belgrade, Serbia*
E-mail obrat@ff.bg.ac.rs, kuki@ff.bg.ac.rs

Abstract. Plasma modification of textiles has a great potential to replace conventional wet chemical methods and becomes one of the leading processes in textile finishing. Plasma devices opposite to the wet treatments have many advantages, i.e. small energy and no chemical consumption, reduced duration of the treatment, and ease of implementation into existing facilities. In this work, atmospheric pressure dielectric barrier discharge (DBD) was used for modification of hemp (lignocellulosic) fibers with different chemical composition. Raw hemp (containing cellulose, lignin and hemicelluloses), hemp fibers with low content of lignin and with low content of hemicelluloses were used as experimental material. Wettability of each type of fibers increased significantly due to the changes in fibers morphology analyzed by SEM. The highest wettability improvement (estimated by measurement of capillary rise) was recorded for samples with lower content of hemicelluloses, followed by raw hemp fibers. Having in mind that wettability of hemp is conventionally improved by chemical treatments, this work shows that plasma processing can be successfully used for lignocellulosic fibers modification.

1. INTRODUCTION

Lignocellulosic materials, such are hemp, flax and jute, represent very unique type of fibers. They have heterogenic structure, main constituent being cellulose, with significant amount (15-20 %) of noncellulosic components such are pectin, waxes, lignin and hemicelluloses (Lazić et al. 2018). Hemp fibers (lat. *Cannabis Sativa*) can have various applications, e.g. as textile material for clothing and tehnical textile production, as composite material reinforcement, as biosorbent for wastewater treatment and removal of heavy metal ions etc. (Wang et al., 2003). In order to be used as textile material, lignocellulosic fibers must be subjected to various chemical treatments to remove non cellulosic components without cellulose damage (Wang et al., 2003). Removal of these components influences hydrophylicity of lignocelluloses fibers, by changing their sorption properties. Different conventional chemical treatments are being used to remove noncellulosic components. However, using plasma treatment instead chemical procedures is a

challenge with outstanding potential, due to the possibility to reduce environmental impact of chemical processing. The main advantage of plasma treatment of textiles is that it is a surface treatment while bulk of material is preserved. Furthermore, plasma treatment is a dry method, does not require use of water or any chemicals except gas (Shishoo, 2007). However, there are only few reports about plasma treatment of lignocellulose fibers. In the paper by Ibrahim et al. (2010) air DBD was used to improve wettability, increase functional groups and surface roughness of flax fibers. Li et al. (2014) used the DBD in helium after pretreatment of ramie fibers in ethanol and plasma treatment to improve interfacial adhesion between ramie fibers and poly(butylene succinate) PBS, a thermoplastic polymer. Ventura et al. (2016) studied the effect of plasma treatment on the flax nonwoven intended to be used as a composite reinforcement and they studied several types of plasma, both atmospheric pressure plasma (APP) and low pressure plasma. Hydrophilicity of flax material was significantly increased when APP in air was used.

In this work, atmospheric pressure DBD in air was used for modification of hemp fibers. Hemp fibers with different contents of hemicelluloses and lignin were used in order to determine the sensitivity of hemp constituents to the plasma treatment and to compare effects of chemical processing and plasma on wettability of hemp fibers.

2. EXPERIMENTAL MATERIALS AND METHODS

1.1. EXPERIMENTAL MATERIAL

Raw hemp fibers from Backi Brestovac (Serbia) were used as experimental material. To obtain different precursors for DBD treatments, hemp fibers were modified with 17.5 % sodium hydroxide for 5 and 45 min (to remove hemicelluloses) and 0.7 % sodium chlorite for 5 and 60 min (to remove lignin), as described in literature by Pejic et al. (2020).

1.2. PLASMA TREATMENT

Hemp fibers were treated with DBD plasma device described by Pejic et al. (2020) following regime of discharge 80 W, 10 kV, 300 Hz, 60 Jcm^{-2}, and treatment time of 2 min.

1.3. MORPHOLOGY STUDIES (SEM)

Investigation of surface morphology was carried out with scanning electron microscopy (SEM), using a JEOL 840A instrument, on samples previously coated with gold using a JFC 1100 ion sputter.

1.4. WETTABILITY MEASUREMENT AND SORPTION PROPERTIES

Wettability of samples was characterized by capillary rise method according to the procedure described by Pejic et al. (2020). Water retention power (WRP) was measured by standardized centrifuge method according to ASTM D 2402 – 01 (2001) in triplicate for each sample.

3. RESULTS AND DISCUSSION

In this work DBD in air was used for hemp fibers modification. The starting materials were fibers with various quantities of hemicelluloses and lignin (Fig 1), in order to study the effect of plasma on different components (cellulose, hemicellulose and lignin).

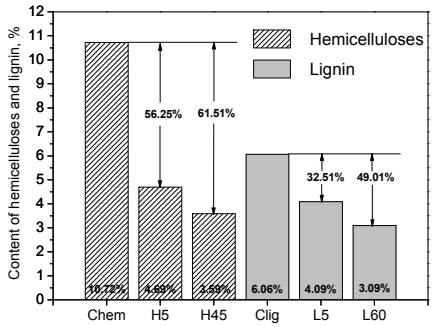

Figure 1: Composition of hemp fibers precursors used for DBD treatments

After plasma treatment, wettability, i.e. equilibrium height during capillary rise, was the highest for hemp fibers with lower content of hemicelluloses (H5 and H45) (Fig 2a) while wettability of raw hemp fibers (C) and fibers with lower content of lignin (L5 and L60) increased about 5 and 2 times, respectively. The significant change of surface morphology contributed to these results of improved sorption (Fig 2b). Compared to the raw hemp fibers and hemp with lower content of hemicelluloses (C and H5), plasma treated samples (C300 and H5/300) have more pronounced surface roughness which promotes better wettability. This confirms the surface targeted treatment of used DBD.

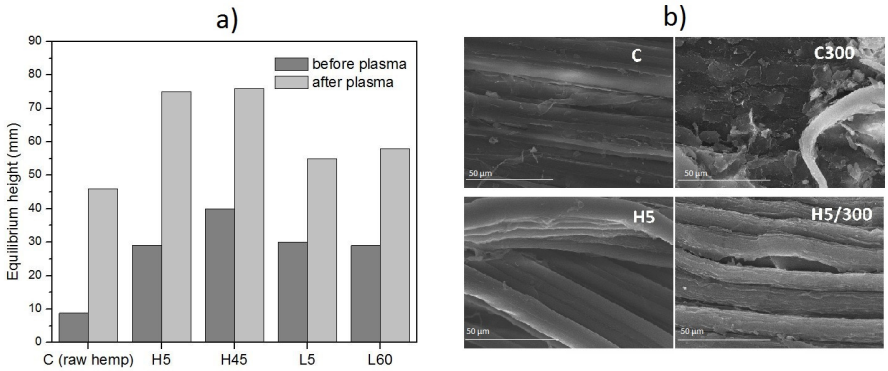

Figure 2: The effect of DBD in air on a) wettability and b) morphology of raw hemp (C) and hemp fibers with lower content of hemicelluloses (H5 and H45) and with lower content of lignin (L5 and L60) (Pejic et al. 2020)

Water retention power is sorption property related to the entire sample not just the surface of material. WRP represents the total water holding capacity of all

voids and pores in the fiber structure (Lazić et al. 2018). Therefore, we have examined the influence of plasma treatment on WRP, and found that it is almost unchanged by plasma treatment (Fig 3). It can be concluded that even though plasma influences capillarity and morphology of samples, plasma effect is limited to the surface, while bulk of material and properties related to the bulk such is WRP underwent almost no changes after plasma treatment. Initial increase of WRP of precursor hemp fibers L5 and L60 (with lower content of lignin) remained the same after plasma treatment and exhibited the highest WRP of all samples.

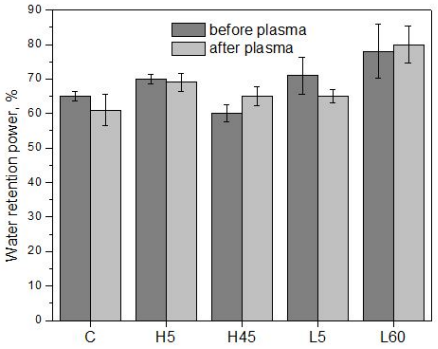

Figure 3: Water retention power (WRP) of different hemp samples before and after plasma treatment

CONCLUSION

In this work, DBD treatment was applied on hemp fibers with different content of hemicelluloses and lignin. Plasma treatment of raw hemp fibers led to a significant improvement of wettability (5 times) estimated through capillary rise. The maximum equilibrium height was obtained by DBD treatment of hemp fibers with lower content of hemicelluloses (H5 and H45). Improved wettability is mainly the consequence of change in fibers morphology while the bulk of material is preserved which was corroborated by no changes in water retention power, i.e. property related to the bulk of material. Overall, this investigation showed that plasma has a potential to substitute the chemical treatments for some applications of hemp, which require improved wettability or increased surface roughness.

References

Ibrahim, N. A., Hashem, M. M., Eid, M. A., Refai, R., El-Hossamy, M., Eid, B. M.: 2010, *The Journal of The Textile Institute*, **101**, 1035.

Lazić, B. D., Pejić, B. M., Kramar, A. D., Vukčević, M. M, Mihajlovski, K. R., Rusmirović, J. D., Kostić, M. M.: 2018, *Cellulose*, **25,** 697.

Li, Y., Zhang, J., Cheng, P., Shi, J., Yao, L., Qui, Y.: 2014, *Industrial Crops and Products*, **61**, 16.

Pejic, B. M., Kramar, A. D., Obradovic, B. M., Zekic, A., Kuraica, M. M., Kostic, M. M.: 2020, *Carbohydrate Polymers,* **236***,* 116000.

Shishoo, R.: 2007, *Plasma Technologies for Textiles,* Woodhead Publishing Limited, Cambridge.

Ventura, H., Claramunt, J., Navarro, A., Rodriguez-Perez, M. A., Ardany, M.: 2016, *Materials*, **9**, 93.

Wang, H., Postle, R., Kessler, R., Kessler, W.: 2003, *Textile Research Journal*, **73**, 664.

Publ. Astron. Obs. Belgrade No. 99 (2020), 221 - 224 *Contributed Paper*

FORMATIVE TIME DELAY DISTRIBUTIONS FOR MULTIELECTRON INITIATION AND TOWNSEND BREAKDOWN IN NEON (II)

V. Lj. MARKOVIĆ and S. N. STAMENKOVIĆ

Department of Physics, Faculty of Sciences and Mathematics, University of Niš, PO Box 224, 18001 Niš, Serbia
E-mail vidosav@pmf.ni.ac.rs,
ssuzana@pmf.ni.ac.rs

Abstract. Formative time delay distributions for multielectron initiation and Townsend breakdown mechanism in neon are derived. The derived theoretical distributions for the formative time delay are compared to the experimental distributions measured in neon and a good agreement was found.

1. INTRODUCTION

Study of electron avalanche multiplication is important for the electrical breakdown of gases (Raether 1964, Meek 1978), as well as for the operation of radiation and particle detectors (Sauli 2014, Titov 2012). By studying the fluctuation phenomena in the passage of electrons through lead and gases, Furry 1937 and Wijsman 1949 derived the electron number distributions of avalanches initiated by one particle, which for a large number of electrons are approximated by the exponential distributions. As for our studies in the field of avalanche statistics, the statistical analyses and Monte Carlo simulation of the size distribution of electron avalanches were carried out in Jovanović et al. 2019, Stamenković et al. 2018, 2020, and Marković et al. 2019. In Jovanović et al. 2019, the experimental results for the single electron initiation from, were modeled using the Monte Carlo simulation, and the shape of the distribution under different conditions was discussed. A generalization of the primary electron avalanche statistics for multielectron initiation based on the negative binomial distribution (NBD) and the continual Gaussian approximation was proposed in Stamenković et al. 2018. Besides that, when the emission of initiating electrons is a homogeneous (stationary) and an inhomogeneous (non-stationary) Poisson process, the weighted mixtures of NBDs for electron avalanche statistics are applied in Marković et al. 2019. In Stamenković et al. 2020, the statistics of secondary electron avalanches

with ion-induced electron emission in air was based on NBD and its mixtures, as well as on their Gaussian continual approximations.

On the other hand, it is well known from early breakdown studies that there is a time interval between the moment of voltage application to the spark gap and the electrical breakdown. This time interval is referred as the breakdown time delay t_d and consists of the statistical time delay t_s and the formative time delay t_f (Meek 1978). The time which elapses between the application of a voltage greater than the static breakdown voltage U_s and the appearance of a free electron initiating breakdown is the statistical time delay and from this moment to the collapse of the applied voltage and occurrence of a self-sustained current is the formative time delay (Meek 1978). By measuring the statistical time memory curve $t_s(\tau)$, the formative time memory curve $t_f(\tau)$ and the dynamic breakdown voltage memory curve $U_b(\tau)$, (τ is the afterglow period or relaxation time), the transition regimes of gas discharges have been studied (Marković et al. 2009, 2005a, 2005b). The memory effect in nitrogen and nitrogen mixtures was observed with different voltage pulses (DC, RF, linearly rising or ramp voltage pulses and others) (Huo et al. 2014, Dyatko et al. 2018, Marković et al. 2018), as well as in RPC and Compass RICH (Fonte et al. 2008).

In this paper, we compared the experimental formative time distributions with theoretical distributions for multielectron initiation and Townsend breakdown mechanisms in neon. The paper is organized as follows. In Section 2, the experimental details for the breakdown time delay measurements are shortly quoted, while in Section 3, the experimental formative time distributions in neon are compared with derived theoretical distributions.

2. EXPERIMENTAL DETAILS

The breakdown time delay measurements were carried out on a gas tube made of borosilicate glass (8245, Shott technical glass) with volume of $V \approx 300\ cm^3$ and gold-plated copper cathode, with the diameter $D = 0.6\ cm$ and the gap distance $d = 0.6\ cm$. The tube was filled with research purity neon at the pressure of (Matheson Co. with a nitrogen impurity below $1\ ppm$. Prior to measurements, the cathode surface was conditioned by running a glow discharge and several thousands breakdowns. The static breakdown voltage was $U_s = 271\ V$ DC. The time delay measurements were carried out by applying step pulses, at glow current $I_g = 0.1\ mA$, glow time $t_g = 1\ s$, working voltage $U_w = 320\ V$ and at different afterglow periods τ. The personal computer with interface was used to control the value of afterglow period and other basic parameters of the experiment, as well as for collection and analysis of data, achieving the voltage rise time and resolution limit below 0.2 microseconds. During the measurements the tube was protected from external light. More details about the experimental procedure, measuring system and tube preparation can be found in Marković et al. 2009, 2005a, 2005b.

3. THE FORMATIVE TIME DELAY DISTRIBUTIONS FOR MULTIELECTRON INITIATION IN NEON

According to I, the formative time delay distribution for streamer breakdown mechanism as a function of number of initiating electrons k is given by:

$$\rho_T{}^{str}(t_f) = \frac{\alpha w_e}{\Gamma(k)}\left[\frac{kn_c}{\exp(\alpha w_e t_f)}\right]^k \exp\left(-\frac{kn_c}{\exp(\alpha w_e t_f)}\right), \quad (1)$$

where α is the Townsend first electron ionization coefficient, w_e is the electron drift velocity and $n_c \approx 10^8$ is the critical number of electrons. For Townsend breakdown mechanism, the formative time delay distribution when the number of initiating electrons k is high, is given by similar relation:

$$\rho_T^{Town}(t_f) = \frac{\alpha\gamma w_i}{\Gamma(k)}\left[\frac{kn_T}{\exp(\alpha\gamma w_i t_f)}\right]^k \exp\left(-\frac{kn_T}{\exp(\alpha\gamma w_i t_f)}\right) \quad (2)$$

where γ is the secondary ionization coefficient, w_i is the ion drift velocity and n_T is the critical number of electrons for Townsend breakdown, before the fast super-exponential current rise (Marković et al. 2007, 2008).

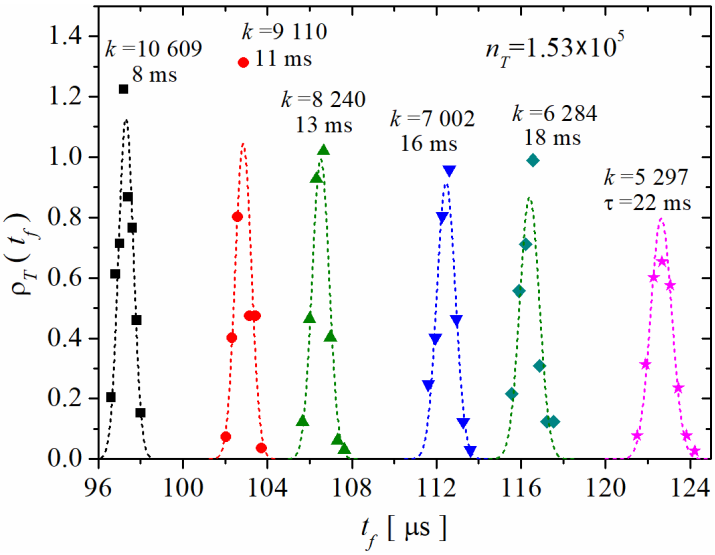

Figure 1: The formative time delay distributions for the Townsend breakdown mechanism in neon fitted by the theoretical distributions (2) with different number of initiating electrons k.

The memory effect in atomic and molecular gases was studied by measurements of the statistical time memory curves, the formative time memory curves, as well as the breakdown voltage memory curves (Marković et al. 2009, 2005a, 2005b,

2018, Huo et al. 2014, Dyatko et al. 2018). While studying the memory effect in neon (Marković et al. 2009), the statistical and formative time delay distributions were measured at different preionization levels (afterglow periods). The derived theoretical distributions (2) are compared to the experimental distributions measured in neon, taking into account that $\bar{t}_f = \ln(n_T/k)/(\alpha\gamma w_i)$ (Marković et al. 2008), and a good agreement was found with $\gamma = 2.2 \times 10^{-2}$, $w_i = 1.62 \times 10^5\ cm/s$ and $n_T = 1.53 \times 10^5$ (Figure 1).

Acknowledgments: The authors are grateful to the Ministry of Education, Science, and Technological Development of the Republic of Serbia for partial financial support (contract number 451-03-68/2020-14/200124)

References

Dyatko, N., Ionikh, Yu., Meshchanov, A., Napartovich, A. : 2018, *Plasma Phys. Rep*., **44**, 334.

Furry, H. : 1937, *Phys. Rev.* **52**, 569.

Fonte, P., Peskov, V. : 2008, Report at the RD51 collaboration meeting in Amsterdam, https://indico.cern.ch › contributions › attachments › WG-2_presentation

Huo, W. G., Jian, S. J., Yao, J., Ding, Z. F. : 2014, *Phys. Plasmas*, **21**, 053505 (2014).

Jovanović, A. P., Stamenković, S. N., Stankov, M. N., Marković, V. Lj. : 2019, *Contrib. Plasma Phys*., **59**, 272.

Marković, V. Lj., Gocić, S. R., Stamenković, S. N., Petrović, Z. Lj. : 2005a, *Physics of Plasmas*, **12**, 073502.

Marković, V. Lj., Stamenković, S. N., Gocić, S. R., Petrović, Z. Lj. : 2005b, *Contrib. Plasma Phys*. **45**, 476.

Marković, V. Lj., Stamenković, S. N., Gocić, S. R. : 2007, *Contrib. Plasma Phys*., **47**, 413.

Marković, V. Lj., Stamenković, S. N., Gocić, S. R. : 2008, *Canad. J. Phys*., **86**, 947.

Marković, V. Lj., Gocić, S. R., Stamenković, S. N. : 2009, *J. Phys. D*, **42**, 015207.

Marković, V. Lj., Jovanović, A. P., Stamenković, S. N., Stankov, M. N. : 2018, Contrib. papers of 29th Summer School and Int. Symposium on the Physics of Ionized Gases (Belgrade, Serbia) 202

Marković, V. Lj., Stamenković, S. N., Jovanović, A. P. : 2019, *JINST*, **14**, P06009.

Meek, J. M., Craggs, J. D. (Eds.): 1978, *Electrical Breakdown of Gases*, John Wiley & Sons, Chichester.

Raether, H. : 1964, *Electron Avalanches and Breakdown in Gases*, Butterworths, London.

Sauli, F. : 2014, *Gaseous Radiation Detectors, Fundamentals and Applications*, University Press, Cambridge.

Stamenković, S. N., Marković, V. Lj., Jovanović, A. P., Stankov, M. N. : 2018, *JINST*, **13**, P12002.

Stamenković, S. N., Marković, V. Lj., Stankov, M. N., Jovanović, A. P. : 2020, *Eur. Phys. J. Plus*, 135: 51.

Stamenković, S. N., Marković, V. Lj., Jovanović, A. P. : 2020, Contributed papers of 30th Summer School and International Symposium on the Physics of Ionized Gases (Šabac, Serbia) (previous paper at this conference, designated as I).

Titov, M. : 2012, *Gaseous Detectors*, in: C. Grupen, I. Buvat (Eds.) *Handbook of Particle Detection and Imaging*, Springer, Berlin.

Wijsman, R. A. : 1949, *Phys. Rev.*, **75**, 833.

Publ. Astron. Obs. Belgrade No. 99 (2020), 225 - 228 *Contributed Paper*

APPLIED VOLTAGE WAVEFORM SUITABLE TO CONTROL PARAMETERS OF DIELECTRIC BARRIER DISCHARGE PLASMA JET

M. E. PINCHUK[1], A. M. ASTAFIEV[1], R. A. AZNABAEV[1,2] and O. M. STEPANOVA[1]

[1] *Institute for Electrophysics and Electrical Power of the Russian Academy of Sciences, Dvortsovaya naberezhnaya 18, St. Petersburg 191186, Russia*

[2] *Saint Petersburg State University, Universitetskaya naberezhnaya, 7-9, St. Petersburg, 199034*
E-mail pinchme@mail.ru

Abstract. The paper demonstrates that it is possible to control a guided streamer traveling along a helium dielectric-barrier discharge plasma jet by means of varying the output transformer capacitance. It has realized with the additional output capacitance for the stepwise propagation of the streamer in the numeric simulation.

1. INTRODUCTION

Non-equilibrium atmospheric plasmas are currently used in a wide range of new technologies. Novel approaches to apply such plasmas and unexpected ways to develop them are constantly appearing (Adamovich et al. 2017; Nikiforov et al. 2019). Here, the challenge to use atmospheric plasmas, including plasma jets based on dielectric-barrier discharge (DBD) in biomedicine is one of the powerful driving tasks (Metelmann et al. 2018; Bekeschus et al. 2019; Brandenburg et al. 2017).

The type of the applied voltage determines the characteristics of plasma jets significantly: their parameters are different for ns- and μs- pulsed voltage and sinusoidal voltage (Walsh et al. 2006; Xiong et al. 2010; Zhang et al. 2014, Florez et al. 2019). The development of the power supplies for such a gas-discharge system can be considered as a separate research topic (Bonnin et al. 2013; Dragonas et al. 2015, Moshkunov et al. 2018). And to fit the applied voltage mode to the load, a set of issues should be figured out (Bonnin et al. 2013; Dragonas et al. 2015, D'iez et al. 2007).

Previously, we recorded a stepwise mode of the guided streamer propagation (Pinchuk et al. 2019, 2020; Stepanova et al. 2020) along a helium plasma jet fed by voltage of a special waveform consisting of a superposition of bipolar rectangular pulses and oscillating sinusoidal signals shifted relatively ground potential.

This paper considers the possibility of controlling guided streamer stepwise propagation by varying the output capacitance of the power supply transformer (Martin-Ramos et al. 2008; Rueda et al. 2019) owing to the addition of a filtering capacitance.

2. APPLIED VOLTAGE WAVEFORM AND GUIDED STREAMER PROPAGATION

The studied discharge system was the same as in (Pinchuk et al. 2019, 2020; Stepanova et al. 2020). It was designed to generate the atmospheric pressure plasma jet (APPJ) based on a DBD in a helium flow in an axisymmetric electrode system "inner electrode (central rod) – gas gap – dielectric barrier (quartz tub) – outer electrode (outer ring)". A diameter of inner electrode is 1.5 mm; the inner diameter and thickness of the quartz tube are 4.6 and 1 mm, correspondingly. A ring grounded electrode 5 mm wide is located 5 mm from the edge of the discharge tube. The experimental setup is described in more detail in Stepanova et al. 2017.

To simulate the propagation of the plasma jet, we used an equivalent circuit of APPJ made up of RC-circuits cascades (see Figure 1) (Slutsker et al. 2017). The developed numerical model (Pinchuk et al. 2018a, 2018b) was implemented in XCOS/Scilab. It adequately describes the experimental data on slowing down a guided streamer at adding air admixture into the helium plasma jet and the stepwise propagation of the streamer (Pinchuk et al. 2015, 2019).

In XCOS, a cascade of ten RC-circuits simulating a space with a length of 1 cm is put in one block. Then, the series of blocks are equivalent to the space of a definite extension. A section of the equivalent circuit (see Figure 1) with Rg, Cg and Cd elements substitutes DBD inside the discharge cell, whereas the circuit section of RN-CN is of APPJ propagation space.

The calculations were done with taking account the following assumptions: (i) the distance of 5 cm along the jet's axis was divided into 50 elements; (ii) each element of the jet length was substituted by the corresponding capacity and resistance (Pinchuk et al. 2019, 2018a).

The schematics of the power supply is presented in Figure 2. The power supply is built according to the half-bridge circuit with a step-up transformer. Adding the capacity C_0 decreases the frequency of the self-oscillations of an output circuit with the plasma jet. The experimentally measured applied voltage for the helium APPJ with the gas rate of 5 l/min is shown in Figure 3. At C_0 = 20 pF the changing of the frequency is about 35 kHz.

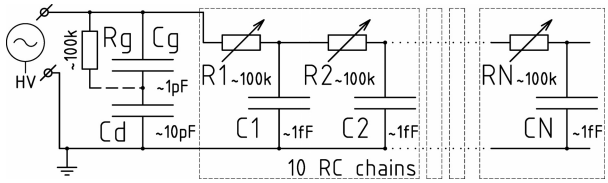

Figure 1: Equivalent circuit of APPJ.

The dynamics of the jet's propagation has been considered. To simplify the analysis, the oscillating part of the applied voltage was simulated without damping. We obtained (see Figure 4) that the additional capacity makes the streamer stop a little further with a little longer period of slowing down at the same jet's length.

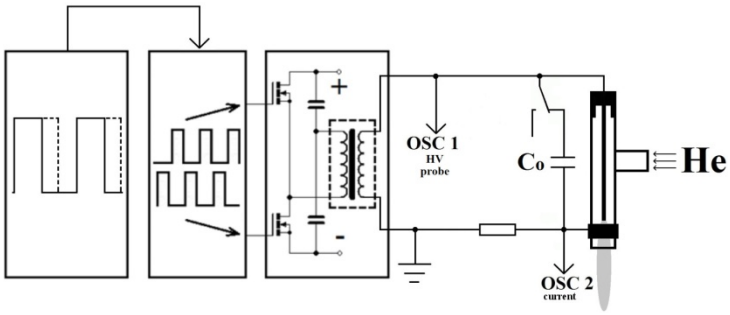

Figure 2: Power supply for APPJ generation.

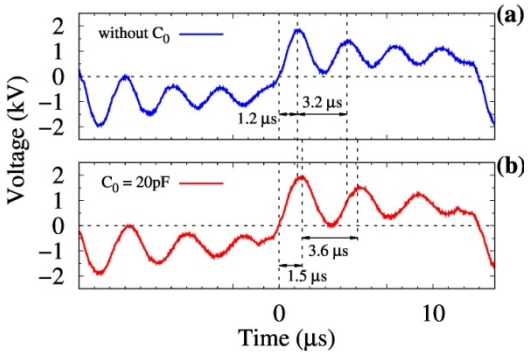

Figure 3: Applied voltage signal for helium APPJ without capacitance C_0 **(a)** and with additional capacitance C_0 **(b)**.

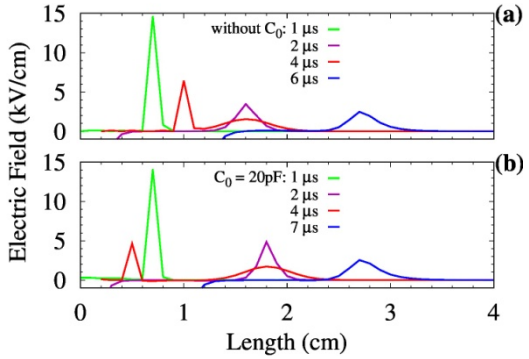

Figure 4: Calculated profiles of the electric field along the APPJ without capacitance C_0 **(a)** and with additional capacitance C_0 **(b)**.

3. CONCLUSION

The streamer propagation variation at tailoring applied voltage was calculated by means of numerical modeling. The way of flexible plasma jet control has been demonstrated. It is realized by changing the capacitance of the power supply transformer.

The study was financially supported by the Russian Science Foundation (project 18-79-10048).

References

Adamovich, I., et al : 2017, *J. Phys. D: Appl. Phys.*, **50**, 323001
Bekeschus, S., et al : 2019, *Plasma Process Polym.*, **16**, 1800033.
Bonnin, X., et al : 2013, *Eur. Phys. J.: Appl. Phys.*, **64**, 10901.
Brandenburg, R. : 2017, *Plasma Sources Sci. Technol.*, **26**, 53001.
D'iez, R., et al : 2007, *Eur. Phys. J.: Appl. Phys.*, **37**, 307.
Dragonas, F.A., et al : 2015, *IEEE Trans. Ind. Appl.*, **51**, 3334.
Florez, D., et al : 2019, In: 2019 *IEEE International Conference on Environment and Electrical Engineering and 2019 IEEE Industrial and Commercial Power Systems Europe (EEEIC/I&CPS Europe)*, Genova, Italy, doi 10.1109/eeeic.2019.8783361.
Martin-Ramos, J.A., et al : 2008, *IEEE Trans. Power Electron.*, **23**, 1608.
Metelmann, H.-R., von Woedtke, T., Weltmann K.-D. : 2018, *Comprehensive Clinical Plasma Medicine*, Berlin: Springer -- Verlag.
Moshkunov, S.I., et. al : 2018, *In: International Congress on Energy Fluxes And Radiation Effects (EFRE 2018),* Book of Abstracts, Tomsk, Russia, p 160.
Nikiforov, A., Chen, Z. : 2019, *Atmospheric Pressure Plasma - from Diagnostics to Applications*, London: IntechOpen.
Pinchuk, M., et al : 2015, *In: Proc. VIII Int. Conf. on Plasma Physics and Plasma Technology (PPPT-8)*, Minsk, Belarus, vol **I**, p 51.
Pinchuk, M., Stepanova, O. : 2018a, *In: First International Conference on Cold Plasma Sources and Applications (COPSA-2018)*, Ypres, Belgium, p 147.
Pinchuk, M.E., et al : 2018b, *In: 29th Summer School and International Symposium on the Physics of Ionized Gases (SPIG-2018)*, Belgrade, Serbia, p 214.
Pinchuk, M.E., et al : 2019, *Appl. Phys. Lett.*, **114**, 194103.
Pinchuk, M.E., et al : 2020, *Appl. Phys. Lett.*, **116**, 164102.
Rueda, V., : 2019, *IEEE Trans. Ind. Appl.*, **55**, 6567.
Slutsker, Y.Z., et al : 2017, *Phys. Plasmas*, **24**, 103510.
Stepanova, O., et al : 2017, *Plasma Medicine*, **7**, 3, 187.
Stepanova, O., et al : 2020, *Jpn. J. Appl. Phys.*, **59**, SHHC03.
Walsh, J.L. et al : 2006, *Appl. Phys. Lett.*, **88**, 171501.
Xiong, Q., et al : 2010, *Phys. Plasmas*, **17**, 43506.
Zhang, C., et al : 2014, *Phys. Plasmas*, **21**, 103505.

Publ. Astron. Obs. Belgrade No. 99 (2020), 229 - 232 *Contributed Paper*

TRANSITION FROM ELECTRON AVALANCHE NUMBER DISTRIBUTIONS TO FORMATIVE TIME DELAY DISTRIBUTIONS FOR MULTIELECTRON INITIATION AND STREAMER BREAKDOWN MECHANISM (I)

S. N. STAMENKOVIĆ and V. Lj. MARKOVIĆ

Department of Physics, Faculty of Sciences and Mathematics, University of Niš, PO Box 224, 18001 Niš, Serbia
E-mail ssuzana@pmf.ni.ac.rs,
vidosav@pmf.ni.ac.rs

Abstract. Transition from number distributions of electron avalanches to formative time delay distributions for streamer breakdown mechanism and multielectron initiation is derived. When the number of initiating electrons k is small, the formative time delay distributions are asymmetric with pronounced right tail, while for $k > 10$ the formative time delay distributions are Gaussians.

1. INTRODUCTION

By studying the fluctuation phenomena in electron avalanches initiated by one particle, Furry 1937 and Wijsman 1949 derived the electron number distribution of an avalanche, which for a large number of electrons can be approximated by the exponential distribution. Numerous experimental distributions of carrier numbers of electron avalanches have been reported by Raether 1964 and coworkers. However, some experimental distributions (Raether 1964) show a deviation from the Furry and Wijsman distribution at higher values of the reduced electric field. The Polya distribution function was therefore introduced (Byrne 1962, Lansiart et al. 1962, Cookson et al. 1966a, Genz 1973) to describe this deviation. The calculation of the carrier number distribution function was presented in Legler 1964 and Cookson et al. 1966b, where the influence of the secondary ionization coefficient was taken into account. A review of avalanche models can be found in Alkazov 1970.

In Jovanović et al. 2019, the experimental results for the single electron initiation were modeled using the Monte Carlo simulation, and the shape of the distribution under different conditions was discussed. A generalization of the electron avalanche statistics for multielectron initiation with fixed and Poisson-

distributed number of initiating electrons was proposed in Stamenković et al. 2018, Marković et al. 2019. In Stamenković et al. 2020, the statistics of secondary electron avalanches with ion-induced electron emission in air was based on NBD and its mixtures, as well as on their Gaussian continual approximations.

In Devismes et al. 2002, a search for an optimum time response function of spark counters was undertaken, changing voltage, content of noble and quencher gases, pressure and energy-loss. The time response function of a spark counter was then calculated considering that the time delay and its fluctuations originate from the avalanche growth (Mangiarotti et al. 2002). Analytic expressions for the shape of the time response function were derived for the single cluster avalanche without the space charge effect, as well as for the multicluster environment with the effects of space charge. It was found that a peak and a tail of the time response probability density correlate with an increase of the overall time delay (Mangiarotti et al. 2002). Afterwards, in Gobbi et al. 2003, the fluctuation theory developed in Mangiarotti et al. 2002 was applied to measurements of spark counters Devismes et al. 2002 and extended to other counters. In this paper (designated as I), the number distributions of electron avalanches and formative time delay distributions for streamer breakdown mechanism are studied, while in Marković et al. 2020 (designated as II) the formative time delay distributions for Townsend breakdown mechanism are studied.

2. TRANSITION FROM THE ELECTRON AVALANCHE NUMBER DISTRIBUTIONS TO THE FORMATIVE TIME DELAY DISTRIBUTIONS FOR STREAMER BREAKDOWN MECHANISMS AND MULTIELECTRON INITIATION

According to Raether 1949, the formative time delay t_f is approximately equal to the time the avalanche takes to build up to the certain magnitude n (usually to the critical number of electrons $n_c \approx 10^8$). Therefore, the fluctuation in avalanche growth can be described as a fluctuation in avalanche length instead of final number of electrons. For mathematical derivation of probability density form, the multiplication N at fixed length d is transformed into the length L at fixed n_c. During the derivation, the replacement of random variables was carried out and probability $P_N(n) = \int \rho_N\,(n)dn$ that the multiplication N is less than n is replaced by the probability $P_L(l) = \int \rho_L\,(l)dl$ that avalanche length is less than l:

$$P_N(n)dn = P_L(l)dl \tag{1}$$

The form of $\rho_L(l)$ is obtained by taking into account probability $P(L > l)$ that the avalanche will grow longer than a length l, which is equal to the probability that over a length l it has not yet reached the critical number of electrons n_c, $P(N < n_c, d = l)$:

$$P_L(l) = 1 - P(L > l) \tag{2}$$

Assuming the probability density $\rho_N(n)$ dependence on avalanche length d into the form:

$$\rho_N(n) \equiv \rho_N(n,d) = \frac{1}{\bar{n}(d)} f\left(\frac{n}{\bar{n}(d)}\right), \tag{3}$$

and introducing the new variable $x = n/\bar{n}$, as well as $\bar{n}(l) = \exp(\alpha l)$, $\rho_L(l)$ follows

$$\rho_L(l) = \alpha\, x(l) f[x(l)] = \frac{\alpha n_c}{\bar{n}(l)} f\left(\frac{n_c}{\bar{n}(l)}\right), \tag{4}$$

In the case of Polya probability density distribution for the electron number in the avalanche at fixed distance d:

$$\rho_N(n) \equiv \rho_N(n,d) = \frac{k}{\Gamma(k)\bar{n}(d)} \left[\frac{kn}{\bar{n}(d)}\right]^k \exp\left(-\frac{kn}{\bar{n}(d)}\right), \tag{5}$$

probability density $\rho_L(l)$ takes the form:

$$\rho_L(l) = \frac{\alpha k n_c}{\Gamma(k)\bar{n}(l)} \left[\frac{kn_c}{\bar{n}(l)}\right]^k \exp\left(-\frac{kn_c}{\bar{n}(l)}\right), \tag{6}$$

The previous relation is further transformed into the formative time delay probability density $\rho_T(t_f)$ by using $\bar{n}(l) = \exp(\alpha l) = \exp(\alpha w_e t_f)$:

$$\rho_T(t_f) = \frac{\alpha w_e}{\Gamma(k)} \left[\frac{kn_c}{\exp(\alpha w_e t_f)}\right]^k \exp\left(-\frac{kn_c}{\exp(\alpha w_e t_f)}\right), \tag{7}$$

where α is the Townsend first electron ionization coefficient, w_e is the electron drift velocity and k is the number of initiating electrons. According to Genz 1973, the formative time distributions for streamer breakdown mechanism at different number of initiating electrons k are presented in Figure 1. When the number of initiating electrons k is small, the formative time delay distributions are asymmetric with pronounced right tail. With increasing k, the formative time distributions shift to the shorter formative times and become narrower and higher, more symmetric and Gauss-like. As statistical tests show, for $k > 10$ the hypothesis that the formative time distributions are Gaussians cannot be rejected (Fig. 1).

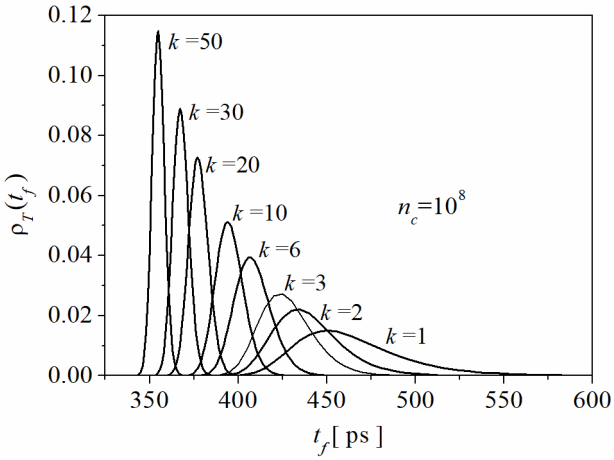

Figure 1: The formative time distributions for streamer breakdown mechanism at different number of initiating electrons k.

Acknowledgments: The authors are grateful to the Ministry of Education, Science, and Technological Development of the Republic of Serbia for partial financial support (contract number 451-03-68/2020-14/200124)

References

Alkazov, G. D. : 1970, *Nucl. Instrum. Meth*., **89**, 155 (1970).
Byrne, J. : 1962, *Proc. Roy. Soc*. Edinburgh Section A, **66**, 33.
Cookson, A. H., Ward, B. W., Lewis, T. J. : 1966a, *Brit. J. Appl. Phys*., **17**, 891.
Cookson, A. H., Lewis, T. J. : 1966b, *Brit. J. Appl. Phys*., **17**, 1473.
Devismes, A., Frank, Ch., Kress, T., Gobbi, A., Eschke, J., Herrmann, N., Hildenbrand, K. D., Koczon, P., Petrovici, M. : 2002, *Nucl. Instr. and Meth.* A, **482**, 179.
Furry, H. : 1937, *Phys. Rev.* **52**, 569.
Genz, H. : 1973, *Nucl. Instr. and Meth.* **112**, 83 and references therein.
Gobbi, A., Mangiarotti, A. : 2003, *Nucl. Instr. and Meth.* A, **508**, 23.
Jovanović, A. P., Stamenković, S. N., Stankov, M. N., Marković, V. Lj. : 2019, *Contrib. Plasma Phys*., **59**, 272.
Lansiart, L., Morucci, J. P. : 1962, *J. Phys. Phys. Appl.* (Suppl. 6), **23**, 102.
Legler, H. : 1964, *Z. Naturforsch*. **19A**, 481.
Marković, V. Lj., Stamenković, S. N., Jovanović, A. P. : 2019, *JINST*, **14**, P06009.
Marković, V. Lj., Stamenković, S. N., Jovanović, A. P. : 2020, Contributed papers of 30th Summer School and International Symposium on the Physics of Ionized Gases (Šabac, Serbia, 2020) (subsequent paper at this conference, designated as II).
Mangiarotti, A., Gobbi, A. : 2002, *Nucl. Instr. and Meth*. A **482**, 192.
Raether, H. : 1964, *Electron Avalanches and Breakdown in Gases*, Butterworths, London.
Stamenković, S. N., Marković, V. Lj., Jovanović, A. P., Stankov, M. N. : 2018, *JINST*, **13**, P12002.
Stamenković, S. N., Marković, V. Lj., Stankov, M. N., Jovanović, A. P. : 2020, *Eur. Phys. J. Plus*, 135: 51.
Wijsman, R. A. : 1949, *Phys. Rev.*, **75**, 833.

Publ. Astron. Obs. Belgrade No. 99 (2020), 233 - 236 *Contributed Paper*

OPTICAL EMISSION SPECTROSCOPY OF A GLIDING ARC TORNADO DEVICE

RUGGERO BARNI[1], PRINCE ALEX[1], ANIKA SALANTI[1], CARMEN CANEVALI[2], LUCA ZOIA[3], MARCO ORLANDI[3] and CLAUDIA RICCARDI[1]

[1]*Dipartimento di Fisica G.Occhialini, Università degli Studi di Milano-Bicocca, piazza delle Scienza 3 Milano I-20126, Italy*

E-mail: claudia.riccardi@mib.infn.it

[2]*Dipartimento di Scienza dei Materiali, Università degli Studi di Milano-Bicocca,*

[3]*Dipartimento di Scienze dell'Ambiente e della Terra, Università degli Studi di Milano-Bicocca*

Abstract. Optical emission spectroscopy was used to characterize the gas-phase in a gliding arc tornado reactor used for plasma applications. Results concerning the transition between spark and fully developed arc regimes are presented.

1. INTRODUCTION

The Gliding Arc Tornado (GAT) was proposed long ago to improve properties of gliding arcs reactors, in particular a better insulation of the device walls from the discharge, with a higher level of non-equilibrium and much larger residence times (see Kalra et al. 2005). These devices were mostly used for industrial applications including fuel conversion, carbon dioxide conversion and waste treatment (see Liu et al. 2016, Bublievsky et al. 2015). Their name refers to the formation of a reverse vortex flow configuration, a tornado, usually achieved by tangential gas injection near the walls in a cylindrical chamber. We have developed and used a kind of these devices for the treatment of lignin by plasmas (see Zanini et al. 2008). Milled lignin can be easily in a sustained gas fluxes and advected in the hydrodynamical flow. So optimal interaction with the discharge gas phase could be achieved. Here we will present some results concerning the characterization of the process and its optimization, based on optical diagnostics. Optical Emission Spectroscopy (OES) is a suitable technique to investigate the plasma gas-phase, since it is passive and non-perturbing, and takes advantage of the rich emission pattern in/near visible range of such systems. Besides gathering information about the discharge, it is possible to get insight on the interactions of lignin particles with plasma and the mechanism of the treatment.

2. EXPERIMENTAL SETUP

The discharge was ignited and supplied by means of a high-voltage dc generator (SHV9000 by Alintel). Its performances cannot exceed 5 kV and 2 A at most. It also provided integrated measurements of the total charge effectively delivered and the mean applied high voltage, which could be used to estimate the actual power absorbed by the device. Besides the HV setting, the generator was controlled with a tunable mean current regulation. It also provided integrated measurements such as the total charge effectively delivered before being switched off and the mean applied high voltage. The actual electrical characteristics of the discharge are controlled by the supply, by setting a fixed mean current intensity value. The supply was connected to the anode electrode through an electrical circuit (a set of 16 high voltage, high power resistances, with a global resistance of 4 kΩ), which helps to control the electrical characteristics of the discharges. HV sensors were inserted in the circuit also to measure the instantaneous values of the voltages on a digital scope. Due to the limitation in the output current provided by the generator and the external circuit impedance, the discharge assumed an intermittent spark character at low current settings (see Barni et al. 2008). It develops to a full arcing above a certain threshold of the current set, slightly depending on the inlet flow pressure and gas mixture composition. A three turns molybdenum electrode acts as the arc anode, figure 1. HV sensors measure the instantaneous voltage at the ends of the resistors set and thus of the discharge current, as it is shown in Figure 2. It could be grasped as the system shows intense current bursts with a limited duration, separated by dead times, corresponding to a sequence of spark discharges. Although not exactly constant, the shape, the amplitude, the duration, and the repetition rate of bursts were comparable and fairly cyclic. These parameters were measured and averaged using long time series (10 MSamples) with a digital scope and their statistical properties were studied.

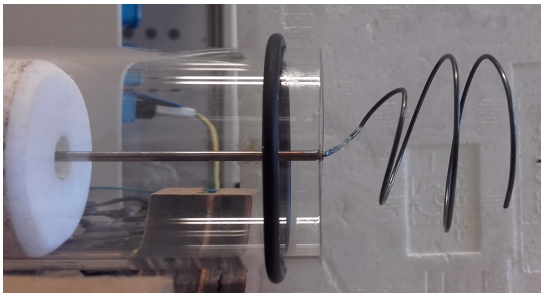

Figure 1: Experimental layout of the GAT device.

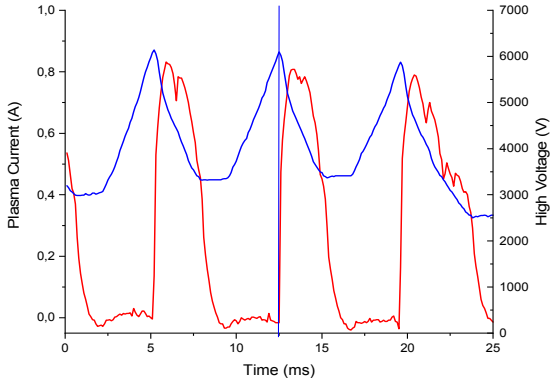

Figure 2: Electrical characteristics of the GAT device in sparking mode.

3. RESULTS AND DISCUSSION

While the pattern of the single discharge is somewhat fuzzy, it appears that most of the flow cross section is affected by the discharge and emits light. OES of the discharge is used to gain insight in the excited species produced. Measurements of the emission spectra are obtained with a wide band, low resolution spectrometer. The spectrometer (PS2000 by Ocean Optics) has a resolution of about 0.4 nm and a spectral band extending from 180 to 860 nm. It is equipped with a 10 μm slit, a holographic grating (600 lines/mm, blazed at 400 nm), and a coated quartz lens to increase sensitivity in UV (see Barni et al. 2008). Emission line intensity was measured and atoms and molecules have been identified (see Pearse et al. 1976). The light emitted from the plasma sheet was collected by means of a UV enhanced optical fibre placed just in front of the exit 10 cm apart, to not perturb the outflowing gas jet. The view-field of the optical fibre was large enough to cover the whole light-emitting region and to smear possible discharge disuniformities. A typical spectrum is shown in Figure 3.

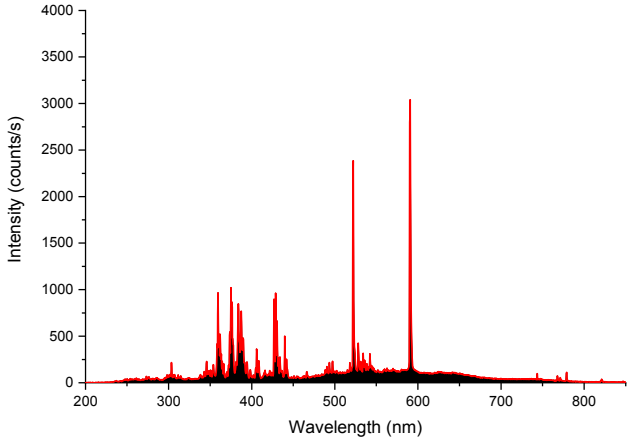

Figure 3: A typical emission spectra of the plasma in an air GAT.

Spectra of the light emitted from the discharge show a broad continuum peaking at about 500-550 nm, with superimposed a rich structure of lines, some quite narrow, comparable to the spectrometer resolution and other that appears larger, clearly emitted by molecular states and appearing together due to their unresolved rotational substructure. As the mean current setting is increased the continuum contribution increases at expenses of the lines, until transition to arcing is achieved and the spectra approaches a structureless shape. The reported trend is displayed in Figure 4, where the transition could be clearly appreciated.

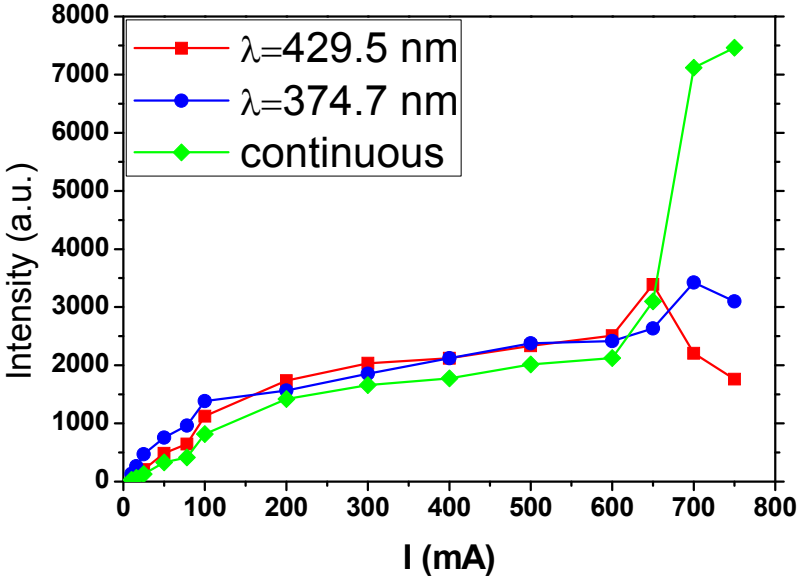

Figure 4: Intensity of a few emission lines and of the continuous as a function of the total current drawn by the GAT.

Acknowledgements

We are pleased to acknowledge the support of our technical staff at the PlasmaPrometeo Center and the funding through the POLISTE project by Cariplo Foundation.

References

Adler, E.: 1977, *Wood Sci. Technol.*, **11**, 169.
Barni, R. et al.: 2008, *Vacuum*, **82**, 217.
Barni, R. et al.: 2008, *J. Appl. Phys.*, **103**, 063302.
Bublievsky, A. F. et al. : 2015, *IEEE Trans. Plasma Sci.*, **43**, 1742.
Kalra, C. S. et al.: 2005, Rev. Sci. Instr., **76**, 025110.
Liu, J. L. et al. : 2016, *Plasma Chem. Plasma Proc.*, **36**, 437.
Pearse, R. W. B., Gaydon, A. G.: 1976, *The Identification of Molecular Spectra*, New York, NY, US: Wiley.
Zanini, S.: 2008, *Bioresources*, **3**, 995.

Publ. Astron. Obs. Belgrade No. 99 (2020), 237 - 240 *Contributed Paper*

NEXT GENERATION OF UNIVERSAL PULSE RESONANCE ATMOSPHERIC PLASMA SYSTEMS

MIROSLAV GULAN[1] and VLADIMIR MILOSAVLJEVIĆ[1,2]

[1]*School of Physics & Clinical & Optometric Science, Technological University Dublin, Ireland*

[2]*Faculty of Physics, University of Belgrade, P.O.B. 368, Belgrade 11000, Serbia*
E-mail miroslav.gulan@gmail.com, vladimir.milosavljevic@tudublin.ie

Abstract. New generation of atmospheric plasma generator was designed to create atmospheric plasma discharge between 2 electrodes with gap which is useable in food industry for plasma treatment of food or for any low conductive material in industry. Design was leaded to reach parameters of plasma which are unique on the market to simplify application of plasma treatment in real industry. System allow to create plasma discharge in gap from 5 to 60 mm in space of hundreds of cm2. The plasma source is based on a pulse resonance circuit which allow create high voltage pulses with ability to control and reduce a current of the plasma discharge. This ability allows to keep a temperature of the treated sample's (organic or inorganic) material at the room temperature.

1. INTRODUCTION

New plasma system was designed to fulfil needs of researchers from academic area with ability to transfer plasma treatment from academic laboratory to industry area. In last several decades, in many papers, impact of the plasma technologies to a surface structure and functionality are studied (Park et al. 2000, Abourayana et al. 2016). In most cases the plasma systems were operated at a low pressure (i.e. vacuum) and they are used for treatment of inorganic materials (Milosavljević and Cullen 2015). There are also available plasma systems which are able to create plasma discharge in atmospheric pressure known as plasma jet or microwave plasma (Cullen and Milosavljević 2015). The main disadvantage of all those systems is, they are able to create only small (local) atmospheric plasma discharge. Therefore, unavailability of such plasma systems to generate atmospheric plasma discharge in volume of thousands cm^3 with possibility to control energy of discharge to keep temperature of treated material low, makes a big obstacle for those systems to be used in food industry.

New pulse resonance atmospheric plasma systems were designed and manufactured to increase possibility of study of plasma treatment impact on sensitive organic and inorganic materials.

2. EXPERIMENTAL SETUP

The plasma system is based on tuned pulse resonance circuit which allows reaching high voltage on electrodes and reducing current via plasma to keep temperature of treated material low. A special new design of pulsing plasma power generator allows setting parameters of plasma which help to tune requested plasma treatment applying to different materials. Our plasma system allows to increase the surface-plasma interaction selectivity and to reduce plasma induced damages to the surface.

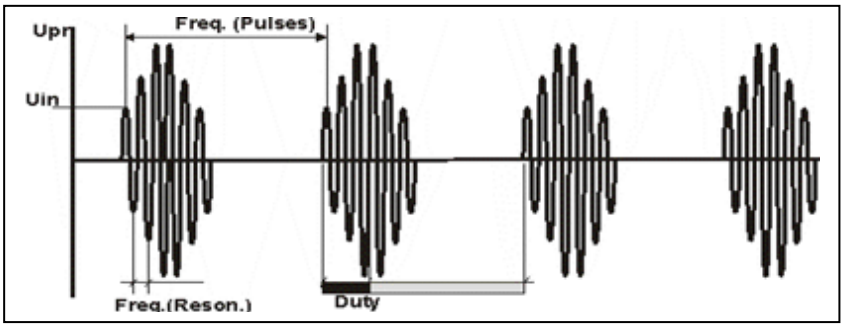

Figure 1: Pulse resonance pulses.

All parameters showed on Fig.1 can be changed. Namely, resonance frequency (Freq.(Reson.)) can be set from 30 kHz to 120 kHz and depend on configuration of the HV transformer and plasma electrodes. Currently used HV transformers are used with frequency about 55kHz. Correct setting of resonance frequency increase output voltage of HV transformer. Pulse frequency (Freq.(Pulses)) can be set from 100 Hz to 3000 Hz, and increasing this frequency would lead to increase the power of plasma discharge. Duty cycle influences current-power of each discharge. Input voltage is set following dielectric barrier between electrodes. Output power of system depends on the configuration of all mentioned parameters and can be set from 30W to 700W. Maximum power is limited also by dimension of electrodes. Maximum power for tested electrode with dimension about 12cm x 17cm is up to 400W.

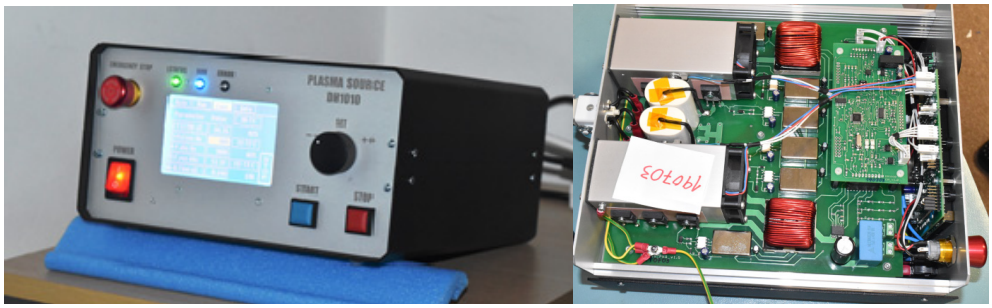

Figure 2: Plasma power supply unit.

The plasma generator (Fig.2) is designed to operate with the customize pin electrode such serves as a HV electrode, and ambient air such serves as a dielectric barrier. No additional dielectric material is required. This pin electrode is used together with flat electrode which is connected to ground. This configuration of electrodes allows to reach gap up to 65 mm between the flat electrode and the pins. Output voltage can go up to 80kVpp (depends on the air gap). On Fig.3 the parallel plate electrodes configuration is presented.

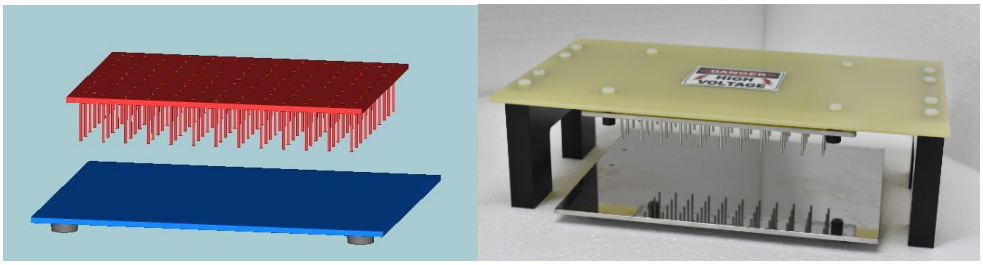

Figure 3: Pin electrodes

In Fig.4 is shown plasma discharge between electrodes. This plasma generator is used to study influence of plasma treatment on organic materials and to find the optimum plasma parameters which would give the best performance of those biological samples at the minimal plasma power (W/cm^2). With increasing the plasma power over a threshold point for the bio-surface activation, the plasma effectiveness stagnate or decrease.

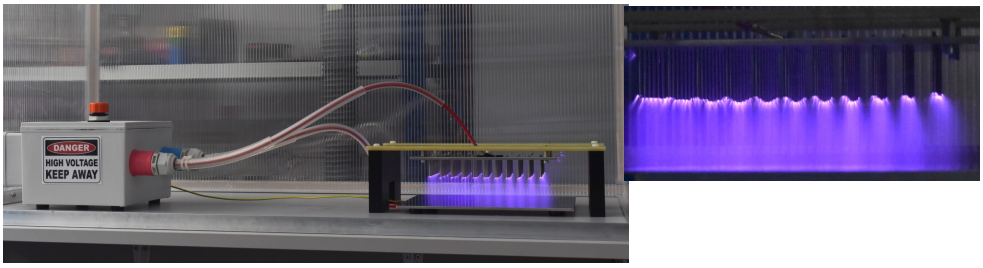

Figure 4: HV Transformer and electrodes with plasma discharge

3. RESULTS AND DISCUSSION

Measured dependence minimum output voltage (peak to peak) in kV to start discharge and number of pins used in top electrode with air gap from 1cm to 6cm between pin and flat electrode is showed on Fig 5. Fig.6 shows max Voltage (peak to peak) in kV before local discharge.

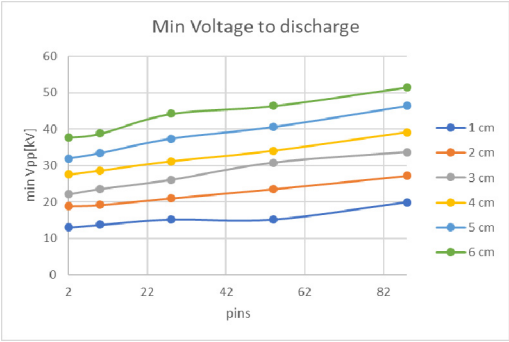

Figure 5: Min. voltage to discharge

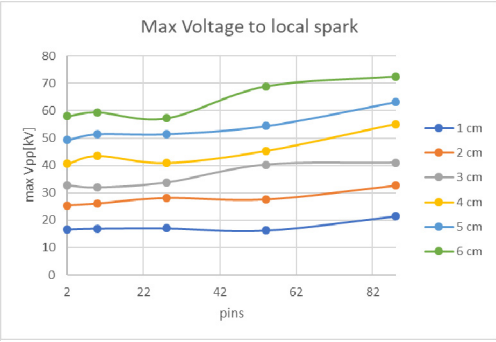

Figure 6: Max. voltage to discharge

4. CONCLUSIONS

The new pulse resonance plasma system, with pins electrode, allows much greater gap between electrodes, and give a possibility to be applied in food industry. Moreover, dielectric material necessary for today's DBD technology, is not required for this system. Therefore there are not issues with sterilization or decontamination of our plasma tool, on the contrary to systems which have thermally and chemical unusable dielectric (e.g. DBD).

References

Abourayana, H. M., Milosavljević, V., Dobbyn, P., Cullen, P. J. and Dowling, D. P.: 2016, *Surf. Coat. Tech.*, **308**, 435.

Cullen, P. J. and Milosavljević, V.: 2015, *Prog. Theor. Exp. Phys.*, 063J01.

Milosavljević, V. and Cullen, P. J.: 2015*, European Phys. Lett.*, **110**, 43001.

Park, J., Henins, I., Herrmann, H. W., Selwyn, G. S., Jeong, J. Y., Hicks, R. F., Shim, D. and Chang, C. S.: 2000*, Appl. Phys. Lett.*, **76**, 288.

Publ. Astron. Obs. Belgrade No. 99 (2020), 241 - 244 *Contributed Paper*

RELATIVISTIC CONFIGURATION INTERACTION OF ENERGY LEVELS AND WAVELENGTHS OF HE-LIKE LITHIUM.

S. MANAI[1] and D.E. SALHI[2]

[1] *Faculty of Sciences of Bizerte, University of Carthage, Tunisia.*
E–mail manai.soumaya12@@gmail.com

[2] *Faculty of Sciences of Tunisia, University of Tunisia, Tunis, Tunisia.*
E–mail salhidhiaelhak@@gmail.com

Abstract. In recent years, there have been extensive spectroscopic studies, both experimental and theoretical, of helium isoelectronic sequence. Such an analysis requires information for a wide range of atomic parameters, including energy levels and wavelengths. Our target is to extend the calculation and present a complete and accurate data for helium-like ions. We expect that our extensive calculations will be useful to experimentalists for identifying the fine-structure levels.

1. Theoretical method

FAC is a fully relativistic code created by Ming Feng Gu which higher efficiency enables user to carry out large-scale computations and allows finding various atomic parameters (Gu., 2008). We employed FAC code to perform the whole three different calculations: FAC, Relativistic Configuration Interaction (RCI) and Many Body Perturbation Theory (MBPT).

The configuration-interaction (CI) method which is based on the variational principle represents one of the approaches for treating many-electron systems. Non-relativistic CI techniques have been used extensively in atomic and molecular systems calculations. However, the generalization to relativistic configuration-interaction (RCI) calculations also presents theoretical as well as technical challenges. While, the MBPT approach starts from the Rayleigh-Schrödinger perturbation theory of a multiconfigurational model space. The self-consistent-field approximation and the Breit interaction Hamiltonian as well as QED effects have been included in the calculations to improve the generated wave functions: Manai et al. 2019.

We review the theoretical background used by the FAC code. Then, the computational details of the calculation of the $1s^2, 1s2l, 1s3l, 1s4l, 1s5l$ and $1s6l$ configurations of He-like lithium which give rise to the lowest 71 fine structure levels. The number of levels of the fine structure which we considered is larger than that in Aggarwal et al. 2010 and Kramida et al. 2018. Then, the transition energy $[cm^{-1}]$ and wavelengths $\lambda[\mathring{A}]$ are presented.

Accurate energy levels calculations among the lowest 71 levels arising of $1s^2$ and

$1snl$ ($n \leq 6$, $l \leq (n-1)$) configurations of He-like lithium have been carried out through the relativistic configuration interaction (RCI) approach, the second-order many body perturbation theory ($MBPT$). We provide accurate calculations of energy levels and wavelengths of types of transitions ($E1$, $E2$, $M1$ and $M2$) for He-like lithium.
Finally, a discussion of our results and a comparison with available theoretical and experimental data are presented.

1. 1. RESULTS

In table.1, the use of the $MBPT$ approach significantly improves the value of the energy levels. The maximum difference relative to the NIST data: Kramida et al. 2018 becomes $651\, cm^{-1}$ while the majority of values of energy levels of RCI method are decreased by approximately $5000\, cm^{-1}$.
From figure.1, the average relative deviation of wavelengths don't exceed 5% for the three methods compared to the results from NIST: Kramida et al. 2018. For the MBPT calculations we have $-0.47 \pm 0.90\%$, for the RCI calculations we have $2.62 \pm 1.70\%$ and for the FAC calculations we have $3.13 \pm 1.60\%$.
The present results are in good agreement with already published data in the literature, theoretical: Aggarwal et all. 2010 and experimental data: Kramida et al. 2018. Several new energy levels were found out where no other theoretical or experimental results are available. We expect that our extensive calculations will be useful to experimentalists for identifying the fine structure levels: Cantu et al. 1977.
We present the average relative deviation between our different methods and the experimental data as by the following equation:

$$[(E_{theory} - E_{NIST})/E_{NIST}] \times 100 \tag{1}$$

Table 1: Restriction of values of energy levels in (cm^{-1}) of He-like lithium chosen arbitrarily, calculated by different methods: FAC, RCI and $MBPT$. Experimental data from the $NIST$ database are also represented.

Index	Configuration	Level	Our work			NIST
			$E_{FAC}(cm^{-1})$	$E_{RCI}(cm^{-1})$	$E_{MBPT}(cm^{-1})$	$E_{NIST}(cm^{-1})$
0	$1s^2$	$^1S_0$	0.00	0.00	0.00	0.00
1	$1s\,2s$	$^3S_1$	468653.14	476659.81	475809.66	476034.98
2	$1s\,2p$	$^3P_1^o$	488226.11	495893.34	492877.69	494261.17
3	$1s\,2p$	$^3P_2^o$	488227.61	495895.88	492883.62	494263.44
4	$1s\,2p$	$^3P_0^o$	488230.97	495897.79	492875.37	494266.57
5	$1s\,2s$	$^1S_0$	489275.25	496473.66	490308.45	491374.60
6	$1s\,2p$	$^1P_1^o$	499233.39	506243.71	501688.74	501808.59
7	$1s\,3s$	$^3S_1$	547214.25	557219.00	554216.70	554754.45
8	$1s\,3p$	$^3P_1^o$	551896.98	561999.88	559309.39	559500.35
9	$1s\,3p$	$^3P_2^o$	551897.37	562000.70	559311.02	559501.42
10	$1s\,3p$	$^3P_0^o$	551898.11	562000.85	559308.59	559502.32

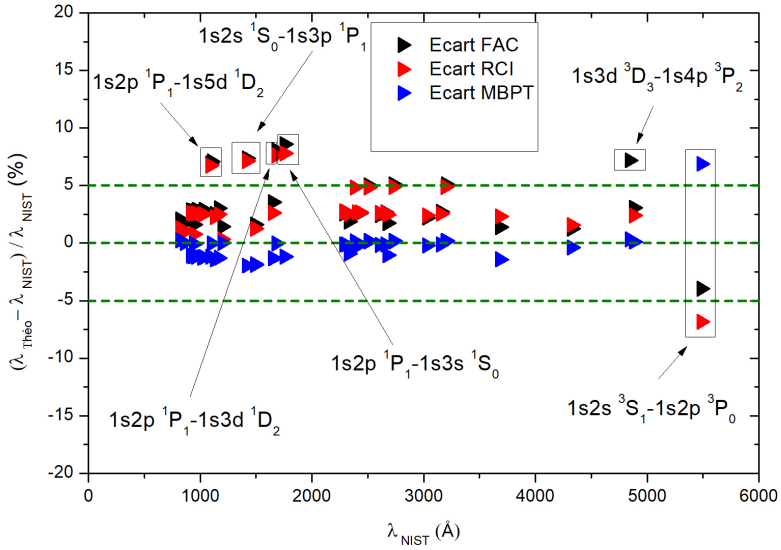

Figure 1: The average relative deviation of wavelengths calculated by different methods (FAC, RCI and MBPT) compared to NIST wavelengths.

References

Aggarwal, K. M., Kato, T., Keenan, F. P., Murakami, I.: 2010, *Physica Scripta*, **83**, 015302.

Cantu, A. M., Parkinson, W. H., Tondello, G., Tozzi, G. P.: 1977, *Opt. Soc. Am*, **67**, 1030-1033.

Gu, M. F.: 2008, *Canadian Journal of Physics*, **86**, 675-689.

Kramida, A., Ralchenko, Yu., Reader, J., NIST ASD Team.: 2018, National Institute of Standards and Technology, Gaithersburg, MD.

Manai, S., Naser, B. S., Salhi, D. E., Jelassi, H.: 2019, *Oriental Journal of Physical Sciences*, **4**, 2.

Publ. Astron. Obs. Belgrade No. 99 (2020), 245 - 248 *Contributed Paper*

RF N_2/Ar GAS MIXTURE PLASMA INDUCED MODIFICATION OF ACOUSTICAL PROPERTIES OF TEXTILE FABRICS MADE OF NATURAL CELLULOSE FIBERS (COTTON, HEMP)

SANJA S. PAVLOVIĆ[1], VLADIMIR M. MILOSAVLJEVIĆ[2,3], PATRICK J. CULLEN[3], SNEŽANA B. STANKOVIĆ[4], DUŠAN M. POPOVIĆ[2] and GORAN B. POPARIĆ[2]

[1]*The Academy of Applied Technical Studies-Belgrade, Brankova 17, 11000 Belgrade, Serbia*
E-mail sanja2104@gmail.com

[2]*University of Belgrade, Faculty of Physics, Studentski trg 12, P.O. Box 44, 11000 Belgrade, Serbia*

[3]*Bio-plasma Research group, Dublin Institute of technology, Dublin 1, Ireland*

[4]*University of Belgrade, Faculty of Technology and Metallurgy, Textile Engineering Department, Karnegijeva 4, 11120 Belgrade, Serbia.*

Abstract. Low temperature plasma is one of the most frequently used treatment for surface modifications of textile fibers. Application of plasma has many advantages for the textile processing relative to other chemical wet processes in terms of cost saving, water saving and eco friendliness. In the present work, we have examined modification of acoustical properties of fabrics made from natural cellulose fibers (cotton, hemp) by plasma treatment in radio frequency (RF) N_2-Ar gas mixtures plasma. It has been observed that the noise absorption coefficient is increased at medium and higher frequency due to the plasma treatment at certain values of reduced electric field.

1. INTRODUCTION

Plasma is a mixture of electrons, positive and negative ions, free radicals and excited molecules. In general, all of these species can interact with the surface of textiles samples (Arefi-Khonsari et al. 2008). Plasma treatment can change the surface properties of materials with no impact on the bulk properties. The depth of surface treatment is less than 100 nm. Plasma treatment affects the mechanical, chemical and microstructural properties of fiber surface, causing the changes in various physical properties of textiles, such as sound absorption coefficient, which

has been already observed for the polyester and jute fabrics (Youngjoo et al. 2010). In previous work we already estimated that there is an increase of SAC of the treated cellulose fiber materials (cotton, hemp) almost in the whole frequency range due to the argon plasma treatment (Pavlović et. al 2019).

2. EXPERIMENTAL SETUP

The cotton/hemp knitted fabrics was treated in the RF capacitively coupled plasma (CCP) reactor filled by the N_2 – Ar gas mixture. The plasma reactor, which was described previously in detail (Pavlović et al. 2018, Pavlović et al. 2019) is presented here only shortly. The reactor was placed in the cylindrical 304 stainless steel chamber. In the center of the cylinder a copper electrode was placed. In order to control gas or gas mixture purity, a vacuum system equipped with gas mass flow controllers was used. The high voltage RF generator at standard 13.56 MHz frequency was applied for RF discharges. The argon gas was fed through mass flow controller at gas flow of 2 sccm and nitrogen gas flow was changed from 10 to 60 sccm. The pressure of the argon gas in the chamber was about 0.7 Torr, 1.1 Torr and 1,6 Torr, respectively, and the maximal voltage was 1200 V peak to peak. The power used during plasma discharges was in the range from 60W to 100 W. The treated samples of materials were placed in the plasma reactor by using specially designed feedthrough connector and the treatments lasted for 20 minutes (this was an estimated optimum). In order to measure and control plasma conditions, the optical emission spectroscopy (OES) was employed. The measurements of the sound absorption coefficient (SAC) of the examined materials were performed before and after plasma treatments. We used a standard two-microphone impedance tube which has been designed as per the ISO 10534-2:1998 standard (Acoustics-Determination of sound absorption coefficient and impedance in impedance tubes-Part 2: Transfer-function method). The diameter of the tube (29 mm) was set up for measuring SAC in the high frequency range (up to 5200 Hz).

3. RESULT AND DISCUSION

The SAC spectra for both untreated and the plasma treated sample, in the frequency range from 0 Hz to 5200 Hz, are presented in Fig 1. SAC spectra for treated sample in pure argon plasma is presented, too. As can be seen from Fig 1, as in the case of samples treated by Ar gas plasma, there is an increase of SAC of the samples treated in N_2-Ar plasma almost in the whole frequency range, but it is the highest in the medium and high frequency values, in the range from 3000 Hz to 4500 Hz. The increase in SAC of the samples treated in N_2-Ar gas mixture plasma at high frequencies is even much more pronounced as compared to the samples treated in pure argon gas plasma. We have found that the maximal increase of SAC can be obtained for medium values of nitrogen gas concentration in the gas mixture (at gas flows of 30-40 sccm) or reduced electric field E/N, which was in the range from 200 to 700 Td. It is also noticed that at the highest values of the observed range of the nitrogen gas concentration (at gas flows of 50 sccm, 60

sccm) in the gas mixture plasma, there are almost no any effect on the SAC values of the treated samples.

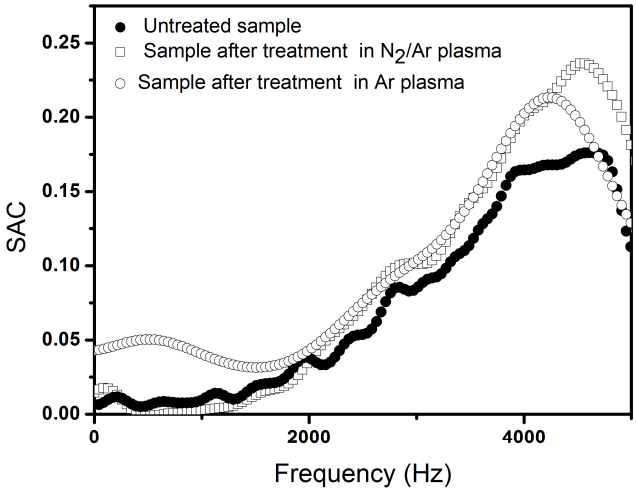

Figure 1: Sound absorption coefficients of the representative sample of treated materials.

In order to investigate and closely explain such behavior of SAC values of the samples treated under different applied values of nitrogen concentration in plasma gas mixtures, we performed an OES diagnostics of RF plasma discharge. The optical measurements were performed in the spectral range from 300 nm to 795 nm. The intensities of spectral lines obtained from relaxation of excited states of neutral argon atoms and of excited argon ions was obtained. The relative intensity of the argon spectral lines for different flow ratios with nitrogen are given in table 1. From table 1. it can be concluded that the argon spectral lines are the most intense in the case when the percentage of nitrogen in the gas mixtures is the lowest. When the participation of nitrogen is greater, relative intensities of the spectral lines decrease as the reduced electric field E/N decreases.

In our previous paper regard to the argon plasma modification of cellulose fabrics, we concluded that such treatments cause the bond-breakage in the fiber polymer macromolecules producing the free radical parts in polymer chains (Pavlović et. al 2018). Free electrons in the argon plasma can perform such bond-breakage, especially at higher energies, due to an increase of cross sections for the processes which can break carbon-hydrogen, carbon-oxygen and carbon-carbon bonds.

When the participation of nitrogen is greater, it increases the number of excited and energetic plasma species which leads to increase the number of bond-breaking processes on the fiber surface. Consequently, the SAC value of the fabrics increases. Also, when the participation of nitrogen more increases, the reduced

electric field E/N decreases which leads to decrease the number of bond-breaking processes on the fiber surface. We can conclude that there is an optimal value of the concentration of the nitrogen gas in the mixture providing the enough number of excited atoms, molecules, ions and free electrons in the plasma chamber which take place in reaction processes with polymer surface, which causes bond breaking in the fiber polymer macromolecules, increasing the fibers elasticity. This optimum is obtained experimentally for medium values of nitrogen gas concentration in the gas mixture.

λ (nm)	Rel. Intensity Rel. flow ratio (2/10)	Rel. Intensity |Rel. flow ratio (2/30)	Rel. Intensity Rel. flow ratio (2/60)
750.38	1	0.3173	0.3601
751.46	0.3644	0.0450	0.1942
763.51	0.4045	0.2535	0.1036
772.42	0.2356	0.0479	0.0633

Table 1: Relative intensity of argon atom spectral lines for different flow ratios in the mixtures with nitrogen

4. CONCLUSIONS

The aim of this work was an investigation of modifications of the acoustical properties of fabrics made from natural cellulose fibers (cotton, hemp) by N_2-Ar gas mixtures plasma treatment. According to the obtained experimental results and previously published results, it can be concluded that modification of cellulose fabrics in the RF N_2-Ar gas mixtures plasma at optimal nitrogen concentration in the gas mixture can cause the greater increase in SAC values, especially at high frequencies, comparing with fabric samples treated in pure argon plasma. The main reason for such distinction is the increase of the number of excited and energetic plasma species which leads to increase the number of bond-breaking processes on the fiber surface.

References

Arefi-Khonsari, F., Tatoulian, M.: 2008, Advanced Plasma Technology, Editors: d`Agostino, R., Favia, P., Kawai, Y., Ikegami, H., Sato, N., Arefi-Khonsari F., Wiley-VCH Verlag GmbH&Co.KgaA.

Pavlović, S. S., Stanković, S. B., Žekić, A., Nenadović, M., Popović, D. M., Milosavljević, V. V., Poparić, G. B.: 2019, *Cellulose*, **26**, 11, 6543.

Pavlović, S. S., Milosavljević, V. M., Cullen, P. J., Stanković, S. B., Popović, D. M., Poparić, G. B.: 2018, 29th Summer School and International Symposium on the Physics of Ionized Gases - SPIG, August 28 – September 1, Belgrade, Serbia, Contributed Papers, **254**.

Youngjoo, N., Gilsoo, C.: 2010 *Fibers and Polymers*, **11,** 782.

Publ. Astron. Obs. Belgrade No. 99 (2020), 249 - 252 *Contributed Paper*

SURFACE DIELECTRIC BARRIER DISCHARGE PLASMA MATLAB SIMULATION

CECILIA PIFERI[1], RUGGERO BARNI[1] and CLAUDIA RICCARDI[1]

[1] *Dipartimento di Fisica G.Occhialini, Università degli Studi di Milano-Bicocca, piazza della Scienza 3 Milano I-20126, Italy*
E–mail c.piferi@campus.unimib.it

Abstract. Dielectric barrier discharge and surface dielectric barrier discharge plasma are a developing field of research. We are interested in knowing the species produced during these plasma discharges. We developed a MATLAB code which simulates the plasma discharge and calculates the produced species according to the reaction rates and the electron temperature. In order to do that, we selected different series of chemical species interesting in and the reaction rates involved between them. We are using this code to simulate atmospheric pressure plasma generated in air with a percentage of pentane.

1. INTRODUCTION

Surface Dielectric Barrier Discharges (SDBD) are a particular configuration of electrodes that could be used for atmospheric pressure non-equilibrium plasma treatments. The presence of an insulating material between the electrodes prevents the transition of the electrical discharge towards arcing, with the formation of a non-thermal plasma at, or near, the atmospheric pressure. The flat geometry implied by SDBD increases the contact area between the discharge region and the device active parts, which is beneficial for the exposure of materials to the plasma. We developed our MATLAB simulation starting from a plasma device composed by an exposed metal electrode glued onto a dielectric surface. Such a configuration allows the formation of a thin plasma layer above the insulating surface. Any material placed there will be in contact with the plasma gas phase and it will receive a large flow of activated and reactive species. This could be used to apply plasma processes to materials at atmospheric pressure without a damaging heat load, because plasma is generated near the room temperature. Besides surface treatments, SDBD were developed and applied also to aerodynamics, by using asymmetrical electrode layouts. Our simulation investigates the SDBD discharge made in air with a small percentage of pentane (C_5H_{12}). We will outline how the code works, the approximations we have done, some results and future implementations.

2. MODEL

The program simulates a single microdischarge of atmospheric plasma produced in air with a less then 1% of pentane. We can set the duration of the microdischarge and the repetition time of the same. The microdischarge shape is a semi-cylinder laying on a surface. We can divide the simulation process in three different parts. The first one, that is of the order of ns, represents a ionization wave during the plasma formation; the second one, of the order of μs, dominates by the chemical kinetic occurring at room temperature since there are no more energetic electrons are involved; the last one describes the diffusion of the molecules between the nearly regions close to the plasma region. In order to model the microdischarge we simulate the ionization wave triggered by an increased of the electronic temperature. For the whole duration of the microdischarge we consider the electrons having a Maxwellian distribution function.

2. 1. APPROXIMATIONS

To develop the code we need to choose the discharge parameters and the species and the reactions involved in the simulation.

The discharge parameters are: the flow temperature and pressure; the electron temperature; the plasma density; the pentane concentration; the microdischarge dimensions; the repetition frequency of the microdischage, also called as HV frequency.

This is a preliminary work so we are using a little number of involved species and reaction. The first species involved is the electron one. We negletted the nitrogen dynamics and we named as Air the species that involes the molecular oxygen dynamics. We are interested in the pentane decomposition, so we concentrated on the hydrocarbons species, that we divided in class as CH_x, C_2H_x, C_3H_x, C_4H_x, C_5H_x, C_6H_x. However, we consider the pentane as a specific species and not in the class C_5H_x. The other species involved are the atomic oxygen (O), the atomic hydrogen (H) and the molecular hydrogen (H_2).

In our code we considered only two body reaction that can produce one or more products. The reaction involved are selected from the NIST Chemical Kinetics Database, GAPHYOR Database and Kinema Database. The reaction rate are evaluated from the Arrhenius experimental formula

$$K = A\ T^b \exp\left(-\frac{E_a}{T}\right) \tag{1}$$

where all the parameters are obtained from the same databases. The reaction we considered are the ionization and neutralizaion of the electrons, the dissociation reaction due to the interaction of a species with an electron, the oxidation reaction and the reaction between species. The latter is composed by hydrogen switch, extraction or acquisition of one or more atomic or molecular hydrogen, and acquisition of C_nH_x. For example we can have $H+C_nH_x \rightarrow C_nH_x+H_2$, $H+C_nH_x \rightarrow C_nH_x$ or $H_2+C_nH_x \rightarrow C_nH_x+H$. After that we also considered the wall reaction and the diffusion of the species form the outside to the inside and the opposite. We do not consider the ionic dynamics.

The whole simulation is based on the resolution of the continuity density differential equations

$$\frac{\mathrm{d}n_k}{\mathrm{d}t} = \sum_{i \le j}^{N} K_{i+j \to k} n_i n_j - \sum_{i,j=1}^{N} K_{i+k \to j} n_i n_k - \frac{D_k}{\Lambda_k^2} n_k \tag{2}$$

since we assumed only two body reaction and we are interested in study density of species (n_k), and where N is the number of the considered species. The first term in the right side of (2) is the sum of all the two body reaction that contribute to the formation of the k-th species of the sistem. The second term is the sum of all the reaction that involes the k-th species in the reagents. The last term is the diffusive one, where we assumed that $-D\nabla^2 n \sim -\frac{D}{\Lambda^2} n$; the Λ^2 are parameters that depends on the system geometry and are discussed by P.J. Chantry. We assumed that the diffusion to the outside can happen through the lateral surface of the semi-cylinder and to the dielectric surface.

2. 2. CODE

The code needs to resolve the differential equation for all the N species involved in the simulation. To do that we used the ode (ordinary differential equation) solver `ode23s` MATLAB function. `ode23s` is based on a modified Rosenbrock formula of order 2. It is a single-step solver, it is efficient at solving problems that permit crude tolerances or problems with solutions that change rapidly, as can happens in our system. The `ode23s` solver evaluates the Jacobian during each step of the integration, so supplying it with the Jacobian matrix is critical to its reliability and efficiency.

We run the simulation in two different stages: in the first one we simulate the plasma discharges, with energetic electrons of the order on the eV, and in the other, due to the chemical kinetic and the diffusion, setting the electron temperature as room temperature. We can outline the code as follows: 1. The simulation starts with a microdischarge. The initial conditions are the starting density ($n_{k,0}$) of the Air, C_5H_{12} and electrons, while the other density are placed to zero. The ode solver returns the density shape of the species for the entire microdischarge duration. 2. Starting from the final density of the previous step, we repeat the ode solver call assuming the room temperature for the electrons. This part of the simulation ends after an HV period. We repeat steps 1 and 2 for the desired number of times, taking care that when we repeat the discharge (point 1) the starting density are the final density of the previous step, except for the electrons that is set as $n_{e,0}$.

3. SIMULATION

We show now the density profile inside the discharge volume of the C_5H_{12}, the electrons and the CH_x (Fig.1). We chose to report this four species in order to show the different trends. The simulation parameters are: repetition frequency 33 kHz; microdischarge duration 2 ns; energetic electron temperature 5 eV; starting electron density 2x10^6 cm^{-3}; starting air (molecular oxygen) density 2.5x10^{19} cm^{-3}; starting C_5H_{12} density 8.3x10^{16} cm^{-3}; room temperature 25 meV; microdischarge radius 100 μm; microdischarge length 0.5 cm; number of repetition 500. In Fig.1 we plot the density in log-log scale. We can see that the C_5H_{12} decreases quickly during the discharge and then, due to the diffusion to the outside it increases. On the opposite the CH_x increases during the discharge and then decreases for the kinetical reactions and the diffusion. The electron density, instead, grows during the discharge, slowly

decreases during the diffusion and then, due to a code setting, returns to $2x10^6$ cm^{-3}. Plotting the density using the relative time (Fig.2), that is t=0 when the microdischarge starts, we can see that all the density inside of the microdischarge reach a plateau after some repetition, that is important for the next implementation of the code when we will investigate the behavior of the outflow.

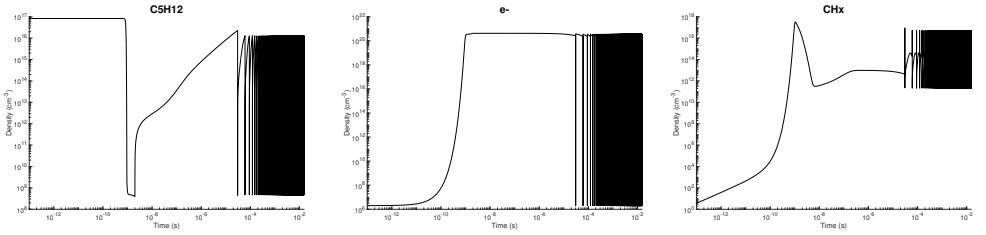

Figure 1: Pentane (left), electrons (center) and CH_x (right) density profile.

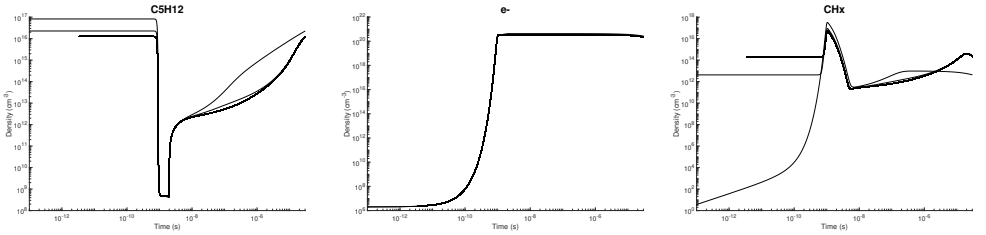

Figure 2: Pentane (left), electrons (center) and CH_x (right) density profile using relative time.

4. FUTURE IMPLEMENTATIONS

This code needs some implementation in order to improve the simulations output. First of all it is important to set good starting parameters (duration of microdischarge, electron density, etc.). It is also important to include other species like nitrogen and ozone. After that we would like to use the code to compare the simulation with the laboratory device output. When we will reach a good accordance between the simulation and the experiment we could use the simulation to have a preview of the outcome saving time and money discarding the worst configurations.

References

Kogelschatz, U. : 2003, *Plasma Chemistry and Plasma Processing*, **23**, 1.
Corke, T. C., Enloe, C. L., Wilkinson S. P. : 2010, *Annu. Rev. Fluid Mech.*, **42**, 505.
Barni, R., Esena, P., Riccardi, C. : 2005, *J. Appl. Phys.*, **97**, 073301.
Li, J., Dhali, S.K. : 1997, *J. Appl. Phys.*, **82**, 4205.
Chantry, P.J. : 1987, *J. Appl. Phy.*, **62**, 1141.
NIST Chemical Kinetics Database : https://kinetics.nist.gov/kinetics/index.jsp.
GAPHYOR Database : https://www-amdis.iaea.org/w/index.php/GAPHYOR_LPGP
Kinema Database : https://kinema.com/
Shampine, L. F., Reichelt, M. W. : 1997, *SIAM Journal on Scientific Computing*, **18**, 1.

Section 4.

GENERAL PLASMAS

Publ. Astron. Obs. Belgrade No. 99 (2020), 255 *Invited Lecture*

THE SHOCK IGNITION APPROACH TO INERTIAL CONFINEMENT FUSION: BASIC CONCEPTS AND PROGRESS

DIMITRI BATANI

University of Bordeaux, France

Abstract. On behalf of the EUROFusion Enabling Research Project ENR-IFE19.CEA-01 "Study of Direct Drive and Shock Ignition for IFE: Theory, Simulations, Experiments, Diagnostics development " and in particular *J.Trela, G.Boutoux, A.Casner, X.Ribeyre, V.Tikhonchuk, E.Le Bel, Ph.Nicolai, D.Raffestin, A.Colaitis, L.Antonelli, N.Woolsey, G.Cristoforetti, L.Gizzi, R.Scott, K.Glize, S.Pikuz, J.Honrubia, R.Florido, S.Atzeni, T.Pisarczyk, S.Guskov, D.Mancelli, A.Tentori, O.Renner, J.Dostal, R.Dudzak, M.Krus, F.Baffigi, E.Filippov, Y.J.Gu, O.Klimo, S.Malko, A.Martynenko, S.Pikuz, T.Chodukowski, Z.Kalinowska, M.Rosinski, …*

Direct-drive "Shock Ignition" is an interesting alternative to the classical approach to ICF investigated on NIF and could relax the problems met on the pathway to ignition, in particular due to hydrodynamic instabilities (Rayleigh-Taylor). In the conventional approach to ICF, hot electrons (HE) are dangerous because they induce target preheating making compression more difficult. In SI, however, HE generated by the final laser spike at the end of compression, when the accumulated target <□r> is large enough, may increase laser-target coupling and strengthen the shock with a positive impact. Hence, their characterization is crucial for assessing SI feasibility. Within our Enabling Research EUROfusion Project on Shock Ignition, we are conducting experiments in Europe and the US to contribute answering these open questions.

In the talk, I will review the basic concepts of shock ignition and ten I will present the results from two series of experiments.

At the PALS laboratory in Prague we characterized HE produced by high-energy laser pulses of 300 ps at 1^{st} and 3^{rd} harmonics of the iodine laser (wavelength λ = 1315/438 nm, focused to intensities 9×10^{15} / 2×10^{16} W/cm^2). We studied the correlation of HE and Stimulated Raman Scattering (SRS) and assessed the impact of HE on target preheating and on shock dynamics. Results were compared to advanced hydro simulations done with the code CHIC that takes into account parametric instabilities and HE in a self-consistent way.

At the Omega facility in Rochester, we characterized HE with K-a spectroscopy and bremsstrahlung cannons. We performed experiments to assess the effect of HE on the performance of spherical implosions with a pulse shaping typical of IS. We also performed a plane experiment on the Omega EP system to characterize HE and evaluate their impact on preheating and shock dynamics which was diagnosed by time-resolved X-ray radiography.

This work contributed to our understanding of SI physics but also to consolidate a European research network on SI, serving as preparation for future experiments to be done on the LMJ/PETAL laser facility at the relevant energy scale.

Publ. Astron. Obs. Belgrade No. 99 (2020), 256 - 257 *Invited Lecture*

CHALLENGES AND PROGRESS ON THE PATH TOWARDS FUSION ELECTRICITY

A. J. H. DONNÉ

EUROfusion, Garching, Germany
E-mail tony.donne@euro-fusion.org

Abstract. The European Roadmap to the Realisation of Fusion Energy[1] breaks the quest for fusion energy into eight missions:

1. Plasma regimes of operation: Demonstrate plasma scenarios (based on the tokamak configuration) that increase the success margin of ITER and satisfy the requirements of DEMO.
2. Heat-exhaust systems: Demonstrate an integrated approach that can handle the large power leaving ITER and DEMO plasmas.
3. Neutron tolerant materials: Develop materials that withstand the large 14MeV neutron flux for long periods while retaining adequate physical properties.
4. Tritium self-sufficiency: Find an effective technological solution for the breeding blanket that also drives the generators.
5. Implementation of the intrinsic safety features of fusion: Ensure safety is integral to the design of DEMO using the experience gained with ITER.
6. Integrated DEMO design and system development: Bring together the plasma and all the systems coherently, resolving issues by targeted R&D activities
7. Competitive cost of electricity: Ensure the economic potential of fusion by minimising the DEMO capital and lifetime costs and developing long-term technologies to further reduce power plant costs.
8. Stellarator: Bring the stellarator line to maturity to determine the feasibility of a stellarator power plant.

Now we are approaching the end of the 8th European Framework Programme (2014-2020), it is a good moment to look back at the achievements since the establishment of EUROfusion in 2014, while at the same time have a peek into the future, to see which challenges lay ahead of us as well as the strategy to tackle them.

EUROfusion has seized the unique opportunity to develop an integrated scientific programme including experiments and modelling on tokamaks with different sizes, i.e., on medium-size tokamaks and on JET to provide a step-ladder approach for extrapolations to JT-60SA, ITER and DEMO. The main development in plasma scenarios (mission 1) has been the move to tokamak operation with metallic walls like ITER and DEMO (previously carbon was the normal plasma-facing material, which proved unsuitable for ITER and DEMO). This has led, as hoped, to strongly reduced tritium retention and much lower levels of dust production. The introduction of metallic walls initially had an adverse effect

on the plasma performance for standard plasma scenarios but various remedies and modified scenarios have been developed to assist rapid progress when ITER starts to operate.

In the challenging area of plasma exhaust (mission 2), there has been good progress in understanding the likely exhaust loads in ITER and DEMO. As a response, a comprehensive high-level strategy was developed, including a range of facility enhancements. Additionally, the Italian government has recently decided to proceed with the funding for the construction a new divertor test tokamak (referred to as DTT) focused on exhaust issues.

In the field of materials (mission 3), beside numerous scientific advances, a preliminary engineering design of IFMIF-DONES has been completed, and a potential European site has been identified.

Fundamental to the European DEMO design development strategy (missions 4-7) has been the establishment of a baseline architecture that integrates all the major DEMO sub-systems into a coherent plant concept. This provides a framework to find holistic designs that are consistent with the DEMO stakeholder requirements and thus reveal the extent to which current plasma, materials, component and systems performance are adequate. The implementation of a philosophy of integrated design and a 'systems orientated' approach represents a significant advance over anything achieved previously. It has brought much greater clarity to a number of critical design issues, and the overall integration challenge. This includes: (i) identification of critical interface issues, project risks and innovation opportunities, (ii) establishment of an 'integration culture', and (iii) system optimisation studies.

A major highlight of mission 8 has been the completion of the superconducting Wendelstein 7-X stellarator. Its commissioning and first years of operation exceeded expectations, demonstrating a strong base for future scientific exploitation and development of the stellarator.

1 European Research Roadmap to the Realisation of Fusion Energy, ISBN 978-3-00-061152-0 (November 2018)

Publ. Astron. Obs. Belgrade No. 99 (2020), 258 *Invited Lecture*

THE TWO CONCEPTS OF MAGNETIC CONFINEMENT: TOKAMAK AND STELLARATOR

SIBYLLE GÜNTER

Max-Planck-Institut für Plasmaphysik, Garching and Greifswald, Germany
E-mail sibylle.guenter@ipp.mpg.de

Abstract. Nuclear fusion could contribute to the energy mix in the second half of this century. For a fusion reactor, matter has to be heated up to extremely high temperatures: more than 100 million degrees - about a factor of 10 hotter than the sun's core. At these temperatures, the material is fully ionized. The charged particles can be confined by magnetic fields, which are also able to provide the required efficient heat insulation. After more than 50 years of research, fusion has advanced to the decisive step on the way to a power plant: the international tokamak experiment ITER is designed to demonstrate the feasibility of net energy production from nuclear fusion reactions. In a joint enterprise by 7 partners (the EU, Japan, Russia, USA, China, the Korean Republic and India) - ITER is currently been built in Cadarache, France. With the Joint European Torus (JET) and the joint exploitation of the medium size tokamaks, the European fusion programme is well equipped to provide essential contributions to the preparation of ITER operation. The tokamak concept as realized in ITER is by far the most advanced confinement configuration. It however requires the continuous flow of an electric current in a donut-shaped plasma. In present devices, this plasma current is driven by a transformer and can therefore be maintained only over a certain time, which – in a reactor – could amount to several hours. A thermal storage would provide for continuity of the electric power production during the short time interval needed to recharge the transformer.

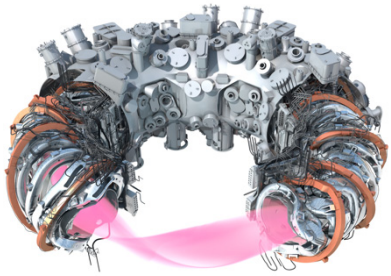

Figure: Sketch of the Wendelstein 7-X geometry.

An alternative to the tokamak is the stellarator, which needs a considerably more complex magnetic field configuration, but is intrinsically stationary without any need of external current drive. The complex magnetic field of a stellarator requires however careful optimization to ensure sufficiently good confinement properties. The first optimized stellarator of sufficient size to proof that the stellarator concept has the potential for a power plant, Wendelstein 7-X, has recently started operation in Greifswald, Germany. Wendelstein 7-X is a superconducting device with 50 non-planar coils, providing the magnetic confinement. In addition, 20 planar coils provide some flexibility of the magnetic field geometry (see figure).

Publ. Astron. Obs. Belgrade No. 99 (2020), 259 *Invited Lecture*

DARK MATTER AND DARK ENERGY: GASES THAT DOMINATE THE UNIVERSE

DRAGAN HUTERER[1]

[1] *Department of Physics, University of Michigan, 450 Church St, Ann Arbor, MI 48109-1040, USA*
E–mail huterer@umich.edu

Abstract. Over the past century, scientists have developed an excellent understanding of the history of the universe from a fraction of a second after the Big Bang when the universe was small, hot and nearly uniformly filled with matter, until the present time when it is filled with galaxies surrounded by empty space. I will discuss the three principal findings that serve as the "pillars" of modern cosmology, establishing the standard Big Bang model of the early universe. These pillars are: the expansion of the universe; the agreement between theory and prediction of primordial abundances of lightest elements produced in the early universe; and the remnant radiation from the early epoch (the cosmic microwave background radiation). I will then discuss two famous modern-day puzzles in the field of cosmology. The first of them is dark matter, which contributes five times more mass/energy as the usual baryonic matter (i.e. particle made of quarks) and for which there is excellent evidence from many observational probes, but whose particle-physics properties have not yet been identified. The second great modern-day mystery is that of dark energy, which makes the universe expand faster and faster, but whose physical origin has not yet been established.

Publ. Astron. Obs. Belgrade No. 99 (2020), 260 *Invited Lecture*

FOLLOWING SUPERMASSIVE BLACK HOLES OVER COSMIC TIME

HAGAI NETZER

School of Physics and Astronomy, Tel Aviv University

Abstract. The first black holes were seeded in pre-born galaxies in the early Universe, at redshift 10 or even higher. Their growth, in parallel to star formation and the growth of their host galaxies is, perhaps, the leading factor that determines the size and mass of the most massive galaxies of today. The mass of the largest black holes of today exceed 10 billion solar mass but, surprisingly, such supermassive black holes are observed also in galaxies whose age is less than a billion years indicating super-fast growth which is not yet fully understood. Active black holes are the lamp-posts of the Universe. Every 50-100 million years they light up for a short period of time, enabling a glimpse of their parent galaxies and their environment. I will present the black hole history of the Universe using recent observations. To each black hole I will assign a measured mass – one of the greatest achievements of modern astronomy – and present evidence that black hole activity is related to mergers of galaxies, and to the clearing of star-forming gas. Such processes shape galaxy evolution and morphology and lead to what astronomers call "red and dead" galaxies.

PLASMA-WALL INTERACTION IN W7-X OPERATING WITH GRAPHITE DIVERTOR

S. BREZINSEK and the W7-X team

[1]*Forschungszentrum Jülich, Institute of Energy and Climate Research – Plasma Physics, 52425 Jülich, Germany*
E-mail s.brezinsek@fz-juelich.de

Abstract The world largest stellarator W7-X finished successfully its first phase in island divertor configuration. Plasma-facing components (PFCs) made of fine grain graphite (carbon C) were used to exhaust the plasma particle and power load the toroidal device with five-fold symmetry. No significant damage occurred to the 10 divertor modules in the executed 3.6h of integral plasma operation in hydrogen (H) and helium (He). The adiabatically cooled divertor with an area of 25m^2, received peak heat loads up to 10MWm^{-2} in ECRH-heated plasma discharges with maximum duration of 100s in attached conditions. With the aid of improved wall conditioning (boronisation), W7-X superseded the expected plasma performance combining high central density ($n > 1.5 \times 10^{20}$m^{-3}) operation with stable, detached divertor conditions (P_{div}<1MWm^{-2}) for 30s in H with 5MW input power. Peak particle fluxes up to few 10^{23}ions s^{-1}m^{-2} to the divertor and 1×10^{22}ions s^{-1}m^{-2} to the first wall - consisting of graphite heat shields, baffles, and stainless steel panels - resulted in a manifold of plasma-surface interaction (PSI) in the 3D geometry. Important with this respect is (i) the C balance, namely the identification of erosion and deposition areas as well as the material transport paths between those in W7-X; (ii) the balance of fuel in W7-X, namely the balance of injection, retention, release, and recycling. In view of upcoming long-pulse operation, these PSI processes will determine the lifetime of divertor PFCs, the fuel cycle and plasma control, as well as the dust production.

Access to these processes is given by the combination of in-situ analysis via spectroscopy, IR thermography, residual gas composition, etc. during plasma operation and ex-situ analysis of PFCs after extraction from the vessel by a variety of techniques including nuclear-reaction analysis, scanning electron microscopy, laser-induced break-down spectroscopy etc. The post-mortem analysis revealed the main C migration paths in W7-X for dedicated plasma configurations, the peak C erosion rates of more than 5nm/s, as well as the net C erosion source of about ~50g in the ~2500s long operational phase prior to boronisation. The peak erosion rates dropped substantially after application of the boronisation confirming the dominant role of oxygen (O) in the PSI in the first phase of W7-X operation with Z_{eff} of ~3.5 and the excellent O gettering with boron (B) associated with a reduction of Z_{eff} to ~1.5 in H plasmas with residual C radiation. Dedicated PSI modelling with the 3D codes ERO2.0 and WallDYN-3D are applied to describe the PSI processes for the standard configuration where both codes are able to describe the main C erosion, transport, and deposition areas. A final benchmark of the codes is presently done using a $^{13}CH_4$ injection through one single divertor module in more than 330s accumulated plasma seconds to mimic the material migration for one single plasma condition. The corresponding PFCs for ^{13}C surface analysis have been extracted after the experiment that no mixture with other plasma conditions perturb the interpretation.

These PSI processes in the full-C W7-X device will be discussed in detail and predictions towards single steady-state plasmas of up to 1800s will be made with the aid of experimental data and PSI modelling. Consequences for operation and the need to control. PSI processes in the novel and actively cooled carbon-fibre composite divertor in W7-X by adapting the divertor plasma solution with enhanced input power capability will be drawn.

COMPACT ELECTRON BEAM ION TRAP FOR SPECTROSCOPY OF MULTIPLE CHARGED IONS

DAIJI KATO[1], HIROYUKI A. SAKAUE[1], IZUMI MURAKAMI[1] and NOBUYUKI NAKAMURA[2]

[1]*National Institute for Fusion Science, Toki, Gifu 509-5292, Japan*
E-mail kato.daiji@nifs.ac.jp

[2]*Institute for Laser Science, The University of Electro-Communications, Chofu, Tokyo 182-8585, Japan*

Abstract. Emission lines from multiple charged ions of heavy elements are useful for diagnostics of laboratory and astronomical plasmas, such as magnetically confined fusion plasmas, solar corona. However, available spectroscopic data are still scarce. Electron beam ion trap (EBIT) can produce and trap multiple charged ions in extreme high vacuum for precise spectroscopic measurements of emission lines. In EBIT, ions produced by a mono-energetic electron beam have a narrow charge state distribution, and primary charge states can be tuned by electron beam energy under suppressed recombination with residual neutral gas. This enables charge state identification of spectra reliable, and direct comparison with spectral modeling becomes much facilitated. In this lecture, a compact EBIT (CoBIT), e.g.: see Nakamura et al. 2008, which is developed for measurements of multiple charged ions formed by electron energies of 0.1 - 1 keV, will be introduced. These energies are relevant to electron temperatures in the solar corona and edge regions of ITER plasmas. A typical electron density of CoBIT is 10^{10} cm^{-3} which lies in between densities of the solar corona and fusion plasmas. Our recent studies on emission line spectra of multiple charged ions with the CoBIT will be reviewed, e.g.: see Kobayashi et al. 2015, Kato et al. 2017, Sakaue et al. 2019.

References

Kato, D. et al.: 2017, *Nucl. Instrum. Meth. B*, **408**, 16.
Kobayashi, Y. et al.: 2015, *Phys. Rev. A*, **92**, 022510.
Nakamura, N. et al.: 2008, *Rev. Sci. Instrum.*, **79**, 063104.
Sakaue, H.A. et al.: 2019, *Phys. Rev. A*, **100**, 052515.

Publ. Astron. Obs. Belgrade No. 99 (2020), 263 *Topical Invited Lecture*

QUARK GLUON PLASMA IN AN EARLY PHASE OF THE UNIVERSE AND IN THE LABORATORY

JOVAN MILOŠEVIĆ[1]

[1] *Vinča Institute of Nuclear Sciences, University of Belgrade, Mike Petrovića Alasa 12-14, Vinca 11351, Belgrade, Serbia*
E–mail Jovan.Milosevic@cern.ch

Abstract. A few microseconds after the birth of the Universe (Big Bang), the Universe was filled with the matter consisting of colored quarks and gluons (particles which constitute hadrons), called quark gluon plasma (QGP) (Shuryak 2017). That primordial QGP lasts for about a few μs until the Universe cooled down and expanded enough that colored quarks had to confine within the colorless new formed hadrons. In high-energy nuclear collisions, where a high baryon density, or a high temperature could be achieved, small pieces of the QGP can be recreated. Such created QGP undergoes an explosion, called the Little Bang. In spite of its small size (about $1000fm^3$) and short duration (a few fm/c, where c is the speed of light), the QGP is well described by relativistic hydrodynamics. Even more, small perturbations on top of the explosion could be also well described by relativistic hydrodynamics. In high-energy nucleus-nucleus collisions which have been performed at the Relativistic Heavy Ion Collider (RHIC) and at the Large Hadron Collider (LHC), the QGP was artificially created with extremely high temperature and the baryon density close to zero (Chatrchyan et al. 2014, Khachatryan et al. 2015, Sirunyan et al. 2017). On the other side, at future experiments as NICA (Dubna), J-PARC HI (Tokai) and CBM (Darmstadt) will explore the region of temperature vs baryo-chemical potential $(T - \mu_B)$ phase diagram at smaller temeperatures and high baryon densities. This will enable to investigate a new domain of quantum-chromodynamic matter created in such collisions. We briefly discuss about some aspects of the QGP formation and its properties.

References

Shuryak, E.: 2017, *Universe*, **3**, 75.

Chatrchyan, S.,... , Milosevic J., et al., CMS Collaboration, 2014, *Journal of High Energy Physics* **1402**, 088.

Khachatryan V., ... , Milosevic J., et al., CMS Collaboration, 2015, *Phys. Rev. C* **92**, 034911.

Sirunyan A.M., ... , Milosevic J., et al., CMS Collaboration, 2017, *Phys. Rev. C* **96**, 064902.

TURBULENCE SIMLATIONS FOR STELLARATOR PLASMA TRANSPORT

Masanori Nunami[1], Motoki Nakata[2], Shinichiro Toda[3] and Hideo Sugama[4]

National Institute for Fusion Science / National Institutes of Natural Sciences, Toki, Gifu 509-5292, Japan
[1]*E-mail nunami.masanori@nifs.ac.jp*
[2]*E-mail nakata.motoki@nifs.ac.jp*
[3]*E-mail toda@nifs.ac.jp*
[4]*E-mail sugama@nifs.ac.jp*

Abstract. In magnetic fusion researches, it is one of the critical issues to understand the physics in the plasma turbulent transport which influences the confinement performances of the plasmas. In recent years, due to the rapid progress of the high-performance computers, the plasma transport phenomena can be accurately predicted by the first-principle simulations based on the gyrokinetics. In the stellarator systems such as Large Helical Device (LHD) [Takeiri et al.2017], which is a promising device for the long-time plasma discharges, the gyrokinetic simulations demand extremely heavy computational cost compared with the tokamak cases. In order to establish the predictable turbulence simulations in the stellarator plasma transport, the local flux-tube gyrokinetic code GKV [Watanabe et al. 2006] has been developed and extended. Using the code, the turbulent transport in the stellarators for the hydrogen isotope plasmas [Nakata et al. 2017] and the multi-species plasmas [Nunami et al. 2020] have been studied. Furthermore, based on the simulation results, we have developed a reduced model for the turbulent transport of the stellarator plasmas [Toda et al. 2019].

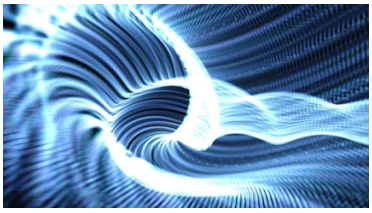

Figure 1: The potential fluctuation obtained by GKV simulation for the LHD plasma.

References

Nakata, M. et al. : 2017, *Phys. Rev. Lett.* **118**, 165002.
Nunami, M. et al. : 2020, *Phys. Plasmas* **27**, 052501.
Takeiri, Y. et al. : 2017, *Nucl. Fusion* **57**, 102023.
Toda, S. et al. : 2019, Phys. Plasmas **26**, 012510.

Publ. Astron. Obs. Belgrade No. 99 (2020), 265 *Topical Invited Lecture*

SPECTROSCOPIC MODELING FOR THE INVESTIGATION OF MAGNETIC FUSION PLASMAS AND STARS WITH MAGNETIC FIELD

J. ROSATO, Y. MARANDET and R. STAMM

Aix-Marseille Université, CNRS, PIIM, UMR 7345, Centre de St-Jérôme, Case 232, F-13397, Marseille Cedex 20, France

Abstract. In this work, we report on a selection of issues present in the elaboration of spectroscopic models for magnetized plasma diagnostic. A focus is put on tokamak edge and white dwarf atmosphere plasma conditions. In both cases, the spectrum exhibits clean lines, either in absorption or in emission, denoting the presence of neutral species (atoms). An analysis of the line shape and intensity yields information on the plasma parameters provided a suitable physical model is used. We examine the broadening of the spectral lines due to the plasma microfield (Stark effect) and due to collisions with the atoms (resonant and van der Waals broadening). A computer simulation method accounting for the microfield dynamics during the radiation time of interest is applied to the calculation of the first lines in the Balmer series. Comparisons to observed spectra are performed. We also address the Zeeman line splitting due to the presence of magnetic fields. While the normal linear Zeeman effect formula can safely be applied to hydrogen in tokamak plasma conditions (B has a value of the order of several teslas), it is strongly inaccurate for white dwarfs that are subject to an extremely strong magnetic field. Observations have indicated that B attains values up to 10 kT in several white dwarfs; at such conditions, the Zeeman splitting becomes comparable to the atomic energy level separation and can no longer be treated as a linear perturbation. This issue is examined in details through dedicated calculations.

THE MODIFIED SEMI-EMPIRICAL STARK BROADENING METHOD OF CALCULATIONS: THE EXAMPLE OF ALKALI LIKE IONS

A. ALMODLEJ [1],N. ALWADIE[1,2], N. BEN NESSIB [1,3] and M. S. DIMITRIJEVIĆ [4,5]

[1] *Department of Physics and Astronomy, College of Sciences, King Saud University, Saudi Arabia*
E–mail nbennessib@ksu.edu.sa

[2] *Department of Physics, College of Sciences, King Khalid University, Saudi Arabia*
E–mail nalwadie@ksu.edu.sa

[3] *GRePAA, INSAT, Centre Urbain Nord, University of Carthage, Tunis, Tunisia*

[4] *Astronomical Observatory, Volgina 7, 11060 Belgrade 38, Serbia*
E–mail mdimitrijevic@aob.rs

[5] *Sorbonne Université, Observatoire de Paris, Université PSL, CNRS, LERMA, F-92190 Meudon, France*

Abstract. In this work, the modified semi-empirical (MSE) Stark broadening method of calculations is presented. The method is compared to the semi-empirical (SE), semiclassical perturbation (SCP) and fully relativistic methods and with more simplest calculation formula. As an example of calculation, we calculate the widths of some alkali like ions as Sr II, Y III and Zr IV.

References

Cowley, C.R.: An approximate Stark broadening formula for use in spectrum synthesis, 1971, *The Observatory*, **91**, 139.

Dimitrijević, M. S. and Konjević, N.: Stark widths of doubly-and triply-ionized atom lines, 1980, *Journal of Quantitative Spectroscopy and Radiative Transfer*, **24**, 451.

Elabidi, H., Ben Nessib, N. and Sahal-Bréchot, S.: Quantum mechanical calculations of the electron-impact broadening of spectral lines for intermediate coupling, 2003, *Journal of Physics B: Atomic, Molecular and Optical Physics*, **37**, 63.

Griem, H.R.: Semiempirical Formulas for the Electron-Impact Widths and Shifts of Isolated Ion Lines in Plasmas, 1968, *Phys. Rev.*, **165**, 258.

Sahal-Bréchot, S., Dimitrijević, M. S. and Ben Nessib, N.: Widths and shifts of isolated lines of neutral and ionized atoms perturbed by collisions with electrons and ions: An outline of the semiclassical perturbation (SCP) method and of the approximations used for the calculations, 2014, *Atoms*, **2**, 225.

A NEW METHOD FOR THE CALCULATION OF COLUMN DENSITY USING THE GR MODEL. AN APPLICATION ON THE C IV, N IV AND N V SPECTRAL LINES IN THE SPECTRUM OF THE O-STAR HD 149757 (ζ OPH)

A. ANTONIOU[1], E.DANEZIS[1], D. STATHOPOULOS[1,2], E. LYRATZI[1,2] and D. TZIMEAS[1]

[1]*National and Kapodistrian University of Athens, Faculty of Physics, Panepistimiopolis, Zographos 157 84, Athens, Greece*
E-mail ananton@phs.uoa.gr, edanezis@phys.uoa.gr, dtzimeas@phys.uoa.gr

[2]*Eugenides Foundation, 387 Syngrou Av., 175 64, Athens, Greece*
E-mail elyratzi@phys.uoa.gr, dstatho@phys.uoa.gr

Abstract. In this context, our research group developed GR model and A.S.T.A. software, which can analyse the complex DAC/BAL profiles to individual components. By applying a series of strict fitting criteria, we analyse each DAC/BAL to the uniquely determined number of components they consist of and guarantee the uniqueness of the best fit. For every absorption component we calculate the radial (V_{rad}) and rotational (V_{rot}) velocity, the FWHM, the optical depth at line centre (τ_0), the EW and the column density (N). By utilizing different epoch spectra, we probe the time variability of each individual component.

The column density is a crucial parameter because it allows the investigation of the internal structure of clouds that produce the DAC/BAL components. Column density is a measure of the amount of intervening matter between an observer and the object being observed and is representative of the projected density of the clouds that produce DACs/BALs along a specific line of sight. Thus, the time scale-variations of the components' column densities can provide useful insights on the relative number of absorbers of each absorbing cloud in the line of sight.

In this paper, in the context of GR model, we present a new method for calculating the column density. We use GR model in order to analyse the broad absorption troughs of C IV, N IV and N V, in different epoch spectra, of the O-star HD149754 (ζ Oph), to the uniquely determined number of components they consist of and we study the variability of the components' column densities in a time interval of 13 years. in multicomponent fitting of the above-mentioned spectral profiles is performed using A.S.T.A. software developed by the Astrophysical Spectroscopy Team of the National and Kapodistrian University of Athens.

MULTI-MESSENGER STUDIES OF COSMIC RAY ACCELERATION IN GALAXY CLUSTER ACCRETION SHOCKS

A. ĆIPRIJANOVIĆ[1] and T. PRODANOVIĆ[2]

[1]*Fermi National Accelerator Laboratory, P.O. Box 500, Batavia, IL 60510, USA*
E-mail aleksand@fnal.gov

[2]*Department of Physics, University of Novi Sad, Trg Dositeja Obradovića 4, 21000 Novi Sad, Serbia*
E-mail prodanvc@df.uns.ac.rs

Abstract. Studying cosmic rays, their acceleration and interactions is of fundamental importance for understanding physics of the highest energies. Cosmic rays interact with magnetic fields, so their direct detection is not possible, but their presence can be measured by detecting different products of their interactions with the interstellar medium through which they propagate. Accretion of gas on the largest scales (around galaxy clusters) has been thought to give rise to shocks that can accelerate cosmic rays. Multi-messenger studies of particular galaxy clusters, as well as the possible contribution of distant unresolved galaxy clusters to the observed background radiation at different wavelengths, can be used to study particle acceleration in accretion shocks. Interactions of cosmic rays will, among other things, produce gamma rays, neutrinos and radio waves. Here we investigate how unresolved galaxy clusters and their accretion shocks contribute to extragalactic gamma-ray background observed by Fermi-LAT (Ackermann et al. 2015). We also study these objects using high-energy isotropic neutrino flux from the IceCube detector (Aartsen et al. 2014) and the cosmic radio background (Fixen et al. 2011). We show that the possible contribution of unresolved galaxy clusters to these backgrounds is not large. For example, even if all detected extragalactic IceCube neutrinos are entirely produced by cosmic rays accelerated in accretion shocks, they can make at best ∼20% of the extragalactic gamma-ray background (Dobardžić et al. 2015).

References

Aartsen, M. G., Ackermann, M., Adams, J. et al.: 2014, *Phys. Rev. Lett.*, **113**, 101101.
Ackermann, M., Ajello, M., Albert, A. et al.: 2015, *Astrophys. J.*, **799**, 86.
Dobardžić, A., Prodanović, T.: 2015, *Astrophys. J.,* **806**, 184.
Fixsen, D. J., Kogut, A., Levin, S. et al.: 2011, *Astrophys. J.*, **734**, 5.

DISSIPATIVE PHENOMENA IN QCD PLASMA STATE CREATED IN HEAVY ION COLLISIONS

DAMIR DEVETAK[1]

[1] *Vinča Institute of Nuclear Sciences, University of Belgrade, Mike Petrovića Alasa 12-14, Vinca 11351, Belgrade, Serbia*
E–mail ddevetak@gmail.com

Abstract. Modern heavy-ion experiments reach collision energies that span the QCD phase diagram in the region of a partonic plasma state called quark-gluon plasma (QGP). The quark-gluon plasma is a strongly-coupled hot medium that lasts only a few fm/c. Being such a ephemeral state of matter the only effective information about QGP is contained in the final particle shower collected by the experiment. Using such high precision experimental data, various observables can be computed for theoretical model comparison. Phenomenologically, the QGP can be treated as a relativistic fluid assuming quick and local thermalization. Plethora of measurements show that the QGP behaves almost a perfect liquid but still contains some dissipative effects to fit the data. In order to study such effects one requires a full theoretical framework of the QGP, which comprises of initial medium conditions, fluid expansion and particle shower (hadronization) phase. Each of these phases affect the predictive power of the model and put a direct quantitative constrain on dissipative contributions when compared to data, see Devetak et al. 2015 and Devetak et al. 2020. In this talk such data to model comparisons are presented, using recent heavy-ion experimental measurements and methods.

References

Devetak D., et al., CMS Collaboration, 2015, *Phys. Rev. C* **92** 034911.
Devetak D., et al., 2020, *JHEP* **06** 044.

RISE OF LSST - DETECTION OF OSCILLATIONS IN AGN EMISSION LIGHT CURVES AT DIFFERENT COSMOLOGICAL SCALES

A. KOVAČEVIĆ[1], D. ILIĆ[1] and L. Č. POPOVIĆ[2] ON BEHALF OF AGN SC LSST

[1] *Department of Astronomy, Faculty of Mathematics, University of Belgrade, Studentski trg 16, 11000 Belgrade, Serbia*
E–mail andjelka@matf.bg.ac.rs
E–mail dilic@matf.bg.ac.rs
[2] *Astronomical Observatory Belgrade, Volgina 7, 11060, Belgrade, Serbia*
E–mail lpopovic@aob.rs

Abstract. We present the first stage in the construction of a publicly available tool for modeling of active galactic nuclei (AGN) emission light curves, and for detection of oscillations in them (see Kovačević et al. 2018, 2019, 2020). This method is a result of our previous research of the time lags and oscillatory characteristics of optical light curves, which are obtained within our long-term monitoring program (up to 3 decades, see Shapovalova et al. 2001, 2004, 2008, 2010, 2012, 2013, 2017, 2019, Ilić et al. 2020).
Moreover, we introduce this tool in the context of the photometric reverberation mapping with the the Rubin Observatory Legacy Survey of Space and Time (LSST). As the dawn of the LSST is approaching, we expect the largest database of AGN light curves, covering a significant portion of the AGN population up to redshift ~ 7.0. Perhaps this large and systematic dataset should enable us to constraint properties of oscillations in AGN light curves at different cosmological scales and thereby probe the properties of the emitting sources.

References

Ilić, D., Oknyansky, V., Popović, L. Č, Tsygankov, S., et al. : 2020, *A&A*, **638**, id. A13
Kovačević, A. B., Pérez-Hernández, E., Popović, L. Č., Shapovalova, A. I., Kollatschny, W., Ilić, D. : 2018, *MNRAS*, 475, 2051.
Kovačević, A. B., Popović, L. Č., Simić, S., Ilić, D. : 2019, *ApJ*, **871**, id. 32.
Kovačević, A. B.,Yi, T., Dai, X., Yang, X., Čvorović-Hajdinjak, I., Popović, L. Č. : 2020, *MNRAS*, **494**, 4069.
Shapovalova, A. I., Burenkov, A., Carrasco, L. et al. : 2001, *A&A*, **376**, 775.
Shapovalova, A. I., Doroshenko, V., Bochkarev, N. et al. : 2004, *A&A*, **422**, 92.
Shapovalova, A. I., Popović L. Č., Collin, S., Burenkov, A. et al. : 2008, *A&A*, **486**, 99.
Shapovalova, A. I., Popović, L. Č., Burenkov, A., Chavushyan, V., Ilić, D., Kovačević, A. et al. : 2010, *A&A.*, **509**, A106.
Shapovalova, A. I., Popović, L. Č., Burenkov, A., Chavushyan, V., Ilić, D., Kovačević, A., Kollatschny, W., Kovačević, J. et al. : 2012, *ApJS*, **202**, 10.
Shapovalova, A. I., Popović, L. Č., Burenkov, A., Chavushyan, V., Ilić, D., Kollatschny, W., Kovačević, A. et al. : 2013, *A&A*, **559**, A10.
Shapovalova, A. I, Popović, L. Č., Chavushyan, V., Afanasiev, V. L., Ilić, D., Kovačević, A. et al. : 2017, *MNRAS*, **466**, 4759.
Shapovalova, A. I, Popović, L. Č., Afanasiev, V. L., Ilić, D., Kovačević, A. et al. : 2019, *MNRAS*, **485**, 4790.

Publ. Astron. Obs. Belgrade No. 99 (2020), 271 *Progress Report*

ON THE TEMPERATURE DEPENDENCE OF STARK WIDTHS

ZLATKO MAJLINGER[1], MILAN S. DIMITRIJEVIĆ[1,2] and VLADIMIR A. SREĆKOVIĆ[3]

[1]*Astronomical Observatory, Volgina 7, 11060 Belgrade, Serbia*
E-mail zlatko.majlinger@gmail.com

[1]*Astronomical Observatory, Volgina 7, 11060 Belgrade, Serbia*
[2]*LERMA, Observatoire de Paris, UMR CNRS 8112, UPMC, 92195 Meudon Cedex, France*
E-mail mdimitrijevic@aob.rs

[3]*Institute of Physics, PO Box 57, 11001 Belgrade, Serbia*
E-mail vlada@ipb.ac.rs

Abstract. Simple estimates and approximations play important role in Stark broadening theory, especially in the use for astrophysical purpose. According to the statistical analysis of Stark widths obtained with modified semiempirical approach, the dependence of Stark widths on temperature is determined. New expression describing the dependence of temperature is tested on calculation of Stark widths using simplified modified semiempirical formula, in order to extend this formula toward higher temperatures above the lower treshold limit, which are significant in research of stellar plasma. Results obtained with extended form of simplified modified semiempirical formula are compared with corresponding Stark width values previously calculated with modified semiempirical approach in order to determine the accuracy of new method.(Dimitrijević and Konjević 1981, Dimitrijević and Konjević 1987, Majlinger et al. 2015, Majlinger et al. 2017)

References

Dimitrijević, M. S., Konjević, N.: 1981, *Spectral Line Shapes*, Walter de Gruyter & Co., Berlin – New York.
Dimitrijević, M. S., Konjević, N.: 1987, *Astron. Astrophys.* **172**, 345.
Majlinger, Z., Simić, Z., Dimitrijević, M. S.: 2015, *J. Astrophys. Astron*., **36**, 0.
Majlinger, Z., Simić, Z., Dimitrijević, M. S.: 2017, *MNRAS*, Vol. **470**, Issue 2, 1911.

PROPAGATION OF ELECTROMAGNETIC WAVES IN PERTURBED LOWER IONOSPHERIC PLASMA

A. NINA

Institute of Physics Belgrade, University of Belgrade, Pregrevica 118, 11080 Belgrade, Serbia
E-mail sandrast@ipb.ac.rs

Abstract. Remote sensing of the lower ionospheric plasma has scientific and practical applications. Namely, this atmospheric layer is continuously exposed to numerous astronomical and terrestrial events, and analyses of variations in its plasma parameters are important for detection of these events as well as modeling of influences of perturbed ionospheric plasma on the propagation of electromagnetic waves within it. Here, we present the recent research related to the lower ionospheric disturbances around the periods of natural disasters, and changes in propagation of satellite signals during D-region perturbations induced by solar X-ray flares. In the first part, attention is focused on research of possible ionospheric earthquake precursor visualized as reduction of the noise of the amplitude of a very low frequency radio signal used for monitoring the lower ionosphere (Nina at al. 2020). Analysis of importance of the perturbed D-region for satellite signal delay is subject of the second part of this study (Nina et al. 2019).

Acknowledgments. The author acknowledges funding provided by the Institute of Physics Belgrade, through the grant by the Ministry of Education, Science, and Technological Development of the Republic of Serbia.

References

Nina, A., Nico, G., Odalović, O., Čadež, V. M., Todorović Drakul, N., Radovanović, M., Popović, L. Č.: 2019, *IEEE Geosci. Remote Sens. Lett.*, **1-5**, DOI: 10.1109/LGRS.2019.2941643

Nina, A, Pulinets, S., Biagi, P. F., Nico, G., Mitrović, S. T., Radovanović, M., Popović, L. Č.: 2020, *Sci. Total Environ.*, **710**, 136406.

PLASMA CHANNEL EVOLUTION IN THE TRIGGERD LIGHTNING DISCHARGE

DRAGAN PAVLOVIC

Lola Institute Ltd., Kneza Višeslava 70a, 11030, Belgrade, Serbia
E-mail dragan.pavlovic1@li.rs

Abstract. Using the results and assumptions given in the papers (see Maslowski et al. 2006 and Tausanovic et al. 2010) detailed and efficient numerical algorithms have been developed for application in the study of the lightning channel evolution. Different engineering models were used in the calculation of the axial electric field along the channel axis – the TL, the MTLE, the MTLP, the MTLL and the GTCS model. Obtained results for electric field as well as the point form of Ohm's law have been used to calculate the profile of longitudinal electrical conductivity on the lightning channel. The comparison with the experimental results was performed. It has been shown that the mean values of the mentioned physical quantities are in accordance with the experimental results Cen et al 2015. After a detailed analysis of all engineering models, it was decided to use the GTCS model to investigate the lightning channel dynamics. For this purpose, it is necessary to precisely calculate the channel discharge function from Volterra integral equation of the first kind. This equation is solved analytically by Laplace transformation, as well as numerically by the modified composite trapezoidal formula method (MCTF method). The results show excellent agreement between analytical and numerical methods. Obtained channel discharge function is used in the calculations of other physical parameters along radial and axial directions of the channel.

Acknowledgements: This work is supported by MPNTR, Serbia, under the contracts number TR35023 and TR37019.

References

Cen, J., Yuana, P., Xue, S., Wang, X.: Resistance and internal electric field in cloud-to-ground lightning channel, 2015, *Appl. Phys. Lett.*, **106**, 054104.

Maslowski, G., Rakov, V.: A study of the lightning channel corona sheath, 2006, *J. Geophys. Res.*, **75**, D14110.

Tausanovic, M., Markovic, S., Marjanovic, S., Cvetic, J., Cvejic, M.: Dynamics of alightning channel corona sheath using a generalized traveling current source return stroke model – theory and calculations, 2010, *IEEE Trans. EMC*, **52**, 646–656.

THE EVOLUTION OF STELLAR INTERIORS IN MASSIVE BINARY SYSTEMS

JELENA PETROVIC

Astronomical Observatory 7, Belgrade, Serbia
E-mail jpetrovic@aob.rs

Abstract. Some of the most exciting cosmic phenomena are though to occur in massive binary systems. For example, gamma-ray bursts (GRBs) are associated with collapsars - rapidly rotating massive stars (Petrovic et al. 2005a). Also, sources of gravitational waves, recently observed by the LIGO and Virgo telescopes, are binary systems containing compact objects, relics of massive stars - black holes and neutron stars (Abbott et al. 2019). Stellar interiors in such systems are evolving different compared to the single stars due to the process of mass transfer between the components, accretion and mixing processes (Petrovic et al. 2005b). In this contribution, evolution of stellar components in close massive binary systems, calculated with the MESA numerical code (Paxton et al. 2015), is presented.

References

Abbot, B. P., Abbott, R. Abbott, T. D. et al. : 2019, Phys. Rev. X, vol. 9, **3**, 031040

Paxton, B., Marchant, P., Schwab, J., Bauer, E. B., Bildsten, L., Cantiello, M., Dessart, L., Farmer, R., Hu, H. Langer, N., Townsend, R. H. D., Dean, M., Timmes, F. X. : 2015, *Astrophys. J. Suppl. Series*, **22**, 15.

Petrovic, J., Langer, N., Yoon, S.-C., Heger, A. : 2005, A*stron. Astrophys*., **435**, 247.

Petrovic, J., Langer, N.., van der Hucht, K. A. : 2005, A*stron. Astrophys*., **435**, 1013.

MODELING BROAD LINE POLARIZATION IN ACTIVE GALACTIC NUCLEI

Đ. SAVIĆ[1], L. Č. POPOVIĆ[1], R. GOOSMANN[2], F. MARIN[2] and V. L. AFANASIEV[3]

[1] *Astronomical Observatory Belgrade, Volgina 7, 11060 Belgrade, Serbia*
E–mail djsavic@aob.rs
E–mail lpopovic@aob.rs

[2] *Observatoire Astronomique de Strasbourg, Université de Strasbourg, CNRS, UMR 7550, 11 rue de l'Université, 67000 Strasbourg, France*
E–mail goosmann@astro.unistra.fr
E–mail frederic.marin@astro.unistra.fr

[3] *Astrophysical Observatory of the Russian Academy of Sciences, Nizhnij Arkhyz, Karachaevo-Cherkesia 369167, Russia*
E–mail vafan@sao.ru

Abstract.

Spectropolarimetry of broad emission lines is a powerful tool for probing the geometry and dynamics of the active galactic nuclei (AGNs) central engine (Smith et al. 2005, Goosmann & Gaskell 2007). It provides two additional observables: the degree of polarization and the polarization plane position angle. The latter can be used for supermassive black hole mass (SMBHs) mass measurements assuming that the equatorial scattering is a dominant polarization mechanism (Afanasiev & Popović 2015, Savić et al. 2018), but also, it can indicate the possible presence of binary SMBHs (Savić et al. 2019).

In this work we use 3D Monte Carlo radiative transfer code STOKES (Goosmann & Gaskell 2007) for modeling scattering induced polarization in AGNs, covering broad spectral range around Hα line. We assume a disk-like geometry and a dominant Keplerian-like motion, however, additional complex motions such as outflows and inflows, as well as binary SMBH scenarios are also considered.

References

Afanasiev, V. L., Popović, L. Č. : 2015, *ApJL*, **800**, L35.
Goosmann, R., Gaskell, M. : 2007, *Astron. Astrophys.*, **465**, 129.
Smith, J. E., Robinson, A., Young, S., Axon, D. J., Corbett, E. A. : 2005, *MNRAS*, **359**, 846.
Savić, Đ., Goosmann, R., Popović, L. Č., Marin, F., Afanasiev, V. L. : 2018, *Astron. Astrophys.*, **614**, A120
Savić, Đ., Marin, F., Popović, L. Č. : 2019, *Astron. Astrophys.*, **623**, A56

CORRELATION ANALYSIS OF SOLAR WIND PARAMETERS AND SECONDARY COSMIC RAYS FLUX

NIKOLA VESELINOVIĆ, MIHAILO SAVIĆ, ALEKSANDAR DRAGIĆ, DIMITRIJE MALETIĆ, DEJAN JOKOVIĆ, RADOMIR BANJANAC, VLADIMIR UDOVIČIĆ and DAVID KNEŽEVIĆ

Institute of Physics Belgrade
Pregrevica 118, Belgrade, Serbia
E-mail veselinovic@ipb.ac.rs

Abstract. Galactic cosmic rays (GCRs) entering the heliosphere are disturbed by solar wind and Sun's magnetic field, see Potgieter 2013 Coronal mass ejections (CMEs) structure and shockwave can additionally modulate GCRs, which could results in a transient decrease followed by a gradual recovery in the observed galactic cosmic ray intensity, known as Forbush decrease (FD) see Maričić et al.2014. CMEs are regularly observed via in-situ measurements of plasma and magnetic field in near-Earth space so it is important to understand the relationship between the FDs and near-Earth particles flux associated with these CMEs.

During last 24th Solar cycle, unprecedented extent of heliospheric observations has been achieved thanks to the several new satellites in orbit and CMEs can be observed throughout the heliosphere from the Sun to the Earth, allowing us to relate ground observations to remote sensing data, for Mars see Freiherr von Forstner et al. 2019. We analyzed the dynamics of the variation of galactic cosmic rays (GCR) combining in situ measurement of the particles species present in solar wind with ground observations (worldwide neutron monitor (NM) network and Belgrade's muon detector). This dynamics compared for several CMEs induced FD events. Variations in interplanetary plasma and field parameters during, before, and after the Forbush decreases were examined. Correlation between the 1-hour variations of GCR and several different one-hour averaged particle fluxes was found during FDs and it depends on energy of the particles of the solar wind as well as cut-off rigidities of secondary cosmic rays detectors on ground. These correlations were compared with correlation between same parameters during quiet period of the solar activity. This cross-correlation analysis can help in better understanding of Earth-affecting CMEs and space weather but also to predict GCR flux during extreme solar events.

References

Freiherr von Forstner, J. L. et al. : 2019, *Space Weather*, **17**, 586– 598.
Maričić, D., Vršnak, B., Dumbović, M. et al. : 2014, *Sol Phys* **289**, 351–368.
Potgieter, M. S.: 2013, *Living Rev. Sol. Phys*. **10**, 3 (2013).

SOLITON STRUCTURES IN DIFFERENT ASTROPHYSICAL SYSTEMS

MIROSLAVA VUKCEVIC

Astronomical Observatory Belgrade, Volgina 7, Serbia
E-mail vuk.mira@gmail.com

Abstract. Soliton or solitary wave is usual name for the perturbation that takes wave structure with constant amplitude and group velocity. It results whenever the dispersion of the system is balanced by nonlinearity. Mathematically speaking, it means that soliton is solution of integrable nonlinear equation. There are many astrophysical systems that are subject of no vanishing nonlinear terms and they can be identified as solitons.

One good example is the spiral galaxy; spirals can exist for a very long time due to mentioned balance and using this approach it was possible to overcome wind-up dilemma as a consequence of linearized equations. This is example of one-dimensional soliton, similar to ocean gravity waves.

Next, there are accretion disks which are able to be described by so-called two-dimensional solitons. Similar structures are Jupiter red spots, some structures in the Earth's atmosphere and ionosphere.

Why solitons are so exclusive? All advantages, as well as catastrophic consequences, of having possible for solitons to create, will be discussed.

This theory can be applied in some other systems that follow the nonlinear dynamics, stock market, for example.

References

Hasegawa, A., Maclennan, C. G., Kodama, Y: 1979, *Phys. Fluids*, **22**, 2122.
Jaffrey, A., Taniuti, T.: 1964, Non-linear Wave Propagation: with Applications to Physics and Magnetohydrodynamics. Academic Press, New York.
Korchagin, V. I., Petviashvili, V. I., Ryabtsev, A. D.: 1987, *Sov. Astron. Lett*., **14**, 134.
Vukcevic, M.: 2014, *MNRAS*, **441,** 565.
Vukcevic, M.: 2019, *MNRAS*, **484,** 3410.
Vukcevic, M.: 2020, *Nonlin. Proceses in Geophys*, accepted.
Zakharov, V. E., Kuznetsov, E. A.: 1974, *Sov. J. Exp. Theor. Phys. JETP*, **39**, 285.

PENNING IONIZATION PROCESSES INVOLVING COLD RYDBERG ALKALI-METAL ATOMS

ALAA ABO ZALAM[1], M. S. DIMITRIJEVIĆ[2], V. A. SREĆKOVIĆ[3], N. N. BEZUGLOV[1,4,5], K. MICULIS[4], A. N. KLYUCHAREV[1] and A. EKERS[5]

[1]*Saint Petersburg State University, St. Petersburg 199034, Russia*

[2]*Astronomical Observatory, Volgina 7, 11060 Belgrade 38, Serbia*
E-mail mdimitrijevic@aob.rs

[3]*Institute of physics, University of Belgrade, P.O. Box 57, 11001, Belgrade, Serbia*

[4]*University of Latvia, Institute of Atomic Physics and Spectroscopy, Riga, Latvia*

[5]*King Abdullah University of Science and Technology, Thuwal, Saudi Arabia*

Abstract. The Penning ionization (PI) processes in cold gas media of alkali atoms are investigated in this contribution. The corresponding autoionization widths show a drastic dependence (by orders of magnitude) on the orbital quantum numbers of Rydberg atoms involved in a long-range dipole-dipole interaction. Nontrivial dependence of PI efficiency on the size of colliding particles was considered, with a particular accent to the applications for the research of cold matter created in experiments with magneto-optical traps. We described analytically optimal, highly asymmetric configurations of atomic Rydberg pairs, which lead to explosive intensification (by several orders of magnitude) of free electron escaping due to PI. This property may be favorable for the generation of primary (seeding) charged particles when a cold Rydberg medium evolves into a cold plasma. Under the frame of the semiclassical approach, we obtained universal analytical formulas containing two fitting parameters which allow one to evaluate PI rate constants. The results of the corresponding calculations are presented in the tabulated form convenient for further use for diverse pairs of alkali-metal atoms.

References

Efimov D. K., Miculis K., Bezuglov N. N., Ekers A. : 2016, *J. Phys.B.*, **49**, 125302.

Publ. Astron. Obs. Belgrade No. 99 (2020), 279 - 282 *Contributed Paper*

COLLISION BETWEEN TWO HYDROGEN ATOMS

SAED J. AL ATAWNEH[1] and K TOKESI[1]

[1]*Institute for Nuclear Research, ATOMKI, Debrecen, Hungary*
E-mail saed.al-atawneh@atomki.mta.hu

[2]*Institute for Nuclear Research, ATOMKI, Debrecen, Hungary*
E-mail tokesi@atomki.mta.hu

Abstract. The interaction in a collision between two hydrogen atoms is studied using the 4-body classical trajectory Monte Carlo method. We present the total cross sections for the dominant channels, namely for single ionization of the target, and ionization of the projectile, resulting from pure ionization and also from electron transfer (capture or loss) processes. We present our cross sections in the projectile energy range between 20 keV and 100 keV and compared with them of previously obtained experimental and theoretical results.

1. EXPERMENTS

1.1. INTRODUCTION

The classical-trajectory Monte Carlo (CTMC) method is largely employed in collision physics from low to high projectile energies to determine the excitation, charge exchange and ionization cross sections (Reinhold and Falcón 1986). The CTMC method has been successful in dealing with the ionization processes in ion–atom collisions (Schultz and Olson 1988, Schultz 1989, Schultz, Reinhold et al. 1989, Schultz, Meng et al. 1992, Sparrow and Olson 1994, Tőkési, DuBois et al. 2014, Tökési, Wang et al. 1994). One of its main advantages is that all interactions among the particles can be taken into account exactly during the collision within the framework of the classical dynamics. The model is based on the numerical integration of the classical equations of motions for the investigated system.

For the case of the collision between two hydrogen atoms all the interactions can be exactly taken into account (Tőkési, DuBois et al. 2014). Here we can take the advantage of the classical treatment that in principle we do not have any

[1] Corresponding author: tokesi@atomki.mta.hu

theoretical limit for the number of particles. We can follow all particle trajectories during the collision with the restriction of the classical dynamics.

In this work, we present the total cross sections for the dominant channels, namely for single ionization of the target, and ionization of the projectile, resulting from pure ionization and from two-step processes of electron transfer (capture or loss). Furthermore, we present cross sections for the complete break of the system resulting in the final channel for free particles

Calculations were carried out at low energies, relevant to the interest of the fusion research. We present our cross sections in the projectile energy range between 20 keV and 100 keV and compared with them of previously obtained experimental and theoretical results.

1.2. SIMULATION

In our model the four particles (target nucleus, target electron and projectile electron, and projectile nucleus) are characterized by their masses and charges. Let us denote the projectile nucleus by P, the projectile electron by P_e, the target nucleus by T and the target electron by T_e. The electron-electron interaction is explicitly included in our 4-body calculation. At the time ($t = -\infty$) we consider four particles as two separate atoms, consisting of the projectile system (P, P_e) labelled as particles (1, 2), and the target system (T, T_e) labelled as particles (3, 4) (Fig. 1). Initially, both the projectile (P, P_e) and the target (T, T_e) are in the ground state. We use Coulomb potential for describing all interactions. Figure 1 shows the relative position vectors of the four-body collision system.

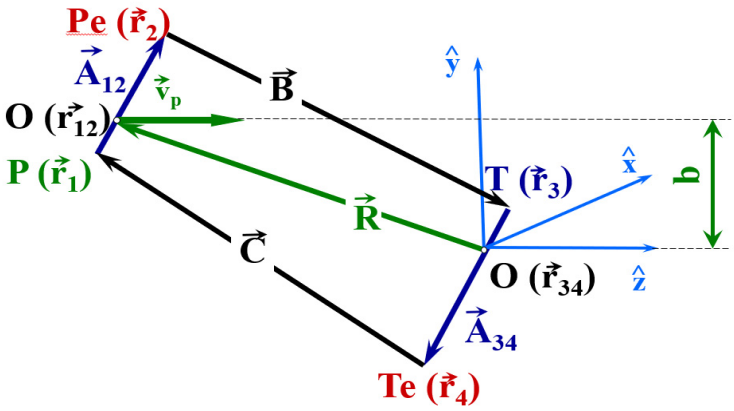

Figure 1: The relative position vectors of the particles involved in 4-body collisions.

In the present CTMC simulations, Newton's classical nonrelativistic equations of motions for four-body system are solved numerically for a statistically large

number of trajectories with initial conditions determined pseudorandomly. The Newton's equations can be written as:

$$m_i \frac{dr_i^2}{dt^2} = \sum_{i \neq j} Z_i Z_j \frac{|r_i - r_j|}{|r_i - r_j|^3} \quad (i, j = 1,2,3,4), \tag{1}$$

where $\mathbf{m_i}$, $\mathbf{r_i}$, and $\mathbf{Z_i}$ denote the mass, the position vector, and the charge of the ith particle, respectively.

The initial conditions are chosen, at relatively large internuclear distances between the projectile and target atoms (**R**, in Fig. l), randomly from an ensemble approximating the quantum mechanical phase space distribution for two separate atoms. After numerically integrating to large distances from the collision center the exit channels are determined according to the relative two body energies.

1.3. RESULT

To study the collision between two ground state hydrogen atoms we performed a classical simulation with an ensemble of 5×10^5 primary trajectories for each energies. In this work we focus on the investigation of the ionization channels.

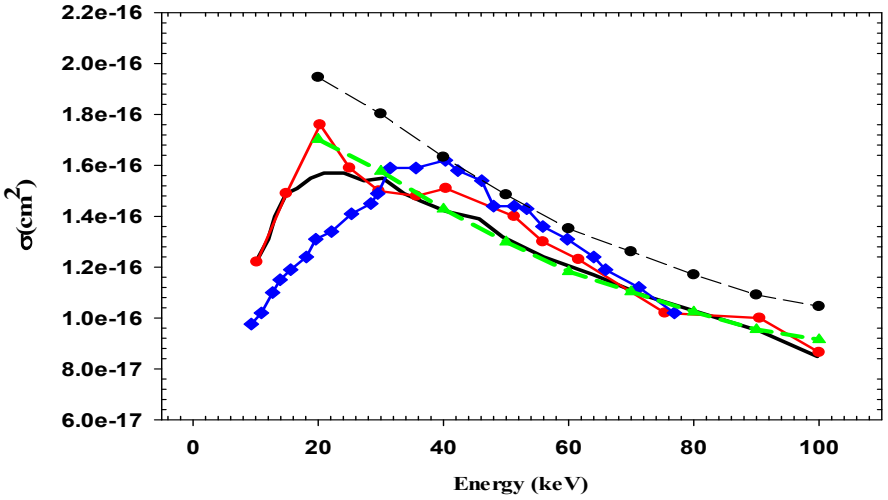

Figure 2: Target ionization cross sections as a function of projectile impact energy. Green dash-line: present CTMC results for H+H collision multiply by 1.75; Black circle with dash-line: present CTMC results for H+H collision multiply by 2; red circle with solid line: experimental data of $H+H_2$ by Solov'ev et al. 1962; blue diamond with solid line: Schwirzke 1960.

Figure 2 shows the energy dependence cross sections of ionization of atomic and molecular hydrogen by atomic hydrogen projectiles impact. Earlier data are available only for ionization of molecular hydrogen; they were obtained by Solov'ev (Solov'ev, Il'in et al. 1962) and Schwirzke (Schwirzke 1960). The ionization cross section for hydrogen molecule is greater than for hydrogen atom target. However the multiplication factor is not 2 as at first we can expect, but 1.75. So the ionization cross section for molecular hydrogen cannot be obtained by simply multiply the cross sections calculated from atomic hydrogen target. The reduction maybe attributed also to the screening of the projectile electron.

Acknowleedgments

The work was support by the National Research, Development and Innovation Office (NKFIH) Grant KH126886. This work has been carried out within the framework of the EURO fusion Consortium and has received funding from the Euratom research and training program 2014-2018 under grant agreement No 633053. The views and opinions expressed herein do not necessarily react to those of the European Commission.

References

Reinhold, C. O., Falcon, C. A.: 1986, *Physical Review A, General Physics*, **33**, 3859-66.
Schultz, D. R.: 1989, *Physical Review A*, **40**, 2330-4.
Schultz, D. R., Olson, R. E.: 1988, *Physical Review A*, **38**, 1866-76.
Schultz, D. R., Reinhold, C. O., Olson, R. E.: 1989, *Physical Review A*, **40**, 4947-58.
Schultz, D. R., Meng, L., Olson, R. E.: 1992, *Journal of Physics B: Atomic, Molecular and Optical Physics*, **25**, 4601-18.
Schwirzke, F.: 1960, *Wasserstoff. Zeitschrift für Physik*, **157**, 510-22.
Sparrow, R. A., Olson, R. E.: 1994, *Journal of Physics B: Atomic, Molecular and Optical Physics*, **27**, 2647-55.
Solov'ev, E. S., Il'in, R. N., Oparin, V. A., Fedorenko, N. V.: 1962, *Ionization of gas by fast hydrogen atoms and protons.*
Tökési, K., Wang, J., Olson, R. E.: 1994, *Nuclear Instruments and Methods in Physics Research Section B: Beam Interactions with Materials and Atoms*, **86**, 147-50.
Tőkési, K., DuBois, R. D., Mukoyama, T.: 2014, *The European Physical Journal D*, **68**, 255.

Publ. Astron. Obs. Belgrade No. 99 (2020), 283 - 286 *Contributed Paper*

IMPACT OF STARK BROADENING ON Co II SPECTRAL LINE MODELLING IN HOT STARS

ABEER ALMODLEJ[1], ZLATKO MAJLINGER[2], NABIL BEN NESSIB[1,3], MILAN S. DIMITRIJEVIĆ[2,4] and VLADIMIR A. SREĆKOVIĆ[5]

[1]*Department of Physics and Astronomy, College of Sciences, King Saud University, Saudi Arabia*

E-mail amodlej@ksu.edu.sa
[2]*Astronomical Observatory, Volgina 7, 11060 Belgrade, Serbia*
E-mail zlatko.majlinger@gmail.com, mdimitrijevic@aob.rs

[3]*GRePAA, INSAT, Centre Urbain Nord, University of Carthage, Tunis, Tunisia*
E-mail nbennessib@ksu.edu.sa

[4]*Sorbonne Université, Observatoire de Paris, Université PSL, CNRS, LERMA,*

F-92190 Meudon, France
[5]*Institute of physics, University of Belgrade, P.O. Box 57, 11001, Belgrade, Serbia*
E-mail vlada@ipb.ac.rs

Abstract. The ignorance of Stark broadening during the modelling of a spectral line profile in hot star spectra can cause significant errors in abundance determination. We choose several Co II, spectral lines observed in stellar spectra to show how Stark broadening influence on their profiles and we calculated Stark widths which can help to determine the abundance of this element in stellar atmosphere more accurate. Using calculated Stark widths, line profiles are synthesized and compared with isolated lines from existing observed stellar spectra. Comparisons of synthetic lines with and without taking of Stark broadening into consideration confirm previous findings that exist cases when synthetic lines with inclusion of Stark widths better fit in the observed spectral lines, especially in the line wings.

1. INTRODUCTION

Stark broadening data are useful for a number of applications as e.g. laboratory plasma diagnostics (Konjević, 1999), the research and modelling of different technological plasmas (Hoffman et al., 2005, Dimitrijević and Sahal-Bréchot, 2014) as well as for inertial fusion (Griem, 1992) and lasers and laser-produced plasmas investigation (Csillag and Dimitrijević, 2004, Dimitrijević and Sahal-Bréchot, 2014). They are particularly useful in astrophysics for a number of

problems like for example stellar plasma modelling, abundance determination, and stellar spectra analysis and synthesis (see e.g. Dimitrijević and Sahal-Bréchot, 2014, Majlinger et al. 2020).

In stellar astronomy, Stark broadening data are of particular importance for white dwarfs of DA (Majlinger et al., 2017), DB (e.g. Simić et al., 2013) and DO (e.g. Popović et al., 2001) type, where Stark broadening is the dominant collisional line broadening mechanism. Such data are also of interest for interpretation, analysis and synthesis of A and B type star spectra (see e.g. Lanz et al., 1988; Popović et al., 2001, Dimitrijević et al., 2007). In particular thanks to large space observatories like Hubble, Chandra, Spitzer, Lyman, and to large, ground-based telescopes, spectra of different celestial objects with very high resolution could be obtained from X to radio wavelength ranges. So the spectral lines of earlier unsignificant trace atoms and ions, like Co II, become important as well as and data for them.

2. RESULTS AND DISCUSSION

Co II spectral lines are observed in stellar spectra (see e.g. Adelman et al., 1993) and recently Stark broadening parameters for lines of 46 Co II multiplets have been calculated (Majlinger et al., 2018, 2020) by using the modified semiempirical method (Dimitrijević and Konjević, 1980).

The aim of this research is to investigate the importance of Stark broadening of Co II lines in the conditions of stellar atmospheres and to synthesize line profile of a Co II line including Doppler and Stark broadening. The --> synthesized profile, obtained using previously calculated data for Stark broadening of Co II lines (Majlinger et al., 2018, 2020) will be compared with the profile observed in stellar spectrum.

As an example of our work we present here the behaviour of Doppler and Stark full line widths at half intensity maximum, as a function of optical depth expressed as the logarithm of Rosseland opacity, for an A type stellar atmosphere using Kurucz (1979) model with log g = 4.5 and *Teff* = 10000 K (Kurucz, 1979). The analysis has been performed for Co II (^{4}P)4sb ^{3}P − (^{4}P)4py ^{3}D^o 2533.2 Å; Co II (^{4}F)4pz ^{3}G^o − (^{4}F)5se ^{3}F 2709.0 Å and Co II (^{4}F)5se ^{3}F − (^{4}F)5p ^{3}G^o 2533.2 Å multiplets and the results are presented in Fig. 1. As we can see, for the multiplet λ9519 the influence of Stark broadening is the highest among the three considered multiplets and for deepest layers it becomes more influencing than the Doppler broadening.

We can also see in Fig. 1 that the influence of Stark broadening on Co II lines increases with the increase of wavelength. This is the consequence of the fact that

Stark width is proportional to λ^2 and the Doppler width to λ, so that the influence of Stark broadening will increase towards the infrared part of the spectrum.

In the continuation of our work we will synthesize a part of χ Lupi spectrum where Co II lines were observed and compare the results of our calculations with the observed spectrum of this star. We will pay particular attention to the line wings, where the largest influence of Stark broadening is expected due to characteristics of the Stark (Lorentzian) and Doppler (Gaussian) line profiles.

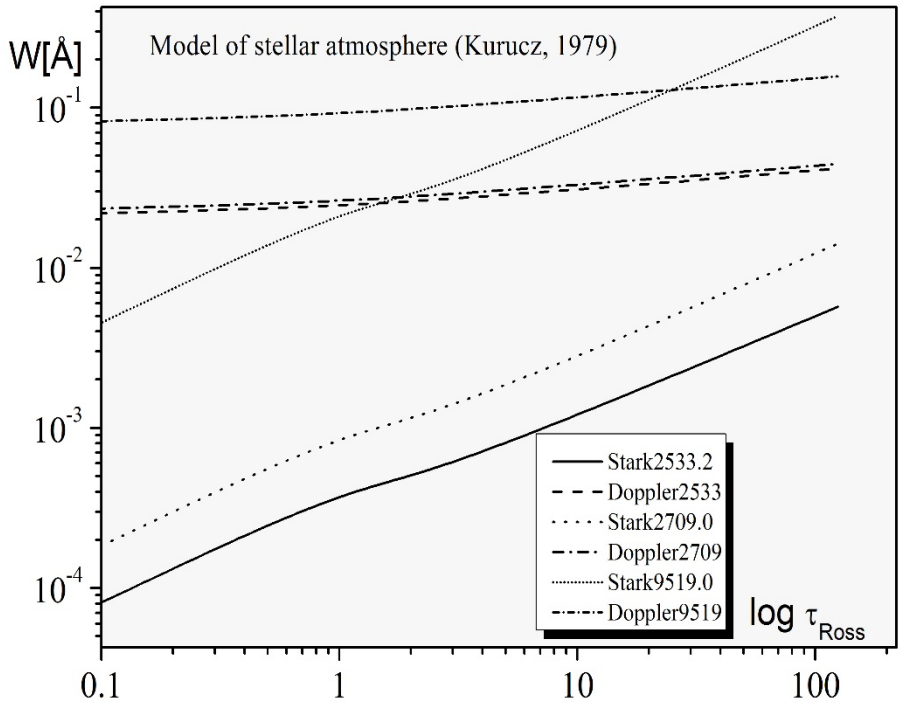

Figure 1: Stark and Doppler broadening for Co II spectral lines λ2533.2, λ2709 and λ9519 as a function of optical depth (log τ_{Ross}) for the model atmosphere (Kurucz, 1979) of A-type star with model parameters log g = 4.5 and Teff = 10000 K.

Acknowledgements

This work was supported by the Astronomical Observatory Belgrade and Institute of Physics Belgrade, through the grant by the Ministry of Education, Science, and Technological Development of the Republic of Serbia.

References

Adelman, S. J., Cowley, C. R., Leckrone, D. S., Roby, S. W.,Wahlgren, G. M.: 1993, *Astrophys. J.*, **419**, 276.
Csillag, L., Dimitrijević, M. S.: 2004, *Appl. Phys. B,* **78**, 221.
Dimitrijević, M. S. and Konjević, N.: 1980, *J. Quant. Spectrosc. Radiat. Transfer*, **24**, 454.
Dimitrijević, M. S. and Sahal-Bréchot, S.: 2014, *Atoms*, **2**, 357.
Dimitrijević, M. S., Ryabchikova, T., Simić, Z., Popović, L. Č. and Dačić, M.: 2007, *A&A,* **469**, 681.
Griem, H. R., 1992, *Phys. Fluids B*, **4**, 2346.
Hamdi, R., Ben Nessib, N., Milovanović, N., Popović, L. Č., Dimitrijević, M. S. and Sahal-Bréchot, S.: 2008, *MNRAS*, **387**, 871.
Hoffman, J., Szymański, Z. and Azharonok, V.: 2006, *AIP Conf. Proc*., **812**, 469.
Konjević, N.: 1999, *Phys. Rep*. **316**, 339.
Kurucz, R. L.: 1979, *Astrophys. J. Suppl.*, **40**, 1.
Lanz, T., Dimitrijević, M. S. and Artru, M.-C.: 1988, *A&A*, **192**, 249.
Majlinger, Z., Simić, Z. and Dimitrijević, M. S.: 2017, *MNRAS*, **470**, 1911.
Majlinger, Z., Dimitrijević, M. S., Simić, Z.: 2018, *Astron. Astrophys. Trans.*, **30(3)**, 323.
Majlinger, Z., Dimitrijević, M. S. and Srećković, V. A.: 2020, *MNRAS*, **496**, 5584.
Popović, L. Č., Simić, S., Milovanović, N. and Dimitrijević, M. S.: 2001, *ApJS,* **135**, 109.
Simić, Z., Dimitrijević, M. S. and Sahal-Bréchot, S.: 2013, *MNRAS*, **432**, 2247.

Publ. Astron. Obs. Belgrade No. 99 (2020), 287 - 290 *Contributed Paper*

KINEMATICAL PROPERTIES OF ELLIPTICAL GALAXIES IN YUKAWA-LIKE GRAVITY

V. BORKA JOVANOVIĆ[1], D. BORKA[1] and P. JOVANOVIĆ[2]
[1] *Department of Theoretical Physics and Condensed Matter Physics (020), Vinča Institute of Nuclear Sciences - National Institute of the Republic of Serbia, University of Belgrade, P.O. Box 522, 11001 Belgrade, Serbia*
E–mail vborka@vinca.rs
E–mail dusborka@vinca.rs

[2] *Astronomical Observatory, Volgina 7, P.O. Box 74, 11060 Belgrade, Serbia*
E–mail pjovanovic@aob.rs

Abstract. Fundamental plane of elliptical galaxies can be used to constrain theories of gravity, i.e. to obtain observational constraints on the parameters of the theories of modified gravity. The fundamental plane is connected to global properties of ellipticals and also can be connected with the parameters of extended theories of gravity. On the other hand several extended gravitation potentials in the weak field limit have Yukawa-like form. That is why in this paper we first analyze the velocity distribution of elliptical galaxies comparing theoretical results in case of Yukawa-like gravity with astronomical data for elliptical galaxies. In that way we constrain the Yukawa parameters α and λ, and analyze the properties of elliptical galaxies in Yukawa-like gravity.

1. THE KINEMATICS OF ELLIPTICAL GALAXIES

There are three main global observables of elliptical galaxies: the central projected velocity dispersion of elliptical galaxies σ_0, the effective radius r_e, and the mean effective surface brightness (within r_e) I_e (Borka Jovanović et al. 2016a,b; Borka Jovanović et al. 2019). Elliptical galaxies do not populate uniformly these three dimensional parameter space, but they are rather confined to a narrow logarithmic plane. Any of the three parameters may be estimated from the other two, and together they describe a plane that falls within their more general three-dimensional space. This correlated plane is now referred to as the fundamental plane (FP) (Dressler et al. 1987; Ciotti et al. 1996). It was defined and discussed in more detail in e.g Bender et al. 1992; Bender et al. 1993; Busarello et al. 1997; Saulder et al. 2013; Taranu et al. 2015 and references therein. The important empirical relation (Busarello et al. 1997):

$$\log(r_e) = a\,\log(\sigma_0) + b\,\log(I_e) + c, \tag{1}$$

gives us the possibility to obtain unique observational constraints on the structure, formation, and evolution of early-type galaxies, as well as on the parameters of the

theories of modified gravity.

Besides, in order to describe the velocity of populations of stars, one can define rotational velocity of a group of stars v_c, and a dispersion σ which represents the characteristic random velocity of stars. The relation v_c/σ characterizes the kinematics of the galaxies. It was shown that it is the main characteristic which differentiates spiral from elliptical galaxies. In case of spiral galaxies $v_c/\sigma \gg 1$, and they are regarded as kinematically cold systems, while elliptical galaxies are characterized with $0 < v_c/\sigma < 1$, and they are kinematically hot systems.

2. STELLAR KINEMATICS IN YUKAWA-LIKE GRAVITY

Several theories of modified gravity in the weak field limit has the Yukawa-like form (Capozziello et al. 2020):

$$\Phi(r) = -\frac{GM(r)}{r}\left[1 + \alpha e^{-\lambda r}\right], \tag{2}$$

where λ^{-1} is the range of Yukawa interaction (scale length) and α is a universal constant which gives the strength of the correction.

In order to use this type of corrections to the gravitational potential for modeling the stellar kinematics in the elliptical galaxies, we assumed that the mass distribution within them may be described by the singular isothermal sphere (SIS) model: $M(r) = 2\sigma_{SIS}^2\, G^{-1}\, r$. In that case $\sqrt{2}\sigma_{SIS} = \sigma_0$, and the expression for circular velocity v_c at the effective radius r_e has the following form (Capozziello et al. 2020):

$$v_c^2(r_e) = \sigma_0^2\left(1 + \alpha\,(1+w)\,e^{-w}\right), \quad w = \lambda r_e, \tag{3}$$

from which one can obtain the following v_c/σ relation at r_e for the ellipticals in the Yukawa-like gravity:

$$\frac{v_c}{\sigma} = \frac{v_c(r_e)}{\sigma_0} = \sqrt{1 + \alpha\,(1+w)\,e^{-w}}. \tag{4}$$

3. FUNDAMENTAL PLANE IN YUKAWA-LIKE GRAVITY

In this section we are going to constrain the parameters α and λ considering a sample of elliptical galaxies given in Busarello et al. 1997. The observations and the method that we are using are described in Capozziello et al. 2020 and references therein. For this purpose, we will study the v_c/σ relation given by the expression (4) for this sample of ellipticals.

In Fig. 1, we show numerically calculated value of the v_c/σ relation for ellipticals as a function of parameter α and product of Yukawa parameter λ and effective radius r_e in case of Yukawa-like potential. With increasing v_c/σ ratio, when approaching to 1, values of α approaches to 0, which is in accordance with our earlier finding (Capozziello et al. 2020). Also, we can notice that for larger values of $\lambda \cdot r_e$ product ($\lambda \cdot r_e \geq 4$) we are in allowed region of parameter space. It means that for this choice of parameters we will expect good agreement between theory and observations.

The theoretical values for the velocity dispersion of elliptical galaxies σ^{theor}, which is assumed to be equal to $v_c(r_e)$, are presented in Fig. 2 as a function of the effective radius r_e, for four different values of the $\lambda \cdot r_e$ product: 2, 3, 4 and 5, and for the three values of Yukawa parameter α: -0.5, -1.5 and -2.0.

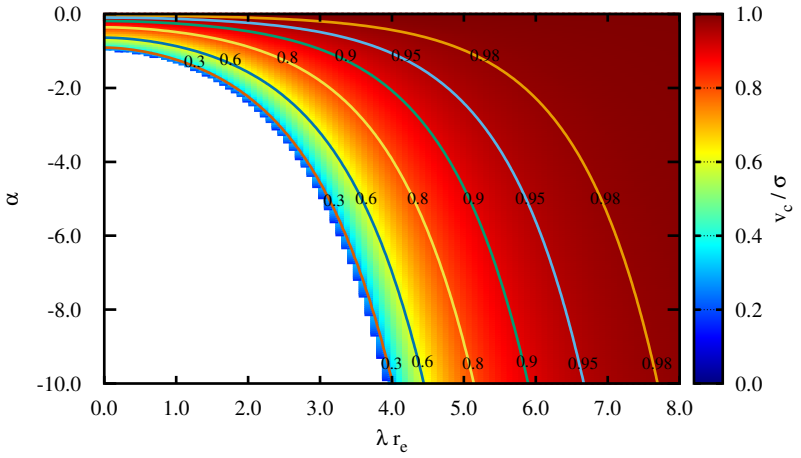

Figure 1: The v_c/σ relation for the elliptical galaxies in the Yukawa-like gravity, given by eq. (4) and represented by different color shades, as well as its dependence on the (λ, α) parameter space of the gravitational potential (2).

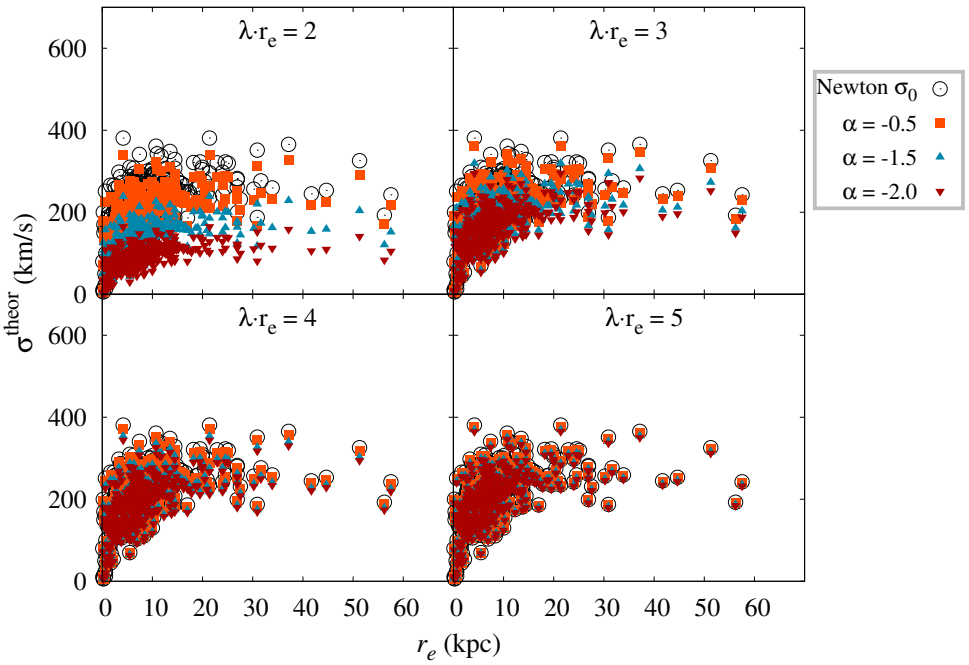

Figure 2: Velocity dispersion σ^{theor} as a function of the effective radius r_e for eliptical galaxies, for four different values of the $\lambda \cdot r_e$ product: 2, 3, 4 and 5. The Newtonian velocity dispersion at the effective radius σ_0 is taken from (Burstein et al. 1997). Theoretical values of velocity dispersion σ^{theor} are calculated for the three values of Yukawa parameter α: -0.5, -1.5 and -2.0.

For all three studied values of Yukawa parameter α, a good agreement is achieved for larger values of $\lambda \cdot r_e$ product of 4 and 5, while in the case of smaller $\lambda \cdot r_e$ product of 2 and 3, agreement is not so good, but it is still satisfactory when parameter α is smaller by magnitude. The values of v_c/σ ratio for different combinations of $(\alpha, \lambda \cdot r_e)$ parameters of Yukawa-like gravity from Fig. 2 are given in Table 1.

α \ λr_e	2	3	4	5
-0.5	0.89	0.95	0.98	0.99
-1.5	0.63	0.84	0.93	0.97
-2.0	0.43	0.78	0.90	0.96

Table 1: The values of v_c/σ ratio for different combinations of (α,λr_e) parameters of Yukawa-like gravity, presented in Fig. 2.

The obtained results show that the Yukawa-like gravity is able to explain elliptical galaxies with different stellar kinematics described by v_c/σ relations shown in Fig. 1 and Table 1, without introducing the dark matter hypothesis. Besides, we can notice from Fig. 2 that the Yukawa-like correction has strong influence on the FP of the elliptical galaxies, and that better agreement with observations is obtained for those gravity parameters α and λ which give a larger v_c/σ relation closer to 1 (i.e. for kinematically less hot systems). Therefore, the v_c/σ relation and the FP can be used as standard tools to probe the Yukawa-like gravity in the weak field limit, as well as to constrain its parameters α and λ.

Acknowledgments. This work is supported by Ministry of Education, Science and Technological Development of the Republic of Serbia. P.J. wishes to acknowledge the support by this Ministry through the project contract No. 451-03-68/2020/14/20002.

References

Bender, R., Burstein, D., Faber, S. M.: 1992, *Astrophys. J.* **399**, 462.
Bender, R., Burstein, D., Faber, S. M.: 1993, *Astrophys. J.* **411**, 153.
Borka Jovanović, V., Jovanović, P., Borka, D., Capozziello, S.: 2016a, *Contributed papers of the 28th SPIG*, Belgrade, Serbia, August 29 - September 2, p. 393.
Borka Jovanović, V., Capozziello, S., Jovanović, P., Borka, D.: 2016b, *Phys. Dark Universe* **14**, 73.
Borka Jovanović, V., Jovanović, P., Borka, D., Capozziello, S.: 2019, *Atoms* **7**, 4.
Burstein, D., Bender, R., Faber, S. M., Nolthenius, R.: 1997, *Astron. J.* **114**, 1365.
Busarello G., Capaccioli M., Capozziello S., Longo G., Puddu E.: 1997, *Astron. Astrophys.* **320**, 415.
Capozziello, S., Borka Jovanović, V., Borka, D., Jovanović, P.: 2020, *Phys. Dark Universe* **29**, 100573.
Ciotti, L.: 1996, *Proceedings of the ESO Astrophysics Symposia "Galaxy Scaling Relations: Origins, Evolution and Applications"*, **1997**, Garching, Germany, 38.
Dressler, A., Lynden-Bell, D., Burstein, D., Davies, R. L., Faber, S. M., Terlevich, R., Wegner, G.: 1987, *Astrophys. J.* **313**, 42.
Saulder, C., Mieske, S., Zeilinger, W., Chilingarian, I.: 2013, *Astron. Astrophys.* **557**, A21.
Taranu, D., Dubinski, J., Yee, H. K. C.: 2015, *Astrophys. J.* **803**, 78.

Publ. Astron. Obs. Belgrade No. 99 (2020), 291 - 294 *Contributed Paper*

APPLICATIONS OF MANIFOLD LEARNING TECHIQUES TO SPECTRAL CLASSIFICATION OF QUASARS

I. JANKOV, D. ILIĆ, and A. KOVAČEVIĆ

Department of Astronomy, Faculty of Mathematics, University of Belgrade, Studentski trg 16, 11000 Belgrade, Serbia
E-mail isidora_jankov@matf.bg.ac.rs, dilic@matf.bg.ac.rs, andjelka@matf.bg.ac.rs

Abstract. In the last three decades, application of different techniques, such as correlation matrix analysis and principal component analysis (PCA), on different spectral parameters of type 1 quasars, has revealed that they occupy a specific parameter space, analogous to main sequence of stars revealed by H-R diagram. Here we investigate a sample of low-redshift ($z < 0.39$) type 1 quasars described by ten spectral features taken from a Sloan Digital Sky Survey catalog using a manifold learning technique called locally linear embedding (LLE). Preliminary results of our investigation indicate that LLE performs better than PCA in terms of clearer visual and functional representation of the quasar main sequence, which may help in future large survey classification of type 1 quasars based on their spectral properties.

1. INTRODUCTION

Much progress was made in the field of active galaxies when larger quasar samples became available, providing spectra with high S/N (Schmidt & Green, 1983). In one of the pioneering research papers that made use of these observations, principal component analysis (PCA) was applied to a sample of 87 quasars (Boroson & Green, 1992). The PCA revealed the main trend in the data – an anti-correlation between [O III] λ5007 Å equivalent width (EW) and the EW ratio of Fe II and broad Hβ - R_{FeII} described by the first principal component. Full width at half maximum (FWHM) of broad Hβ line was also found to be associated with this component (hence the name "Eigenvector 1" or E1). These results set course to many other investigations of spectral properties of quasars based on PCA (Marziani, et al., 2001; Shang, et al., 2003; Grupe, 2004; Yip, et al., 2004; Wang, et al., 2006; Zamfir, et al., 2008; Kuraszkiewicz, et al., 2009) and present the basis for definition of 4DE1 (Sulentic, et al., 2000). More notable example of important leap in understanding the quasar properties was the identification of two main quasar populations (A and B) with different broad line structure, kinematics and spectral

characteristics in optical, UV and X-ray wavelengths (Sulentic, et al., 2000) and the recognition of the Eddington ratio convolved with the line-of-sight orientation of the source as the potential driving mechanism behind the quasar main sequence (MS) revealed by E1 (Marziani, et al., 2001; Shen & Ho, 2014).

In the era of large astronomical surveys, astronomers deal with data sets with ever increasing number of dimensions. Dimensionality reduction (DR) techniques can help us decide which parameters or combinations thereof carry the most information in the data set. In addition, these techniques can be a powerful tool to visualize high-dimensional data while retaining large portion of information contained in the data and potentially help in classification (for a review of DR methods see Łukasik et al., 2016 and Baron, 2019). It was repeatedly demonstrated that PCA is highly effective in tasks of finding important linear relationships in high-dimensional data, but it has its shortcomings when applied to inherently non-linear data sets, such is the case with galaxy spectra where variations of some spectral parameters can be non-linear functions of the galaxy type. This problem can be alleviated by non-linear DR techniques (i.e. manifold learning) such as locally linear embedding – LLE. Goal of LLE is to find a low-dimensional representation of original data set while preserving the geometry of local neighborhoods within the data (Roweis & Saul, 2000). Motivated by previous applications of LLE in astronomical context (e.g. Vanderplas & Connolly, 2009; Daniel et al., 2011; Matijevič et al., 2012) our goal was to see how the interpretation of quasar spectral diversity can be improved by non-linear treatment of type 1 quasars in the context of E1 parameters.

2. DATA ANALYSIS

We use measured spectral properties from the Sloan Digital Sky Survey Data Release 7 quasar catalog (Shen, et al., 2011) and define our sample so it contains only low-redshift objects ($z < 0.39$) with measured both narrow and broad Hα and Hβ components, as well as [O III] λ5007 Å emission line, continuum luminosity ($\log L_{5100}$) and restframe EW of Fe within 4435 – 4685 Å used for calculation of R_{FeII}. Continuum luminosity was corrected for the host galaxy starlight contamination using the empirical fitting formula given by Shen et al. (2011) in their Eq. 1. LLE can be very sensitive to outliers, so before applying the algorithm to our sample, we looked at the density distribution of quasars in E1 optical plane (FWHM Hβ - R_{FeII}) and removed points residing in extremely low-density regions. After excluding outliers from the optical plane using this simple method, we were left with 3720 objects in our sample.

One of the strengths of LLE is the fact that it needs only one free parameter – the number of nearest neighbors (k). The algorithm uses this parameter to learn the local geometry of the manifold. If the value of k is too low, the manifold could be falsely divided into disjoint sub-manifolds. In contrast, if k is too high, the local neighborhood no longer lies on approximately linear surface and Euclidian distances are no longer valid metric for finding the nearest neighbors, leading to

false interpretation of the manifold. Having this in mind, one needs to be cautious when deciding the value of k. Approach that we have used was similar to one used by Tenenbaum et al. (2000) and Kouropteva et al. (2002). In order to choose a value for k, we have calculated a matrix of pairwise geodesic distances of original parameter space, as well as for the resulting low-dimensional space. Then, we compared the matrices by calculating the modified RV coefficient (Smilde, et al., 2008), which is a measure of correlation between two matrices. The process is repeated for a range of values of k, in our case $4 \leq k \leq 30$. Following this approach, we have obtained an optimal number of nearest neighbors ($k_{\mathrm{opt}} = 12$), the one with highest value of modified RV coefficient.

3. RESULTS AND DISCUSSION

After initial preparation of the sample, we have applied LLE with $k = 12$ and specified the output dimension to three in order to provide a visual representation of the original ten-dimensional parameter space. Ten spectral parameters that were used as input in LLE are: broad Hα and Hβ (their EW, FWHM, line luminosity - L), [O III] λ5007 Å (their EW and L), continuum luminosity (log L_{5100}) and R_{FeII}.

Left panel of Fig. 1 presents the resulting 3D space where different quasar populations occupy distinct regions, emphasizing their spectral differences. Objects belonging to populations xA (highly accreting extension of population A, Marzinai & Sulentic, 2014) and B present two extremes of the MS following the direction indicated with an arrow, while population A appears to be an intermediate class. Contrary to PCA, the interpratation of the LLE projection is found in the relationship between the points rather than from the axes (components). In our case, axes present three eigenvectors with lowest nonzero eigenvalues that are obtained by solving a sparse matrix eigenvalue problem which is the last step of the algorithm when low-dimensional projection with perserved local neighborhoods is found (for details see Roweis & Saul, 2000). The resulting LLE projection illustrates the relationships between spectral parameters closest to the original relationships in high-dimensional space and we can use this projection to follow variations of different physical parameters, as presented on the right panel of Fig. 1 in the case of Eddington ratio, the probable principal driving mechanism of the quasar MS. In this way, we can identify parameters that have high correlation with the MS which is an important information needed to further investigate the nature of different quasar populations and potentially help in future large survey classification of type 1 quasars based on their spectral properties.

Preliminary results of our investigation indicate that LLE can be a powerful tool in data exploration and identification of objects with distinct spectral properties. The analysis of our data set showed that it is possible to find three eigenvectors, giving projection in 3D that contains additional information potentially lost in the 2D projection. Our results have confirmed the presence of the quasar MS driven by Eddington ratio in a space with maximum preservation of the original manifold geometry. Further research is needed to investigate the nature of the quasar

populations, mainly by including more spectral parameters as input for LLE and by applying the algorithm to more recent spectral data.

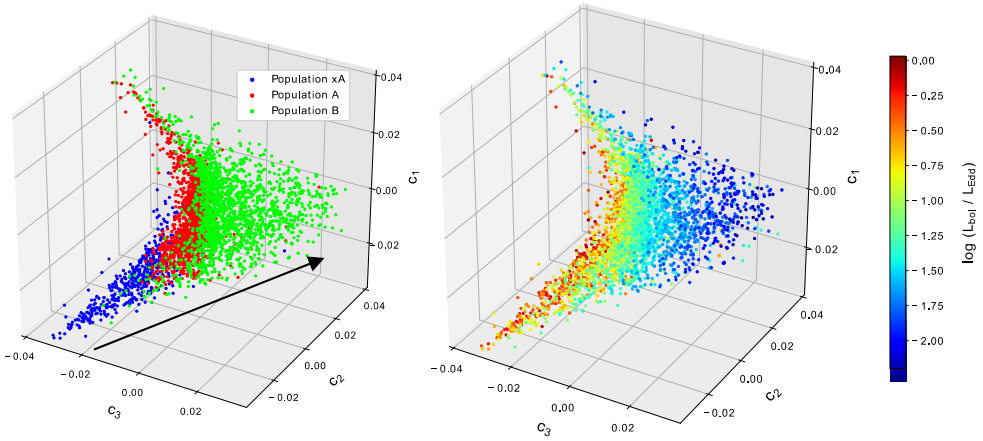

Figure 1: 3D projection of the original manifold embedded in ten-dimensional space. Axes are in arbitrary units and correspond to three components of LLE decomposition. Left – populations xA, A and B are marked with blue, red and green, respectively. The black arrow points in the direction of the quasar MS. Right – gradient of the Eddington ratio in the resulting projection. Direction of the gradient is close to the direction of the MS.

References

Baron, D. : 2019, *arXiv e-prints*, arXiv:1904.07248
Boroson, T. A., Green, R. F. : 1992, *Astrophysical Journal Supplement,* **80**, 109.
Daniel, S. F. et al. : 2011, *The Astronomical Journal,* **142**, 203.
Grupe, D. : 2004, *The Astronomical Journal*, **127**, 1799-1810.
Kouropteva et al. : 2002, *First International Conference of Fuzzy Systems,* 359-363.
Kuraszkiewicz, J. et al. : 2009, *The Astrophysical Journal*, **692**, 1180-1189.
Łukasik, S. et al. : 2016, *Open Physics*, **14**, 64.
Marziani, P. et al. : 2001, *The Astrophysical Journal*, **558**, 553-560.
Marziani, P., Sulentic, J. W. : 2014, *MNRAS,* **442**, 1211-1229.
Matijevič, G. et al. : 2012, *The Astronomical Journal*, **143**, 123.
Roweis, S. T., Saul, L. K. : 2000, *Science*, **290**, 2323-2326.
Schmidt, M., Green, R. F. : 1983, *The Astrophysical Journal*, **269**, 352-374.
Shang, Z. et al. : 2003, *The Astrophysical Journal,* **586**, 52-71.
Shen, Y., Ho, L. C. : 2014, *Nature,* **513**, 210-213.
Shen, Y. et al. : 2011, *The Astrophysical Journal Supplement,* **194**, 45.
Smilde, A. K. et al. : 2008, *Bioinformatics,* **25**, 401-405.
Sulentic, J. W. et al. : 2000, *Annual Review of Astronomy and Astrophysics,* **38**, 521-571.
Tenenbaum, J. B. et al. : 2000, *Science*, **290**, 2319-2323.
Vanderplas, J., Connolly, A. : 2009, *The Astronomical Journal,* **138**, 1365-1379.
Wang, J. et al. : 2006, *The Astrophysical Journal,* **638**, 106-119.
Yip, C. W. et al. : 2004, *The Astronomical Journal,* **128**, 2603-2630.
Zamfir, S. et al. : 2008, *MNRAS,* **387**, 856-870.

Publ. Astron. Obs. Belgrade No. 99 (2020), 295 - 298 *Contributed Paper*

THE SIGNATURE OF THE GAS OUTFLOW IN THE ACTIVE GALACTIC NUCLEI TYPE 2 SPECTRA

JELENA KOVAČEVIĆ-DOJČINOVIĆ[1], MAŠA LAKIĆEVIĆ[1] and LUKA Č. POPOVIĆ[1]
[1] *Astronomical Observatory, Volgina 7, 11000 Belgrade, Serbia*
E–mail jkovacevic@aob.rs

Abstract. We analyse a large sample of the AGNs Type 2 spectra which have a specific spectral characteristic that beside expected narrow emission lines, one broad emission line, Hα, is observed, which is not expected for the Type 2 AGNs. We focus on the fraction of these objects for which some authors (Eun at al. 2017) proposed that observed 'broad Hα' is actually the sum of the wing components of the close narrow emission lines Hα and [N II] doublet, which is misinterpreted as the 'broad Hα'. They propose that wing components of the Hα+NII arise in a gas outflow. In order to check these claims, we search for the outflow signature in the other strong, narrow emission lines in the spectra (Hβ, [O III] and [S II]) and we examine if there are some correlations between the kinematical parameters, widths and shifts, of the wing components of these lines with the Hα+[N II] wing components. We found the significant correlations between the widths and shifts of wing components of all considered emission lines (Hα+[N II], Hβ, [O III] and [S II]) which implies their same origin from the Narrow Line Region outflow, and supports the claims of Eun at al. 2017. However, it seems that Hα line is less affected with outflow kinematics, comparing to the [O III] lines.

1. INTRODUCTION

The most simple scheme of the Active Galactic Nuclei (AGN) structure assumes that in the center of an AGN there is a super-massive black hole surrounded by the high velocity gas of the Broad Line Region (BLR), where broad emission lines arise (with Full Width at Half Maximum - FWHM ~ 4000 km s^{-1}). Around BLR there is a torus of the dust, and out of the dusty torus, there is the Narrow Line Region (NLR), where the narrow emission lines arise (FWHM ~ 400 km s^{-1}). According to the Standard Unified model (Antonucci 1993, Urry & Padovani 1995), the difference in spectral properties between the AGN Type 1 and Type 2, is caused only by the orientation effect. The AGNs Type 2 are observed through dusty torus (edge-on), which covers the broad emission lines from BLR, so only the narrow emission lines can be observed in their spectra. On the other hand, in the spectra of the AGNs Type 1, which are observed with higher inclination angle (~ 45 degrees), both the narrow and the broad emission lines can be observed.

However, some exceptions are found in some spectra of the AGNs type 2, which challenge the classical Unified Model of the AGNs. In these objects, beside the expected narrow emission lines, the broad emission Hα line is observed. Some authors proposed that these objects are Hidden Type 1 AGNs (Greene & Ho 2005, Oh et al.

2015), while Eun et al. 2017 proposed that one fraction of these objects are indeed the Hidden AGNs Type 1, with the true broad Hα, while in the other fraction of these objects, the broad Hα can be explained as the sum of the wing components of the narrow Hα and nearby [N II]$\lambda\lambda$ 6548, 6583 Å doublet, which have the close wavelengths and therefore the sum of their wing components can be misinterpreted as one broad line. They supposed that these wing components arise in the gas kinematically connected with an AGN outflow (Woo et al. 2016).

In this work, we focus to this second fraction of the AGNs Type 2, in which the broad Hα is observed in order to check is it really 'quasi-broad Hα', i.e. the sum of the wing components of the narrow lines, which arise in the gas outflows.

2. THE SAMPLE AND ANALYSIS

We searched the Sloan Digital Sky Survey database (SDSS) DR 14, and found the 314 high quality (signal-to-noise $>$ 20) AGN Type 2 spectra which have 'broad Hα'. Since narrow lines in these spectra have complex shapes and can not be fitted with only one Gaussian, we adopted the fitting model of two Gaussians (narrow core + slightly broader wing component) for each narrow emission line in these spectra. This two-component model of narrow lines is usually applied for [O III] lines in AGN Type 1 spectra (see Dimitrijević et al. 2007). In this way, we fit successfully 258 spectra, in which 'broad Hα' is fitted well with sum of the Hα and [N II] wing components. The rest of the objects are excluded from the sample since they have too broad Hα line, which can not be fitted with sum of the three wing components, and therefore these objects are candidates for the Hidden Type 1 objects. Note, that in this sample of 258 objects, the emission under Hα line can be fitted equally well with one broad Gaussian which can be interpreted as emission of Hα from BLR as well.

In order to check is the broad Hα in these spectra the true broad line or it is the sum of the gas outflow wing components, we analysed several prominent narrow emission lines (Hβ, [O III]$\lambda\lambda$ 4959, 5007 Å, Hα, [N II]$\lambda\lambda$ 6548, 6583 Å and [S II]$\lambda\lambda$ 6717, 6731 Å). The wing components of all these lines have the free parameters for width and shift, except wing components of H and [N II], for which we assume to have the same wing parameters. The example of the fit is shown in Fig. 1.

In the case that 'broad Hα' is the sum of the wing components, which arise in an outflow, we expect the same signature of the gas outflow in the other emission lines as well. Therefore, we search for the correlations between the kinematical parameters (widths and shifts) of the Hα wing component and wing components of the other analysed emission lines. Note that widths of emission lines are given in km s^{-1}, since we assume that main broadening mechanism of emission lines in AGN spectra is Doppler broadening.

3. RESULTS AND CONCLUSIONS

We found the strong correlations between velocity shift of the Hα wing component and velocity shifts of the wing components of all other considered emission lines (Hβ, [O III], [S II]). Also, we found the strong correlation between the width of Hα and [S II] wing components, and weak correlations with widths of the Hβ and [O III] wing components. The coefficients of correlations are given in the Table 1.

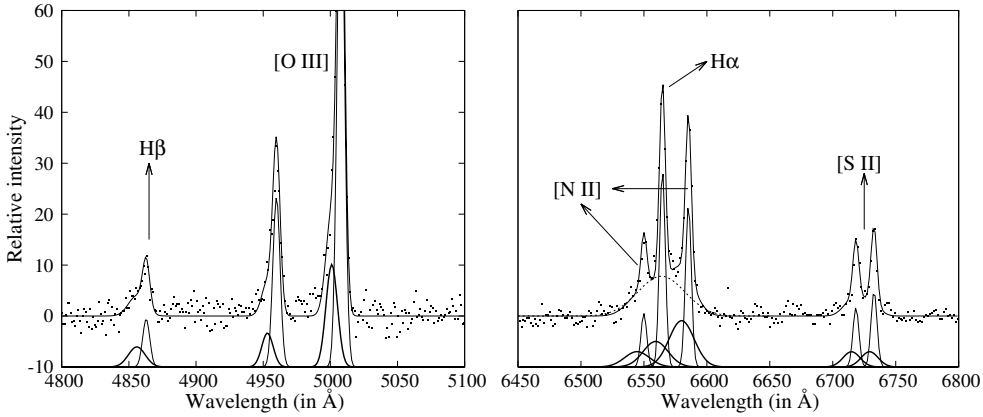

Figure 1: The example of fit of SDSS J112135.17+042647.1. Solid tin Gaussian - core component of narrow lines, solid thick Gaussian - wing component, dashed Gaussian - 'quasi-broad Hα' (FWHM = 2840 km^{-1})

Table 1: (A): The correlations between the shift of the Hα wing component (wc) and shifts of Hβ, [O III] and [S II] wing components (r = Spearman coefficient of correlation, P = significance of correlation). Note, that only 53 objects from this sample have Hβ wing component. (B): The same as in (A), just for the widths.

(A)	shift Hβ wc	shift [O III] wc	shift [S II] wc
shift Hα wc	r = 0.53, P = 4.1E-5	r = 0.46, P = 1.1E-14	r = 0.77, P = 0
(B)	width Hβ wc	width [O III] wc	width [S II] wc
width Hα wc	r = 0.31, P = 0.02	r = 0.28, P = 8.0E-6	r = 0.66, P = 0

These results show clear kinematical connection between the wing components of the Hα and wing components of the other emission lines, [O III], Hβ and [S II]. Since forbidden narrow [O III] and [S II] lines originate from the NLR (they cannot arise in BLR because of the high density in that region), this kinematical connection implies that observed 'broad Hα' in this AGN Type 2 fraction is not emission which originate from the BLR, but indeed the sum of the Hα+[N II] wing components, which arise in the NLR and which are affected with the gas outflow kinematics.

Furthermore, we examined in more details the influence of the gas outflow kinematics to the Hα profile, by comparing it with the [O III] lines which are the most frequently used to trace gas outflows in AGN spectra (Green & Ho 2005, Woo et al. 2016). We compared the distributions of shifts and widths of Hα wing components with the same of [O III] wing components (see Figures 2 and 3). We found that these distributions are similar: Hα wing components are blueshifted in 72% of objects from the sample while [O III] wing components are blueshifted in 75% of objects. However, [O III] wing components have larger blueshifts comparing to the Hα wing components: -108.2$\pm$176.9 km s^{-1} (mean $\pm$ standard deviation), while for Hα wing components it is: -47.2$\pm$84.0 km s^{-1}. The distribution of widths of [O III] wing components is broader than for Hα wing components, and mean FWHM value is slightly larger as

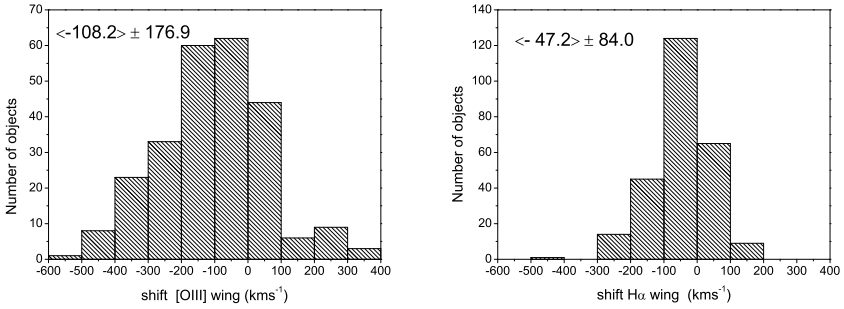

Figure 2: The distribution of the wing component velocity shifts for [O III] lines (left), and for the Hα lines (right).

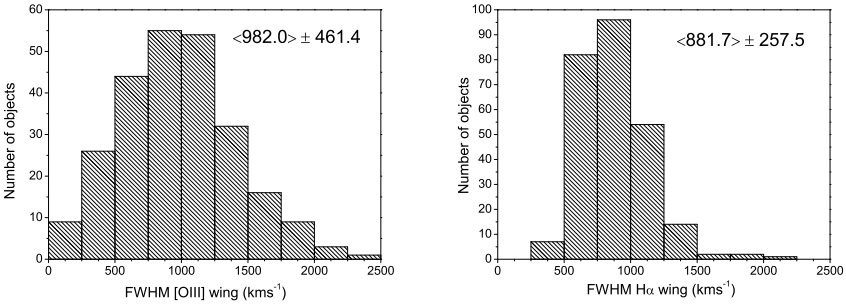

Figure 3: The same as in the previous figure, just for the widths of wing components.

well (982.0±461.4 km s^{-1} for [O III] wing components, and 881.7±257.5 km s^{-1} for Hα wing components). These results imply that influence of the gas outflow to the Hα shape is slightly smaller than to the shape of the [O III] lines.

Our future investigation will be directed towards development of the method for separation of the Type 2 objects with the 'true broad Hα' (Hidden Type 1 objects) from those with 'pseudo-broad Hα', using some differences in their spectral properties. We will focus to the Type 2 objects with 'true broad Hα', because they represent the exception from the Unified model of AGNs, and therefore modelling of their structure is important for understanding the nature of the AGNs.

References

Antonucci R., 1993, *ARA&A*, **31**, 473
Dimitrijević, M.S., Popović, L.Č., Kovačević, J. et al. 2007, *MNRAS*, **374**, 1181
Eun, D., Woo, J.-H. and Bae, H.-J., 2017, *ApJ*, **845**, 5.
Greene, J. E., & Ho, L. C. 2005, *ApJ*, **630**, 122.
Oh K., Yi S.K., Schawinski K., Koss M., Trakhtenbrot B., Soto K. 2015, *ApJ*, **219**, 1.
Urry, C. M. & Padovani, P. 1995, *PASP*, **107**, 803.
Woo, J.-H., Bae, H.-J., Son, D. and Karouzos, M., 2016, *ApJ*, **817**, 108.

Publ. Astron. Obs. Belgrade No. 99 (2020), 299 - 302 *Contributed Paper*

VIRILIZATION OF THE BROAD Hα EMISSION REGION IN ACTIVE GALACTIC NUCLEI TYPE 1

SLADJANA MARČETA-MANDIĆ[1,2], JELENA KOVAČEVIĆ-DOJČINOVIĆ[1], and LUKA Č. POPOVIĆ[1,2]

[1] *Astronomical Observatory, Volgina 7, 11060 Belgrade, Serbia*

[2] *Department of Astronomy, Faculty of Mathematics, Univeristy of Belgrade, Studentski Trg 16, 11000 Belgrade, Serbia*
E–mail sladjana@aob.rs

Abstract. Here we investigate the virialization of the broad Hα emission region using the sample of 68 Type 1 Active Galactic Nuclei (AGN) taken from the Sloan Digital Sky Survey (SDSS). This was done by comparing kinematical parameters of the broad Hα lines with those of the broad Hβ, for which it is assumed that are originating from the virialized emission region. Our results are indicating that other mechanisms should be responsible for the Hα profile broadening and asymmetry, besides black hole gravitation, i.e. the broad Hα emission region is probably not with the same geometry as Hβ one.

1. INTRODUCTION

Active galactic nuclei (AGN) is a compact region in the center of a galaxy with a luminosity over 10^4 higher than those of a normal galaxy, which is attributed to the accretion of gas into the super-massive black hole (SMBH) ($10^6 - 10^{10} M_\odot$) situated in AGN core. Most of the AGNs have a similar structure (Antonucci 1993): SMBH in its center is surrounded by a geometrically thin and optically thick accretion disc (AD) which expands into a dusty torus. Above and below the AD spreads the broad line region (BLR), with optically thick gas, where broad emission lines (BELs) arise (see Osterbrock 1989). Gas in the BLR is ionized by the continuum radiation emitted from the AD and influenced by the gravitational field of SMBH, which causes complexity of structure and kinematics of BLR and affects BELs shapes (Sulentic et al. 2000).

As BELs are originating from the regions close to the SMBH, it is assumed that the BLR emission gas kinematics is virialized, i.e. gas is following the gravitationally driven rotation (see e.g. Sulentic et al. 2000). Such motion of the gas affects the BELs profile, and, in the case of Keplerian-like motion, broadens BELs. Therefore, based on the virial theorem, BELs Full Width at Half Maximum (FWHM) are often used for the estimation of SMBH mass ($M_{\rm BH}$) (Peterson 2014).

The FWHM of the broad Hβ line is most frequently used for $M_{\rm BH}$ estimation (see Peterson et al. 2004), since it is assumed that Hβ is emitted from virialized parts of the BLR. Also, there is an assumption that the red asymmetry frequently seen in

the broad Hβ line profile can be caused by the gravitational redshift, and therefore, it can be $M_{\rm BH}$ indicator as well (Zheng et al. 1990).

Several authors (Green et al. 2005, Mejia-Restrepo et al. 2016, Woo et al. 2015) used the FWHM of Hα line as a virial estimator of $M_{\rm BH}$, relying their calculations on the high correlation of the broad Hα FWHM and the broad Hβ FWHM. This approach is based on their assumption that these two lines have similar profiles, and that Hα region is virialized as Hβ ones. However, there are some indications that broad Hα profiles can be affected by the starburst-driven galactic winds (Shapiro et al. 2009) or by AGN outflows (Eun et al. 2017).

In this work we wanted to investigate: (1) if the assumption that the broad Hα and the broad Hβ profiles are similar is correct; (2) if the broad Hα line is virialized as the broad Hβ is, and (3) is there an influence of the gravitational redshift to the broad Hα line profile.

For this purpose, we compared the broad Hα line profiles with those of the broad Hβ, and the correlations between kinematical line parameters for each of these two lines which should indicate gravitational influence to their emission regions.

2. THE SAMPLE AND ANALYSIS

For our research, we used the sample of AGNs Type 1 spectra taken from the SDSS database, analyzed in Shen et al. 2015 and Harris et al. 2012. We removed several objects with low signal-to-noise ratio, and with the blue asymmetry in the broad Hβ profile, assuming that it is caused by outflows of the gas in Hβ emitting region (see Jonić et al. 2016, Popović et al. 2019). We also removed spectra with no Hα line due to the cosmological redshift of the object, and the final sample consists of 68 AGNs.

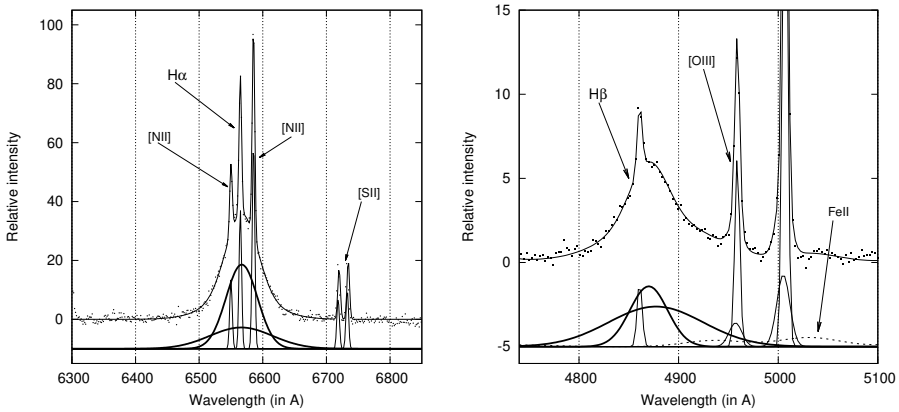

Figure 1: The examples of the decomposition of the Hα and Hβ for object 0439-51877-0566 (SDSS plate-mjd-fiber). The Hα and Hβ are decomposed to one narrow and two broad Gaussians. The observations are denoted with dots, the model with a solid line, an optical Fe II template with a dashed line. The narrow emission line components are denoted with thin, and the broad components with a thick solid line.

The spectra were corrected for the Galactic extinction, cosmological redshift, and host galaxy contribution. Further, continuum emission was removed, and spectra

were fitted using the multi-Gaussian model of optical emission in $\lambda\lambda 4000 - 5500\mathring{A}$ and $\lambda\lambda 6200 - 6900\mathring{A}$ ranges, as it was described in Kovačević et al. 2010. The BLR emission is described with the two-component model, as assumed that BLR consists of two different sub-regions: very broad line region (VBLR) closer to the SMBH, and intermediated line region (ILR), further away from SMBH (see Kovačević et al. 2010 and references therein).

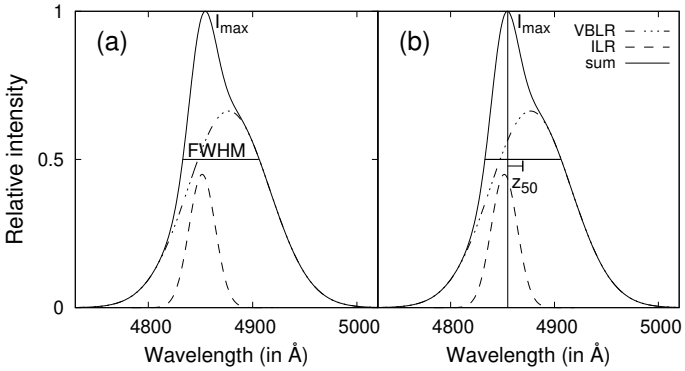

Figure 2: An example of measuring FWHM (a) and intrinsic redshift z_{50} (b) of the broad line component (VBLR + ILR), represented with a different dashed line.

An example of decomposition of the optical emission is shown in Fig. 1. The BEL profile is obtained as a sum of two broad Gaussians, and afterward, the FWHM and asymmetry (intrinsic redshift, z_{50}) of the BEL are measured as shown in Fig. 2. The z_{50} is measured as a difference between the centroid shift and the broad component peak at 50% of I_{max} (see Jonić et al. 2016).

3. RESULTS

We compared the broad Hα and broad Hβ profiles for the sample of 68 objects (see Fig. 3, left). The mean Hα profile is narrower than Hβ one, which may indicate that broad Hα arises in the emission region slightly further away from the SMBH than Hβ emission region. Mean Hα profile shows no asymmetry while mean Hβ profile has red asymmetry indicating a possible influence of the gravitational redshift.

Also, for both lines, we compared the relationships between the width $FWHM^2$ and the intrinsic shift z_{50} of the lines, which are expected to be linearly correlated in the case that line emitting region is virialized and influence of gravitational redshift is not negligible (Popović et al. 2019).

As can be seen in Fig. 3, right, for the Hα profiles there is no correlation between $FWHM^2$ and z_{50} (Spearman correlation coefficient, ρ=-0.09 and P-value of the null-hypothesis, P_0=0.44). On the other hand, the correlation of these profile parameters for the Hβ is significant (ρ=0.69 and $P_0 = 9 \cdot 10^{-11}$).

Furthermore, although there is significant asymmetry measured for the broad Hα profiles, 35% of these profiles are blueshifted and 65% are redshifted, which is not the case with the broad Hβ profiles, as they are only redshifted in this sample, as shown in Fig. 3 (right). As it can be seen in Fig. 3 (left) there is a difference between the

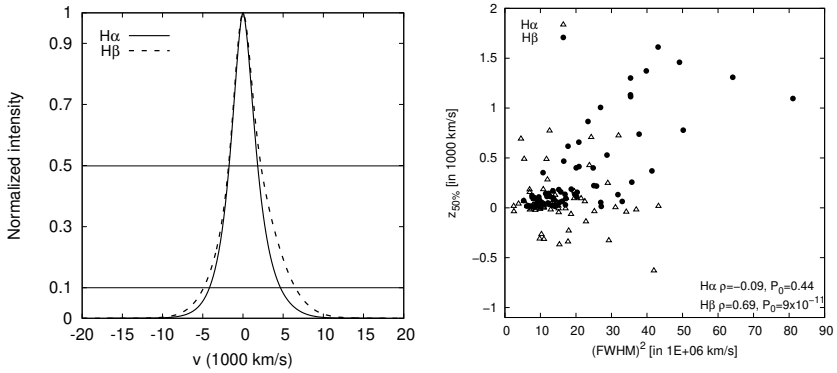

Figure 3: *Left:* Mean normalized profiles for Hα and Hβ. *Right:* The relationship between the $FWHM^2$ and z_{50} of the line measured at 50% of the maximal line intensity. The triangles denote the Hα and the full circles the Hβ lines. Spearman correlation coeff., ρ, and P_0, for both relationships, are given.

mean Hα and Hβ line profiles, especially in the red wing. This indicates that one cannot take 'apriori' that the geometry of the broad Hα and Hβ emission region is the same. The non-existence of the correlation between the Hα FWHM and Hα z_{50} indicates that these two line features probably are not influenced by the same physical mechanism in the case of the Hα line.

It seems that other mechanisms should be partly responsible for the Hα profile broadening and asymmetry, such as AGN outflows or starburst-driven galactic winds (as suggested i.e. in Shapiro et al. 2009), unrelated to the dominant influence of SMBH. Thus, the Hα line emitting region is probably less virialized than Hβ one, and the effect of the gravitational redshift is not observed in the Hα broad profiles in this sample.

References

Antonucci, R. : 1993, Annual Review of *ARA&A*, **31**, 473
Eun, D., Woo, J.-H., & Bae, H.-J. : 2017, *ApJ*, **842**, 5
Green, P. J., Infante, L., Lopez, S., et al. : 2005, *ApJ*, **630**, 122
Harris, C. E., Bennert, V. N., Auger, M. W., et al. : 2012, *ApJS*, **201**, 29
Jonić, S., Kovačević-Dojčinović, J., Ilić, D., and Popović, L. Č.: 2016, *Ap&SS*, **361**, 101.
Kovačević, J., Popović, L. Č., Dimitrijević, M.S. : 2010, *ApJS*, **189**, 15
Mejía-Restrepo, J. E., Trakhtenbrot, B., Lira, P., et al. : 2016, *MNRAS*, **460**, 187
Osterbrock, D. E. : 1989, *Astrophysics of Gaseous Nebulae and Active Galactic Nuclei*, Mill Valley, California.
Peterson, B. M., Ferrarese, L., Gilbert, K. M., et al. : 2004, *ApJ*, **613**, 682
Peterson, B. M. : 2014, *SSRv*, **183**, 253
Popović, L. Č., Kovačević-Dojčinović, J., & Marčeta-Mandić, S. : 2019, *MNRAS*, **484**, 3180
Shapiro, K. L., Genzel, R., Quataert, E., et al. : 2009, *ApJ*, **701**, 955
Shen,Y., Greene, J. E., Ho, L. C., et al. : 2015, *ApJ*, **805**, 96
Sulentic, J. W., Marziani, P. et al. : 2000, *ARA&A*, **38**, 521−571
Woo, J.-H., Yoon, Y., Park, S., et al.: 2015, *ApJ*, **801**, 38
Zheng, W. and Sulentic, J.W. : 1990, *ApJ*, **350**, 512

Publ. Astron. Obs. Belgrade No. 99 (2020), 303 – 306 *Contributed Paper*

REDUCTION OF LOWER IONOSPHERE PLASMA FLUCTUATION – NEW EARTHQUAKE PRECURSOR?

A. NINA[1], S. PULINETS[2], P. F. BIAGI[3], G. NICO[4], S. T. MITROVIĆ[5], M. RADOVANOVIĆ[6] and L. Č. POPOVIĆ[7]

[1]*Institute of Physics Belgrade, University of Belgrade, Pregrevica 118, 11080 Belgrade, Serbia*
E-mail sandrast@ipb.ac.rs

[2]*Space Research Institute, Russian Academy of Sciences, Moscow, Russia*
E-mail pulse1549@gmail.com

[3]*Università di Bari, Physics Department, Bari, Italy*
E-mail pf.biagi@gmail.com

[4]*Istituto per le Applicazioni del Calcolo (IAC), Consiglio Nazionale delle Ricerche (CNR), Bari, Italy*
E-mail g.nico@ba.iac.cnr.it

[5]*Novelic, Belgrade, Serbia*
E-mail mitar027@beotel.net

[6]*Geographical Institute Jovan Cvijić SASA, Belgrade 11000, Serbia*
E-mail m.radovanovic@gi.sanu.ac.rs

[7]*Astronomical Observatory, Volgina 7, 11060 Belgrade, Serbia*
E-mail lpopovic@aob.rs

Abstract. We present analysis of the lower ionosphere plasma short-term disturbances during period around the Kraljevo earthquake that occurred in Serbia on 3 November, 2010. Study is based on analysis of the short-term phase noise of the very low frequency (VLF) radio signal emitted by ICV transmitter located in Italy and received in Serbia. In this study we applied the procedure already described in recent research related to the signal amplitude in period around the considered event which point out the amplitude noise reduction as potential new ionospheric precursor of earthquakes. In this work, we process phase of ICV signal and results indicating phase noise reduction similar like those in the case of the amplitude shows that both signal characteristics, the amplitude and phase, can be used in future research of ionospheric plasma variations as possible precursors of earthquakes.

1. INTRODUCTION

As numerous studies performed during this and previous centuries show, variations in the ionospheric plasma can be considered as earthquake (EQ) precursors (Pulinets and Boyarchuk 2004). Observations of these variations are based on different satellite and ground-based techniques and their applications primarily depend on the considered altitude domain.

In this study we focused on the lower ionosphere and its remote sensing by the very low frequency (VLF) radio waves. This technique provides continuous information related to the waveguide within signal propagate and can be used for the lower ionosphere changes in different time scales. In addition, there are several networks of the VLF receivers which, in combination with numerous VLF transmitters located worldwide, allows monitoring large part of the lower ionosphere and detections of local disturbances like those possible connected with processes relevant for earthquakes. One of these networks, the International Network for Frontier Research on Earthquake Precursors (INFREP, Biagi et al. 2011), is located in the Europe. The data collected with its receivers located in seven European countries showed a typical variation in signal amplitudes several days before earthquake events (see for example Biagi et al. 2011). In addition, the recent research of the short-term amplitude noise shows that its reduction is recoded less than one hour before the Kraljevo EQ occurred in Serbia on 3 November, 2010.

In order to examine if these short-term ionospheric variations can be described also as changes in time evolution of another signal parameter, phase, in this work we analyze the phase noise of the VLF signal emitted by ICV transmitter located in Italy and received in Serbia (Grubor et al. 2005).

2. OBSERVATIONS AND SIGNAL PROCESSING

We analyze data obtained by remote sensing of the lower ionosphere during night-time when Kraljevo EQ occurred with 20.27 kHz signal emitted by ICV transmitter from Isola di Tavolara, Italy (40.92 N, 9.73 E) and received by the Absolute Phase and Amplitude Logger (AbsPAL) receiver located at the Institute of Physics Belgrade in Belgrade, Serbia (44.8 N, 20.4 E). The distance between the propagation path of this signal and the EQ epicentre is 126 km that is usually large for detection of long-term ionosphere variations before not so strong EQs like the considered one. However, better data sampling of 0.1 s provided in our observations allows us to analyze short-term signal changes which, as it is show in Nina et al. (2020), are recorded (in analysis of the signal amplitude) for several EQ events occurred more than 100 km from signal propagation path. Here we analyze the signal phase on the same way like in the previous research of the amplitude.

Changes of the phase noise is visualized in this analysis as variations in time evolution of phase deviation dP defined as difference between recorded, P, and

basic phase P_{base} (mean value of P within defined time bean around time t): $dP(t) = P(t) - P_{base}(t)$.

3. RESULTS AND DISCUSSIONS

Time evolution of phase deviation dP is shown in Fig. 1 where, in order to remove non-natural changes, we exclude values larger and smaller than 60^o and -60^o, respectively. As one can see, significant noise reduction is recorded less than one hour before the EQ event whose time occurrence is indicated with vertical dashed line.

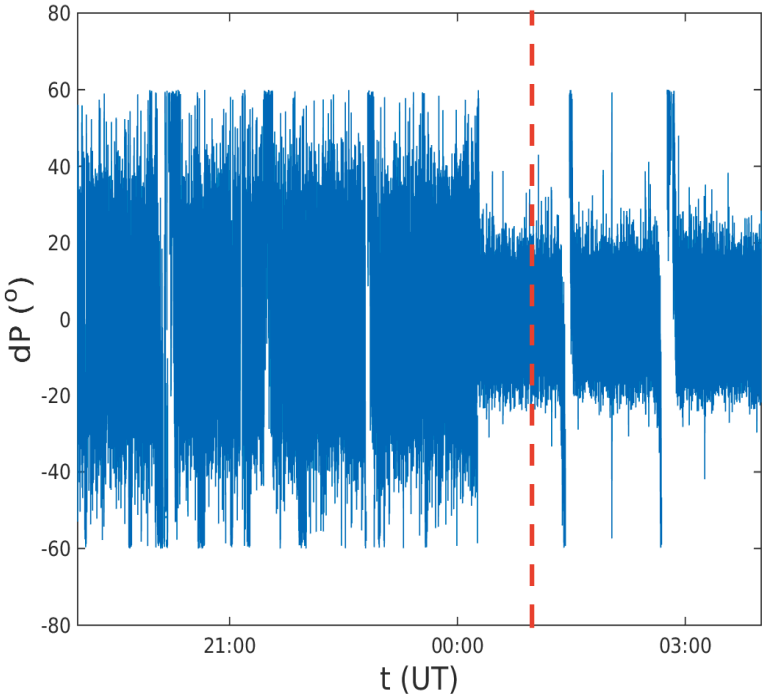

Figure 1: Time evolutions of phase deviation dP of the ICV signal in night-time of the Kraljevo earthquake. Vertical dashed line indicates the time of occurrence of the considered EQ.

In comparison with the amplitude noise, which has been analyzed in Nina et al. 2020, we can conclude that the noticed changes are very similar and that both analyses point out that reduction in lower ionosphere short-term fluctuations can be considered as new possible EQ precursor.

4. SUMMARY

In this paper, we analyzed time evolution of short-term fluctuations of the lower ionosphere plasma processing of data for the phase of the ICV signal recorded in Belgrade around time of Kraljevo EQ occurrence. As in the case of amplitude analysis, the obtained results show that significant reduction of phase noise started less than one hour before the EQ event.

Keeping in mind that this analysis presents a case study, confirmation that the recorded ionospheric changes can be a new type of ionosphere precursors of earthquakes requires statistical analyses. Here, we should point out that recent study shows reductions of amplitude noise are recorded before several other EQ events occurred during 3, 4 and 9 November, 2010 near the propagation path of the considered signal even in some cases of very weak EQ events. Although variations are visible for all of 4 EQs of magnitude greater than 4, studies with larger sample should be made before we can confirm the analyzed relationship and find its possible characteristics.

Acknowledgments

The authors acknowledge funding provided by the Institute of Physics Belgrade, the Astronomical Observatory (the contract 451-03-68/2020-14/200002), and project No 176001 through the grants by the Ministry of Education, Science, and Technological Development of the Republic of Serbia.

References

Biagi, P. F., Maggipinto, T., Righetti, F., Loiacono, D., Schiavulli, L., Ligonzo, T., Ermini, A., Moldovan, I. A., Moldovan, A. S., Buyuksarac, A., Silva, H. G., Bezzeghoud, M., Contadakis, M. E.: 2011, *Nat. Hazards Earth Syst. Sci.*, **11** , 333.

Nina, A, Pulinets, S., Biagi, P. F., Nico, G., Mitrović, S. T., Radovanović, M., Popović, L. Č.: 2020, *Sci. Total Environ.*, **710**, 136406.

Pulinets, S., Boyarchuk, K.: 2004, *Ionospheric precursor of earthquakes*. Heidelberg: Springer.

Publ. Astron. Obs. Belgrade No. 99 (2020), 307 - 310 *Contributed Paper*

IONOSPHERIC D-REGION INFLUENCE ON SAR SIGNAL PROPAGATION

J. RADOVIĆ[1], A. NINA[2] and G. NICO[3,4]

[1]*Faculty of Physics, University of Belgrade, 11000 Belgrade, Serbia*
E-mail radovicj95@gmail.com

[2]*Insitute of Physics Belgrade, University of Belgrade, 11080 Belgrade, Serbia*
E-mail sandrast@ipb.ac.rs

[3]*Instituto per le Applicazioni del Calcolo (IAC), Consiglio Nazionale delle Riecerche (CNR), 70126 Bari, Italy*
E-mail g.nico@ba.iac.cnr.it

[4]*Department of Cartography and Geoinformatics, Institute of Earth Sciences, Saint Petersburg State University (SPSU), 199034 Saint Petersburg, Russia*

Abstract. Many studies have suggested that the signals used for satellite observations can be interrupted by the influence of a certain part of the ionosphere. In the course of our research we observed the perturbed D-region and its influence on the Synthetic Aperture Radar (SAR) signal delay that occurred as a consequence of the perturbation induced by a solar X-ray flare. To model the D-region plasma disturbance we analyse a very low frequency signal emitted by the DHO transmitter located in Germany and recorded in Serbia using Wait's model of the ionosphere. The results of the conducted research can help in further improvement and precision in modeling and measuring regarding SAR instruments.

1. INTRODUCTION

Satellite measurements and their contribution in observing and monitoring the planet Earth has become significant in many scientific fields. Some types of satellites only detect the radiation that comes from the Earth or outer space, whereas others are emitting their own signals which propagate towards the Earth's layers and reflect from some area.

In this paper we only consider the latter type of satellites. Satellites such as Sentinel-1, NASA-ISRO Synthetic Aperture Radar (NISAR) and Constellation of Small Satellites for Mediterranean basin Observations or (SkyMed) hold a

Synthetic Aperture Radar (SAR) which transmits microwave signals towards the Earth. SAR has the ability to operate at wavelengths not hindered by a cloud cover and acquires data over a specific place during day time or night time regardless the weather conditions. Synthetic aperture radar interferometry (InSAR) is a specific method of making observations which has many applications such as providing data for meteorological purposes. In order to acquire information about the target, the satellite emits the signal such as electromagnetic radiation of a certain frequency. During its path through the atmosphere the signal becomes prone to its current state. Moreover, one of the atmospheric layers which can significantly influence the signal and the layer which we contemplated is the ionosphere. Specifically, the D-region which when perturbed can cause a delay which cannot be neglected. The main reason for the signal deviation is the increased electron density which affects signal propagation path. The electron density has larger values in the upper part of the ionosphere, and its and the influences of the lower ionosphere above 100 km are taken into account in various models. However, during perturbations caused by solar X-ray flares the total electron content (TEC) present in the ionospheric D-region (60 km – 90 km) can affect the SAR signal propagation (see Nina et al. 2020). The main goal of this study is to show the example of how the perturbed D-region can affect the propagation of a SAR signal and calculate the D-region phase delay (P_{D}) for different frequencies and incident angles. To calculate the D-region electron density and TEC in the D-region ($\mathrm{TEC_D}$), we process DHO VLF signal used for the lower ionosphere observations and Wait's model of the ionosphere (Wait and Spies 1946).

2. OBSERVATIONS AND MODELLING

The event which caused perturbations in the ionosphere considered in this paper is the X-ray solar flare which happened on 1 May, 2013. Data used for modeling are derived by the $23.4kH_z$ VLF signal emitted by the DHO transmitter located in Rhauderfehn, Germany, and received at the Institute of Physics in Belgrade, Serbia, (Nina et al. 2020). Furthermore, the contemplated SAR frequencies are$f_1 = 1.257GH_z$,$f_2 = 5.405GH_z$ and $f_3 = 9.6$ GHz used in NISAR mission, Sentinel-1 and COSMO-SkyMed, respectively. In order to calculate the influence that the D-region has on the signal propagation it is necessary to determine the total electron content present in the mentioned region ($\mathrm{TEC_D}$) represented by

$$TEC_D = \int_{l_D} N_e dl_D, \tag{1}$$

where l_D represents the signal propagation path in the D-region and N_e represents the electron density. The vertical and temporal electron density distribution is calculated by equation (Tomson 1993):

$$N_e(h,t) = 1.43 \times 10^{13} e^{-\beta(t)H'(t)} e^{(\beta(t)-0.15)h} \quad , \tag{2}$$

where temporal evolution of the "sharpness" β and signal reflection height H' are obtained as the best fit of the recorded and modeled amplitude and phase of the analyzed VLF signal using procedure based on Wait's model of the ionosphere (Wait and Spies, 1964) explained in Grubor et al. 2008 and references therein. In order to calculate TEC, the D-region is divided into N_D horizontally uniform layers of thickness δH_D, each with its own electron density N_{ei}. Ultimately, equation used for calculating the phase delay P_D produced by the D-region can be expressed as (Nina et al. 2019):

$$P_D = \frac{C\delta H_D}{f^2}\sum_{i=1}^{N_D}\frac{N_{ei}n_i}{\sqrt{n_i^2-(n_0 sin(\Theta_0))^2}} \tag{3}$$

where $C = 40.3$ and n_i is the refractive index in the layer i. Θ_0 is the incident angle of the SAR signal in the D-region and f stands for the signal frequency.

3. RESULTS AND DISCUSSION

As mentioned above there are three different SAR frequencies from three different satellites. The first frequency is f_1 = 1.257 GHz (NISAR Earth-observing mission) and it belongs to L-band satellite frequency range $(1\text{-}2\ \mathrm{GHz})$. Furthermore, the second frequency is f_2 = 5.405 GHz, and it is taken from Sentinel-1 SAR instrument. This frequency is the part of the C-band range (4-8 GHz). Finally, the third frequency is from the X-band range (8-12 GHz). Its value is f_3 = 9.6 GHz, and it is taken from COSMO-SkyMed satellites.

We observed dependency of signal delay in the D-region at the moment when the D-region electron density maximum is attained which happened during disturbance induced by the analyzed solar X-ray flare. It is visible from Fig. 1 that the signal delay increases with incident angle for each of the three frequencies. Apparently the signal delay is the smallest for the highest frequency which is in our case f_3 and the highest for the lowest frequency which is f_1 frequency. It is worth noting that the value of P_D decreases as the value frequency is doubled, (see Eq. (3)) which implies that with increasing the frequency value one can get smaller ionospheric D-region influence on the signal.

The highest signal delay is obtained for the lowest, f_1, frequency and it reaches $30mm$ which is not negligible for modeling and applications of SAR signals. Bearing in mind the above-mentioned one can conclude that the signal delay induced by the X-ray solar flare needs to be taken into account.

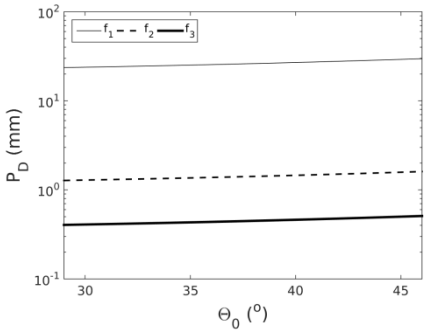

Figure 1: P_D dependence on the signal incident angle Θ_0 in the range from 29° to 46° and SAR frequencies f_1=1.257 GHz, f_2=5.405 GHz and f_3=9.6 GHz.

3. SUMMARY

The final outcome of this work was to present the signal delay that occurs during the ionospheric D-region disturbance. This was achievable by using the proposed modeling methods and the collected data. The signal delay dependence on the signal incident angle was calculated for three different SAR signal frequencies. For each one of the frequencies the signal delay was observed, which indicates the influence that the perturbed D-region has. One prominent thing which needs to be pointed out is that the signal delay decreases with the SAR signal frequency. Furthermore, the increase of the signal incident angle results in higher signal delay. Acquired values of the signal delay, obtained during a not so strong solar flare, indicate that the D-region influence on the SAR signal propagation cannot be neglected.

Acknowledgments

The authors acknowledge funding provided by the Institute of Physics Belgrade, through the grant by the Ministry of Education, Science, and Technological Development of the Republic of Serbia.

References

Grubor, P. D., Šulić., D. M., Žigman, V.: 2008, *Ann. Geophys*., **26**, 1731–1740.

Nina, A., Nico, G., Odalović, O., Čadež, V. M., Todorović Drakul, N., Radovanović, M., Popović, L. Č.: 2019, *IEEE Geosci. Remote Sens. Lett.*, **1-5**, DOI: 10.1109/LGRS.2019.2941643

Tomson, N. R.: 1993, *J. Atmos. Terr. Phys.,* **55**, pp. 173–184

Wait, J., R., Spies, K. P.: 1967, *Characteristics Earth-ionosphere waveguide for VLF radio waves, Tech. Note 300, Nat. Bureau Standards, Boulder, CO, USA.*

Publ. Astron. Obs. Belgrade No. 99 (2020), 311 - 314 *Contributed Paper*

NUMEROV METHOD ANALYSIS WITH A GOAL OF APPLICATION OF COMPLEX PLASMA MODELS

NENAD M. SAKAN[1] and ZORAN SIMIĆ[2]
[1] *Institute of Physics Belgrade Pregrevica 118, Belgrade, Serbia*
E–mail nsakan@ipb.ac.rs

[2] *Astronomical Observatory Volgina 7, P.O.Box 74 11060 Belgrade, Serbia*

Abstract. The dense plasma is a complex system, with it's specifics in describing of related to more common plasma systems. It is proven that a Cut-off coulomb model potential had it's advantages in describing of the hydrogen plasma of moderate up to the higher plasma non ideality. The need for introducing a more complex models of atom in plasma is needed. The further modification and development of a similar or more advanced model potentials is expected to produce a better and more applicable results. There is a need for fast and accurate enough method of their solution. In this paper the analysis of the logarithmic grid of Numerov method for solving a Hydrogen Coulomb potential is analyzed.

1. THEORY

Moderate and high density plasma is characterized by the strong inter particle forces, leading to the coupling of the charged species in plasma, see Fortov et al. 1989, Kobzev et al. 1995., Adamyan et al. 1994 and Adamyan et al. 2004 for example. In order to characterize a non ideality the parameter Γ is defined by

$$\Gamma = \frac{\langle E_{Coul} \rangle}{kT_e} = \frac{q_e^2}{4\pi\varepsilon_0 kT_e} \sqrt[3]{\frac{4\pi n_e}{3}}, \tag{1}$$

for the plasma of temperature T_e and density n_e, note that in the local thermodynamical equilibrium an electron temperature and electron density could be used. Non ideality parameter itself presenting a ratio of Coulomb inter particle interaction in compare to average thermal energy of the plasma system. The Γ parameter for slightly and moderately non ideal plasma is within orders of 0.1 up to 10.

The plasma, as a collective phenomena, could be analyzed in a quantum mechanical approach, as a single particle which potentials is influenced by all the plasma species. The particle-plasma interaction is therefore described with the help of the pseudo potential. Having in mind that the closest neighbors reflect onto the mid range zone of the potential, where Coulomb potential weakness in comparison to their influence, while average plasma influence reflects as a constant potential level in a far field region. The cut-off Coulomb potential presents a good description of plasma influence in close vicinity of the analyzed particle, as well as in far field zone, so the

more complex forms of the pseudo potential is needed, see Mihajlov et al. 2011, Sakan 2010, Sakan et al. 2018 and Srećković et al. 2010. In general the potential of arbitrary form does not posses an analytical solution, so that numerical method for solution of a Schrödinger equation is needed.

In this paper an initial analysis of the stability of the numerical solution method took a place. As a main candidate the Numerov method with the logarithmic grid is selected.

1. 1. RADIAL PART OF THE SCHRÖDINGER EQUATION

In description of the plasma atom interaction a radial part of Schrödinger equation is used in order to calculate the radiative parameters of plasma

After introducing a new function $R(r) = P(r)/r$ into the radial part of the Schrödinger equation, as well as the use of a modified potential $\tilde{V}(r) = V(r) + (\hbar^2/2m)(l(l+1)/r^2)$, simplifies the form of the radial part

$$-\frac{\hbar^2}{2m}\frac{d^2P(r)}{dr^2} + \tilde{V}(r)P(r) = EP(r). \tag{2}$$

1. 2. NUMEROV METHOD FOR RADIAL SCHRÖDINGER EQUATION

The differential equation 2 is solvable with the help of Numerov method behind which a Taylor expansion of the differential equation is used. If the new function $q(r) = \tilde{V}(r) - E$, the differential equation tooks the form $P''(r) = q(r)P(r)$. Having in mind that the Taylor expansion is valid for the linear mesh, e.g. $r_i = i * h$, where the notation $P(r_i) \equiv P_i$ and $q(r_i) \equiv q_i$ is used here. As it is known a solution for the radial function P_i is given by

$$P_{i+1} = \frac{12\left[2P_i - P_{i-1}\right] + h^2\left[10q_iP_i - q_{i-1}P_{i-1}\right]}{12 - h^2q_{i+1}} - \frac{P_i^{(6)}h^6}{20\left(12 - h^2q_{i+1}\right)}, \tag{3}$$

where $P_i^{(n)} \equiv \frac{d^n}{dr^n}P(r_i)$. The first order differential is given by

$$\begin{aligned} P_i' \quad = \quad & \tfrac{1}{12h}\left[P_{i-2} - 8P_{i-1} + 8P_{i+1} - P_{i+2}\right] - \\ & \tfrac{h}{60}\left[q_{i-2}P_{i-2} - 2q_{i-1}P_{i-1} + 2q_{i+1}P_{i+1} - q_{i+2}P_{i+2}\right] - \tfrac{11}{2520}P_i^{(7)}h^7. \end{aligned} \tag{4}$$

More details about the application of the Numerov procedure from Noumerov 1924, and the application onto the radial Schrödinger equation could be seen in Paolo Giannozzi 2012/2013 and Havlová et al. 1984. It could be seen from the previous equations that an error of the Numerov method could be estimated easily and is well behaved in most of the radial part of the function space. In order to avoid the problems related to the accumulation of the numerical error as well as to adopt for a more realistic grid for the differential equation that has to be solved, a new variable is introduced, $x = x(r)$, $dx = x'(r)dr$. For the logarithmic grid a function is given by

$$x(r) = \log\left(\frac{Zr}{a_0}\right), \qquad \Delta x = \frac{a_0}{Zr}\delta r. \tag{5}$$

in order for system to be solvable by a Numerov method on a different grid $x_i = x_0 + h*i$. In a case of logarithmic grid a function $y(x) = P(r(x))/\sqrt{r(x)}$ neutralizes the first

order differential and preserves a form of differential equation $y''(x) = q(r(x))y(x)$, solvable by a Numerov method.

2. TEST PROCEDURE AND RESULTS

The analysis is performed using the Coulomb potential, e.g. the solution are for the hydrogen atom without the influence of the plasma, since the stability is expected to be the same with more complex pseudo potentials and the Coulomb one have an analytical and known solutions.

Here we applied the Numerov procedure method that uses two separate solution, outward integration, from the smallest radius values to the end of the classical solution zone, and other, inward integration, from the largest values of the radius down to the joining point. The solution is possible only for some values of the energy levels, so the shooting method is applied in order to search for the values of the bond state energy.

As it is known, the convergence of the potential and physical meaning of the wave function led to asymptotic solutions used for the initial values of the numerical solution presented by

$$R(r)|_{r\to 0} \sim r^l, \qquad P(r)|_{r\to 0} \sim r^{l+1}, \tag{6}$$

and for the large values of r

$$R(r)|_{r\to \infty} \sim r^{n-1} \exp\left\{-\frac{Zr}{na_0}\right\}, \qquad P(r)|_{r\to \infty} \sim r^n \exp\left\{-\frac{Zr}{na_0}\right\}. \tag{7}$$

In order to study a stability of the procedure of variation of a second initial value is involved. With the help of varying parameter ε the second bond value in both inward and outward integration is varied, mathematically could be presented as

$$\begin{array}{cccc} F_0 = F_0, & F_1^{NEW} = k * F_1, & F_N = F_N, & F_{N-1}^{NEW} = k * F_{N-1}, \\ F \equiv [R(r), P(r)] & k = (1+\varepsilon), & \varepsilon \in (-1, 1) & \end{array} \tag{8}$$

In this analysis a parameter ε took values [-0.1, -0.05, -0.01, -0.005, -0.001, 0, 0.001, 0.005, 0.01, 0.05, 0.1]. All of these parameter values, in exception of -0.1, that are smaller or equal to 0, led to the same energy values with the relative error smaller than 10^{-5}. In the case of the smallest values for $\varepsilon > 0$ the result yields a lower energy state, otherwise the numerical solution will be colapsed.

3. CONCLUSION

The preliminary test led a conclusion that the numerical integration method, particularly the Numerov type integration method with logarithm and $1/r^3$ grid could be used for solving of model potential of dense hydrogen plasma, Havlová et al. 1984. In analyzed cases there is an exact mathematical form of the wave function. The analysis of the stability of the solution with the initial values on the Coulomb potential led us to conclusion that the model is also usable for cut-off Coulomb model potential. The method possesses fast convergence toward to a solution, and because of that is very applicable when using it in more complex analysis, as well as for coupling with molecular dynamics codes. Even more, it gave an opportunity to solve more complex

n	l	E_{calc}/E_H	dE/E
1	0	0.9998168	-0.0001832
2	0	0.9999084	-0.0000916
	1	1.0000000	0.0000000
3	0	0.9999387	-0.0000613
	1	1.0000000	0.0000000
	2	1.0000000	0.0000000
4	0	0.9999442	-0.0000458
	1	1.0000000	0.0000000
	2	1.0000000	0.0000000
	3	1.0000000	0.0000000
5	0	0.9999632	-0.0000368
	1	1.0000000	0.0000000
	2	1.0000000	0.0000000
	3	1.0000000	0.0000000
	4	1.0000000	0.0000000

Table 1: Calculated energy for the unmodified initial values.

model potential in order to describe different atoms in dense plasma. The further analysis is needed for development of a method for determination and avoid of numerical errors in solution, as well as to optimize a procedure for best mesh densities selection.

References

Adamyan, V. M., Djurić, Z., Ermolaev, A. M., Mihajlov, A. A., Tkachenko, I. M.: 1994, *J.Phys.D*, **27**, 111.

Adamyan V. M., Djurić Z., Mihajlov, A. A., Sakan, N. M., Tkachenko, I. M.: 2004, *J.Phys.D.*, **37**, 1896.

Fortov V. E., Iakubov I. T.: 1989, *Physics of Nonideal Plasma*, Hemisphere, New York

Havlová, H., Smrčka, L.: 1984, *Czech J Phys* **34**, 961.

Kobzev G., Jakubov I., Popovich M. (Eds.): 1995., *Transport and Optical Properties of Non-Ideal Plasmas*, Plenum Press, New York, London.

Mihajlov, A. A., Sakan N. M., Srećković V. A., Vitel Y.: 2011, *Baltic Astron.* **20**, 604.

Noumerov, B. V.: 1924, *MNRAS* **84**, 8., 592.

Paolo Giannozzi: 2012/2013, lecture notes: *Numerical Methods in Quantum Mechanics*, Corso di Laurea Magistrale in Fisica Interateneo Trieste.

Sakan, N. M.: 2010, *Journal of Physics: Conference Series*, **257**, 012036.

Sakan, N.M., Srećković, V.A., Simić, Z.J., Dimitrijević, M.S.: 2018, *Atoms* **6**, 4.

Srećković, V. A., Ignjatović, L. M., Mihajlov, A. A., Dimitrijević, M. S.: 2010, *MNRAS*, **406** 590.

Publ. Astron. Obs. Belgrade No. 99 (2020), 315 - 318 *Contributed Paper*

INFLUENCE OF LIGHT-CURVE SAMPLING ON THE PERIODICITY DETERMINATION IN CASE OF SUBPARSEC SUPER-MASSIVE BLACK HOLE BINARIES

SAŠA SIMIĆ[1], LUKA Č. POPOVIĆ[2], ANDJELKA KOVAČEVIĆ[3] and DRAGANA ILIĆ[3]

[1] *Faculty of Sciences, Department of Physics, Radoja Domanovića 12, 34000 Kragujevac, Serbia*
E–mail ssimic@kg.ac.rs

[2] *Astronomical Observatory, Volgina 7, 11000 Belgrade, Serbia*
E–mail lpopovic@aob.rs

[3] *Department of Astronomy, Faculty of Mathematics, University of Belgrade, Studentski trg 16, 11000 Belgrade, Serbia*

Abstract. Here we explore the periodicity determination in the light curves of super-massive binary black holes (SMBBHs) considering different observation sampling during a monitoring period. We use a theoretical model of an SMBBH system which assumes that the variability in the light curves is due to dynamical effects. We simulate several observational light curves assuming different cadences, and estimate the periodicity using the Lomb-Scargle (LS) algorithm. We found that the lack of observational data could reduce the significance level of periodicity determination, but still a rough periodicity could be estimated.

1. INTRODUCTION

In the case of merging galaxies, one can expect that subparsec super-massive binary black holes (SMBBHs) are present in their central parts (Begelman et al. 1980). Many galaxies are observed to be in a collision, and they potentially have a SMBBH in their center. One can expect that even the sub-parsec SMBBHs may be very often in the centers of merging galaxies, however, the problem is to detect these objects. E.g. direct imaging in the high resolution radio observations could be potentially a good method for SMBBH detection (see e.g. Burke-Spolaor 2011, Roland et al. 2013), but only on the kpc scale distances between the components (see Fu et al. 2011).

On the other hand, it seems that sub-parsec scale SMBBHs may be possibly detected using the spectral characteristics, in which one can expect to see dynamical signature of binary orbital motion (see e.g. Gaskell 1983, Tsalmantza et al. 2011, Shen & Loeb 2010, Eracleous 2012, Popović 2012, Bon et al. 2012, Simić & Popović 2016, Li et al. 2019, Kovačević et al. 2019, Popović et al. 2020), especially in the case in which both black holes (BHs) in a binary system have accretion discs and emit broad lines (see for a review, Popović 2012).

Here we continue our investigation of the detection of possible periodicity in the SMBBHs light curves. We explore the perspective of monitoring of active galactic nuclei (AGN) in large surveys and possibility to find good candidates for SMBBHs. Particularly in this work we consider influence of different observation sampling to determination of the periodicity, that is expected to be present in the SMBBHs light curves.

2. THE MODEL OF THE SMBBH SYSTEM

We consider the system in which both components have accretion discs, and each disc is surrounded with its broad line region (BLR), and a common BLR, as shown in Figure 1. We describe briefly the main concepts of the theoretical model, but more details will be given in Simić et al. (2020). We accept the model of a standard optically

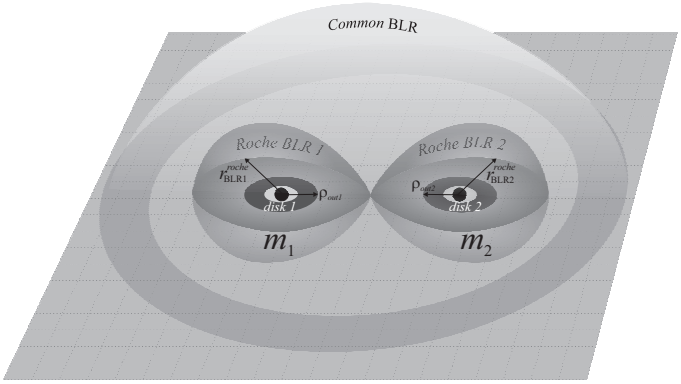

Figure 1: SMBBH system in the compact configuration, with designated BLR of particular components (BLR1 and BLR2) inside each Roche lobe, with an additional common BLR, located outside of Roche lobes.

thick, geometrically thin, black body accretion disc (see Pringle & Rees 1972, Shakura & Sunyaev 1973, Novikov & Thorne 1973), and we take that the effective temperature as a function of the radius from the center is as given in Woo et al. (2014). The BLR can have different geometries (see e.g. Sulentic et al. 2000), but we assume that it is homogeneously distributed around the BH disc. The BLR inner radius is very close to disc outer radius and spans a few tens of light days in diameter, while keeping probably spherical shape around the BH and disc. This region is photoionized by the X-ray and UV radiation from the accretion disc. We estimate the BLR size by using the empirical formulas given in Kaspi et al. (2005), i.e. using the continuum luminosity at 5100Å (for Hβ line emitting region).

Taking the dynamical effects of an SMBBH system we assume that the total line emitting region is actually composed from three different BLRs. First two regions are defined by the local Roche lobes of each component in the SMBBH system (BLR1 and BLR2), and third is a circumbinary region that is surrounding both components (common BLR), as shown in Fig. 1. As we can see, BLRs defined by Roche lobes are moving and following the host BH component, whereas the common BLR is static. We also connect the line intensities and width of each BLR component with the total

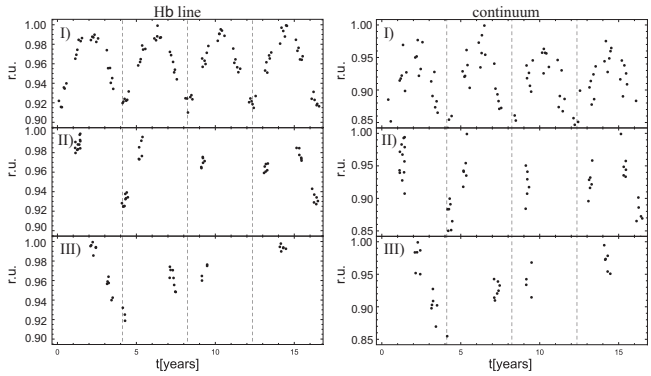

Figure 2: Light curves for emission in Hβ (left panel) and continuum (right panel) of SMBBH system during four full rotation. Presented luminosity scaled to its maximal values.

component masses.

We model the total emitted spectra in a wide wavelength range, from the UV to the IR band, but here we only consider the variability of the region around the Hβ line. First, we model the spectra in the Hβ wavelength band, then we measure the Hβ and continuum at λ5100Å luminosity. We take four full orbits, and consequently find the light curves of the total Hβ emission and continuum at λ5100Å.

3. RESULTS AND DISCUSSION

We distinguish three different cases: *I*) when observations are made in the first half of the year, randomly once per month for entire time period of $4 \times P_{orb}$, *II*) when observations are made in the first half of the randomly chosen year with the number of observing years reduced by half in comparison to case *I*), and *III*) with significantly reduced number of observations and random cadence in total observed time.

During the orbital motion of SMBBH system, we expect to observe dynamical variation of the luminosity in line and continuum. However, this variability could be masked by many different reasons, like enormous line width, high mass ratio system, or some other issues. In case of very compact sub-parsec SMBBHs, imprinted dynamical variability is the only way to detect such systems. In order to test how quantity and quality of observations influence the periodicity determination, we examine spectral features (Hβ line and continuum at $\lambda = 5100$Å) in details. First, we compute luminosity in a given spectral range for continuum and line segment during four full rotation of the binary system, see Fig. 2. We can see variation of luminosity in the line (left panel) and continuum (right panel), with luminosities scaled to their maximal value. Continuum variability (Fig. 2, right panel) has similar variation as in line, since in this case the Hβ line is broad enough and affect continuum measurement at $\lambda = 5100$Å.

We apply Lomb-Scargle (LS) to compute orbital periods of SMBBHs. We generated periodograms (Fig. 3) for each observational case for Hβ line and continuum. As we can see, peaks of the periodogram curves are placed at the extracted orbital period of the SMBBH system.

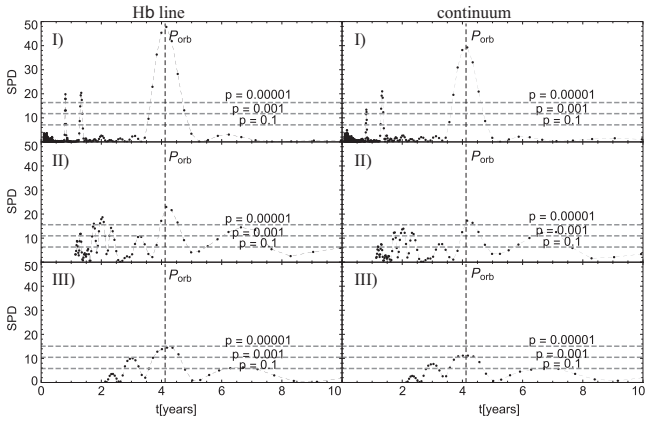

Figure 3: Periodograms for Hβ line and continuum flux in case of SMBBH system. Horizontal dashed lines present significance level lines.

We found that the lack of observational data, i.e. poor sampling of light curves, could reduce significantly the certainty of periodicity determination, however, a rough estimate of periodicity is still possible. More details on the model and perspectives of the periodicity estimates and detection of possible SMBBH systems in AGN light curves will be given elsewhere.

References

Begelman, M. C., Blandford, R. D., Rees, M. J.: 1980, *Nature*, **287**, 307
Bon, E., Jovanović, P., Marziani, P.: 2012, *ApJ*, **759**, 118
Burke-Spolaor, S.: 2011, *MNRAS*, **410**, 2113
Eracleous, M., Boroson, T. A., Halpern, J. P., Liu, J.: 2012, *ApJSS*, **201**, 23
Fu, H., Zhang, Z-Y., Assef, R. J., Stockton, A. et al.: 2011, *ApJ*, **740L**, 44
Gaskell, C. M.: 1983, *Liege International Astrophys. Colloq.*, **24**, 473
Kaspi, S.,Maoz, D., Netzer, H.: 2005, *ApJ*, **629**, 61
Kovačević, A. B., Popović, L. Č., Simić, S. Ilić, D., 2019, *ApJ*, **871**, 32
Li, Y.-R., Wang, J.-M., Zhang, Z.-X. et al. 2019, *ApJS*, **241**, 33
Novikov, I.D., Thorne, K.S.: 1973, *in Black Holes, ed. C. DeWitt and B. DeWitt (New York: Gordon & Breach)*
Popović, L. Č.: 2012, *NewAR*, **56**, 74
Popović, L.Č., Simić, S., Kovačević, A., Ilić, D. 2020, in preparation
Pringle, J. E., Rees, M. J.: 1972, *A&A*, **21**, 1
Roland, J., Britzen, S., Caproni, A.: 2013, *A&A*, **557A**, 85
Shen, Y., Loeb, A.: 2010, *ApJ*, **725**, 249
Shakura, N.I., Sunyaev, R. A.: 1973, *A&A*, **24**, 337
Simić, S., Popović, L. Č. 2016, *Ap&SS*, **361**, 59
Simić, S., et al. 2020, in prep.
Sulentic, J. W., Marziani, P. Dultzin-Hacyan, D.: 2000, *Astronomical Review*, **38**, 521
Tsalmantza, P., Decarli, R., Dotti, M., Hogg, D. W.: 2011, *ApJ*, **738**, 20
Woo, J. H., Cho, H., Husemann, B., Komossa, S., Park, D. Bennert, V. N.: 2014, *MNRAS*, **437**, 32

Publ. Astron. Obs. Belgrade No. 99 (2020), 319 - 320 *Contributed Paper*

COLLAPSE OF POLARIZED ATOMIC STATES IN MAGNETIC FIELDS

E. A. VIKTOROV[1], M. S. DIMITRIJEVIĆ[2,3,4], V. A. SREĆKOVIĆ[4,5], N. N. BEZUGLOV[1,6], K. MICULIS[6], A. A. PASTOR[1] and P. Yu. SERDOBINTSEV[1]

[1]*Saint Petersburg State University, St. Petersburg 199034, Russia*
E-mail bezuglov50@mail.ru

[2]*Astronomical Observatory, Volgina 7, 11060 Belgrade 38, Serbia*
E-mail mdimitrijevic@aob.rs

[3]*Sorbonne Université, Observatoire de Paris, Université SL, CNRS, LERMA, F-92190 Meudon, France*

[4]*Isaac Newton Institute of Chile, Yugoslavia Branch, Volgina 7, 11060 Belgrade, Serbia*

[5]*Institute of physics Belgrade , University of Belgrade, P.O. Box 57, 11001, Belgrade, Serbia*
E-mail vlada@ipb.ac.rs.rs

[6]*University of Latvia, Institute of Atomic Physics and Spectroscopy, Riga, Latvia*

Abstract. On the basis of graphical techniques, we have derived analytical expressions for the photoelectron current upon photoionization of polarized atomic states by polarized light in magnetic fields. We show as an example the observed signal when two-photon excited xenon state with J=2, M=2 (jl-coupling) is photoionized by right-circular polarized photons in an applied magnetic field which results in the Paschen–Back effect. The presented results are of interest in spectroscopy of low temperature laboratory plasma as well as for astrophysical research.

1. RESULTS AND DISCUSSION

In this contribution we present a progress of our cooperative work in newly open areas of our investigation. On the basis of graphical techniques described in the book by E. El-Baz and B. Castel (Graphical Methods of Spin Algebras, New York, 1972) we have derived analytical expressions for the photoelectron current I(t) upon photoionization of polarized atomic states by polarized light in magnetic fields. Figure 1 exhibits as an example the observed signal when two-photon

excited xenon state with J=2, M=2 (jl-coupling) is photoionized by right-circular polarized photons in an applied magnetic field which results in the Paschen–Back effect.

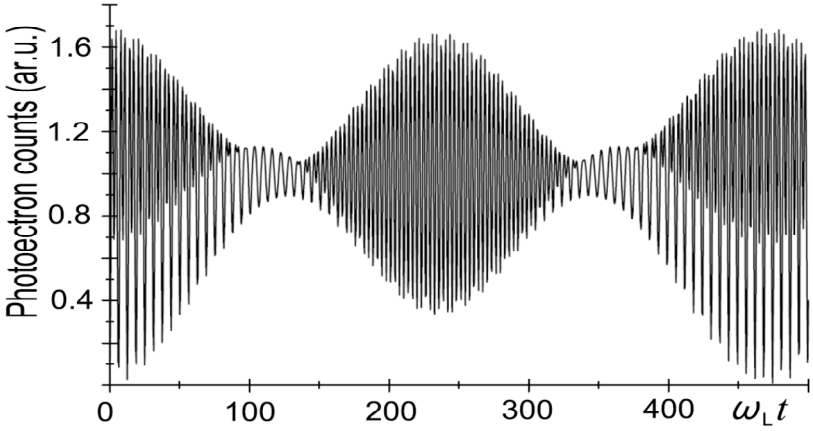

Figure 1: Graphical presentation of the photoionization current *I* for the polarized Xe state $P_{3/2}\, 6p^2[3/2]_3$.

.

2. CONCLUSION

We show that the results of presented investigation are very important not only in physics such as astrophysics, plasma physics but also in spectroscopy of laboratory plasma (see e.g. Condon& Shortley 1959, Foot 2005, Dimitrijević et al. 2019).

Acknowledgements

This work was supported by the Astronomical Observatory Belgrade and Institute of Physics Belgrade, through the grant by the Ministry of Education and Science of the Republic of Serbia and by the Russian Science Foundation under the grant NO 18-12-00313

References

Condon, E. U., Shortley, G. H.: 1959, *The theory of atomic spectra,* Cambridge University Press, Cambridge.

Dimitrijević, M. S., Srećković, V. A., Zalam, A. A., Bezuglov, N. N. and Klyucharev, A. N.: 2019, *Atoms*, **7(1)**, 22.

El-Baz, E. and Castel, B.: 1972, *Graphical methods of spin algebras in atomic, nuclear, and particle physics* New York.

Foot, C. J.: 2005, *Atomic Physics,* Oxford masters series.

Special Session
“Atomic Collisions in Plasmas”
Devoted to Ratko Janev

Publ. Astron. Obs. Belgrade No. 99 (2020), 323

ELECTRON-MOLECULE COLLISIONS IN FUSION PLASMAS: a long-standing collaboration with Professor Ratko Janev

R. Celiberto[1] and A. Laricchiuta[2]

[1]*Dipartimento di Ingegneria Civile, Ambientale, del Territorio, Edile e di Chimica (DICATECh) – Politecnico di Bari, Bari, Italy*
E-mail roberto.celiberto@poliba.it
[2]*Istituto per la Scienza e Tecnologia dei Plasmi (ISTP) - Consiglio Nazionale delle Ricerche, Bari, Italy*
E-mail annarita.laricchiuta@cnr.it

Abstract. It is well known that the temperature reached in thermonuclear fusion reactors (tokamak) is extremely high, and that the hydrogen gas, completely ionized, can be confined by a properly shaped magnetic fields. If this is true in the core of the tokamak, however in the peripheral regions the temperature can get strongly reduced, so that atomic and molecular species can condensate. This is the case of the divertor chamber, where the plasma cools down by delivering the excess of thermal energy, along with fusion ash and impurities. Also close to the container walls, where the hydrogen particles, getting outside the closed field lines, give rise to chemical reactions yielding to molecular compounds. In these regions, electron-molecule collisions play a role of utmost importance, by inducing a plethora of interconnected molecular processes (ionization, dissociation, excitations…), which strongly affect the plasma evolution. Modeling and simulations of these *low-temperature* plasmas, as well as experimental determinations, require large sets of electron-molecule scattering data. Cross sections, rate constants, Einstein's coefficients etc. are the basic input quantities in plasma modeling and they can be obtained by resorting to theoretical calculations. In this seminar, we will present the production of plasma information achieved in decades of collaboration of our group with Professor Janev, starting from the first work aimed to collect vibrationally-resolved cross section data for excitations induced by electron impact in H_2 and H_2^+ molecules and their isotopes (Celiberto et al, 2001), going through the study of resonant processes (Celiberto et al, 2008), till the recent IAEA project on "*Atomic Data for Vapour Shielding in Fusion Devices*" (Heinola, 2019).

References

Celiberto, R., Janev, R.K., Laricchiuta A., Capitelli M,, Wadehra J.M., and Atems D.E. : 2001, *Atomic Data and Nuclear Data Tables*, **77,** 161.
Celiberto, R., Janev, R.K., Wadehra, J. M. and Laricchiuta, A. : 2008, Phys. Rev. A **77**, 012714.
Heinola, K. : 2019, IAEA report INDC(NDS)-0781**,** Vienna, Austria.
Celiberto, R., Janev, R.K., Laricchiuta A.: 2020 *Plasma Sources Sci. Technol.*, **29**, 035008.

Publ. Astron. Obs. Belgrade No. 99 (2020), 324

DYNAMICAL ADIABATIC THEORY OF ATOMIC COLLISIONS

TASKO P. GROZDANOV[1] and EVGENI A. SOLOV'EV[2]

[1]*Institute of Physics, University of Belgrade, 11001 Belgrade, Serbia*
E-mail tasko@ipb.ac.rs

[2]*BLTP, Joint Institute for Nuclear Research, 141980 Dubna, Russia*
E-mail esolovev@theor.jinr.ru

Abstract. The concept of dynamical adiabatic states has originally been proposed to describe low-energy one-electron atom(ion)-ion collision systems (see chapter 7 in Solov'ev 2017 and references therein). In the impact parameter approach the essential steps of the method are: the scaling of electronic coordinates by the internuclear distance R and transformation to rotating molecular frame. The advantages of a dynamical adiabatic basis are threefold. First, it is compatible with the physical boundary conditions, whereas in standard adiabatic two-Coulomb center basis we have nonvanishing inelastic transitions when internuclear distance $R\rightarrow\infty$. Second, rotational transitions are transformed into radial transitions via a type of hidden crossings in contrast with the standard adiabatic basis, where these transitions could only be included by numerical close-coupling calculations. And third, the ionization process can be described using a basis of the complete discrete orthogonal wave packets, which is much more satisfactory for the process compared with the standard adiabatic approach where the continuum states which have no direct physical meaning are employed. The properties of the dynamical adiabatic potential energy curves have been studied for a complete range of internuclear separations R as well as their hidden crossings in the complex R-plane (Grozdanov et al. 2013, 2014).

Results of calculation for the $(HeH)^{2+}$ quasimolecular system have been used to study the low-energy charge-exchange processes: $He^{2+}+H(1s) \rightarrow He^{+}+H^{+}$ and $H^{+}+He^{+}\rightarrow H+He^{2+}$ (Grozdanov et al. 2015, 2018). The obtained results for transition probabilities and cross sections are in good agreement with hyperspherical and standard close-coupling calculations as well as with experiments. We shall discuss also an earlier application of dynamical adiabatic theory to a model problem of electron detachment process: $A+A^{-}\rightarrow A+A+e$, where the electron-atom interactions are described by the zero-range potentials (Grozdanov et al. 1999).

References

Grozdanov, T. P., Solov'ev, E. A.: 1999, *Eur. Phys. J. D*, **6**, 13.
Grozdanov, T. P., Solov'ev, E. A.: 2013, *Phys. Rev. A*, **88**, 022707.
Grozdanov, T. P., Solov'ev, E. A.: 2014, *Phys. Rev. A*, **90**, 032706.
Grozdanov, T. P, Solov'ev, E. A.: 2015, *Phys. Rev. A*, **92**, 042701.
Grozdanov, T. P, Solov'ev, E. A.: 2018, *Eur. Phys. J. D,* **72**, 64.
Solov'ev E.A.: 2017, *The foundations of quantum physics: new interpretation and systematic application*, Lambert Academic Publishing, Saarbrucken.

Publ. Astron. Obs. Belgrade No. 99 (2020), 325

VIBRATIONALLY RESOLVED COLLISIONS OF HYDROGEN IONS AND MOLECULES

PREDRAG KRSTIĆ[1] and RATKO JANEV[2]

[1]*Institute for Advanced Computational Science, Stony Brook University, Stony Brook, New York 11794-05250, USA*
Predrag.Krstic@Stonybrook.edu

[2]*Macedonian Academy of Sciences and Arts, 1000 Skopje, Macedonia*

Abstract. Because of its fundamental role in hydrogen plasmas such as those in certain astrophysical (Walker et al, 2018) or fusion reactor environments (Janev at al, 2003), and as a prototype for the study of similar processes in other plasmas, slow collisions (0.1-100 eV) of hydrogen atoms and ions with vibrationally excited hydrogen molecules and molecular ions are studied using fully quantum-mechanical (below 10 eV) and semiclassical (E > 15 eV) approaches, the latter within impact parameter, straight-line approximation. Considered transitions include charge transfer, excitation (Krstić 2002), dissociation (Krstić et al, 2003), three body diatomic association (often referred by the general term three-body recombination) (Krstić et al, 2003), as well as energy and angular spectra of dissociation fragments. Mutual relations of various elastic and inelastic processes, the relevant physical mechanisms governing vibrational dynamics in inelastic channels and comparison of the fully quantal and semi-classical results are also reported. The cross section calculations are performed by solving the Schrödinger equation for the nuclear and electronic motions on the two lowest diabatic electronic surfaces of H_3^+, and by using an expansion of nuclear wave function in a vibrational basis containing all discrete H_2 and H_2^+ states and a large number of pseudo-states from each of the corresponding discretized continua. The rotational dynamics of H_2 and H_2^+ is treated with the infinite order sudden approximation prescription.

References

Janev, R. K, Reiter, D., Samm, U.: 2003, *Collision Processes in Low-Temperature Hydrogen Plasma*, Berichte des Forschungszentrums Jülich, **4105**.
Krstić, P. S.: 2002. *Physical Review A*, **66**, 042717.
Krstić, P. S. , Janev, R. K: 2003, *Physical Review A,* **67**, 022708.
Krstić, P. S., Janev, R. K., Shultz, D. R.: 2003, *J. Phys. B*, **36**, L249.
Walker, K. M., Porter, R. L., Stancil, P. C.: 2018, *The Astrophysical Journal*, **867**, 1.

Publ. Astron. Obs. Belgrade No. 99 (2020), 326

ADIABATIC REPRESENTATION OF ATOMIC COLLISION PROCESSES

RONALD McCARROLL

Sorbonne Université, CNRS (UMR 7614), Laboratoire de Chimie-Physique : Matière et Rayonnement,75231 Paris, France
E-mail ronald.mac_carroll@upmc.fr

Abstract. The use of an adiabatic representation to describe collision between atomic systems dates from the early days of quantum mechanics, when Landau recognized the importance of avoided crossings of the adiabatic potential energies, leading to excitation and charge exchange in collision between ions and neutral atoms and molecules. The early models, such as those developed by Landau and Zener were successful for certain specific processes but the development of a consistent theoretical model going beyond the Born-Oppenheimer approximation proved difficult. The first fully quantum mechanical formulation, proposed by Bates et al. in 1947 (Bates and Massey 1947) raised many inconsistencies. A decade later, an impact parameter method was developed, but this involved the introduction of a time variable, which cannot be uniquely was different, the notion of translation factors was introduced. Such factors have proved useful cannot be well defined. It was only in the late 1970's that a fully quantum mechanical description of the adiabatic representation by Thorson et al was made possible by the introduction of appropriate reaction coordinates. This solved many problems but not all. Indeed, the outstanding question was to ensure that an adiabatic basis including only those involved in an avoided crossing was sufficient to describe all the reaction channels. This was only achieved at the turn of the century. It had taken 70 years to finally develop a method which enables the use of an adiabatic basis to represent the collision. A review of methods using an adiabatic representation been given recently (Rabli and McCarroll 2018).

References

Bates, D. R. and Massey, H. S. W.: 1947, *Proc. Roy. Soc. A*, **192**.
Rabli, D. and McCarroll, R.: 2018, *J. Phys. B: At. Mol. Opt. Phys.*, **51**, 032002.

Publ. Astron. Obs. Belgrade No. 99 (2020), 327

TWO-STATE VECTOR MODEL FOR THE ION-SURFACE INTERACTION: FOUNDATION AND APPLICATION

N.N. NEDELJKOVIĆ[1] and M.D. MAJKIĆ[2]

[1] *University of Belgrade, Faculty of Physics, P.O. Box 368, 11001 Belgrade, Serbia*
E–mail hekata@ff.bg.ac.rs

[2] *University of Pristina, Faculty of Technical Sciences,*
Kneza Milosa 7, 38220 Kosovska Mitrovica, Serbia
E–mail milena.majkic@pr.ac.rs

Abstract. Studies of the intermediate stages of the Rydberg state population of multiply charged ions impinging upon a solid surface are not only of fundamental scientific interest, but also highly relevant in the analysis of the various surface modifications such as the recently obtained surface nanostructures (craters, hillocks and some other structures such as calderas, nanopores etc.): see Aumayr et al 2011, and Lake et al 2011. The appropriate theoretical model which takes into account both the initial and final electron states has to be founded within the framework of the time-symmetrized quantum mechanics. The corresponding two-state vector model has been firstly formulated for the analysis of the proton neutralisation at solid surface: see Nedeljković et al 1991, and further elaborated to the case of highly charged ions: see Nedeljković et al 1994 and a series of articles by the same group of authors.

In our recent theoretical study we apply the model to obtain the final ionic charge in front of the metal surface and to calculate the corresponding neutralization energy: see Majkić et al 2019. We discuss the interplay of the collision geometry and the surface parameters in the neutralization process for the metal surface covered with a thin dielectric film. The ionic velocity plays a decisive role for the particular surface modification. For very low ionic velocity, the neutralization energy gives the main contribution in the surface nanostructuring, while for large ionic velocity the nanofeatures are created due to the kinetic energy loss (nuclear and electronic stopping power). The existence of the critical velocity, which separates these two regions, is discussed. At the conference we consider the role of the critical velocity in the appearance of the particular nanostructures at various types of surfaces.

References

Aumayr, F., Facsko, S., El-Said, A. S., Trautmann, C., Schleberger, M. : 2011, *J. Phys.: Condens. Matter*, **39**, 393001.

Lake, R., Pomeroy, M., Grube, H., Sosolik, C. E. : 2011, *Phys. Rev. Lett.* **107**, 063202.

Majkić, M. D., Nedeljković, N. N., Mirković, M. A. : 2019, *Vacuum*, **165**, 62.

Nedeljković, N. N., Nedeljković, Lj. D., Janev, R. K., Mišković, Z. L. : 1991, *Nucl. Instr.* **58**, 806.

Nedeljković, N. N., Nedeljković, Lj. D., Vojvodić, S. B., Mirković, M. A. : 1994, *Phys. Rev. B.* **49**, 5621.

Publ. Astron. Obs. Belgrade No. 99 (2020), 328

ATOMIC STRUCTURE AND DYNAMIC PROCESS IN IDEAL AND NON-IDEAL PLASMA WITH PROF. RATKO JANEV

YUE YING QI[1], SONG BIN ZHANG[2], LING LIU[3], YONG WU[3] and JIAN GUO WANG[3]

E-mail yying_qi@zjxu.edu.cn

[1] *School of Mathematics & Physics and Information Engineering, Jiaxing University, Jiaxing 314001, China*

[2] *School of Physics and Information Technology, Shaanxi Normal University, Xi'an 710119, China*

[3] *Institute of Applied Physics and Computational Mathematics, Beijing 100088, China*

Abstract. Atomic levels and electronic wave-functions including bound and continuum states are affected by plasmas shielding influence. And thus the physical quantum relevant to the atomic levels and electronic wave-functions demonstrated the remarkable changes. Since the year of 2008, Prof. Janev has suggested and mentored our group in China to perform comprehensive investigations of plasma shielding effects on atomic physics. Prof. Janev congratulated on the publication of my work about bound-bound process in ideal plasmas in PRA 2008, I still remembered his smile. Lots of important and coauthored works have been published in the past decade to reveal the importance of plasma screening effects on atomic electronic structure, photon excitation and ionization, electron/positron impact excitation and ionization, and excitation, ionization and charge transfer of ion-atom/ion collisions. In this talk, we will review the shift of the atomic energy levels and the changes of the physical quantum and spectrum parameters in ideal and non-ideal plasma environments collaborated with Prof. Janev.

References

Qi, Y. Y., Wang, J. G., Janev, R. K.: 2008, *Phys. Rev. A*, **78**, 062511.
Qi, Y. Y., Wang, J. G., Janev, R. K.: 2009, *Phys. Rev. A*, **80**, 032502.
Qi, Y. Y., Wang, J. G., Janev, R. K.: 2009, *Phys. Rev. A*, **80**, 063404.
Qi, Y. Y., Wang, J. G., Janev, R. K.: 2016, *Phys. Plas.*, **23**, 073302.

Publ. Astron. Obs. Belgrade No. 99 (2020), 329

ATOMIC AND MOLECULAR PROCESSES IN NUCLEAR FUSION PLASMA SCIENCE

DETLEV REITER

Institute for Laser and Plasma Physics,
Heinrich-Heine-University, D-40225 Düsseldorf, Germany
E–mail reiterd@uni-duesseldorf.de

Abstract. Fusion plasma science combines plasma physical challenges from the highly un-isotropic and turbulent plasma in electromagnetic fields, with a rich plasma chemistry due to the presence of nearby material surfaces and plasma surface interactions at the reactor vessel. It was recognized as early as 1968 by Bo Lehnert that a zone of powerful gas–plasma interaction, formed near fusion reactor vessel components, can be the key to solving the plasma surface interaction issues for sustainable nuclear fusion reactor operation.

Hydrogen - in the form of deuterium and tritium - is the fuel of fusion energy plasma devices. One might have hoped that the first element in the periodic table might behave in a simple way in this context. But in fact, see Janev 1984, a great variety of complexities arises. Ratko Janev certainly was the most influential and respected bridgehead, world wide, between the fusion plasma and atomic physics communities, for nearly four decades. Today the chemically rich "divertor detachment" plasma regime in tokamaks, anticipated in Janev 1984, is regarded as the feasible technical solution for a nuclear fusion power plant, e.g. also underlying the current construction of the ITER fusion reactor in Cadarache, France, in a joint world wide effort. Historically fusion research had not developed very far before it was recognized that it is essential to quantify and fully understand these processes. In the mid eighties, a quantum step occurred in this field: the first comprehensive atomic and molecular database for complex fusion analysis codes appeared, including all the important physics and chemistry involved, see Figure 1, Janev, 1987. We will present this development, the prominent role of Ratko Janev in it, and current knowledge on collision processes involving fuel (H), ash (He), wall material (e.g., C, Be, W) and seeding particles (e.g., N_2).

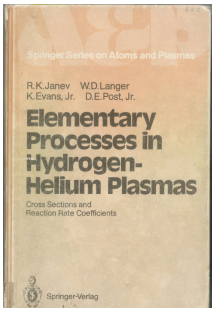

Figure 1: Three decades the unchallenged standard reference for atomic and molecular physics in fusion plasmas: Janev, R.K., et al, 1987, Springer Verlag.

References

Lehnert, B. : 1968 *J. Nuclear Fusion* **8**, 173.
Janev, R.K., Post, D.E., Langer, W.D., et al. : 1984, *J. of Nuclear Materials*, **121**, 10

Publ. Astron. Obs. Belgrade No. 99 (2020), 330

QUANTUM COLLISION DYNAMICS INVOLVING PLASMA SHIELDING EFFECTS WITH PROF. RATKO JANEV

SONG BIN ZHANG[1], YUE YING QI[2], LING LIU[3], YONG WU[3] and JIAN GUO WANG[3]

[1]*School of Physics and Information Technology, Shaanxi Normal University, Xi'an 710119, China*
E-mail song-bin.zhang@snnu.edu.cn

[2]*School of Mathematics & Physics and Information Engineering, Jiaxing University, Jiaxing 314001, China*

[3]*Institute of Applied Physics and Computational Mathematics, Beijing 100088, China*

Abstract. Hot, dense plasmas exhibit screened Coulomb interactions, resulting from the collective effects of correlated many-particle interactions. Since 2008, Prof. Janev has suggested and mentored our group in China to perform comprehensive investigations of plasma shielding effects on atomic physics. Lots of important and coauthored works have been published in the past decade to reveal the importance of plasma screening effects on atomic electronic structure, photon excitation and ionization, electron/positron impact excitation and ionization, and excitation, ionization and charge transfer of ion-atom/ion collisions. In the talk, we will review the typical progresses and physical results we have achieved on quantum collision dynamics involving plasma shielding effects collaborated with Prof. Janev.

References

Janev, R. K., Zhang, S. B., Wang, J. G. : 2016, *Matter Radiat. at Extremes*, **1**, 237.
Liu, L., Wang, J. G., Janev, R. K. : 2008, *Phys. Rev. A*, **78**, 062511.
Wu, J. Y., Wu, Y., Qi, Y. Y., Wang, J. G., Janev, R. K., Zhang, S. B. : 2019, *Phys. Rev. A*, **99**, 012705.
Zhang, S. B., Wang, J. G., Janev, R. K. : 2010, *Phys. Rev. Lett.*, **104**, 023203.

AUTHORS' INDEX

SPIG2020 - Program by day

Monday, Aug 24th (Day 1)

- Organized bus transfer* for SPIG2020 - time (TBA)
- 17:30 Opening ceremony
- 18:00 Session dedicated to 30th jubilee of SPIG conferences
- 20:00 Welcome cocktail* with the concert of traditional music and dance

Tuesday, Aug 25th (Day 2)

- 9:00-19:30 SPIG 2020

Wednesday, Aug 26th (Day 3)

- 9:00-18:00 SPIG 2020
- 18:00 Organized bus transfer to Belgrade*

Thursday, Aug 27th (Day 4) – ONLY VIRTUAL (through Webex Event)

- 9:00-20:00 SPIG 2020

Friday, Aug 28th (Day 5) – ONLY VIRTUAL (through Webex Event)

- 9:00-14:00 SPIG 2020

*IMPORTANT NOTE:

In the case of unfavorable epidemic situation in Serbia, SPIG2020 will be shifted to fully virtual conference. This will be announced in the Final Announcement on August 1, 2020.

SPIG 2020 PROGRAMME

Šabac, Serbia, August 24 – 28, 2020

Monday 24th August 2020 **SPIG 2020 (day 1)**	**REGULAR**	
PL *– Plenary lecture: 35+10 min*	***TL*** *– Topical lecture: 25+5 min*	***PR*** *– Progress Report: 15+5 min*
16:00-17:30	***Arrival and registration***	
17:30-18:15	***Opening ceremony***	
	Plenary Session 1, Hall A, *Chair: L. Č. Popović*	
18:15-19:00	**Zoran Petrović** (Serbia): Review talk on History and Importance of SPIG (dedicated to the 30th jubilee)	
20:00-22:00	*Welcome Cocktail*	

Tuesday 25th August 2020 **SPIG 2020 (day 2)**	**REGULAR+VIRTUAL**	
	Plenary Session 2, Hall A, *Chair: Z. Petrović*	
09:00-09:45	**Jean-Paul Booth** (France): A new look at oxygen plasmas - quantitative spectroscopy for rigorous testing of models *(Virtual)*	
09:45-10:30	**Tőkési Károly** (Hungary): Multiple electron scattering in atomic and surfaces collisions *(Virtual)*	
10:30-11:00	*Coffee break*	
	Plenary Session 3, Hall A, *Chair: A. Milosavljevic*	
11:00-11:45	**Oskar Asvany** (Germany): High-resolution spectroscopy of cation-helium complexes at low temperature (*Virtual*)	
11:45-12:30	**Tony Donne** (Germany): Challenges and Progress on the path towards Fusion Electricity *(Virtual)*	
12:30-14:30	*Lunch break*	
	Hall A - Parallel Session: Collisions (devoted to R. Janev) *Chair: N. Simonović*	***Hall B - Parallel Session*** *Chair: B. Obradović*
14:30-15:00	**Tasko P. Grozdanov** (Serbia): Dynamical adiabatic theory of atomic collisions	**Mario Janda** (Slovakia): The transient spark discharge driving circuit optimizations for enhanced NOx generation
15:00-15:30	**Nataša N. Nedeljković** (Serbia)*:* Two-state vector model for the ion-surface interaction: foundation and application	**Eric Griglio** (France): Ion transport through insulating capillaries: Self-organized focusing revealed

15:30-16:00	**Ronald McCarroll** (France): Adiabatic Representation of Atomic Collision Processes *(Virtual)*	**Suvasthika Indrajith** (France): Effects of ionizing radiations on the reactivity inside clusters of linear hydrocarbons: polymerization vs. cyclization **[15:30-15:50]**
16:00-16:30	**Roberto Celiberto** (Italy): Electron-molecule collisions in fusion plasmas: a long-standing collaboration with Professor Ratko Janev *(Virtual)*	**Dragan M. Pavlović** (Serbia): Plasma channel evolution in the triggered lightning discharges **[15:50-16:10]**
		Aliaksandra Kazak (Belarus): The atmospheric pressure air plasma jets for innovative medical applications **[16:10-16:30]**
16:30-17:00	*Coffee break*	
	Hall A - Parallel Session Collisions (devoted to R. Janev) *Chair: T. Grozdanov*	***Hall A - Parallel Session*** 4. GENERAL PLASMAS *Chair: I. Savić*
17:00-17:30	**Song Bin Zhang** (China): Quantum collision dynamics involving plasma shielding effects with Prof. Ratko Janev *(Virtual)*	**Miroslava Vukčević** (Serbia): Soliton structures in different astrophysical systems **[17:00-17:20]**
17:30-18:00	**Yue Ying Qi** (China): Atomic structure and dynamic process in ideal and non-ideal plasma with Prof. Ratko Janev *(Virtual)*	**Nikola Veselinović** (Serbia): Correlation analysis of solar wind parameters and secondary cosmic rays flux **[17:20-17:40]**
18:00-18:30	**Predrag Krstic** (USA): Vibrationally resolved collisions of hydrogen ions and molecule *(Virtual)*	**Đorđe Savić** (Serbia): Modeling broad line polarization in active galactic nuclei **[17:40-18:00]**
18:30-20:00	***Poster session (1)*** □ Regular and virtual poster presentation [*Optional: 3min presentation of posters]	
20:00	***Conference dinner***	

Wednesday 26th August SPIG 2020 (day 3)	**REGULAR+VIRTUAL**	
PL *– Plenary lecture: 35+10 min*	***TL*** *– Topical lecture: 25+5 min*	***PR*** *– Progress Report: 15+5 min*
	Plenary Session 4, Hall A, *Chair: B. Marinković*	
09:00-09:45	**K.-D. Weltmann** (Germany): Physical Applications in Life Science *(Virtual)*	
09:45-10:30	**Nigel Mason** (UK): New frontiers in Atomic and Molecular Physics *(Virtual)*	
10:30-11:00	*Coffee break*	
	Hall A - Parallel Session 3. LOW TEMPERTURE PLASMAS *Chair: G. Poparić*	***Hall B - Parallel Session*** 1. ATOMIC COLLISION PROCESSES *Chair: M. S. Dimitrijević*
11:00-11:30	**Nikša Krstulović** (Croatia): Cavity Ring-Down Spectroscopy as a Tool for Plasma Diagnostics *(Virtual)*	**Miloš Ranković** (Czech Republic): Electron collisions with dielectric gases considered as SF6 replacement

11:30-12:00	**Daiji Kato** (Japan): Compact electron beam ion trap for spectroscopy of multiple charged ions *(Virtual)*	**Nikolay Shvetsov-Shilovskiy** (Germany): Semiclassical two-step model for strong-field ionization: Further developments and applications
12:00-12:20	**Sanja Živković** (Serbia): Analytical capabilities of TEA CO2 laser based LIBS setup	**Dejan Miličević (Serbia);** Study of structural modifications in poly(L-lactide) (PLLA) induced by high-energy radiation
12:30-14:30	*Lunch break /SPIG Committee meeting at 13h*	
	Hall A - Parallel Session 4. GENERAL PLASMAS *Chair: D. Marić*	
14:30-15:00	**Gregor Primc** (Slovenia): Probing neutral oxygen atoms by laser-optic catalytic sensor	
15:00-15:20	**Ivan Krstić** (Serbia): Spectroscopic investigation of discharge and afterglow phase of microsecond pulsed glow discharge	
15:20-15:40	**Jelena Marjanović** (Serbia): Breakdown and characteristics of non-equilibrium low-pressure DC discharges in vapours of liquids	
16:00-18:00	*Excursion (visit of the city museum)*	

Thursday 27th August 2020 **SPIG 2020 (day 4)**	**ONLY VIRTUAL**	
PL *– Plenary lecture: 35+10 min*	***TL*** *– Topical lecture: 25+5 min*	***PR*** *– Progress Report: 15+5 min*
	Plenary Session 5, Room A*, Chair: A. Ivković*	
09:00-09:45	**Masaharu Shiratani** (Japan): Materials Processing with Low Pressure Plasma: Present Issues and Possible Solutions	
09:45-10:30	**Sibylle Günter** (Germany): The two concepts of magnetic confinement: tokamak and stellarator	
10:30-11:00	*Coffee break & Chat Room*	
	Plenary Session 6, Room A, *Chair: D. Ilić*	
11:00-11:45	**Netzer Hagai** (Israel): Following Supermassive Black Holes Over Cosmic Time	
11:45-12:30	**Dimitri Batani** (France): Current status of the laser fusion research and the shock ignition approach	
12:30-14:00	*Lunch break*	
	Room A - Parallel Session 4. GENERAL PLASMAS *Chair: M. Škorić*	***Room B - Parallel Session*** 3. LOW TEMPERATURE PLASMAS *Chair: M. Kuraica*
14:00-14:30	**Alicja Domaracka** (France): Ion processing of astrophysical ices	**Andrew Gibson** (Germany): Numerical simulation-based optimisation of plasma sources for medical applications

14:30-15:00	**Sebastijan Brezinsek** (Germany): Plasma-wall interaction in W7-X operating with graphite divertor	**Marie-Lise Dubernet** (France): VAMDC – Results and Perspective
15:00-15:20	**Damir Devetak** (Germany): Dissipative phenomena in QCD plasma state created in heavy ion collisions	**Željko Mladenović** (Serbia): Atmospheric pressure helium plasma jet propagating in humid air - influence of water vapour on chemical composition and plasma parameters
15:20-15:40	*Coffee break & Chat Room*	
	Room A - Parallel Session 4. GENERAL PLASMAS *Chair: S. Tošić*	***Room B - Parallel Session*** 2. PARTICLE AND LASER BEAM INTERACTION WITH SOLIDS *Chair: Z. Mišković*
15:40-16:10	**Joël Rosato** (France): Spectroscopic modeling for the investigation of magnetic fusion plasmas and stars with magnetic field	**Régis Bisson** (France): Simulating plasma-wall interaction in fusion reactors with beam-surface experiments
16:10-16:40	**Masanori Nunami** (Japan): Turbulence simulations for stellarator plasma transport	**Kamran Akbari** (Spain): Relativistic Theory of the Interaction of Two-Dimensional Materials with Moving Charged Particles **[16:00-16:20]**
16:40-17:00	*Coffee break & Chat Room*	
	Room A - Parallel Session 3. LOW TEMPERATURE PLASMAS *Chair: S. Djurović*	***Room B - Parallel Session*** 1. ATOMIC COLLISION PROCESSES *Chair: I. Mančev*
17:00-17:30	**Augusto Stancampiano** (France): Plasma jets and multijets in contact with liquids in biomedical experiments: electro fluid dynamic and reactive species distribution	**Dmitry Voloshin** (Russia): PIC MCC and fluid simulation of processing plasmas: collision radiative models and ion energy distribution functions
17:30-17:50	**N. Ben Nessib** (Saudi Arabia): The Fully Relativistic Multiconfiguration Dirac-Hartree-Fock Method for Atomic Structure Calculations for Multiply Charged Ions: The Example of Ca XV	**Ramón L. Panadés-Barrueta** (France): On the automatic computation of global (intermolecular) potential energy surfaces for quantum dynamical simulations
17:50-18:10	**Aleksandra Nina** (Serbia): Propagation of electromagnetic waves in perturbed lower ionospheric plasma	**Luca Vialetto** (Netherlands): Monte Carlo flux modelling of electron kinetics in CO2
18:10-20:00	**Poster session (2)** - Virtual presentation of posters [*Optional: 3min presentation of posters]	

Friday 28th August 2020 **SPIG 2020 (day 5)**	**ONLY VIRTUAL**	
PL *– Plenary lecture: 35+10 min*	***TL*** *– Topical lecture: 25+5 min*	***PR*** *– Progress Report: 15+5 min*

	Room A - Parallel Session 4. GENERAL PLASMAS *Chair: V. Srećković*	***Room B - Parallel Session*** 1. ATOMIC COLLISION PROCESSES *Chair: M. Trtica*
9:00-9:30	**Jovan Milošević** (Norway): Quark gluon plasma in an early phase of the Universe and in the laboratory	**Tiago Silva** (Portugal): A detailed reaction mechanism set for vibrational chemistry in CO2 plasmas
9:30-9:50	**Andjelka Kovačević** (Serbia): Rise of LSST - detection of oscillations in AGN emission light curves at different cosmological scales	**Jasper Peschel** (Sweden), Dissociation dynamics of the diamondoid adamantane upon photoionization by XUV femtosecond pulses
9:50-10:10	**Jelena Petrović** (Serbia): The evolution of stellar interiors in massive binary systems	**Ilija Simonović** (Serbia): Kinetic and fluid modelling of non-equilibrium transport of charged-particle swarms in neutral gases and nonpolar liquids
10:10-10:30	**Aleksandra Ćiprijanović** (Serbia): Multi-messenger studies of cosmic ray acceleration in galaxy cluster accretion shocks	**Ana Silva** (Netherlands): A reaction mechanism for vibrationally cold CO2 plasmas
10:30-10:50	**Nikolai Bezuglov** (Russia): Penninning ionization processes involving cold Rydberg alkali metal atoms	**Abeer Almodlej** (Saudi Arabia): The Modified Semi-Empirical Stark Broadening method of calculations: The example of Alkali like ions
11:00-11:30	*Coffee break & Chat Room*	
	Plenary Session 7, Room A, *Chair: D. Borka*	
11:30-12:15	**Dragan Huterer** (USA) Dark Matter and Dark Energy: Gases that Dominate the Universe	
12:15-13:00	**Jaime de Urquijo** (Mexico) The measurement of electron and ion swarms transport and reactivity: Current state and future challenges	
13:00-13:30	*Discussion and Chat Room (D. Ilić, V. Srecković)*	
13:30-14:00	***Closing of the conference***	

LIST OF POSTERS

Maximum dimensions of your poster should be 60cm (width) x 90cm (height).

No	Session	Title	Author
1	1.1.	A DFT study of dissociative electron attachment to C5XH4N and C4XH3N2 (X=H,Cl,Br) aromatic molecules	N. Tańska
2	1.1.	Excitation of the (001) mode of CO2 IN 2.45 GHz microwave E field and DC B field	M. M. Vojnović, V. V. Stanković, M. M. Ristić, G. B. Poparić
3	1.1.	Rates for excitation of the CO2 Fermi resonance members in rf electric field	V. V. Stanković, M. M. Vojnović, M. M. Ristić, G. B. Poparić
4	1.1.	Cross sections calculations for electron scattering from rhodanine and cyanoacetic acid	B. Zywicka, P. Mozejko

5	1.1.	The m4,5nn auger spectrum of krypton in kinetic energy region 24 – 64 eV	B. P. Marinković, J. J. Jureta, L. Avaldi
6	1.1.	Analytical Formula for the Output Factor calculation of Small Radiation Beams	S. J. Al Atawneh, L. M. Abu-Arida, K. Tokesi
7	1.1.	Determining extrapolated differential cross sections from data sets in BEAMDB using machine learning algorithms	S. Ivanović, N. Uskoković, B. P. Marinković, N. J. Mason
8	1.1.	Resonant electron scattering by metastable nitrogen - revisited	I. Čadež
9	1.1.	Hyperfine splitting of the lowest state energy of positronium in strong electric field	M. Z. Milošević, A. Bunjac, D. B. Popović, N. S. Simonović
10	1.1.	Selective multiphoton ionization of sodium by femtosecond laser pulses	A. Bunjac, D. B. Popović and N. S. Simonović
11	1.2.	Single-electron capture in p-He^+ collisions	D. Delibašić, N. Milojević, I. Mančev
12	1.2.	Introducing a new guided ion beam instrument - NOVion	I. Savić, S. Schlemmer, D. Gerlich
13	1.3.	Rate coefficients for Ar^+ in Ar/BF3 mixtures	Z. Nikitovic, M. Gilic, J. Mitric, Z. Raspopovic
14	2.1.	Ionic velocity as a measure of an interplay of the neutralization energy and the deposited kinetic energy in the surface nanostructure creation	M.D. Majkić, N.N. Nedeljković and M.A. Mirković
15	2.1.	State-selective charge exchange cross sections in $Be4^+$+ H(1s) collision	I. Ziaeian, K. Tőkési
16	2.1.	Channeling potential through radial deformed triple wall carbon nanotubes	D. Borka, V. Borka Jovanovic
17	2.1.	Potential energy calculations of a charged particle outside a real metal surface	S. M. D. Galijaš, G. B. Poprаić, V. Milosavljević
18	2.1.	Interactions of ions with graphene-sapphire-graphene composite system: stopping force and image force	A. Kalinic, I. Radovic, L. Karbunar, V. Despoja, Z. L. Miskovic
19	2.2.	Characterization of Plasma Deposited Carbon-Silicon Oxide Thin Films	C. Carra, R. Barni, D. Dellasega, A. Natalello, M. Fanciulli, A. Medvids, C. Riccardi
20	2.3.	Tungsten and ods steel behavior at high intensity, 1015 W/cm^2, laser irradiation in air and vacuum ambience: comparative study	M. Trtica, J. Stasic, J. Limpouch, P. Gavrilov
21	2.3.	Principal components analysis of printed circuit board LIBS data	D. Sevic, M. S. Rabasovic, P. Gregorcic, M. D. Rabasovic, B. P. Marinkovic
22	2.3.	Numerical investigation of the plasma formation in skin tissue by nanosecond Nd: Yag laser pulse	H. Delibašić, V. Petrović, I. Petrović, C. Molpeceres, S. Lauzurica
23	2.3.	Treatment of steel surfaces by plasma flow generated in magnetoplasma compressor	N. Trklja Boca, Ž. Mišković, B. Obradović, R. Mitrović, M. Kuraica
24	2.3.	Appearance of Be II 436.1 nm line with forbidden component in LIBS plasma	B. D. Stankov, M. R. Gavrilović Božović, M. Ivković

25	3.1.	The electron number density measurement from pulsed pin-to-cylinder gas discharge source at atmospheric pressure in helium	J. Jovović
26	3.1.	Measurement of electric field distribution along the cathode sheath of an abnormal glow discharge using Ne I 556.277 nm line	N. V. Nedić, N. V. Ivanović, Dj. Spasojević, N. Konjević
27	3.1.	Temperature relaxation process and expansion of laser induced plasma	M. Skocic, D. Dojic, S. Bukvic
28	3.1.	Determination of the temperature distribution in the cathode sheath region of hydrogen glow discharge using q-branches of Fulcher-a band	M. M. Vasiljević, G. Lj. Majstorović, Dj. Spasojević
29	3.1.	Accurate calculations of energy levels, weighted oscillator strengths, transitions probabilities and lifetimes of He-like oxygen	D. E. Salhi, H. Jelassi
30	3.1.	Comparison of experimental and semi-classical results for Ar II stark broadening parameters for (3P) 4s 2P – (3P) 4p 2Do multiplet	S. Djurović, B. Blagojević, N. Konjević
31	3.1.	Stark broadening of spectral lines within copper-like emitters	N. Trklja Boca, I. P. Dojčinović, I. Tapalaga, J. Purić
32	3.1.	Stark line broadening within spectral series of potassium isoelectronic sequence	I. P. Dojčinović, N. Trklja Boca, I. Tapalaga, J. Purić
33	3.1.	Optical emission spectroscopy of H2 in a toroidal magnetised plasma	R. Barni, P. Alex, E. Ghorbanpour, C. Riccardi
34	3.1.	Radial distribution of plasma electron density and temperature in atmospheric plasma jet	Z. Mijatović, S. Djurović, I. Savić, L. Gavanski, T. Gajo
35	3.1.	Diagnostics of plasma produced by laser ablation of carbon-based polymer material	M. Kuzmanovic, D. Rankovic, J. Savovic, V. Kiris, A. Nevar, M. Nedelko, N. Tarasenko
36	3.1.	Nanostructures assisted tea-CO2 based LIBS: improvement of the limit of detection	S. Živković, J. Petrović, M. Ognjanović, J. Ciganović, D. Blaženka, N. Krstulović, M. Momčilović
37	3.1.	LIBS technique based on TEA CO2 laser for elemental analysis of impurities in graphite	J. Petrovic, M. Kuzmanovic, D. Rankovic, M. Trtica, J. Savovic
38	3.1.	VUV Spectroscopy of the He II - Lyman Series for Electron Density Estimation	I. Traparić, M. Ivković
39	3.1.	Investigation of a microsecond-pulsed cold plasma jet	N. Cvetanović, M. A. Shahriar. B. M. Obradović, Z. Liu, K. Yan, M.M. Kuraica
40	3.2.	A new look at surface-wave sustained plasma: magnetic current model treated by a fixed-point method	M. S. Kovačević,M. M. Milošević, Lj. Kuzmanović, A. Djordjevich
41	3.2.	Transition from electron avalanche number distributions to formative time delay distributions for multielectron initiation and streamer breakdown mechanism (I)	S. N. Stamenković, V. Lj. Marković
42	3.2.	Formative time delay distributions for multielectron initiation and Townsend breakdown in neon (II)	V. Lj. Marković, S. N. Stamenković
43	3.2.	Plasma modification of lignocellulosic textile materials	A. Kramar, B. Pejić, B. Obradović, M. Kuraica, M. Kostić

44	3.2.	Applied voltage waveform suitable to control parameters of dielectric barrier discharge plasma jet	M.E. Pinchuk, A.M. Astafiev, R.A. Aznabaev, O.M. Stepanova
45	3.3.	Relativistic configuration interaction of energy levels, wavelengths, oscillator strengths, radiative rates and lifetimes of He-like lithium.	S. Manai, D.E. Salhi
46	3.3.	Optical emission spectroscopy of a gliding arc tornado device	R. Barni, P. Alex, A. Salanti, C. Canevali, L. Zoia, M. Orlandi, C. Riccardi
47	3.3.	Surface Dielectric Barrier Discharge plasma MATLAB simulation	C. Piferi, R. Barni, C. Riccardi
48	3.3.	Next generation of universal pulse resonance atmospheric plasma systems	M. Gulan, V. Milosavljević
49	3.3.	RF N2/Ar gas mixture plasma induced modification of acoustical properties of textile fabrics made of natural cellulose fibers (cotton, hemp)	S. S. Pavlović, V. M. Milosavljević, P. J. Cullen, S. B. Stanković, D. M. Popović, G. B. Poparić
50	4.1	Collision between two hydrogen atoms	S. J . Al Atawneh, K. Tokesi
51	4.2.	Collapse of polarized atomic states in magnetic fields	E. A. Viktorov, M. S. Dimitrijević, V. A. Srećković, N. N. Bezuglov, K. Miculis, A. A. Pastor, P. Yu. Serdobintsev
52	4.2.	Ionospheric D-region influence on SAR signal propagation	J. Radović, A. Nina, G. Nico
53	4.2.	Influence of light-curve sampling on the periodicity determination in case of subparsec super-massive black hole binaries	S. Simić, Luka Č. Popović, A. Kovačević, D. Ilić
54	4.2.	Reduction of lower ionosphere plasma fluctuation – new earthquake precursor?	A. Nina, S. Pulinets, P.F. Biagi, G. Nico, S.T. Mitrović, M. Radovanović, L.Č. Popović
55	4.2.	Applications of Manifold Learning Techniques to Spectral Classification of Quasars	I. Jankov, D. Ilić, A. Kovačević
56	4.2.	The signature of the gas outflow in the active galactic nuclei type 2 spectra	J. Kovačević-Dojčinović, M. Lakićević L. Č. Popović
57	4.2	Virilization of the broad Hα emission region in active galactic nuclei type 1	S. Marčeta-Mandić, J. Kovačević-Dojčinović, L. Č. Popović
58	4.2.	Numerov method analysis with a goal of application of complex plasma models	N. M. Sakan, Z. Simic
59	4.2.	Kinematical properties of elliptical galaxies in Yukawa-like gravity	V. Borka Jovanovic, D. Borka, P. Jovanovic
60	4.2	Impact of Stark broadening on Co II spectral line modeling in hot stars	A. Almodlej, Z. Majlinger, N. Ben Nessib, M. S. Dimitrijević, V.A. Srećković

ACKNOWLEDGEMENT

30th SUMMER SCHOOL AND INTERNATIONAL SYMPOSIUM ON THE PHYSICS OF IONIZED GASES

is organized by

Faculty of Mathematics, Department of Astronomy

Institute of Physics, University of Belgrade

Astronomical Observatory of Belgrade

and

with the support of the

Ministry of Education, Science and Technological Development, Republic of Serbia

Republic of Serbia
Ministry of Education, Science and Technological Development

sponsored by

City of Šabac

SPECS™

Telekom Srbija

media sponsors:

EPJ D
Atomic, Molecular, Optical and Plasma Physics

universe
an Open Access Journal by MDPI

RoentDek Handels GmbH
Supersonic Gas Jets
Detection Techniques
Data Acquisition Systems
Multifragment Imaging Systems

atoms

technical organizer

PANACOMP - Zemlja čuda d.o.o.